Targeting GPR84: a receptor involved in regulating inflammation

A thesis submitted for the degree of

Doctor of Philosophy

Daniel Lucy

Balliol College

University of Oxford

Michaelmas 2019

Declaration

The work presented in this thesis is my own, except where otherwise stated, and has been generated as a result of my original research conducted under the joint supervision of Prof. Angela Russell and Prof. David Greaves. No part of this thesis has been submitted for any other degree at this or any other university.

Daniel Lucy

24th September 2019

Abstract

GPR84 is a G protein-coupled receptor that is activated by medium-chain fatty acids and is highly expressed in macrophages, suggesting a role for dietary fatty acids in the regulation of inflammatory responses. The validation of GPR84 as a therapeutic target has been hindered by the structural homogeneity and poor selectivity of available chemical tools, and the consequent poor understanding of GPR84 physiology. The aim of this thesis was to develop structurally novel GPR84 agonists that may reveal new aspects of GPR84 biology.

A ligand-based virtual screening approach was used to identify a compound active in recombinant cell cAMP assays that represents a new scaffold of GPR84 agonist. The compound was chemically optimised and extensively characterised for potency, stability, solubility, and selectivity, resulting in DL-175 which shows properties appropriate for an *in vitro* chemical probe. Furthermore, unlike previously reported GPR84 ligands, DL-175 is inactive in β-arrestin recruitment assays, showing a marked bias for G protein signalling pathways.

In primary murine bone marrow-derived macrophages (BMDMs), DL-175 induced dose-dependent responses in impedance signalling assays that were absent in GPR84$^{-/-}$ BMDMs. Moreover, the BMDM response to DL-175 was significantly more sustained than that induced by range of published GPR84 agonists, indicative of biased signalling in disease-relevant primary cells. The functional consequences of biased agonism at GPR84 in immune cells were investigated by a direct comparison between DL-175 and widely used GPR84 agonist 6-OAU. Both agonists enhance U937 macrophage phagocytosis, but have strikingly different abilities to promote chemotaxis in the same cells. This work demonstrates that biased agonism enables the selective activation of functional responses in immune cells and delivers a high-quality chemical probe for further investigation.

Acknowledgements

Firstly I would like to thank Prof. Russell and Prof. Greaves for taking me into their labs and for their brilliant supervision. Thanks for giving me the space to take this project in my own direction, while still giving ample guidance to keep me on the right track. I also want to thank the British Heart Foundation CRE for generously funding my DPhil project.

In the Russell lab, particular thanks goes to Maria, Carole, and Graham for your constant help, advice, and support over the past 3 years, I'm very grateful. Thanks also to Laurence, the Toms, Dan, Morgan, Laura, Nicky, Kate, Liam, Aini, and all the other Russell group members who made it such a great place to work. Special mention goes to Seb for his sage advice and unsolicited marathon coaching. I would also like to thank the two GPR84 Master's students, Bridget and Jacob, for their contribution to the project.

Next, I want to thank all the Greaves lab members who've made the lab an enjoyable and productive workplace over the years. In particular, thanks to Carlota and Gareth for teaching me most of the biology lab techniques I know today and for occasionally reminding me that DPhil students are supposed to have fun too. Lynda, thanks for helping with the flow cytometry experiments and for teaching me French. Agata, thanks for the cake - I officially promote you to Senior DPhil. I'm also grateful to Lewis for always being free to answer my many questions about his thesis, and to Lior for showing me the ropes in molecular biology.

After 8 years at Balliol, I would like to thank all the staff, tutors, and friends who have made it such a difficult place to leave. Anna, you are the most unexpected and best result of me staying in Oxford for a second round, thanks for making the last couple of years so much fun. Finally I want to thank my whole family, especially my Mum and Dad, whose support I sometimes take for granted, but without which this thesis wouldn't have been possible.

Abbreviations

6-OAU 6-Octylaminouracil

AhR . . . . . Aryl hydrocarbon receptor

AOX . . . . . Aldehyde oxidase

BMDM . . . . . Bone marrow-derived macrophage

CAC . . . . . Critical aggregation concentration

cAMP . . . . . Cyclic adenosine monophosphate

CDI . . . . . 1,1'-Carbonyldiimidazole

CHO . . . . . Chinese hamster ovary

CI . . . . . Cell index

CYP450 . . . . . Cytochrome P450

D_2R . . . . . Dopamine D_2 receptor

DIAD . . . . . Diisopropyl azodicarboxylate

DIM . . . . . 3,3'-Diindolylmethane

DMSO . . . . . Dimethyl sulfoxide

EL . . . . . Extracellular loop

Et . . . . . Ethyl

ESI . . . . . Electrospray ionisation

FITC . . . . . Fluorescein isothiocyanate

FFA . . . . . Free fatty acid

FFAR . . . . . Free fatty acid receptor

GPCR . . . . . G protein-coupled receptor

GRK . . . . . G protein-coupled receptor kinase

GTP . . . . . Guanosine triphosphate

HEK . . . . . Human embryonic kidney

HRMS . . . . . High-resolution mass spectrometry

IL . . . . . Intracellular loop

IR . . . . . Infrared

LC-MS . . . . . Liquid chromatography-mass spectrometry

LCFA . . . . . Long-chain fatty acid

LPS . . . . . Lipopolysaccharide

MACS . . . . . Magnetic-activated cell sorting

MAPK . . . . . Mitogen-activated protein kinase

Me . . . . . Methyl

MEK . . . . . Methyl ethyl ketone

MCFA . . . . . Medium-chain fatty acid

MCS . . . . . Maximum common substructure

MP . . . . . Melting point

mRNA . . . . . Messenger ribonucleic acid

MS . . . . . Mass spectrometry

NAM . . . . . Negative allosteric modulator

NF-κB . . . . . Nuclear factor kappa-light-chain-enhancer of activated B cells

NMR . . . . . Nuclear magnetic resonance

NOE . . . . . Nucelar Overhauser effect

PBMCs . . . . . Peripheral blood mononuclear cells

PBS . . . . . Phosphate-buffered saline

Ph . . . . . Phenyl

PI3K . . . . . Phosphoinositide 3 kinase

PMA . . . . . Phorbol 12-myristate 13-acetate

PTX . . . . . Pertussis toxin

PUFA . . . . . Polyunsaturated fatty acid

PAM . . . . . Positive allosteric modulator

PKC . . . . . Protein kinase C

Py . . . . . Pyridine

QSAR . . . . . Quantitative structure-activity relationship

rt . . . . . Room temperature

RT-qPCR . . . . Quantitative reverse-transcription polymerase chain reaction

S1P$_1$R . . . . . Sphingosine-1-phosphate receptor 1

sat. . . . . . Saturated

SCFA . . . . . Short-chain fatty acid

SAR . . . . . Structure-activity relationship

TLR . . . . . Toll-like receptor

TM . . . . . Transmembrane

THF . . . . . Tetrahydrofuran

μOR . . . . . μ-opioid receptor

UV . . . . . Ultraviolet

WaterLOGSY . . Water-ligand observed via gradient spectroscopy

WT . . . . . Wild type

Contents

Chapter 1

Introduction

1.1 G protein-coupled receptors

G protein-coupled receptors (GPCRs) are membrane bound proteins that transduce extracellular signals into cellular responses. With over 800 GPCRs in the human genome, they form by far the largest receptor family and have important physiological roles in virtually every cell and tissue that constitutes the human body.[1] An extraordinary range of stimuli can activate GPCRs including small molecules, peptides, proteins, ions, and photons, and this diversity of activation is reflected in the wide range of functions regulated by GPCRs: the rate and strength of the beating heart is regulated by adrenergic receptors; the detection of neurotransmitters in the brain occurs through dopamine and serotonin receptors; and the recruitment of immune cells to sites of infection is controlled by chemokine receptors.[2,3] Approximately 400 GPCRs are olfactory receptors involved in smell and taste sensations, while at least 100 of the non-olfactory GPCRs are orphans with mostly unknown function, representing an untapped resource of physiological understanding and potential therapeutic intervention.[4,5]

The diversity of ligands and physiological roles for GPCRs stands in contrast to their relatively conserved structure and signalling mechanisms. GPCRs feature a characteristic seven transmembrane topology which allows extracellular ligand binding to be converted into intracellular signalling through receptor conformational changes. Following the formation of ligand-receptor complexes, heterotrimeric G proteins within the cell are activated and in-

duce signalling cascades through interactions with effector molecules such as ion channels or enzymes that generate second messengers within the cell. Further signalling apparatus such as β-arrestin or G protein-coupled receptor kinases (GRKs) can interact with the various active conformations of GPCRs, enabling the receptors to act as allosteric microprocessors to control signalling within the cell.[6]

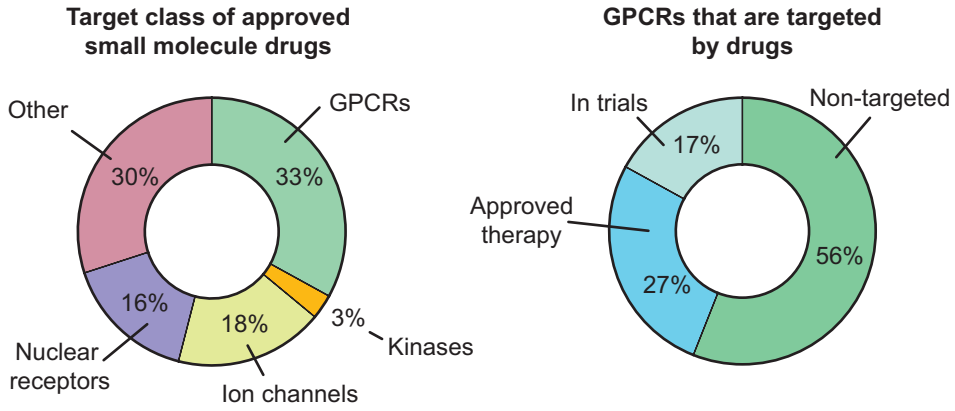

Figure 1.1: GPCRs are both the most successful drug target class and an underexploited resource of new therapies. GPCRs are the target for 33 % of approved small molecule drugs, more than any other major family (left).[7] Only 27 % of non-olfactory GPCRs are established drug targets (right), with a further 17 % having a novel therapy currently in clinical trials.[4] The remaining 56 % are currently not targeted by any approved or experimental medications.

GPCR drugs such as the β-blocker propranolol and the antihistamine cimetidine, both developed by James Black, were among the first blockbuster drugs that revolutionised the drug discovery process in the second half of the 20th century.[8] To this day, GPCRs occupy a central position in pharmaceutical development with approximately 33 % of approved drugs targeting GPCRs (Figure 1.1) for a combined 27 % global market share of drug sales between 2011 and 2015.[7,9] The utility of GPCRs as therapeutic targets stems from their role in many pathophysiological processes and their ability to bind extracellular ligands with high affinity and specificity. The many GPCRs yet to be exploited therapeutically (Figure 1.1), combined with emerging concepts such as allosteric agonism and biased signalling, ensures that GPCRs are likely to be a rich source of new medications for years to come.[4]

1.1.1 Structure

GPCRs comprise an intracellular C-terminal domain and an extracellular N-terminal domain linked by 7 transmembrane spanning α-helices (TM1-7) organised into a central bun-

dle, with three extracellular loops (EL1-3) and three intracellular loops (IL1-3) connecting them (Figure 1.2).[10] The extracellular domain mediates ligand recognition and access to the receptor, the TM domain binds the ligand and transduces the signal to the intracellular domain, which interacts with heterotrimeric G proteins, β-arrestin, and various kinases that together initiate downstream signalling. Within the confines of this conserved transmembrane topology there is significant structural diversity in the GPCR superfamily, and the receptors are therefore classified according to their primary sequence into five main families: rhodopsin (class A), secretin (class B), glutamate (class C), frizzled/taste, and adhesion.[11] The secretin-like class B GPCRs, for example, primarily bind peptides and possess an extracellular N-terminal domain of 120–160 residues, whereas glutamate-like class C GPCRs have a characteristically large "venus flytrap" extracellular domain and form constitutive dimers.[12,13] The class A GPCRs, which this thesis will exclusively focus on, have limited extracellular N-terminal domains and form by far the largest sub-family, with the adrenergic, opioid, cannabinoid, histamine, and chemokine receptors as representative examples.[11]

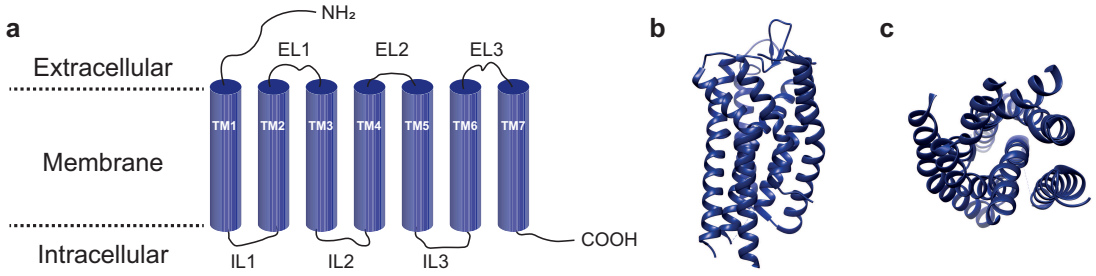

Figure 1.2: The 7-transmembrane domain architecture common to all GPCRs. **(a)** A cartoon representation of a GPCR transmembrane and loop regions. **(b)** Crystal structure of a class A GPCR with the helical transmembrane bundle visible from the membrane perspective and **(c)** viewed from the extracellular side. PDB: 4PHU.

Although the common 7-TM architecture of GPCRs was first predicted by sequence analysis of the β-adrenergic receptor (βAR) in the 1980s, the almost negligible concentration of GPCRs in the membrane and their poor stability upon isolation has made them a challenging target for X-ray crystallography. Until 2007, the only solved eukaryotic GPCR crystal structure was that of bovine rhodopsin which benefits from a high natural abundance and structural stability conferred by the covalently bound, light-sensitive ligand 11-*cis*-retinal.[14] Innovations such as GPCR antibody stabilisation, lipidic cubic phase crystallography, and lysozyme incorporation enabled the structure of the β_2AR to be solved,[14,15] and further in-

novations such as nanobody stabilisation of receptors in the active state has facilitated the solving of structures for 44 more GPCRs in the ensuing 12 years.[16] These structural advances have provided a wealth of information and advanced our understanding of GPCR pharmacology.

Orthosteric ligand binding

The orthosteric ligand binding site in class A GPCRs is a conserved binding pocket within the transmembrane bundle, with residues from TM3, TM6, and TM7 contributing binding interactions in all solved structures.[17] The position and size of the binding site varies according to receptor class, as exemplified by the structure of the peptide sensing neurotensin receptor which displays a larger binding site with reduced penetration in the TM bundle compared to aminergic receptors, presumably to accommodate the larger ligand.[18] Although topologically conserved, the sequences composing the TM helices are diverse with appropriate residues reflecting the nature of the cognate ligand. Binding sites for peptide receptors are therefore more hydrophilic than the lipid receptors, where binding specificity is determined by steric compatibility and the limited polar interactions.[19]

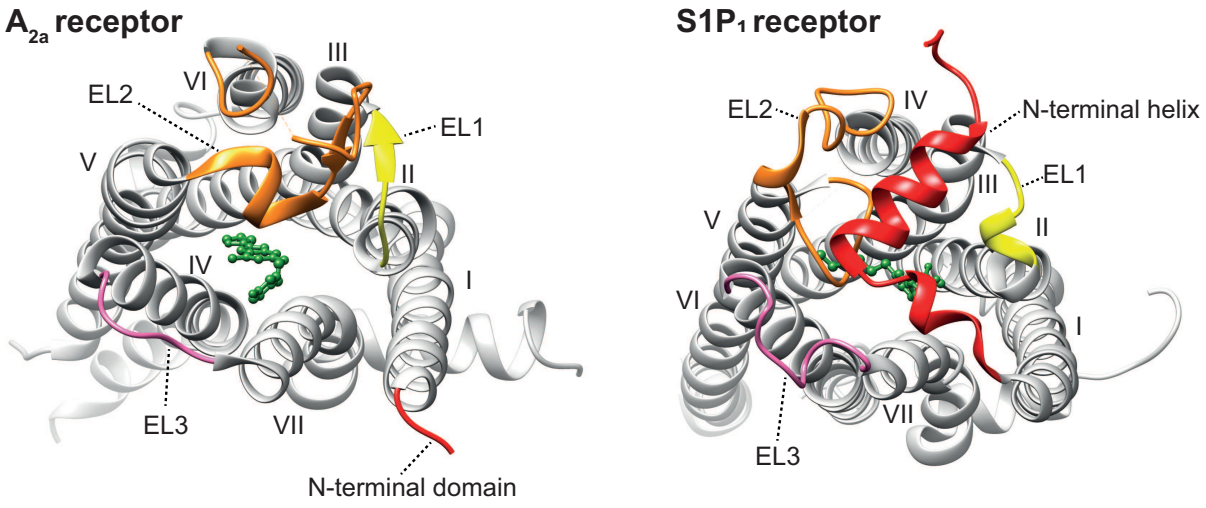

Figure 1.3: Class A GPCRs have structurally diverse extracellular domains to accommodate various ligand classes. Crystal structures of the adenosine A_{2a} receptor and the lipid $S1P_1$ receptor. The binding pocket of the $A_{2a}R$ is open and solvent accessible enabling direct access for its water soluble ligands. In contrast, the N-terminal domain and EL2 of the $S1P_1R$ form a lid that provides additional ligand binding interactions and forces the hydrophobic ligand to enter laterally between TM1 and TM7 from the membrane. PDB: 3EML and 3V2Y.

In comparison to the structurally conserved TM domain, the extracellular domains of GPCRs are highly divergent, reflecting the diversity of ligands that can be recognised. The N-terminus and extracellular loops, particularly EL2, play an important role in ligand entry into the binding site. Receptors that bind water-soluble small molecules such as the adenosine A_{2a} receptor have small, solvent accessible binding pockets within the TM helical bundle. In contrast, 7 out of 8 solved lipid sensing GPCRs show tight folding of the extracelluar N-terminal domain that effectively occludes the ligand-binding site.[20] For example, the α-helical N-terminal domain of sphingosine-1-phosphate receptor 1 ($S1P_1R$) folds over the ligand binding site to contribute binding interactions and, together with EL2 and EL3, prevent access from the extracellular space (Figure 1.3).[21]

Allosteric ligand binding

Aside from the orthosteric GPCR binding site, ligands can additionally bind to various allosteric sites across the receptor. These binding pockets may overlap with the orthosteric site or may be spatially distinct, as exemplified by the ternary crystal structure of CC chemokine receptor 2 bound to both an orthosteric antagonist and a second allosteric antagonist bound to the intracellular domain (Figure 1.4).[22] Allosteric ligands can be agonists or antagonists in their own right, but can additionally provide positive allosteric modulation (PAM) or negative allosteric modulation (NAM) by increasing or reducing the activity of orthosteric ligands respectively. Allosteric modulation of other protein classes such as enzymes is a ubiquitous biological process, and evidence is increasing to suggest that many natural ligands target allosteric sites on GPCRs *in vivo*. For example, many class A GPCRs are subject to allosteric modulation by sodium ions,[23] while various natural peptides are suggested to be endogenous allosteric ligands of the M_2 muscarinic acetylcholine receptor.[24]

Historically, small molecule drugs have targeted the orthosteric binding site as the endogenous ligand can often provide a molecular starting point for drug development. However, targeting allosteric binding sites can be advantageous and is emerging as an attractive therapeutic strategy in certain cases. The orthosteric binding site is generally well conserved between receptor sub-types, so targeting less conserved allosteric sites can confer greater

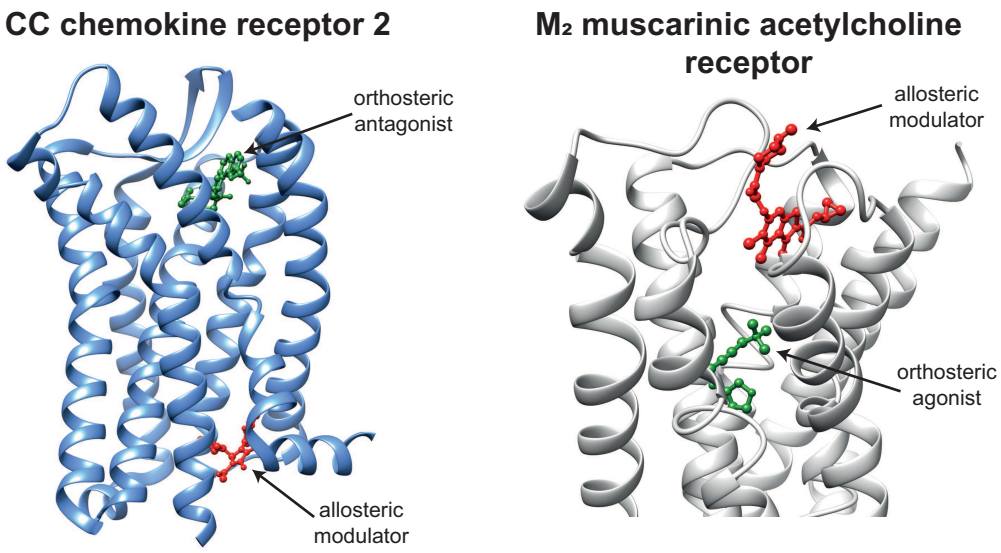

Figure 1.4: Representative examples of GPCR crystal structures bound to allosteric ligands. An allosteric antagonist of CC chemokine receptor 2 binds in the intracellular domain distal to the orthosteric binding pocker (left). A positive allosteric modulator of the M_2 muscarinic acetylcholine receptor binds closely to the orthosteric ligand (right).[25] PDB: 5T1A and 4MQT.

sub-type selectivity.[26] Furthermore, the ability of allosteric modulation to tune the activity of endogenous ligands by acting as a "dimmer switch" offers a new paradigm for drug discovery in the selective regulation of GPCR activity in a tissue-specific manner.[27]

Structural features of GPCR activation

Upon receptor activation by ligand binding, the cytoplasmic side of the receptor undergoes significant conformational changes that enable effective engagement with G proteins, GRKs, β-arrestin, and other signalling apparatus. In the agonist-bound β_2AR-G_s ternary complex, TM6 has undergone a significant 14 Å outward shift and TM5 a small outward rotation when compared with the inactive state structure of the same receptor.[14,28] This opening up of the intracellular face accommodates binding of a C-terminal α-helix from the G protein and subsequent G protein activation. Crystal structures provide an insight only into a single static low-energy conformation, whereas in reality GPCRs are in flux between many different conformational states that have different interactions with intracellular signalling proteins.[29] Understanding the structural dynamics of GPCRs will be of crucial importance in future understanding of GPCR physiology and the structure-based design of GPCR modulating drugs.

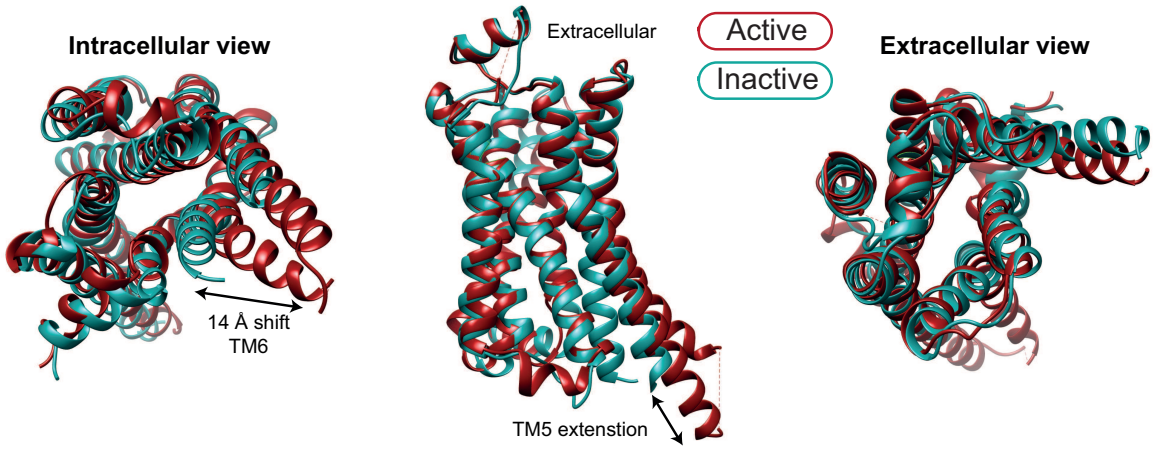

Figure 1.5: GPCR activation causes conformation changes in the intracellular domain. The inactive (blue) and active (red) state β_2AR structures are shown overlaid. The major conformational changes are a 14 Å shift in TM6 and an extension of TM5 by two helical turns. Only minor changes are observed in the extracellular domain. PDB: 2RH1 and 3SN6.

1.1.2 GPCR signalling

The GPCR structural changes induced by agonist binding causes activation of various signalling effectors distal to the receptor that ultimately leads to a physiological response. These downstream signalling activities are mediated by G proteins or β-arrestin that couple directly to effector molecules. Unlike other cellular signalling systems such as receptor tyrosine kinases that incorporate an effector element into the receptor, the modular system employed by G proteins and GPCRs enables significant functional diversity by the regulation of multiple possible signalling pathways.[30]

G proteins

G proteins are a family of membrane proteins that are activated by GPCRs and regulate various effector systems to generate cellular responses. G proteins are named for their interactions with guanine nucleotides and consist of three subunits: α, β, and γ. In the classical model of G protein activation (Figure 1.6), nucleotide exchange on the G protein-active-state receptor complex results in dissociation of the α subunit which, alongside the $G_{\beta\gamma}$ dimer, goes on to modulate various membrane effector proteins.[31] The 23 known human G_α subunits are divided into four families according to sequence similarity: $G_{\alpha i/o}$, $G_{\alpha s}$, $G_{\alpha q}$, and $G_{\alpha 12/13}$. Broadly, the $G_{\alpha i/o}$ and $G_{\alpha s}$ families have inhibitory and stimulatory effects on the enzyme adenylyl cyclase respectively, thus modulating downstream pathways by the regula-

tion of cyclic adenosine monophosphate (cAMP) production;[32] $G_{\alpha q}$ activates β isoforms of phospholipase C to initiate inositol lipid signalling;[33] and $G_{\alpha 12/13}$ regulates the Rho family of GTPases.[34]

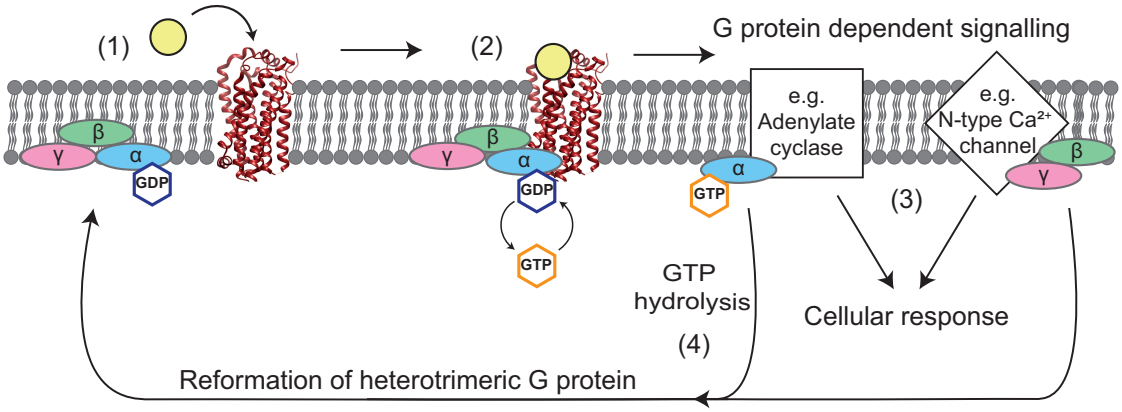

Figure 1.6: The classical model of G protein activation. (1) Agonist binding to a GPCR induces conformational changes that reveals a G protein binding site. (2) The α subunit of the G protein binds to the active state receptor causing the bound GDP to exchange for an guanine triphosphate (GTP) molecule. (3) The α-GTP complex then dissociates from the receptor and the βγ complex, leaving the α and βγ complexes free to diffuse through the membrane and modulate the activity of target effector proteins to cause cellular responses. (4) The α subunit has enzymatic GTPase activity that slowly hydrolyses GTP to GDP, causing the heterotrimeric G protein to reform and G protein dependent signalling pathway activation to cease.

The function of the $G_{\beta\gamma}$ complex was initially thought to be limited to negatively regulating the activity of the Gα subunit by inhibiting the dissociation of GDP when bound together in the heterotrimeric form.[35] It is now clear, however, that the $G_{\beta\gamma}$ complex has important and diverse signalling functions that are still being unravelled. In 1987 Logothetis et al. demonstrated that perfusing the intracellular surface of atrial cell membranes with purified $G_{\beta\gamma}$ was sufficient to activate the cardiac muscarinic-gated inwardly rectifying K^+ channel.[36] Since that seminal discovery, $G_{\beta\gamma}$ has been demonstrated as capable of acting on various other signalling effectors including voltage-dependent Ca^{2+} channels,[37] a subset of adenylyl cyclase isoforms,[38] mitogen-activated protein kinases (MAPK),[39] and phosphoinositide 3 kinases (PI3K).[40] It remains unclear if the diversity of $G_{\beta\gamma}$ dimers, composed from 5 G_β and 13 G_γ subunits in humans, results in any specificity of functional interactions with effectors.[41] The role of $G_{\beta\gamma}$ in regulating many physiological processes makes it an attractive therapeutic target, and small molecules and nanobodies capable of selectively blocking $G_{\beta\gamma}$ signalling are being developed for this purpose.[42]

Receptor desensitisation and β-arrestin signalling

A key feature of G protein signalling systems is the reduced response that is elicited from a receptor that has been previously activated. This process, termed desensitisation, prevents deleterious overstimulation of G protein signalling and maintains cellular homoeostasis.[43] The primary mechanism of GPCR desensitisation involves phosphorylation of the C-terminal tail by GRKs and subsequent recruitment of cytosolic β-arrestin that bind the receptor and block further signalling (Figure 1.7). The β-arrestin-receptor complex is internalised and either recycled back to the membrane or targeted for degradation in lysosymes, the latter enabling a sustained reduction in GPCR signalling by downregulation.[44] Although this mechanism is generally well conserved, different combinations of the various isoforms of GRK1-7 and β-arrestin1-2 are involved for different GPCRs, and some GPCRs, such as the M_1 muscarinic acetylcholine receptor, undergo β-arrestin independent internalisation.[45]

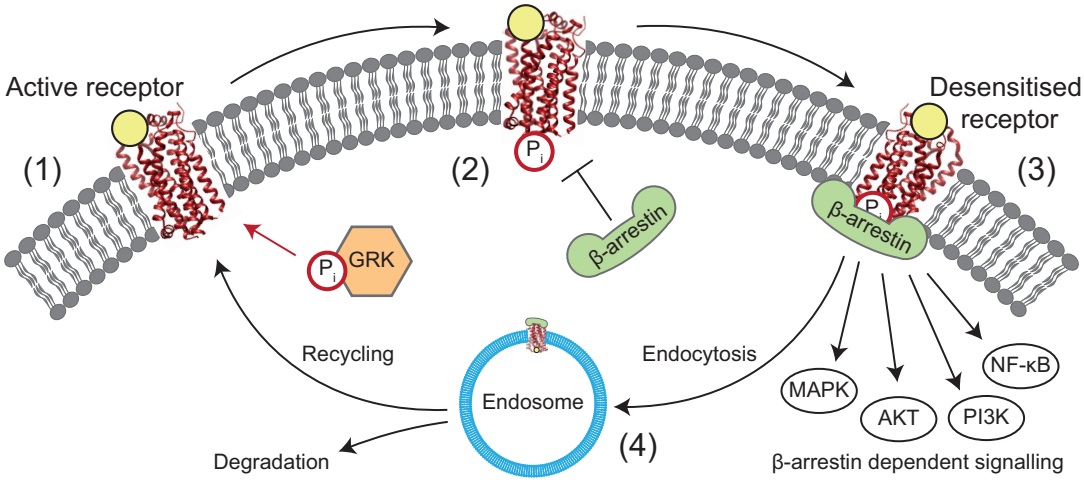

Figure 1.7: β-arrestin dependent desensitisation and signalling. (1) Agonist bound receptors are targeted for phosphorylation by GRKs on the C-terminal tail of the receptor. (2) Phosphorylation increases the affinity of the receptor for cytosolic β-arrestin which are recruited and bind to the receptor. (3) β-arrestin binding blocks further G protein signalling by the GPCR and additionally scaffolds for β-arrestin dependent signalling pathways. (4) The β-arrestin-GPCR complex is internalised by endocytosis through clathrin-coated pits[46] and the receptor is subsequently recycled back to the cell surface or sorted for degradation in lysosymes.

Beyond their canonical role in GPCR desensitisation and trafficking, it is now established that β-arrestin directly couple to multiple signalling effectors by acting as scaffolds, adapters, or transducers. The initial evidence came from the Lefkowitz group who demonstrated that the β_2AR mediated activation of c-Src pathways was dependent on the formation of a β_2AR-c-Src-β-arrestin mitogenic signalling complex.[47] Importantly, overexpression of β_2AR and

c-Src alone did not induce formation of signalling complexes, with β-arrestin 1 required to directly bind both receptor and c-Src, thus acting as a signalling adapter. β-arrestin has subsequently been demonstrated to be involved in regulating NF-κB, MAPK, AKT, and PI3K pathways.[48–50] These signalling pathways are often regulated by both β-arrestin and G proteins, but in a temporally distinct manner.[6] The extent to which β-arrestin acts as a genuine initiator of signalling independent of G proteins remains controversial, with a recent study demonstrating that β-arrestin MAPK signalling requires initiation by G proteins.[51] However, β-arrestin signalling continues to draw significant interest for the ability of certain ligands to show selective activation of β-arrestin recruitment without G protein signalling or *vice versa*; a phenomenon known as biased agonism with significant implications for GPCR drug discovery.

1.2 Biased agonism

Biased agonism is the selective activation of specific signalling pathways by ligands acting at receptors that are coupled to multiple downstream effectors. This effect arises due to agonists stabilising different active-state receptor conformations that differentially engage the intracellular machinery to produce distinct cellular responses. The possibility of biased signalling was first appreciated in the 1990s, where it was initially observed in GPCRs that couple to multiple G proteins.[52] In recent years particular interest has focused on ligands that display bias between β-arrestin and G protein signalling, and numerous examples of synthetic biased ligands displaying novel biology at key pharmacological targets have been reported. Increasing evidence also suggests that endogenous biased ligands play a key role in regulating some physiological processes. In the chemokine system, for example, numerous natural peptides act with biased signalling at the same chemokine receptors to create distinct, rather than redundant responses.[53,54] Investigating bias signalling at GPCRs will therefore improve our understanding of GPCR physiology and enable the development of more effective drugs.

1.2.1 Defining agonist bias

In general signalling bias can be observed by comparing the responses induced by agonists in assays that measure activation of different pathways (Figure 1.8). However, there are multiple sources of bias that may contribute to give a misleading illusion of biased agonism. This apparent bias, a combination of system and observational bias, can arise for many different reasons: certain signalling pathways may be coupled more efficiently within the same cell system; the sensitivity of an assay may be greater for one specific pathway; the signalling properties of a GPCR may depend on the receptor and transducer expression in the cell type or tissue being studied.[55] A common form of system bias arises from the significant amplification of signal by G protein 2nd messenger cascades, which presents as greater apparent potency for agonists in G protein over arrestin signalling.[6] To account for system bias, the activities of agonists are compared relative to an endogenous ligand which is considered unbiased. Various methods for quantifying the extent of agonist bias are employed in the literature which will not be considered here, but are extensively reviewed by Rajagopal et al. and Kenakin and Christopolos.[55,56]

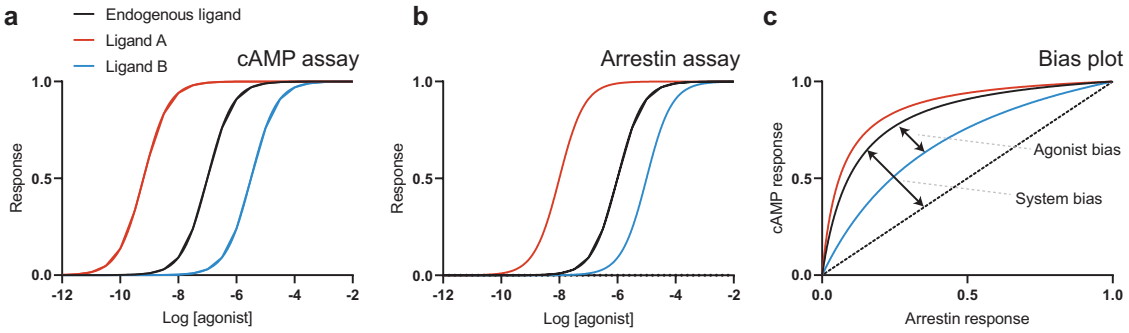

Figure 1.8: Simulated concentration-response curves to illustrate the detection of bias. The responses of two agonists and an endogenous ligand are measured for **(a)** cAMP and **(b)** β-arrestin recruitment. **(c)** The responses for each pathway are plotted against each other to enable visualisation of bias. All three compounds show greater potency in the cAMP assay, reflecting significant system bias which is also visible in the curvature of the bias plot for the endogenous ligand. Ligand A is relatively unbiased, and ligand B shows β-arrestin bias when compared to the endogenous ligand.

System bias can also have important consequences when translating *in vitro* studies into physiological systems. For example, the β-arrestin biased ligands of the dopamine D_2 receptor (D_2R) only display efficacious signalling in the presence of high GRK2 and β-arrestin expression in HEK293 cells.[57] Furthermore, given that higher levels of β-arrestin 2 and GRK2 are found in the prefrontal cortex (PFC) compared with the striatum in the brain, these bi-

ased ligands therefore show pharmacological action consistent with D_2R β-arrestin 2 activation in the PFC but antagonism in the striatum.

1.2.2 Biased therapies: a case study of opioid analgesics

The potential for biased signalling at GPCRs to lead to pharmaceuticals with reduced side effects has generated significant interest, with efforts to deliver improved opioid analgesics a foremost example. Small molecule opioid agonists such as morphine (**1**), fentanyl, and oxycodone are among the most effective clinically used painkillers, with powerful pain relief achieved by activating the μ-opioid receptor (μOR) expressed on neurons.[58] However, μOR agonists have significant adverse side effects including gastrointestinal dysfunction, pyschotropic effects, and potentially fatal respiratory depression. Furthermore, the rapid tolerance and dependence developed through repeated use gives opioid drugs very high abuse potential, as reflected in the ongoing opioid epidemic in the United States where over 40 000 people died through opioid overdose in 2016.[59] There is therefore significant unmet medical need for opioid drugs with reduced side-effects.

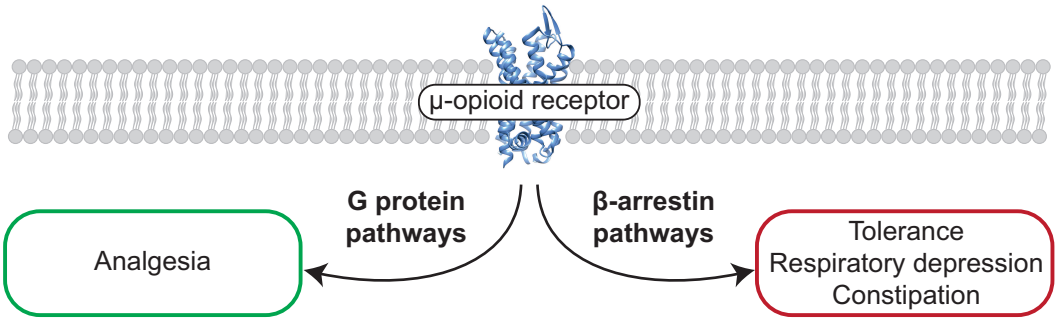

Figure 1.9: A model suggesting the separation of beneficial and negative effects of morphine treatment according to signalling pathways. This model was largely proposed according to studies in β-arrestin 2 knockout mice by Bohn et al.

Interest in exploiting biased signalling at μOR was first sparked by a series of experiments in β-arrestin 2 knock-out mice that demonstrated that the various biological effects of opioids could be attributed to specific pathways downstream of μOR (Figure 1.9). Previous experiments in $\mu OR^{-/-}$ mice resulted in a complete loss of all morphine biological activity, suggesting that the adverse side-effects of morphine were inextricable from the beneficial analgesia.[60] In β-arrestin 2 deficient mice, however, morphine treatment showed enhanced

analgesia and did not result in the development of antinociceptive tolerance, although the mice did experience physical dependence through the upregulation of adenylyl cyclase.[61,62] These results suggested a G protein biased μOR agonist that lacked β-arrestin dependent desensitisation and signalling may have therapeutic advantages.

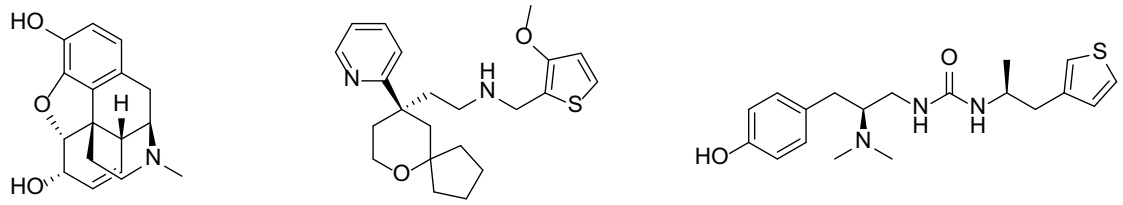

Figure 1.10: Chemical structures of selected opioid ligands. TRV130 and PZM21 are reported as G protein biased agonists, whereas morphine is a balanced agonist.

G protein biased μOR agonist TRV130 (**2**) was developed through a structure-activity-relationship (SAR) programme that optimised a high-throughput screening hit for activity in cAMP assays and for inactivity in β-arrestin recruitment assays.[63] Manglik et al. used a docking strategy with the published μOR crystal structure to develop new chemotypes of agonist with unique binding modes, resulting in PZM21 (**3**) which has a potency of 4.6 nM in $G_{\alpha i}$ assays but negligible activation of β-arrestin recruitment in HEK293 cells.[64] In preclinical rodent models, PZM21 induces analgesia lasting 180 min longer than morphine treatment in wild-type but not $\mu OR^{-/-}$ mice, and importantly shows significantly reduced constipation and respiratory depression compared to morphine.[64] Schmid et al. additionally demonstrated in mice that the *in vitro* bias factor of a μOR agonist was heavily correlated with the *in vivo* therapeutic window, such that increasing G protein bias of a compound improved the therapeutic index.[65] Human clinical trials of G protein biased agonists have not met the high expectations from preclinical data, with the majority finding TRV130 to provide effective relief from acute pain but only modest reductions in side effects compared to morphine.[66–68]

Recently, the potential of biased analgesics to offer improved therapies has been hit by a series of high profile setbacks. The United States Food and Drugs Association (FDA) rejected the application of TRV130 to be approved as an improved analgesic, questioning its safety profile and limited evidence of benefit over established opioid medications. In a recent paper Hill et al. failed to recapitulate the favourable pharmacological profile of PZM21, finding

instead that the compound showed weak efficacy for both G protein and β-arrestin pathways and induced respiratory depression to a similar extent to morphine.[69] Finally, a series of studies with TRV130 have suggested that G protein biased agonists show similar abuse potential to currently available opioid agonists.[70,71] Overall, the promising studies with β-arrestin knockout mice have largely failed to translate into improved pain relief medication in the clinic. One possible explanation for this is the almost exclusive characterisation of compound bias in artificial transfected cell systems. The use of disease-relevant cells to demonstrate bias may prevent contradictory results such as those observed for PZM21 and provide compounds with improved *in vivo* bias and clinical efficacy.

1.3 Free Fatty Acid Receptors

1.3.1 Receptor deorphanisation and metabolite sensing GPCRs

Advances in molecular biology at the turn of the last century facilitated the identification of many previously unknown GPCRs through techniques such as homology cloning.[72] The majority of these newly discovered receptors had no known activating ligand or function, and were termed orphan receptors. The discovery of cognate ligands for many orphan receptors was achieved through reverse pharmacology: orphan receptors were exogenously expressed in cellular systems and libraries of potential ligands were screened for functional activity.[73] While many orphan receptors were paired with pharmacologically well characterised ligands, other receptors were unexpectedly found to be activated by ligands previously not thought to have signalling function. For example, GPR91, an orphan receptor highly expressed in the kidney, was deorphanised by purifying an active compound, succinate, from pig kidney extracts capable of activating the orphan receptor.[74] Succinate, previously thought to be a simple metabolic intermediary in the citric acid cycle, was therefore demonstrated to have signalling properties now known to exert influence over various immunological processes and diseases.[75,76]

Around the same time, three groups independently identified that medium chain and long chain fatty acids (MCFAs and LCFAs) were capable of activating GPR40, now known as

Free Fatty Acid Receptor 1 (FFAR1).[77–79] In the following years a further four orphan GPCRs were deorphanised with fatty acids: GPR43, GPR41, GPR120, and GPR84, with the former three renamed FFAR2–4 respectively.[80–82] The discovery that nutrients and metabolites such as dietary fatty acids could signal through specific extracellular receptors has had an enduring impact on our understanding of how diet can influence physiology.[83] Many metabolite-sensing receptors are expressed on key cells of the immune system, providing a direct mechanism between the regulation of energy homeostasis and the chronic inflammation that is characteristic of metabolic diseases such as diabetes.[84] The FFARs are therefore of significant therapeutic interest and are the target of several drugs currently progressing in clinical trials. I will first introduce the biological roles of fatty acids and provide a brief overview of FFAR1-4, before focusing on the least studied fatty acid receptor, GPR84, in section 1.4.

1.3.2 Fatty acids

A fatty acid is a carboxylic acid with an aliphatic tail that can vary considerably in length, and may be saturated or unsaturated. Fatty acids are generally classified according to the length of their aliphatic tail, with SCFAs typically classified as having fewer than 6 carbons in the chain, MCFAs having 7–12, LCFAs having 13–22, and very long chain fatty acids having > 22 carbon atoms.[85] They can be further categorised into saturated fatty acids (SFAs), monounsaturated fatty acids (MUFAs) that contain a single *cis* double bond, polyunsaturated fatty acids (PUFAs) that contain multiple such double bonds, and trans fats that possess a *trans* double bond.

In humans, the majority of fatty acids can be synthesised *de novo*, but the primary source of MCFAs and LCFAs is dietary fat.[85] Certain fatty acids therefore fluctuate in concentration in the body significantly with diet, as highlighted by one study that showed capric acid blood plasma levels were below the micromolar range in humans with a normal diet but rose as high as 10 μM in humans eating a diet rich in medium-chain triglycerides.[86] Longer chain fatty acids and their derivatives play many crucial roles in biology: both LCFAs and MCFAs are a key cellular energy source through β-oxidation,[87] and LCFAs additionally constitute both the major structural component of cell membranes and the major bodily energy

reserve as phospholipids and triglycerides respectively. Many long chain PUFAs serve as precursors to important signalling molecules involved in regulating inflammation, with pro-inflammatory prostaglandins and pro-resolution resolvins deriving from arachadonic acid and eicosapentaenoic acid respectively.[88,89] Common saturated MCFAs and LCFAs can also influence physiological processes by directly acting on targets, both intracellularly on nuclear receptors such as peroxisome proliferator-activated receptors (PPARs), and extracellularly through the FFARs.[90]

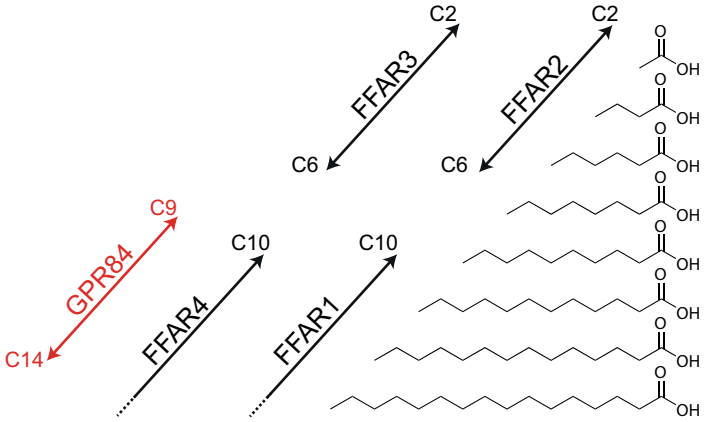

Figure 1.11: Different chain length saturated fatty acids activate different GPCRs. SCFAs activate FFAR2 and FFAR3, MCFAs activate GPR84, and MCFAs, LCFAs, and PUFAs (not shown) activate FFAR1 and FFAR4.[91]

SCFAs are primarily produced in the body by bacterial fermentation of dietary fibre in the gastrointestinal tract. As much as 600 mmol of SCFAs are produced in the gut each day, primarily as acetate, propionate, and butyrate, and are variously used as an energy substrate or in the biosynthesis of more complex lipids.[92] Additionally, SCFAs are now recognised to have important signalling functions, with SFCAs affecting gene expression by histone deacetylase inhibition[93] and impacting on various physiological processes by activating FFAR2 and FFAR3.

1.3.3 Overview of the free fatty acid receptors 1–4

Five GPCRs have been demonstrated to be activated *in vitro* by fatty acids of varying chain lengths: FFAR1–4 and GPR84 (Figure 1.12). Of the four officially classified FFARs, FFAR1–3 are structurally related with 30 % to 40 % sequence homology, whereas FFAR4 and GPR84 are phylogenetically unrelated to each other and all other FFARs.[72] FFAR1 and FFAR4 have

drawn particular interest for the treatment of metabolic diseases, while SCFA receptors FFAR2 and FFAR3 are researched for the apparent link they provide between the microbiota and human health.

Free Fatty Acid Receptor 1 (GPR40)

FFAR1 is activated by a relatively wide range of fatty acids compared to other FFARs, with saturated MCFA/LCFAs of 12–16 carbons all activating the receptor in addition to various PUFAs that are potent agonists, such as docosahexaenoic acid (**4**).[91] FFAR1 is primarily coupled with $G_{\alpha q}$ Ca^{2+} flux signalling pathways, with $G_{\alpha s}$ activation also observed in certain cases.[72] The β-cells of the pancreas show particularly high FFAR1 expression, and early studies demonstrated the ability of LCFAs to enhance glucose stimulated insulin secretion though FFAR1 activation.[78] FFAR1 remains an important anti-diabetic target, with FFAR1 partial agonist TAK-875 (**5**) improving hyperglycaemia in diabetic mice[94] and demonstrating efficacy in phase II clinical trials for type 2 diabetes.[95] Although TAK-875 would go on to fail phase III clinical trials due to off-target liver toxicity,[96,97] the efficacy demonstrated in these trials has validated FFAR1 activation as a promising target for diabetes.

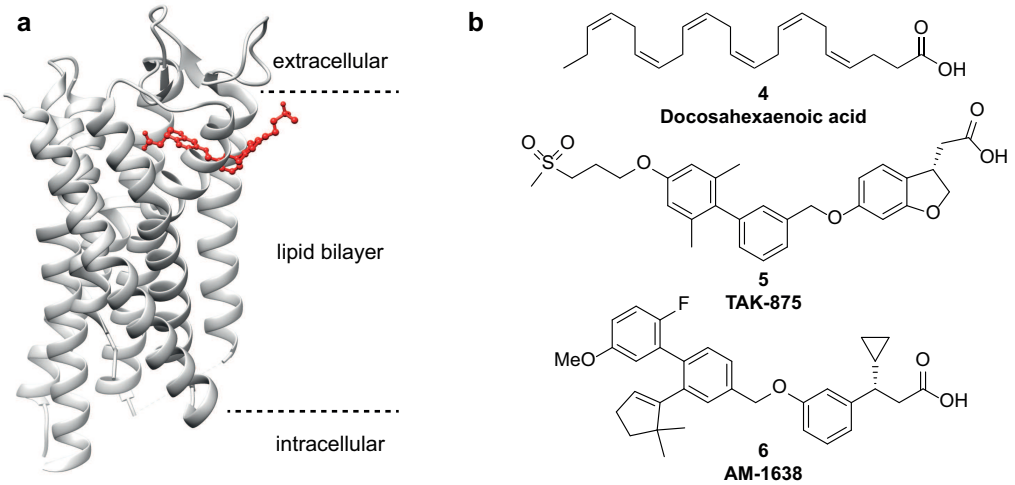

Figure 1.12: An allosteric ligand of FFAR1 shows a unique binding mode. **(a)** The crystal structure of FFAR1 bound to TAK-875 reveals a non-canonical binding interaction in which the ligand extends into the lipid bilayer. PDB: 4PHU. **(b)** Chemical structures for FFAR1 ligands, including endogenous PUFA docosahexaenoic acid, allosteric partial agonist TAK-857, and allosteric full agonist AM-1638.

FFAR1 is notable for the varied pharmacology and unique binding modes of its ligands. In radioligand binding studies, two distinct sets of synthetic FFAR1 agonists were demon-

strated to display high cooperativity at the receptor, while endogenous fatty acid agonists exhibited cooperativity with both sets of synthetic agonists.[98] These complex results suggest there are three, allosterically linked FFAR ligand binding sites. In Ca^{2+} flux assays in Chinese hamster ovary (CHO) cells, TAK-875 itself was demonstrated to be an ago-PAM by enhancing the agonist response of γ-linolenic acid, while acting as a partial agonist when used alone.[99] Unlike TAK-875, synthetic full FFAR1 agonists such as AM-1638 (**6**) can additionally engage $G_{\alpha s}$ signalling and show more efficacious incretin and insulin secretion, enabling better glucose control in rodents.[100,101] Extensive FFAR1 structural studies have sought to explain this disparate pharmacology. The first FFAR1 crystal structure was solved bound to TAK-875 and revealed a unique non-canonical binding site between TM3, TM6, and EL2 that extends into the lipid bilayer (Figure 1.12a).[102] Subsequently, synthetic full agonist-bound FFAR1 crystal structures have demonstrated binding to a second allosteric site that more effectively stabilises IL2, potentially facilitating greater G protein interactions that likely explain the greater efficacy and additional $G_{\alpha s}$ coupling of these compounds.[103,104] Further research into how FFAR1 signalling pathways correlate with functional outcomes in physiological cells may enable greater therapeutic efficacy in the next generation of FFAR1 clinical candidates.

Free Fatty Acid Receptors 2 and 3 (GPR43 and GPR41)

FFAR2 and FFAR3 share 52 % sequence similarity and accordingly display similar activation by SCFAs C2 to C6. The two receptors also show similar expression profiles in immune cells, adipocytes, and epithelial cells that line the gut.[80] These common features of the SCFAs receptors has made characterising their respective physiological roles challenging. A further obstacle is the relative paucity of selective FFAR2–3 ligands. Synthetic carboxylic acid **7** is reported as a potent FFAR2 orthosteric agonist that lacks activity at FFAR3,[105] but no selective orthosteric agonists for FFAR3 are known to date (Figure 1.13). Achieving selectivity by targeting receptor allosteric sites has been a successful strategy, and **8** and **9** are selective allosteric ligands for FFAR2 and FFAR3 respectively.[106,107] Despite the challenges in characterising the SCFA receptors, the production of SFCAs by bacteria in the gut has focused particular interest on FFAR2–3 as a direct link between the gut microbiome and its well reported

effects on inflammation and metabolism.[108]

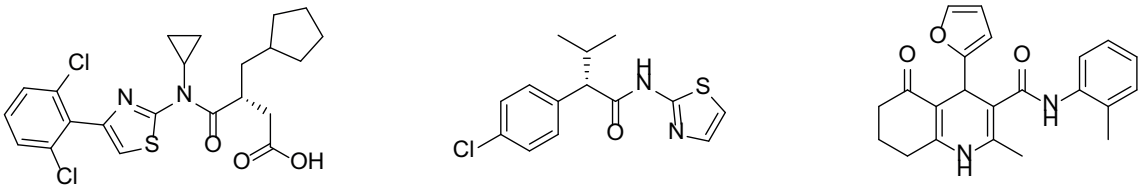

Figure 1.13: Reported sub-type selective ligands for FFAR2 and FFAR3.

The role of FFAR2 in regulating inflammation is apparent from its expression across a variety of immune cells including neutrophils, macrophages, dendritic cells, and lymphocytes.[80] Various *in vivo* experiments have confirmed this link, notably a study by Maslowski et al. that used models of colitis and arthritis in FFAR2 deficient mice to demonstrate that stimulation of FFAR2 with SCFAs was necessary for the resolution of certain inflammatory responses.[109] FFAR2$^{-/-}$ mice with dextran sulfate sodium induced colitis showed exacerbated inflammation compared to wild-type controls, with increased production of inflammatory mediators and immune cell recruitment. Strikingly, mice raised in a germ-free environment showed similarly enhanced inflammation due to the consequent lack of bacterial SCFA production, while supplementing drinking water with acetate reversed these effects. Further studies have shown that a high intake of dietary fibre protects against colitis through microbiota derived SCFA-FFAR2 signalling that helps regulate the inflammasome[110] and control the number and function of colonic T_{reg} cells.[111] The complexity of the interactions between microbiota SCFAs and human physiology was recently highlighted by the identification of FFAR2-FFAR3 heteromers in primary monocytes and macrophages that display distinct signalling to the respective homomers.[112] The development of high quality FFAR2–3 chemical probes to be used *in vivo* would enable further characterisation of these receptors as novel immunometabolic disease targets.

Free Fatty Acid Receptor 4 (GPR120)

FFAR4 is activated by LCFAs and PUFAs and primarily couples to $G_{\alpha q}$ pathways, with clear similarities to FFAR1.[72] Unlike FFAR1, however, FFAR4 is primarily found in immune cells, with expression in adipose tissue, intestines, lung, and spleen. Many FFAR4 ligands also

activate FFAR1 despite the relative lack of homology, although the absence of expression of FFAR1 on cells such as macrophages enables ligands with dual pharmacology to be used as specific FFAR4 probes on those cell types. A number of FFAR4 selective ligands have been reported: TUG-891 (**10**) shows 288-fold greater potency for hFFAR4 over hFFAR1, but shows only limited selectivity between the murine orthologues;[113,114] and carboxylic acid **11** is a potent, selective, and orally available FFAR4 ligand with significant selectivity over FFAR1.[115]

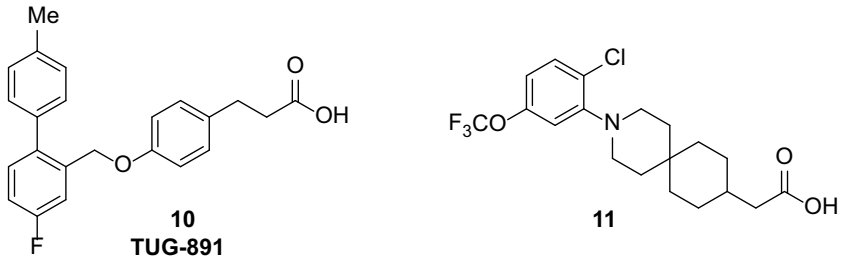

Figure 1.14: Selected orthosteric FFAR4 ligands.

The abundant FFAR4 expression in macrophages has provoked particular interest as the possible mechanism by which omega-3 fatty acids may exert their reputed anti-inflammatory effects *in vivo*.[72] This theory is supported by *in vitro* evidence that shows omega-3 fatty acid or **11** stimulation of macrophages reduces LPS induced NF-κB activation, cytokine secretion, and expression of inflammatory genes in a FFAR4 dependent fashion.[115] A number of studies in mice have also suggested a role for FFAR4 in alleviating inflammation associated with metabolic disease *in vivo*. FFAR4 deficient mice fed a high fat diet developed more serious obesity, insulin resistance, and systemic inflammation than wild-type litter controls,[116] while supplementing high-fat diets with omega-3 fatty acids reduced the severity of obesity and improved insulin sensitivity in WT but not FFAR4$^{-/-}$ mice.[117] FFAR4 has been linked to metabolic disease in humans by the identification of a loss-of-function p.R270H mutation that reduces $G_{\alpha q}$ FFAR4 signalling in HEK293 cells and is heavily associated with obesity in European populations.[116] Follow-up studies in other populations, however, have reported no association of the p.R270H mutation with type 2 diabetes,[118] while a study in the Danish population found no link with obesity,[119] suggesting additional studies are required to genetically validate FFAR4 activation for the treatment of metabolic diseases.

Of particular note in the pharmacology of FFAR4 is the ability to attribute different func-

tional effects to specific downstream signalling pathways. For example, while FFAR4 mediated stimulation of GLP-1 secretion from enteroendocrine cells occurs through the primary $G_{\alpha q}$ signalling pathway, the ability of FFAR4 agonists to inhibit ghrelin secretion is sensitive to $G_{\alpha i/o}$ inhibition by PTX.[120] FFAR4 additionally couples strongly to β-arrestin signalling, as illustrated by the rapid phosphorylation and internalisation of FFAR4 in HEK293 cells stimulated with TUG-891.[114] The anti-inflammatory functions of FFAR4 have been linked with β-arrestin pathways, such that knockdown of β-arrestin 2 in Raw 264.7 macrophages blocked FFAR4 mediated anti-inflammatory signalling, whereas β-arrestin 1 and $G_{\alpha q}$ knockdown had no effect.[117] The identification of biased FFAR4 ligands may therefore enable selective activation of different FFAR4 mediated functional outcomes, although no studies have investigated this yet due to a lack of appropriately biased FFAR4 chemical probes.[72]

1.4 GPR84

GPR84 is a GPCR that is activated by MCFAs and is suggested to be the fifth member of the FFAR family. The gene encoding GPR84 was discovered independently in 2001 by two groups using expressed sequence tag data mining and, separately, cloning from a human neutrophil cDNA library.[121,122] The human and murine GPR84 genes both consist of a single coding exon that encodes a 396 amino acid protein, and the two orthologues share 85 % sequence identity. The primary sequence of GPR84 has a classical 7-transmembrane domain arrangement, although the sequence has poor conservation with other GPCRs and no close homologues.[121] GPR84 primarily couples to $G_{\alpha i}$ signalling pathways in recombinant cells, and this signalling is maintained in primary cells where the action of GPR84 agonists is sensitive to $G_{\alpha i}$ inhibition by PTX.

1.4.1 Expression

GPR84 is primarily expressed in cells of the immune system, with neutrophils and mononuclear phagocytes of the innate immune system having the highest expression and lymphocytes including T cells, B cells, and natural killer cells expressing GPR84 to lower levels.[82] In

murine tissue GPR84 is found most abundantly in the bone marrow, spleen, lymph nodes, and lung. Notably, GPR84 expression is particularly high in microglia, the resident macrophage cells of the brain and central nervous system. GPR84 displays a limited expression profile outside of the immune system, with low levels of the receptor found in murine 3T3-L1 adipocyte cells and in human Het-1A oesophagus epithelial cells.[123,124] GPR84 expression at basal levels is relatively low, but the receptor is significantly induced by pro-inflammatory stimuli, both *in vitro* and *in vivo*.[125] This upregulation of GPR84 expression on inflammatory insult suggests a role for the receptor in regulating immune responses (section 1.4.5).

1.4.2 MCFAs at GPR84

Saturated fatty acids with chain lengths between C9 and C14 are activators of GPR84, although the weak potency of this interaction means that the receptor is still officially classified as an orphan.[126] A clear SAR trend for carbon chain length is observed for MCFAs at GPR84, with capric acid (**14**) showing the highest activity (Figure 1.15). The equivalent methyl ester of capric acid is inactive at GPR84, highlighting that both polar and hydrophobic elements are required for activity at the receptor.[127] Suzuki et al. additionally demonstrated that MCFAs hydroxylated at the 2- or 3-position activate GPR84 more effectively, although the physiological relevance of this is yet to be clarified.[128] While numerous studies have confirmed that MCFAs activate GPR84 in recombinant cells, fewer reports have demonstrated GPR84 activation by MCFAs on primary cells. In a label-free impedance sensing assay, for example, MCFAs fail to induce robust responses in primary macrophages when compared to potent surrogate GPR84 agonists.[125] Further evidence of physiologically relevant effects of MCFAs acting at the receptor *in vitro* and *in vivo* will be required before MCFAs can be officially confirmed as endogenous ligands for GPR84.

1.4.3 Surrogate GPR84 ligands

The low potency and poor selectivity of the MCFA endogenous GPR84 ligands has spurred the development of new pharmacological tools for investigating GPR84 biology. These ligands can be broadly separated into three classes: orthosteric agonists that structurally re-

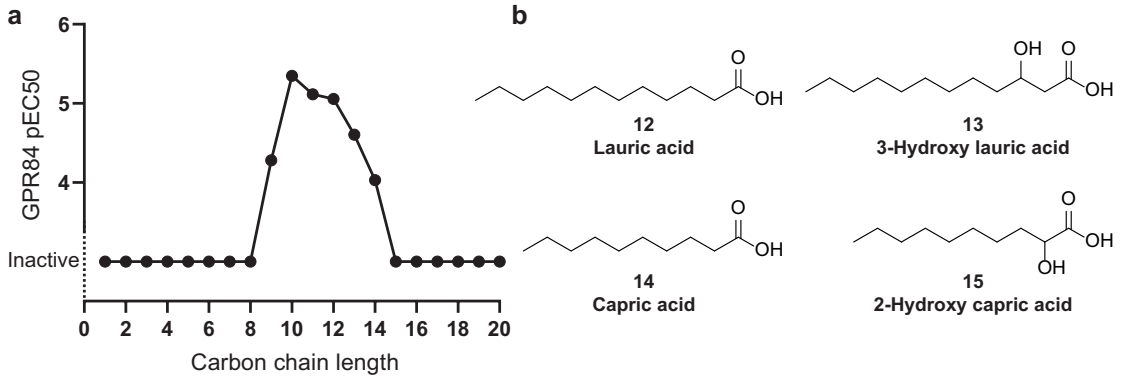

Figure 1.15: Saturated MCFAs are activators of GPR84 *in vitro*. **(a)** The activity of saturated fatty acids with different chain lengths at GPR84 in a CHO cAMP assay (data from Wang et al.)[82] **(b)** Representative fatty acids and their hydroxylated analogues that are agonists at GPR84.

semble fatty acids; ago-allosteric modulators developed around the natural ligand 3,3-diindolylmethane; and dihydropyrimidineisoquinolinones that act as non-competitive antagonists of the receptor.

Orthosteric surrogate agonists

Embelin (**16**) is a natural product derived from *embelia ribes* that activates GPR84 with improved potency over MCFAs[129] and finds use in traditional medicine with purported analgesic, anti-inflammatory, anti-tumour, and anti-bacterial effects.[130,131] Embelin consists of a dihydroxybenzoquinone polar head group with an attached alkyl chain and, as expected from the structural resemblance to MCFAs, binds to GPR84 in the orthosteric binding pocket.[127] Multiple biological activities besides GPR84 activation are known, with embelin variously reported to: inhibit the X-linked inhibitor of apoptosis (XIAP);[132] bind to CXCR2 (K_i = 93 nM) and adenosine A_3 receptors;[129] and display antioxidant properties.[133,134] The GPR84 selectivity of embelin over other GPCRs can be improved by truncating the alkyl chain length, but no data regarding other off-target activities has been reported.[129] Embelin remains a frequently employed GPR84 tool compound, despite the myriad off-target activities that render it unsuitable for these applications.

A second series of GPR84 agonists was developed around high-throughput screening hits 6-octylaminouracil (6-OAU, **17**) and structurally related thiobarbituric acid derivative ZQ-16 (**18**).[128,135] These two agonists both possess polar head groups and alkyl tails reminiscent of MCFAs, and mutagenesis studies suggest they occupy the same ligand binding site as capric

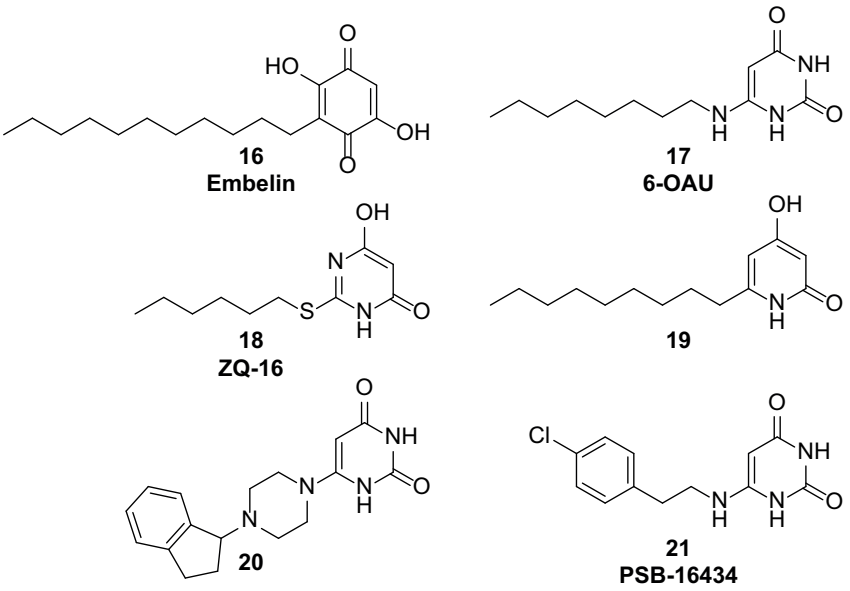

Figure 1.16: GPR84 surrogate ligands believed to bind in the orthosteric pocket. Compounds **16** and **18** have been demonstrated to bind orthosterically by mutagenesis studies and competition assays.[127] Compound **19** shows sub-nanomolar potency at GPR84, and **21** shows significant G protein signalling bias.

acid.[127] Modifying the head group of ZQ-16 to 4-hydroxy-2-pyridone yielded highly potent agonist **19** with sub-nanomolar activity in both GPR84 Ca^{2+} flux and cAMP assays.[136] Although **19** exhibits the highest activity of any reported GPR84 agonist, its high lipophilicity (cLogP = 4.02) suggests the possibility of selectivity issues which have not yet been addressed in the literature. In contrast, the GPR84 specificity of functional responses induced by ZQ-16 and 6-OAU has been confirmed by testing in primary murine GPR84$^{-/-}$ neutrophils and macrophages respectively,[125,137] although wider selectivity profiling of the compounds is yet to be performed.

Pillaiyar et al. recently reported a series of 6-OAU derivatives incorporating alternative lipophilic groups connected to the uracil head.[138] This study demonstrated that diverse hydrophobic groups are tolerated as replacements for the alkyl chain of 6-OAU, with agonists such as piperazine linked 2,3-dihydro-1*H*-indene **20** exhibiting only slightly reduced potency compared to 6-OAU. In addition, they report GPR84 agonists with G protein signalling bias, including **21** whose bias factor of 1.9 represents an almost 100-fold preference for activating G protein over β-arrestin pathways. Although demonstrated not to activate the other FFARs 1-4, the wider selectivity profile of these compounds is unknown and further characterisation using GPR84$^{-/-}$ primary cells is required for them to be confidently used.

Allosteric agonists

3,3'-Diindolylmethane (DIM, **22**) is an ago-allosteric modulator of GPR84. DIM is a naturally occurring metabolite of phytochemicals found in brassica vegetables such as broccoli and activates GPR84 with a relatively low potency of >10 μM.[139,140] The very different structure of DIM compared to other orthosteric agonists first suggested that it may occupy a distinct GPR84 binding site, and unlike all known orthosteric agonists DIM retains agonist activity in a GPR84 receptor with arginine172 mutated to lysine.[127] Consistent with allosteric binding, DIM shows significant positive allosteric modulation (PAM) of the action of capric acid, embelin, and 6-OAU at GPR84, and can therefore be classified as a GPR84 ago-PAM. However, DIM also activates the cannabinoid CB_2 receptor[141] and aryl hydrocarbon receptor (AhR).[142] Both these off-target substrates of DIM are expressed in immune cells and play a role in regulating inflammation,[143144] limiting the utility of DIM as a GPR84 chemical probe.

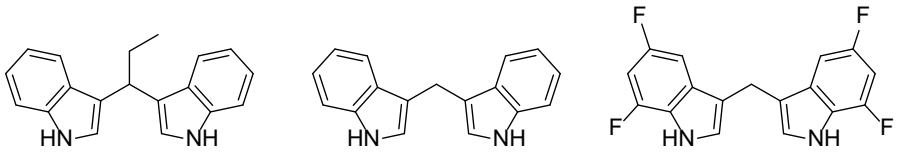

Figure 1.17: GPR84 ago-allosteric agonist DIM and derivatives. DIM analogue **23** is reported to have β-arrestin signalling bias, while **24** shows significantly enhanced potency over DIM.

A series of DIM analogues with improved potency and selectivity were recently reported, including compound **23** which shows apparent β-arrestin biased signalling.[145] The most potent compound at GPR84, **24**, lacked any activity against AhR, although activity at CB_2 was not investigated. Accordingly, activation of $G_{\alpha i}$ by **24** is retained in primary murine GPR84$^{-/-}$ neutrophils,[137] likely due to CB_2 activation. Further optimisation of this compound series is required before it can be used to study GPR84 biology.

GPR84 antagonists

Labuguere et al. have reported in the patent literature a series of dihydropyrimidinoisoquinolinones (**25**) that act as effective antagonists of GPR84 in both recombinant cells and primary immune cells.[146] Antagonism of both embelin and DIM by a compound of this se-

ries is non-competitive and neither agonist is able to competitively displace a radiolabelled derivative, suggesting this compound class binds to a third distinct site on the receptor.[127] An antagonist from this structural class passed phase I clinical trials in humans, and therefore likely shows good tolerability and bioavailability for use as an *in vivo* chemical probe. Notably, however, certain antagonists of this series show substantially lower affinity for the murine GPR84 orthologue, which may limit their utility in preclinical models.[137]

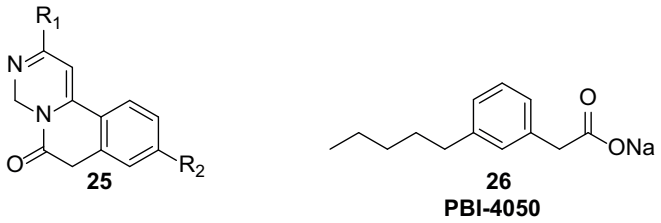

Figure 1.18: Reported GPR84 antagonists. Compound series **25** consists of over 170 analogues with a common fused tricyclic structural core that act as non-competitive GPR84 antagonists. PBI-4050 is a dual GPR84 antagonist/FFAR1 agonist.

Finally, PBI-4050 (**26**) is a synthetic fatty acid analogue reported as a dual GPR84 antagonist/FFAR1 agonist.[147] PBI-4050 blocks capric acid activation of human GPR84 in a HEK293 BRET assay with an IC_{50} of 398 μM and activates various signalling pathways mediated by human FFAR1 with similarly low potency. This compound has entered clinical trials for the treatment of idiopathic pulmonary fibrosis (section 1.4.5),[148] but its low potency and polypharmacology make it less useful as a GPR84 tool compound.

1.4.4 Ligand binding mode

A crystal structure of GPR84 is yet to be reported, so the available information on the 3-dimensional topology of GPR84 and ligand binding mode is limited to studies that use a combination of homology modelling and mutagenesis. Two such studies have been reported to date, and have returned contradictory results for the binding mode of capric acid and the key GPR84 residues involved (Figure 1.19). The first model, based upon the β_2AR that has low homology with GPR84, predicted that the carboxylate fatty acid head would bind deep within the helical bundle to a ligand-binding pocket devoid of positively charged residues.[149] This predicted binding mode is at odds with FFAR1-4 in which a protonated arginine is predicted to act as a charge partner for binding the ligand carboxylate.[72] The second study used the

recently published orexin OX_1 receptor structure which has higher homology to GPR84, and predicted that the capric acid carboxylate would interact with Arg172 in EL2, with the alkyl tail extending into the receptor. This binding mode is in line with the ligand binding mode predicted for the other FFARs. In addition, pharmacological competition experiments with GPR84 agonist DIM and antagonist series **25** suggest that each binds at distinct sites when compared to MCFAs, implying the existence of at least three druggable sites on GPR84.[127]

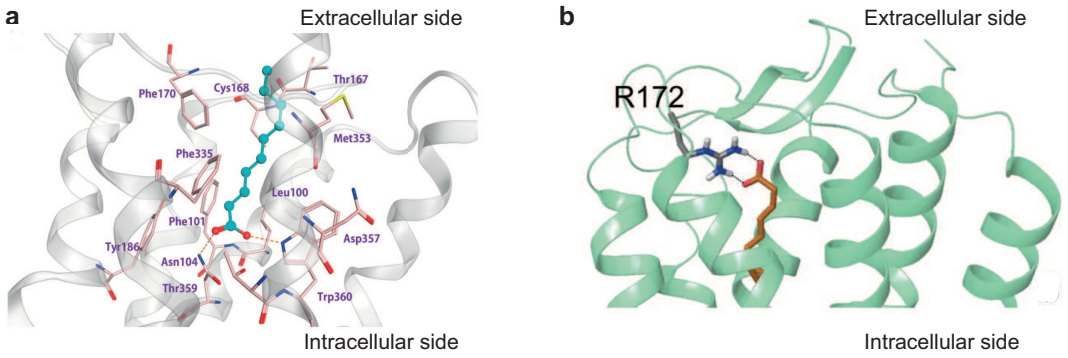

Figure 1.19: Two studies on capric acid binding mode at homology models of GPR84 are contradictory. **(a)** Nikaido et al. predicted the carboxylate would bind deep within the GPR84 transmembrane bundle, whereas **(b)** Mahmud et al. predicted capric acid would have the opposite orientation, with the carboxylate binding Arg172 of EL2.[127,149] Figures are adapted from the referenced publications with permission from the copyright holder and under the Creative Commons licence (https://creativecommons.org/licenses/by/4.0/) respectively.

1.4.5 GPR84 in health and disease

Although the nature of the endogenous ligands that activate GPR84 *in vivo* remains unclear, the receptor has been implicated in various pathophysiological processes that suggest it may be a useful therapeutic target. Generally considered a pro-inflammatory receptor, GPR84 antagonism is the primary therapeutic strategy explored to date and is the subject of several completed and currently running clinical trials. Other studies, however, suggest that GPR84 agonism may also be therapeutically beneficial in certain disease states.

Inflammatory disease

The expression of GPR84 in leukocytes is markedly increased on exposure to pro-inflammatory stimuli, generating particular interest in GPR84 as an immunomodulatory receptor. Stimulation of macrophages to a pro-inflammatory "M1" state with lipopolysaccharide (LPS) rapidly

upregulates GPR84 mRNA expression and this is accompanied by increases in surface receptor expression, as demonstrated by GPR84 radioligand binding studies with THP-1 cell membranes.[125,137] Injection of mice with LPS results in widespread induction of GPR84 at the tissue level, demonstrating the importance of GPR84 in acute inflammatory states. Furthermore, Recio et al. demonstrated that GPR84 is also upregulated in tissue from diabetic mice or mice fed a high fat diet, suggesting GPR84 is associated with the chronic low-grade inflammation that accompanies hyperglycaemic or dyslipidaemic conditions *in vivo*. In addition, GPR84 expression in adipocytes is enhanced by co-culture with macrophages, further linking GPR84 with inflammatory obesity.[123]

GPR84 activation on immune cells is associated with various pro-inflammatory responses. Stimulation of human polymorphonuclear leukocytes (PMNs) with 6-OAU increases secretion of interleukin-8 (IL-8),[128] and similarly 6-OAU treatment of primary bone marrow-derived macrophages results in pro-inflammatory ERK, AKT, and NF-κB signalling and TNF-α, CCL2, and IL-6 secretion.[125,129] Moreover, 6-OAU treatment of murine BMDMs also enhances phagocytosis of heat-killed pHrodo labelled bacteria in a real-time assay.[125] GPR84 has also been described as a chemotactic receptor, with primary human and murine neutrophils undergoing chemotaxis to embelin, and 6-OAU inducing migration of U937 macrophage-like cells.[128] Only limited data on the action of GPR84 agonists *in vivo* is known, but 6-OAU injection into the dorsal air pouch of rats leads to the accumulation of PMNs and macrophages.[128]

The growing body of evidence for the pro-inflammatory role of GPR84 has resulted in blockade of the receptor being pursued as a possible treatment for inflammatory disease. Notably, compounds from GPR84 antagonist series **25** are reported to block embelin mediated neutrophil chemotaxis and showed a good safety profile in phase I clinical trials with healthy volunteers. However, the GPR84 antagonists showed no efficacy in phase II clinical trials with patients suffering from ulcerative colitis. Further research into the immunoregulatory role of GPR84 may provide better knowledge for the treatment of other chronic inflammatory diseases such as atherosclerosis.

Microglia and neuroinflammation

Microglia, the specialised macrophages of the brain and central nervous system, display significantly higher basal GPR84 expression than other immune cells.[150,151] Similar to other immune cells, an inflammatory challenge such as endotoxin treatment enhances GPR84 expression in microglia *in vitro* and broadly enhances GPR84 expression in the brain *in vivo*. Mouse models of neuronal injury, multiple sclerosis, and Alzheimer's disease also show significantly enhanced GPR84 levels.[152–154] Unlike macrophages, however, 6-OAU stimulation of primary murine microglia does not induce secretion of pro-inflammatory cytokines, although GPR84 agonists do induce membrane ruffling and increased motility in microglia.[155] In a murine model of Alzheimer's disease, GPR84$^{-/-}$ mice showed reduced recruitment of microglia to amyloid plaques and increased β-amyloid-induced dendritic degeneration.[154] GPR84 activation is therefore suggested to be required for β-amyloid-induced microgliosis and GPR84 agonists may be therapeutically beneficial in Alzheimer's disease.

Fibrosis

GPR84 activity has been associated with increased progression of organ fibrosis in various disease models. Expression of GPR84 is upregulated in adenine-induced nephropathy, and GPR84$^{-/-}$ mice show significantly reduced renal fibrosis in an adenine-induced chronic kidney disease mouse model.[147] Treatment of wild-type mice with GPR84 antagonist/FFAR1 agonist **26** reduces renal fibrosis, but these antifibrotic effects are mostly maintained in GPR84$^{-/-}$ mice. **26** also reduces fibrosis in CCl_4-induced liver fibrosis rodent models, and showed efficacy in a phase II clinical trial for idiopathic pulmonary fibrosis.[148,156] However, the polypharmacology of **26** prevents a clear understanding of the role of GPR84 in fibrosis pathophysiology. Galapagos, the pharmaceutical company behind the selective GPR84 antagonist series **25**, recently announced promising antifibrotic preclinical data with GPR84 antagonists and are now running a phase II clinical trial for idiopathic pulmonary fibrosis. Publication of this data may provide insight into the mechanism by which GPR84 could exert profibrotic effects.

1.5 Aims and objectives of this thesis

The current literature suggests that GPR84 activation regulates numerous physiological and pathophsyiological processes and may therefore be a useful therapeutic target for inflammatory related diseases. Pharmacological target validation of GPR84, however, is hindered by the relatively narrow range of available chemical tools, with many showing off-target effects that limit their utility. Furthermore, investigations of GPR84 biology have almost exclusively used GPR84 agonists that conform to fatty acid mimetic structures and show similar signalling in GPR84 recombinant cells. No study to date has reported on the consequences of biased signalling at GPR84 in physiologically relevant cells. In this thesis I therefore aim to:

- Develop structurally novel GPR84 agonists and comprehensively characterise their chemical and biological properties so they can be used as high-quality GPR84 chemical probes.
- Determine if novel chemotypes of GPR84 agonist show biased signalling at the receptor and/or bind allosterically and exhibit cooperativity with other GPR84 agonists.
- Investigate if biased agonists display different novel signalling and functional regulation in disease-relevant cell-lines and primary immune cells.

Chapter 2

Screening for GPR84 agonists

2.1 Introduction

The identification of novel bioactive molecules is a key concern in pharmaceutical development and academic drug discovery. A multitude of different strategies are used, from the isolation and testing of complex natural products, to high-throughput screens of vast libraries comprising millions of compounds. *In silico* approaches to identifying new molecules active at specific targets are resource efficient methods for rapidly sampling large regions of chemical space, and are now widely used throughout industrial and academic drug discovery.[157] In this section I will introduce virtual screening and the different methodologies that have been used to identify potential GPCR ligands, before outlining my aims for this chapter.

2.1.1 Virtual screening

Virtual screening uses computational methods to aid in the discovery of new compounds capable of modulating a biological target. By predicting the activity of compounds, either through comparisons to known ligands (ligand-based) or by analysing potential ligand-receptor binding interactions (structure-based), virtual screening is commonly used as a filter for large compound libraries to increase the efficiency of compound screening. Structure-based methods are more widely used than ligand-based screens, but a variety of factors determine the most appropriate method for any given project, including availability of protein struc-

tures, potency and diversity of reported ligands, and the class of the target protein.[158] GPCRs have been disproportionately successful as virtual screening targets compared to soluble proteins, probably due to the encapsulated, well defined orthosteric binding sites that enable efficient ligand recognition.[159] GPCR screening campaigns are further advantaged because sustained medicinal chemistry campaigns against GPCRs have resulted in compound libraries containing an estimated 3–12 times as many small molecules similar to GPCR ligands compared to other drug targets like kinases, proteases, and ion channels.[160]

Structure-based virtual screening

In structural approaches to virtual screening, ligands are docked to experimentally or computationally determined protein structures and the binding affinity of the compound is scored. Structure-based virtual screening for GPCR ligands has traditionally been limited by the poor availability of GPCR crystal structures. Over the past decade, however, technical advances in protein engineering and crystallography have resulted in a new wave of published GPCR structures.[161,162] Various lipid sensing GPCR structures have been solved, including FFAR1,[102] the cannabinoid CB_2 receptor,[163] and the prostaglandin D_2 receptor;[164] however no structures of GPR84 have yet been reported. In total, structures are now available for 62 unique receptors, although this still covers only around 17 % of all non-olfactory GPCRs.[16]

The continuing paucity of GPCR crystal structures means that structure-based virtual screens often rely on homology models of the target receptor. For example, the first small molecule ligand that activates neuropeptide receptor GPR171 was identified through molecular docking to a homology model based on an agonist-bound structure of the phylogenetically related purinergic $P2Y_{12}$ receptor.[165] Homology models exploit the conserved topology of GPCRs by using receptors with experimentally determined structures as templates for modelling the receptor of interest. The accuracy of homology modelling techniques for predicting ligand binding to GPCRs has repeatedly been tested by blind community modelling competitions prior to the release of the experimentally determined structure.[166–168] These blind tests have confirmed that accurate models can be generated for receptors with high homology to structural templates, but receptors such as CXCR4 that are only distantly related

to GPCRs with known structures are very challenging to predict.[168] Importantly, Carlsson et al. demonstrated that virtual screening by docking to a homology model of the dopamine receptor performed almost identically to the experimental structure when the same ligands were screened against it.[169] This, and other similar studies, have shown that molecular docking to carefully designed homology models is a viable tactic for novel ligand discovery.[170]

A further complication for virtual screening using molecular docking is that most structures are solved bound to an antagonist, with the receptor in an inactive state. The conformational flexibility of GPCRs means that a ligand capable of stabilising a GPCR active state may not be identified through docking with an inactive state structure. The agonist-bound structure of cannabinoid CB_1 receptor, for example, shows significant conformational changes relative to the antagonist state, including a 53 % reduction in the size of the ligand-binding pocket.[171] In general, docking studies identify ligands that correspond to the function of the ligand-receptor complex of the structure used.[172] A structure of the β_2AR bound to inverse agonist carazalol therefore primarily identified novel inverse agonists,[173] whereas a structure of antagonist-bound adenosine A_{2A} discovered only antagonists.[174] Screening for agonists using antagonist-bound structures can be made more efficient using GPCR binding pocket refinements with molecular dynamics or ligand directed modelling of binding sites, but experimentally determined active state structural models still display superior ability to identify novel agonists.[175]

Ligand-based virtual screening

Ligand-based methodologies use the properties of known ligands for a target to identify new active compounds. A primary advantage of these approaches is that there are no requirements for structural information on the target protein. Additionally, as no macromolecules are involved in the calculations, ligand similarity approaches tend to be computationally cheap to perform and thus often appear early in a virtual screening workflow.[176] Major disadvantages of ligand similarity searches, however, include a reduced likelihood of identifying novel chemotypes compared to structural approaches. Furthermore, receptor deorphanisation or the discovery of molecules that bind at new allosteric sites by these methods are

precluded due to the requirement for an existing reference ligand.

Virtual screening by ligand-based methods can range from simple structural fingerprint database searches, to 3D shape and electrostatic comparisons, to complex 3D pharmacophore models such as quantitative structure-activity relationship (QSAR) analysis. Due to the increasing computational complexity of these methods, a common virtual screening workflow will involve a series of screening filters, with the number of compounds reduced each pass (Figure 2.1). For example, novel agonists and antagonists of FFAR1 were identified from the 2.6 million compound ZINC database[177] through multiple *in silico* steps: a 2D fingerprint similarity search reduced the library to 704 772 compounds of which a diverse selection of 10 % were taken into 3D pharmacophore searches that identified 1536 promising hits.[178] 17 % of compounds biologically tested were verified as active at FFAR1, demonstrating the effectiveness of this approach for targeting GPCRs.

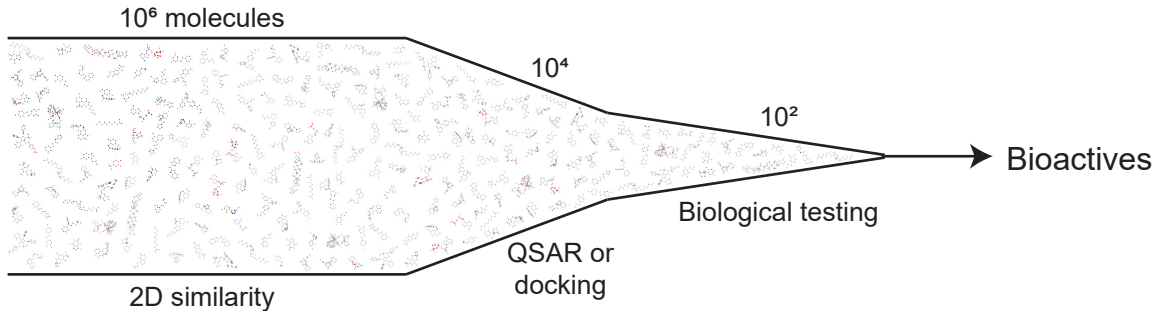

Figure 2.1: A typical virtual screening workflow, with gradually more complex computational filters applied until the most promising compounds are biologically tested

Fingerprints quantify patterns in molecular structure as sequences of bits to enable numerical comparisons. Tanimoto similarity of fingerprints, for example, can then be used to easily rank compounds by similarity.[179] These 2D methods are well suited to identifying new molecules that are structurally very similar to the reference ligand, but are less effective at identifying new chemical classes of bioactive compounds. In contrast, 3D methods that compare the shape and electrostatics of compounds are better suited to identifying novel chemotypes that share similar features to the reference compound but are structurally distinct. For example, 3D similarity searches were used to identify novel scaffolds of cannabinoid CB_2 agonists by virtually screening 25 000 compounds for shape similarity to a potent published agonist, HU-308.[180]

QSAR models attempt to model the physical and chemical features of compounds and relate them to their biological activity. First introduced almost 60 years ago by Hansch et al,[181] modern QSAR techniques use 3D descriptors and machine learning to create models capable of predicting the activity of untested compounds.[182] Traditional QSAR models are usually generated from a series of congeners, typically arising from a lead optimisation programme, and then used to inform future compound design. More recently, QSAR models have been used in virtual screening to identify novel ligands from diverse libraries. These approaches have yielded new scaffolds of anti-malaria, cannabinoid, and dopamine receptor ligands.[183–185] The huge growth in availability of compound libraries and datasets has further established chemoinformatics and machine learning approaches, such as QSAR, for virtual screening applications.[186,187]

2.1.2 Aims and overview

In this chapter I aim to identify new GPR84 ligands that are suitable for development into tool compounds for probing the biology of the receptor. A key objective is that the new compounds should be structurally distinct from previously reported GPR84 tools, as novel chemotypes will often confer new biology at a GPCR through biased signalling.[188] Moreover, the screening hits should display good selectivity and potency at GPR84, while having suitable physicochemical properties for progression into a medicinal chemistry programme.

First I will synthesise previously reported GPR84 agonists and antagonists, and use them to validate a cellular second messenger screening platform for GPR84 ligands. I will then develop a predictive 3D-QSAR model based on published GPR84 ligand activity data, and use it to virtually screen a compound library for potential new GPR84 agonists. Finally, I will perform a focused biological screen to identify any compounds with GPR84 activity, and use both counterscreens and a secondary impedance sensing assay to confirm that the screening hits possess genuine activity at the receptor. I will end the chapter by evaluating the newly identified GPR84 ligands as candidates for further development in section 2.5.2.

2.2 Validating a GPR84 screening platform

2.2.1 Synthesis of GPR84 tool compounds

Initially I set out to synthesise a range of published GPR84 tool compounds for use as controls to validate the correct functioning of a GPCR cellular screening platform. Capric acid, 6-OAU, and embelin are commercially available GPR84 agonists, while the more potent agonist, ZQ-16, was synthesised in one-step through alkylation of thiobarbiturate with 1-bromohexane in low yields comparable to those previously reported (Scheme 2.1).[136]

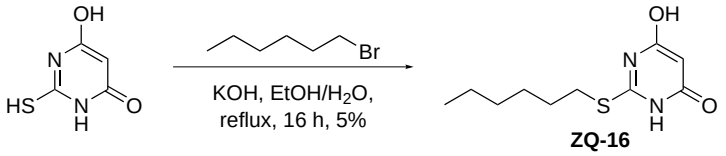

Scheme 2.1: Synthesis of GPR84 agonist ZQ-16

In order to test a selection of GPR84 ligands with a range of different activities, I also synthesised the highly potent agonist, **19**. This 4-hydroxy-2-pyridone derivative is reported to have sub-nanomolar potency at the receptor and was readily synthesised following literature procedures (Scheme 2.2).[136] Briefly, ethylacetoacetate was alkylated using 1-bromooctane to form **27** which was hydrolysed using NaOH to acid **28**. Cyclisation with 1,1'-carbonyldiimidazole afforded substituted pyrone **29** and subsequent deacylation formed **30** in good yield. Finally, heating with aqueous ammonia gave GPR84 agonist **19** in an overall yield of 8 % over five steps.

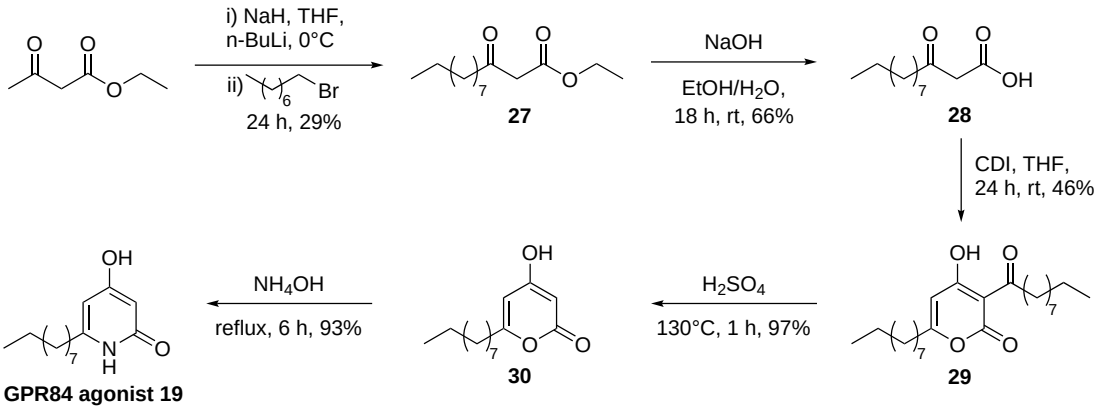

Scheme 2.2: Synthesis of GPR84 agonist **19**

Next, I sought to synthesise a member of the dihydropyrimidinoisoquinolinone GPR84 antagonist series developed by Galapagos. Pharmacological blockade of GPR84 can be used to demonstrate that observed responses are due to receptor engagement, and not off-target effects or non-specific assay artefacts. I adapted a partially reported synthetic procedure in the patent literature[146] which was subsequently published by our group (Scheme 2.3).[125] Refluxing 3-methoxyphenethylamine with urea in aqueous acid and subsequent demethylation of **31** gave phenol **32** in good yield. Allyl ether protection to **33** enabled reaction with diethyl malonate to give barbituric acid derivative **34** in good yield. Chlorination with $POCl_3$ facilitated cyclisation in a Bischler-Napieralski like reaction to form tricyclic compound **35**. Substitution with commercially available (1,4-dioxan-2-yl)methanol and NaH formed **36** which was readily deprotected using $Pd(PPh_3)_4$ to **37**. Finally, alkylation with 2-(chloromethyl)pyridine afforded the reported antagonist **38** in an overall yield of 6 % over eight steps.

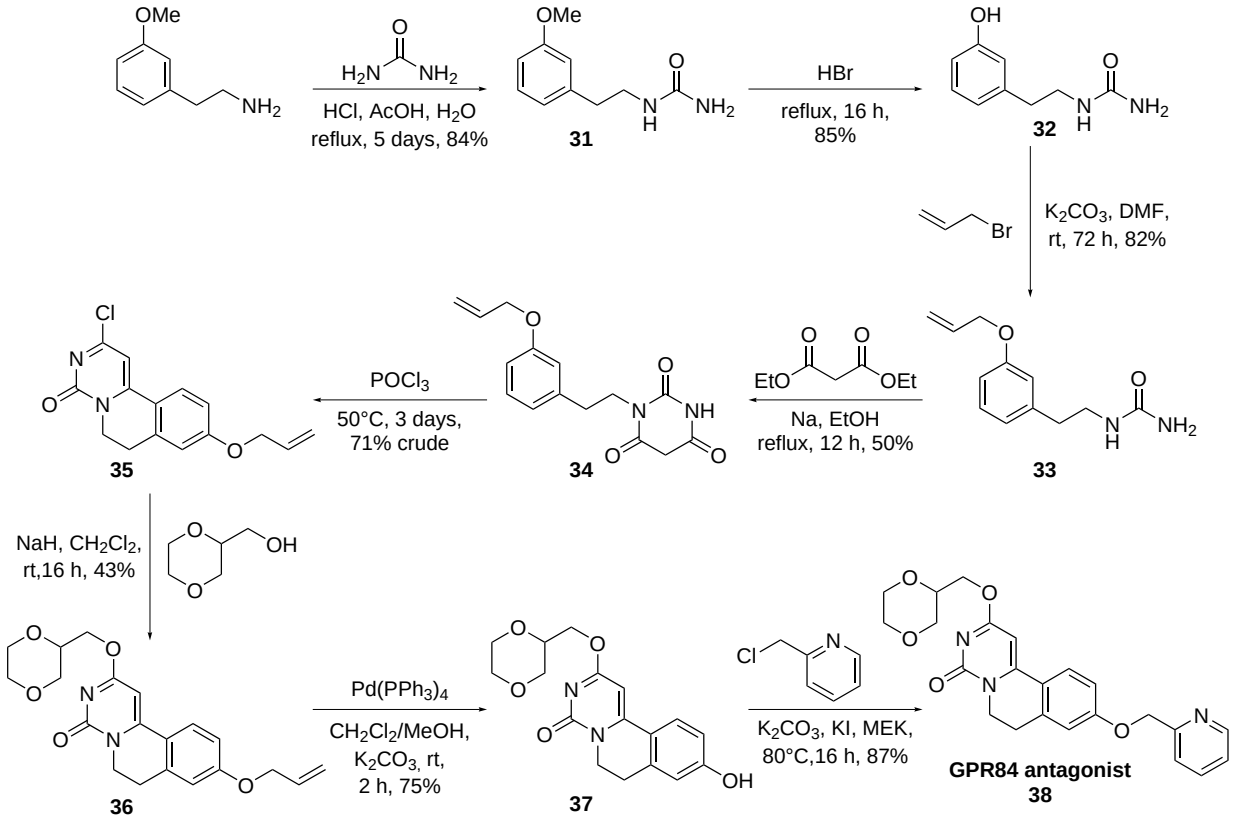

Scheme 2.3: Synthesis of GPR84 antagonist **38**

2.2.2 Biological testing of GPR84 ligands

I next set out to use the GPR84 ligands to validate a DiscoverX cAMP accumulation assay in chinese hamster ovary (CHO) cells that overexpress the human GPR84 receptor (GPR84-CHO). In this assay, forskolin stimulation activates adenylate cyclase and leads to an accumulation of cAMP within the cell. Co-treatment with a GPR84 agonist activates the $G_{\alpha i}$ subunit which negatively regulates adenylate cyclase and causes a decrease in cAMP levels. Following agonist incubation, the cells are lysed and and the cAMP levels detected using a competition assay in which cellular cAMP competes with introduced, labelled cAMP for binding to an anti-cAMP antibody.[189] Each GPR84 agonist induced a concentration-dependent reduction in luminesence, corresponding to inhibition of forskolin induced cAMP production by GPR84 mediated $G_{\alpha i}$ activation (Figure 2.2a). The rank order of potency for the compounds was similar to that reported in previous publications and, furthermore, my determined EC_{50} values are directly comparable to those determined using the same cAMP assay system.[136,138] Pre-incubation with GPR84 antagonist **38** reversed the 6-OAU induced inhibition of cAMP production in GPR84-CHO (Figure 2.2b), demonstrating the specificity of both compounds.

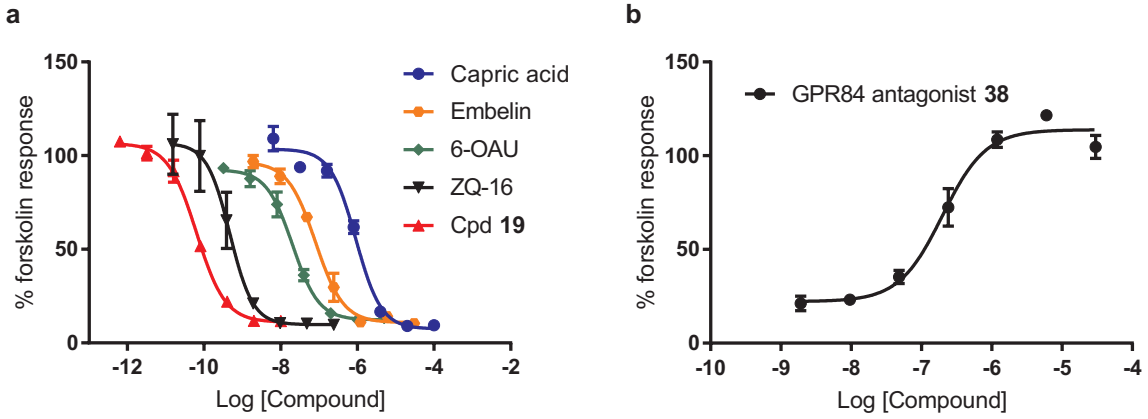

Figure 2.2: GPR84 agonists and antagonists produced the expected responses in GPR84-CHO cells (a) GPR84 agonists capric acid, 6-OAU, embelin, ZQ-16 and **19** have the same rank potency at GPR84 as previously reported. **(b)** Pre-treatment with GPR84 antagonist **38** dose-dependently blocks the negative regulation of cAMP levels in response to 6-OAU agonist challenge at the EC_{80} concentration (24 nM). Data are representative curves from 2–3 independent experiments and are displayed as mean ± SD of 2 technical replicates.

2.3 Ligand-based virtual screening

2.3.1 Developing a QSAR model

Immediately prior to the initiation of this project, Liu et al. published a structure-activity optimisation of GPR84 agonist ZQ-16.[136] Through small modifications to the polar head group and testing various lipophilic tail groups, they improved the potency of the compound by almost three orders of magnitude to **19**. This published dataset fulfils all the basic criteria for the development of a QSAR model: the dataset is relatively large with over 50 compounds reported; the majority of the compounds are structurally very similar and can be expected to bind the same site; the activity of the agonists covers a wide range, from 43 µM to 189 pM. I therefore undertook to use the software package Forge® to generate a QSAR model to predict the activity of potential new GPR84 agonists (Figure 2.3).

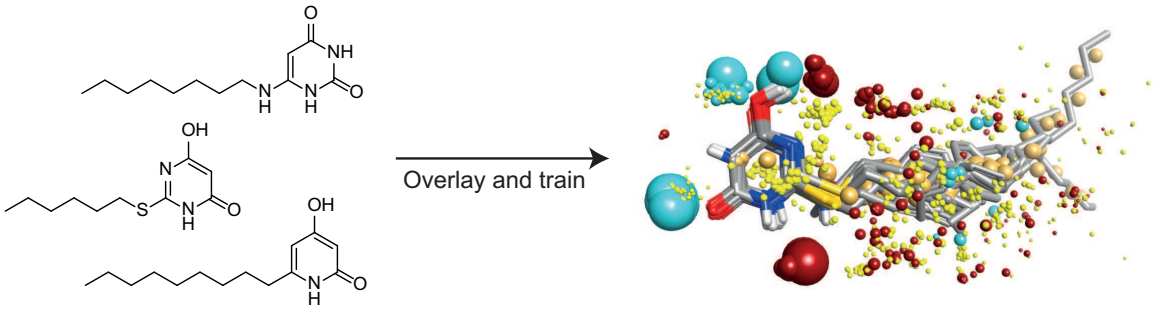

Figure 2.3: A published dataset of 32 GPR84 agonists were overlaid in Forge® and used to generate Quantitative Structure Activity (QSAR) models. Regions of common positive charge (red), negative charge (blue), and hydrophobic regions (gold) are highlighted.

An initial challenge for computationally modelling this dataset is that many of the compounds, including the derivatives of 6-OAU, ZQ-16, and **19**, are capable of existing as multiple different tautomers (Figure 2.4). Tautomerisation has a significant impact on the performance of QSAR models and it is challenging to determine the bioactive tautomer of a small molecule under physiological conditions.[190] As such, it is generally recommended to develop separate QSAR models for each tautomer in turn. In this case, developing a separate QSAR model for each possible permutation of possible tautomeric active forms within the dataset is not feasible. I therefore developed two QSAR models: one in which derivatives of ZQ-16 and **19** are entirely in their respective lactim forms, and another in which the compounds adopt the 2-keto form. The 2-keto form was chosen over the 4-keto form for this

comparison because structural studies of similar compounds have shown the 2-keto form is preferred over the 4-keto.[191] Uracil is known to strongly favour its diketo tautomer,[192] and so I assumed all uracil derivatives would adopt this form.

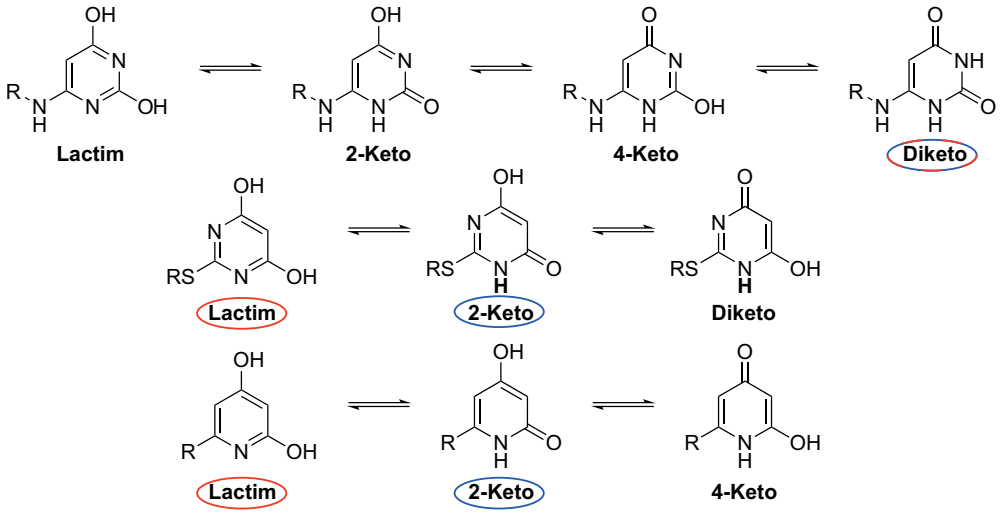

Figure 2.4: The possible tautomeric structures of GPR84 agonists. From top to bottom: tautomers of uracil derivatives, ZQ-16 derivatives, and **19** derivatives. The tautomers used in generating the lactim model or the 2-keto model are labelled red and blue respectively.

I next set out to test the predictive power of the QSAR models based on the two different tautomers. Given the size of the dataset, I used all the compounds in generating the model and none were held back as a test set for externally validating the model. Instead, I used Leave-Many-Out cross-validation to internally validate the QSAR models (Figure 2.5a-b). The two models based on different tautomers were both internally predictive according to widely cited guidelines of $R^2 > 0.6$ and $Q^2 > 0.5$.[193] In order to see which model was better at predicting the activity of compounds unknown to the model, a small compound dataset of 10 novel 6-OAU analogues was synthesised by a Master's student, Bridget Reeve (Appendix Table 1). The activity of the compounds was predicted by both the models and then compared to the actual activity as tested in the cAMP assay (Figure 2.5c-d). The QSAR model based on the 2-keto form showed good correlation between the predicted and observed values ($R^2 = 0.73$), and additionally has a slope close to the unity slope of the ideal model, suggesting the model has moderately good predictivity. In contrast, the lactim model shows no correlation ($R^2 = 0.16$) and a slope of 0.33, showing the model has no predictive power. These data support the keto tautomer as the active form of that compound series, and this model was therefore used in the virtual screening of compounds with unknown activity.

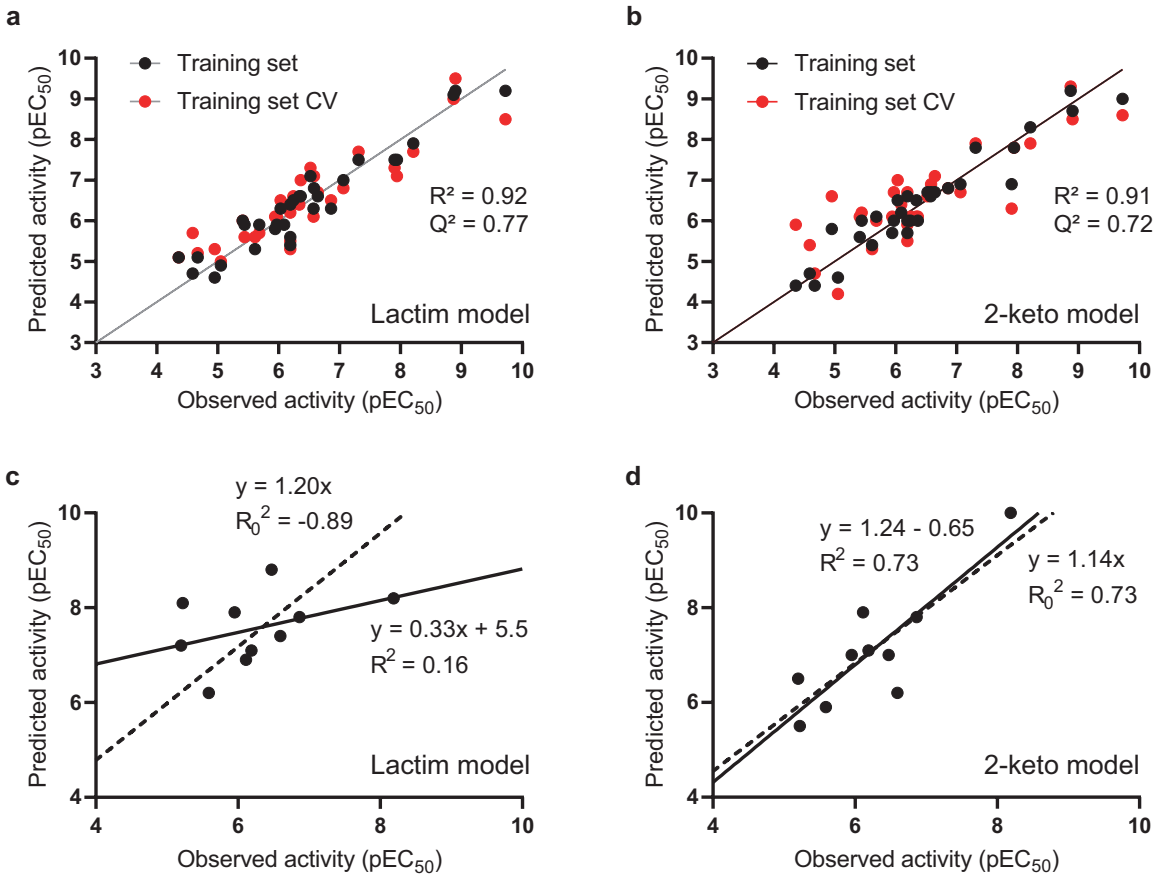

Figure 2.5: The QSAR model based on the 2-keto tautomer is the more predictive model **(a)** and **(b)** show the internal validation of the lactim and the 2-keto QSAR models respectively. Black points represent predicted activity for compounds in training set, and red points show predicted activity for the same compounds in models generated by Leave-Many-Out cross validation. The models based on both tautomers show good fit ($R^2 > 0.9$) and good internal predictivity ($Q^2 > 0.7$). **(c)** and **(d)** show each models predictive performance on a small compound dataset unknown to the models, where a predictive model should be expected to have a coefficient of regression through the origin (R_0^2) of close to 1. The 2-keto model shows moderately good predictivity, whereas the lactim model displays no predictive power.

2.3.2 Screening

Following the successful validation of the GPR84 agonist QSAR model, I next aimed to employ the model to identify potential new agonists from a diverse compound library. I used an in-house library of 10000 compounds to enable rapid experimental testing of any hits predicted by the QSAR model. Each compound was assessed by the model and the activity at GPR84 predicted. I then excluded those compounds occupying a ligand space very different to the training set, as assessed by a "fit to model" of OK, poor, or bad within the Forge software. I ranked the remaining compounds by predicted potency and then manually chose a chemically diverse selection of 45 compounds for biological testing (Appendix Table 2). Each compound was tested using the GPR84-CHO cell cAMP assay at 30 µM in technical triplicate,

and 7 compounds were identified to reduce cAMP levels to below 50 % compared to stimulation with the vehicle, 0.3 % DMSO. Upon retesting of solid samples of each compound, six retained activity and were confirmed to show reproducible activity in GPR84-CHO cells. The hit compounds cover a diverse range of structures (Figure 2.6), with highly potent **40** of particular note as a thiobarbituric acid derivative that is structurally similar to GPR84 agonists reported in previous publications.[136,138]

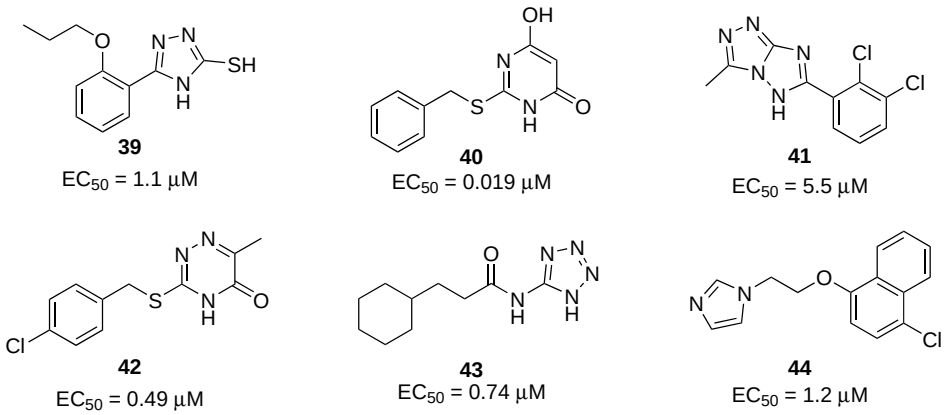

Figure 2.6: The chemical structures of the six screening hits identified as active at GPR84

2.4 Secondary screening

2.4.1 Counterscreening

Each GPR84 screening hit was counterscreened against different CHO cell lines expressing the $G_{\alpha i}$ coupled cannabinoid CB_1 receptor, the $G_{\alpha s}$ coupled β_2AR, and untransfected CHO cells (Figure 2.7). Compounds **40**, **41**, **42**, **43**, and **44** only act to reduce cAMP levels in GPR84-CHO cells, suggesting they specifically interact with GPR84. However, compound **39** showed activity in CB_1-CHO and untransfected CHO cells with a similar potency to GPR84 cells, indicating it is acting non-specifically to reduce luminescence in a non-GPCR mediated fashion and likely does not bind GPR84.

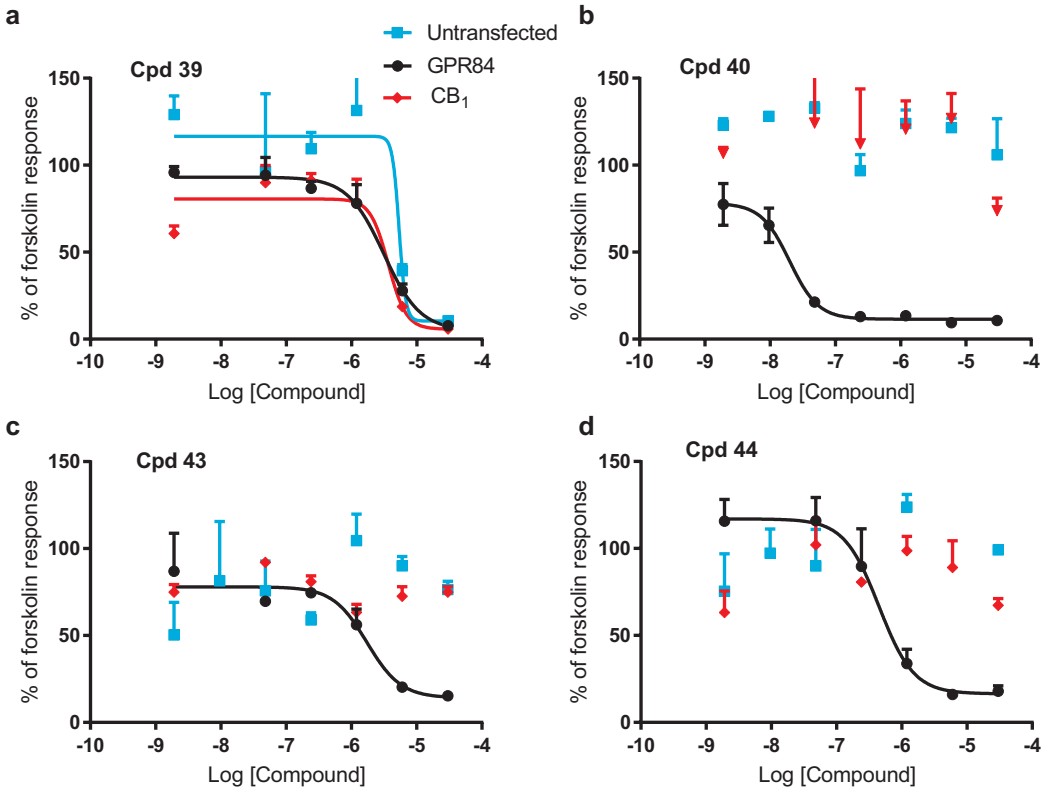

Figure 2.7: cAMP Screening data for selected hit compounds in GPR84-CHO, CB_1-CHO, and untransfected CHO cells. Compounds **40**, **43**, and **44** only show activity at GPR84, whereas **39** also shows similar levels of activity in CB_1-CHO and untransfected cells, so likely has non-specific effects on the assay. Data are n=1 screening data and are shown as means ± SD of two technical replicates.

2.4.2 Orthogonal screening assay

An effective screening campaign should include a secondary assay format with an orthogonal readout to the primary assay to minimise the possibility of false positives and increase confidence in the hit validation process.[194] I chose to use a label-free impedance sensing assay in which cytoskeletal and adhesion changes in cells are measured following drug stimulation, and quantified as an arbitrary cell index (CI) measure.[195] The real-time, integrated response measured in this biosensing assay is complementary to the end-point cAMP signalling primary assay and enables monitoring of response kinetics.[196] Additionally, the response profile can indicate the downstream pathways triggered by receptor activation, with G_i, G_s, and G_q pathways demonstrated to elicit diverse responses in differentially stimulated CHO cells.[197] My initial impedance experiment with GPR84-CHO cells showed an increase in baseline corrected cell index, consistent with G_i activation,[197] upon addition of 6-OAU before returning to the basal level within an hour (Figure 2.8a). Importantly, no response to 6-OAU was observed in untransfected CHO cells (Figure 2.8b).

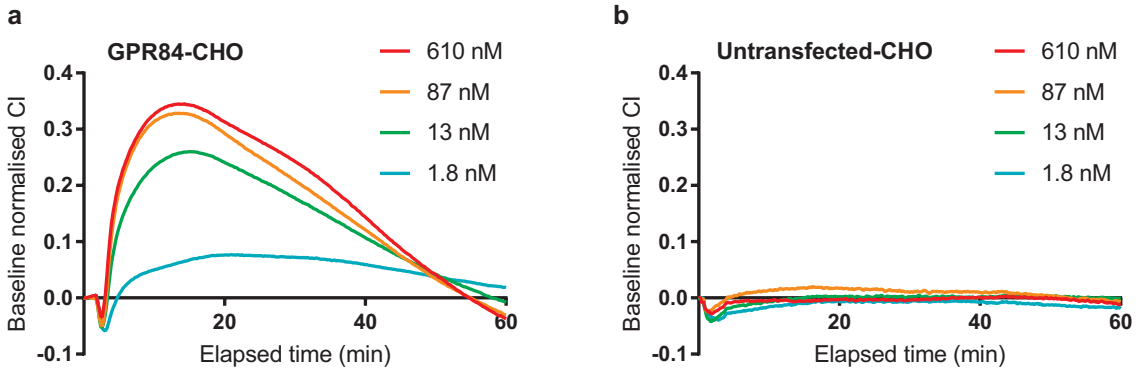

Figure 2.8: GPR84 activation by 6-OAU can be detected in GPR84-CHO cells using impedance sensing. 6-OAU induces dose-dependent responses in **(a)** GPR84-CHO cells but not **(b)** untransfected CHO cells. Traces are representative of n = 2 experiments and are background corrected for the response to DMSO alone.

The GPR84 screening hits were tested in the impedance assay at a variety of concentrations with both untransfected and GPR84-CHO cells (Figure 2.9). All the compounds induced dose-dependent cytoskeletal responses in the GPR84-CHO cells, but in many cases non-specific activity was also observed. **41** induced identical responses in untransfected cells as in GPR84-CHO cells, implying the compound is having other effects beyond GPR84 agonist activity. **42** causes significant non-specific effects at 30 µM, and at lower concentra-

tions induces little response in the GPR84-CHO cells. Compounds **41** and **42** were therefore considered lower quality screening hits.

Both the screening hits **43** and **44** induce significant responses in GPR84-CHO cells at all concentrations. Similar responses are not observed in untransfected cells, although **44** does appear to cause a decrease in cell index at the highest concentration, possibly due to cell toxicity or poor solubility. To confirm that the screening hits don't affect cell viability, the compounds were incubated with CHO cells for 30 min before measuring cellular metabolic activity using the PrestoBlue® reagent (Appendix Figure 1). No decrease in cell viability was observed with any of the compounds compared to DMSO treatment.

2.5 Discussion

In this chapter, I aimed to identify structurally novel GPR84 agonists appropriate for further development as chemical probes. To achieve this, I developed and validated a ligand-based virtual screening approach that I used for prioritising compounds for a focused biological screen. Through a series of *in vitro* assays, I identified compounds with reproducible and selective activity at GPR84 across different cell signalling readouts.

The importance of developing structurally novel ligands for understudied GPCRs such as GPR84 is twofold: using multiple, chemically distinct, tools to investigate a target is an important aspect of pharmacological target validation, and reduces the likelihood of confounding off-target effects; and secondly, targeting GPCRs with novel chemotypes can impart new signalling modalities or functionality through biased agonism or the targeting of allosteric sites.[188] In particular, the ability of GPCRs to adopt many active or inactive states is perhaps best exploited by novel chemotypes that can stabilise the GPCR in unique conformations.

Ultimately, any promising screening hits identified will subsequently be optimised for use as *in vitro* and *in vivo* GPR84 tool compounds. Accordingly, selecting screening hits with appropriate properties for further development is essential to avoid issues with compound selectivity or physicochemical properties at a later stage. In this section I will discuss the merits and limitations of the virtual screening strategy I used to discover new GPR84 ligands, and then go on to evaluate my screening hits as candidates for further development.

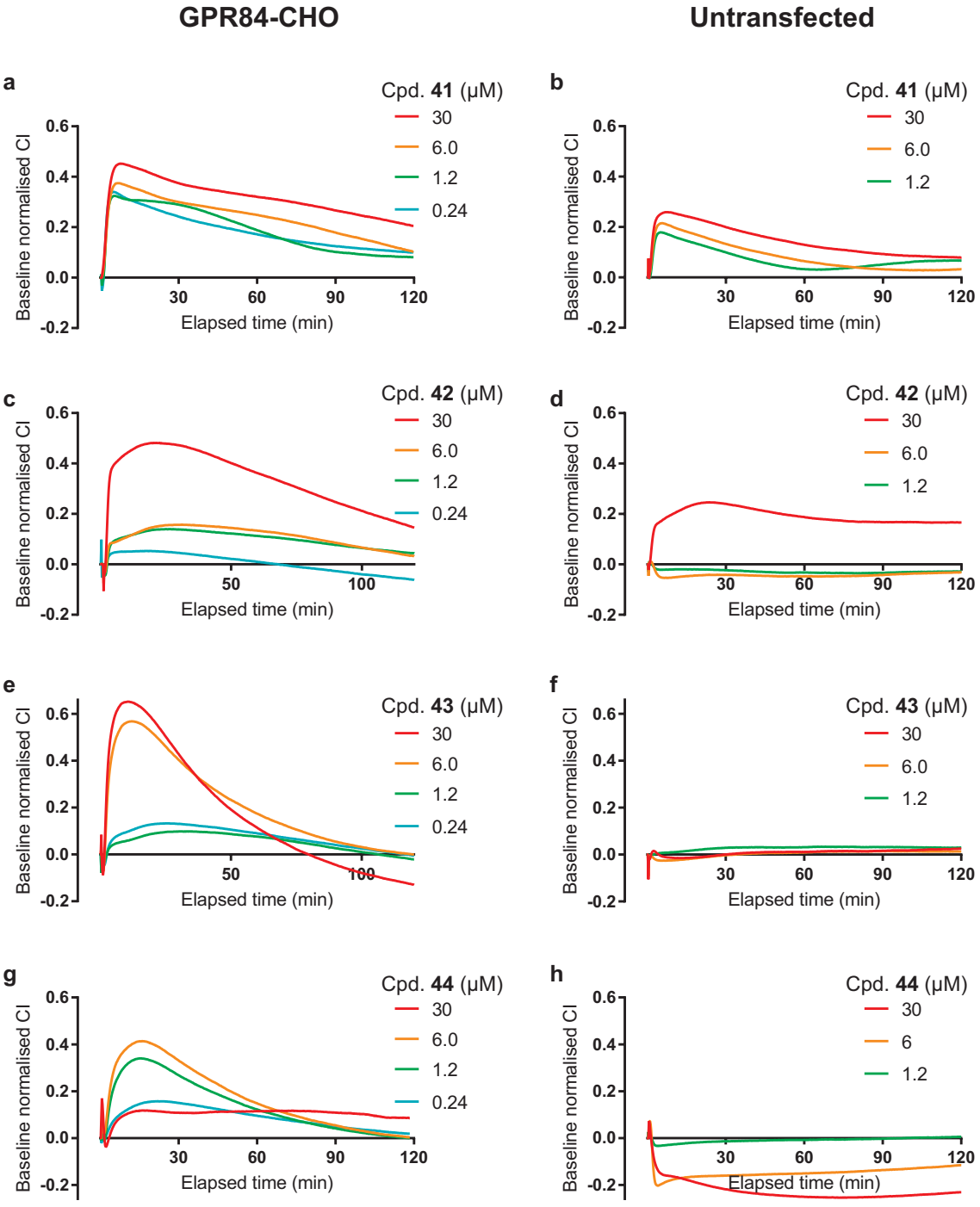

Figure 2.9: Cellular impedance sensing secondary screen for hit validation. Each compound was tested in a concentration-response with GPR84-CHO cells (left) and untransfected-CHO cells (right). **(a-d)** Screening hits **41** and **42** show significant activation in both GPR84 and untransfected CHO cells. **(e-f)** Compound **43** specifically activates only GPR84-CHO cells. **(g-h)** **44** activates GPR84-CHO cells but also induces a non-specific decrease in cell index at high concentrations. Traces are representative of 2 independent experiments and are background corrected for the response to DMSO vehicle.

2.5.1 Virtual screen

A key aim of my screening campaign was to identify GPR84 agonists structurally distinct to those previously reported. The identification of new chemotypes is best achieved with structure-based virtual screening methodologies as they can predict binding affinity of new compounds independently of reference ligands. Initially then, I investigated the feasibility of using molecular docking to a GPR84 structure as a means of discovering new ligands. To date, no crystal structures of GPR84 have been published and so homology modelling and mutagenesis studies provide the only structural insight into ligand binding at the receptor. Two homology models of GPR84 have so far been reported, and they offer conflicting reports as to the mode of ligand interactions in the orthosteric binding site (section 1.4.4).[127,149] The relatively low sequence similarity of the β_2AR template used by one study may explain these inconsistent results, but it serves to highlight the difficulties in accurately generating homology models even for known ligands. Homology modelling is most likely to be accurate if templates with high sequence identity or rigid orthosteric ligands are available.[168] The receptor with the highest sequence homology to GPR84 is the dopamine D_2 receptor at 26 %, well below the 30 % limit of sequence identity beyond which the accuracy of homology models is greatly reduced.[198] Furthermore, the only published D_2R structure is in the inactive state bound to antagonist risperidone, and so is less suitable as a template for an agonist-targeted virtual screen.[199] Finally, even with accurate structural models, ligand docking itself can return questionable results and often requires computationally intensive molecular dynamics simulations to verify a virtual hit.[200] For these reasons I chose not to pursue a structure-based virtual screening strategy.

In contrast, there are a number of GPR84 ligand datasets that are well suited for use as a basis for virtual screening. As alluded to above, however, a major limitation of ligand-based approaches to virtual screening is their inherent bias towards molecules similar to the input compound.[201] The tension between my aims of identifying novel ligands and the propensity of ligand similarity searches to return relatively non-novel compounds therefore guided my choice of ligand-based screening method. Whereas simple structure similarity virtual screens are likely to return ligands similar to the input compound, 3D models of shape and

electrostatic similarity can return novel chemotypes capable of occupying the same binding site.[176] In particular, 3D-QSAR models have been used for discovering novel scaffolds of GPCR ligands, exemplified by the identification of new 5-hydroxytryptamine 6 receptor antagonists by Hajjo et al.[202] In my project, the use of QSAR enabled the exploitation of the information-rich published GPR84 compound datasets to aid in the search for new compounds. I therefore believe it was the most effective *in silico* technique available to me in the continuing absence of GPR84 crystal strutures.

The importance of externally validating QSAR models is well established in the literature,[203] and this was exemplified in my project by the QSAR model based on the lactim tautomer which shows strong internal predictivity but no ability to predict the bioactivity of unknown compounds. In contrast, the 2-keto QSAR model ultimately used for virtual screening was demonstrated to be both internally predictive and have moderately good external predictivity according to published guidelines.[203] However, there are a number of limitations to this external validation. Firstly, the relatively small dataset of 10 compounds should be larger to enable greater confidence in the model validation. Additionally, the compounds comprising the dataset are almost entirely uracil derivatives and thus fail to cover the structural diversity of the model training set. This is important considering the ambiguity around the active tautomeric structures of the differently substituted GPR84 agonists. Ideally, additional QSAR models covering all the possible tautomers would be generated and then validated using a large external dataset containing derivatives of uracil, ZQ-16, and **19**.

My screening campaign was successful, and identified a number of structurally diverse GPR84 agonists, some of which are completely new scaffolds. However, it is difficult to apportion credit to the QSAR methodology used without further studies being conducted. The QSAR model can only be confirmed as an effective virtual screening tool in this project if it could be demonstrated that other, simpler, techniques would have performed worse. For example, a 2D structural similarity filter or a 3D shape comparison search should be performed on the same library and the number of biologically active compounds identified should be compared between the techniques. This would enable a direct comparison of the effectiveness of the different approaches, and true validation of the methods applied in this project.

2.5.2 Hit evaluation

In total, I identified six compounds with reproducible activity in GPR84-CHO cAMP accumulation assays through my ligand-based virtual screening campaign. In order to validate the screening hits I performed a series of secondary assays and counterscreens. Compounds that retain their activity in untransfected cells are likely acting through a non-specific mechanism and can be considered assay artefacts, while compounds that also activate the CB_1 or β_2 receptors do not have the selectivity expected of a high-quality chemical probe. To further confirm the compounds are capable of activating GPR84, I used a secondary assay with an orthogonal readout based on cell impedance changes following stimulation. Genuine GPR84 agonists should induce a prolonged increase in cell index for GPR84-CHO cells that correlates with G_i activation, as previously observed with dopamine stimulation of the Gi linked D_2 receptor in CHO cells.[197] The real-time, integrated response recorded by impedance sensing also enables more complex reactions to the compounds to be observed, such as response kinetics or non-specific interactions that would be missed with an end-point signalling assay like the cAMP primary screen.

In addition to assessing the specificity and robustness of GPR84 activation, I will also evaluate the physicochemical properties, synthetic accessibility, and structural novelty of my screening hits. The characteristics of the chemical starting point for a medicinal chemistry programme has significant impact on future development, and screening out compound liabilities early can reduce attrition at later stages.[204] Optimising screening hits for potency and selectivity typically increases the lipophilicity and size of the compounds, and consequently smaller, more polar screening hits are generally preferred.[205] To identify compounds containing functional groups that are metabolic or toxicological liabilities that would impact on *in vivo* usage, I score the "druglikeness" of each compound using the DataWarrior software package.[206] A more positive druglikeness score indicates a compound that primarily contains fragments frequently present in commercial drugs, whereas a negative score is associated with a compound comprised of groups not found in drugs. Finally, each screening hit will be assessed for its structural novelty compared to known GPR84 agonists. To quantify the screening hit novelty, I perform a Maximum Common Substructure (MCS) Tanimoto 2D

structural similarity comparison with 6-OAU.[207] The MCS Tanimoto coefficient calculated by ChemMine software has a value between 1 and 0, with higher values indicating greater structural similarity.[208]

Screening hit 39

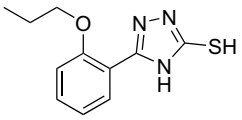

Chemical properties
MW : 235
cLog P : 2.1
Similarity to 6-OAU : 0.14
Druglikeness : -1.8

Bioactivity
GPR84 cAMP EC_{50} : 1.1 µM
Impedance response : N/A
Counterscreening : Active

Heterocyclic thiol **39** exhibits similar potency in all cAMP assays regardless of cell type, suggesting a non-specific mechanism of action that is not suitable for further development. In loss-of-signal assays false positive hits are commonly caused by compound toxicity,[209] but incubating CHO cells with **39** showed no decrease in cell viability. Possible explanations for the non-specific activity seen for this compound include the reactive thiol group causing inhibition of the adenylate cyclase or the enzymes catalysing the chemiluminescent reaction that detects cAMP levels.

Screening hit 40

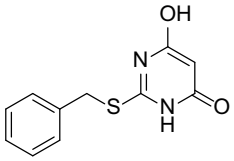

Chemical properties
MW : 234
cLog P : 1.2
Similarity to 6-OAU : 0.27
Druglikeness : 0.62

Bioactivity
GPR84 cAMP EC_{50} : 0.019 µM
Impedance response : Not tested
Counterscreening : Inactive

Compound **40** was the most potent screening hit identified and showed good selectivity when tested in other cAMP assays. However, **40** belongs to the thiobarbituric acid GPR84 agonist series that constituted part of the training set for the QSAR model and correspondingly has a relatively high similarity score with 6-OAU. The SAR of this and related series has been extensively explored[136,138] and the structural novelty of this screening hit is therefore limited.

Screening hit 41

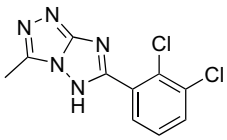

Chemical properties
MW : 268
cLog P : 1.7
Similarity to 6-OAU : 0.17
Druglikeness : 3.43

Bioactivity
GPR84 cAMP EC_{50} : 5.5 µM
Impedance response : Non-specific
Counterscreening : Inactive

Triazolotriazole **41** shows low potency activity against GPR84 while not activating other GPCRs. In the impedance sensing assay format, however, identical responses were observed in both GPR84-CHO and untransfected cells. This suggests that **41** not only fails to induce significant responses in GPR84 expressing cells, but additionally induces non-specific effects. The triazolotriazole motif is uncommon with few reported syntheses or characterisations,[210] however the poor specificity and robustness of the responses induced by **41** outweigh its structural novelty.

Screening hit 42

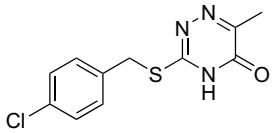

Chemical properties
MW : 268
cLog P : 3.2
Similarity to 6-OAU : 0.21
Druglikeness : 3.7

Bioactivity
GPR84 cAMP EC_{50} : 0.49 µM
Impedance response : Non-specific
Counterscreening : Inactive

42 shows good potency and selectivity for GPR84 in cAMP assays. In impedance sensing secondary assays, however, weak responses at GPR84 are seen alongside significant non-specific effects. The novelty of this compound is also less compared to other screening hits, as can be seen by the presence of the 6-thio-2-pyridone motif common to previously reported GPR84 agonist series.[136] Quantification of this lack of novelty by MCS Tanimoto comparison shows that **42** shares more structural features with 6-OAU than other screening hits.

Screening hit 43

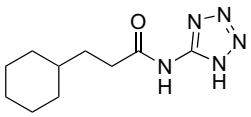

Chemical properties
MW : 223
cLog P : 1.6
Similarity to 6-OAU : 0.50
Druglikeness : -3.3

Bioactivity
GPR84 cAMP EC_{50} : 0.74 µM
Impedance response : GPR84 mediated
Counterscreening : Inactive

Tetrazole **43** induces robust responses in GPR84-CHO cells in both cAMP and impedance assays, and shows good selectivity across all counterscreens. The physicochemical proper-

ties of **43** are also good, with a relatively low molecular weight and lipophilicity providing room for further chemical optimisation. However, **43** shows higher MCS Tanimoto similarity to 6-OAU than other screening hits and structurally resembles a medium-chain fatty acid mimetic. Tetrazoles are commonly used bioisosteres for carboxylic acids,[211] and the saturated alkyl tail is similar to previously reported GPR84 agonists. The druglikeness score for **43** is negative, indicating that many of the features of this molecule are not usually found in commercial drugs. In addition, the only reported synthesis of (1*H*-tetrazol-5-yl)amides requires the use of 5-aminotetetrazole, a compound with significant explosive potential due to its 80 % nitrogen content.[212] While overall a good candidate for further development, the lower structurally novelty of **43** and challenging synthesis makes it a less attractive proposition for exploring new modes of GPR84 activation.

Screening hit 44

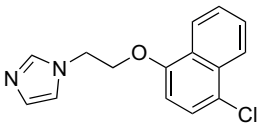

Chemical properties
MW : 273
cLog P : 3.0
Similarity to 6-OAU : 0.13
Druglikeness : 3.3

Bioactivity
GPR84 cAMP EC_{50} : 1.2 μM
Impedance response : GPR84 mediated
Counterscreening : Inactive

Imidazole derivative **44** shows robust activation and good specificity for GPR84 in cAMP assays. In impedance sensing assays, high concentrations of **44** induced a non-specific decrease in cell index, but lower concentrations showed specific, dose-dependent GPR84-activation. The compound is structurally simple and readily synthetically accessible through multiple different routes, enabling rapid optimisation. The cLogP of **44** is higher than other screening hits, but within an acceptable range for further development. The positive druglikeness score for this compound suggests it contains fragments common in commercial drugs. Importantly, **44** is structurally distinct from all previously reported GPR84 agonists. The MCS Tanimoto similarity to 6-OAU of **44** is the lowest of all screening hits, increasing the chances that it will interact uniquely with GPR84 and could confer new biology. For these reasons, I will proceed to further optimise and develop **44** into a chemical probe for investigation of the biological effects of GPR84 activation.

Chapter 3

Optimising a GPR84 chemical probe

3.1 Introduction

Chemical probes are small molecules used to inhibit, activate, or otherwise modulate a protein target for the interrogation of its biological function. The discovery and use of chemical probes for target validation has facilitated many breakthroughs in the understanding and treatment of various diseases. This is exemplified by the publication of small molecule probes of the BET family of bromodomains[213] in 2010 that kick-started biomedical research into the field to such an extent that bromodomain inhibitors entered clinical trials for the treatment of cancer only a few years later.[214,215] In this chapter I will briefly introduce the key properties of chemical probes, before describing the development of screening hit **44** into a novel GPR84 agonist probe.

3.1.1 Chemical probes for target validation

Pharmacological target validation with chemical probes has significant translational relevance as it closely reflects the actions of a drug in a biological system. In the GPCR field for example, the discovery that hallucinogenic natural product Salvinorin A was a selective opioid agonist identified that receptor as a target for psychotherapeutic drugs.[216] In addition, target validation with chemical probes is complementary to genetic approaches such as CRISPR or RNAi. While genetic ablation of a target removes the protein entirely from a

system, small molecule inhibition may block only one function of the target while allowing other protein-protein interactions to remain. For example, siRNA depletion of the kinase TNIK was used to demonstrate its role as key activator of the carcinogenic Wnt signalling pathway, suggesting TNIK inhibitors as a viable target for disease states with aberrant Wnt activation such as colorectal cancer.[217] Upon the discovery of a potent small molecule TNIK inhibitor, however, it became clear that direct competitive inhibition had minimal effects on Wnt signalling and scaffolding interactions may instead explain the genetic knockdown results.[218] Such examples illustrate the importance of chemical probes in characterising and validating new drug targets for treating disease.

3.1.2 Properties of a chemical probe

While chemical probes can be invaluable in biomedical research, the use of low-quality or poorly characterised tool compounds is widespread and negatively impacts on our understanding of biology.[219] The qualities that make a good chemical probe are distinct to those for a drug, and many drugs make poor quality chemical probes. For example, the polypharmacology exhibited by central nervous system drugs such as clozapine and risperidone is essential to their therapeutic efficacy, but makes them poor chemical probes for the interrogation of any one target.[220] On the other hand, chemical probes for *in vitro* use do not need such stringent requirements for safety and pharmacokinetics that are necessary requirements for any drug.

Target engagement

It is important that a chemical probe is demonstrated to be directly interacting with its supposed target in an appropriate cellular or *in vivo* context, although numerous examples of chemical probes that fail to show even basic target engagement exist in the literature. Reported probes for the enzyme N-myristoyl transferase (NMT) include 2-hydroxy-myrystic acid and tris-DBA palladium, and have been used to validate NMT as a target for viral infection and melanoma respectively.[221,222] Subsequent investigation has shown that neither specifically inhibit NMT in a variety of biochemical and cellular assays, and the activity of

the compounds can be attributed variously to off-target effects and non-specific toxicity.[223] Such cases highlight the need for rigorous demonstration of target engagement through biochemical or cellular assays, or techniques such as activity-based protein profiling.

Chemical properties

High-quality probes must be appropriately soluble and stable for use in the chosen biological system. Compounds that are unstable under assay conditions can produce confounding results, both by the formation of reactive byproducts and by the reduction in effective concentration of the probe itself. Such chemical instability is surprisingly common even for apparently well established chemical probes, as illustrated by the MDMX inhibitor SJ-172550 (**45**), which is a widely used commercial chemical probe despite rapidly degrading in aqueous media.[224] Reactive chemicals in particular can cause promiscuous effects by non-specifically modifying proteins. A notorious example is iniparib (**46**), an alleged PARP inhibitor which was cited in numerous publications and entered phase III clinical trials for breast cancer before it was later demonstrated to non-specifically form adducts with cysteine residues in tumour cells.[225]

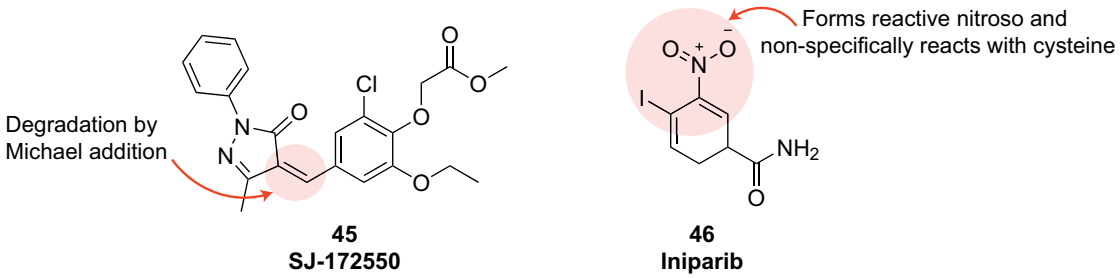

Figure 3.1: Examples of low-quality chemical probes.

Selectivity

Selectivity for its intended target is a key attribute for any chemical probe. The use of chemical probes with consequential off-target effects can undermine confidence in the literature, as exemplified by the cannabinoid field where supposedly selective CB_2 receptor agonists such as JWH133 and HU308 are widely used tool compounds. Taylor et al. demonstrated that these CB_2 probes induced functional chemotaxis responses in both wild-type and CB_2

knock-out macrophages, while truly selective CB_2 agonists fail to induce chemotaxis at all.[226] To confirm that data obtained from small molecules is on-target, candidate chemical probes should be tested for selectivity against structurally related targets, should provide an inactive analogue as a structure matched control, and should be used in conjunction with a second, structurally unrelated chemical probe for the same target.[227]

3.1.3 Aims and overview

In this chapter I aim to develop the screening hit **44** into a high quality chemical probe suitable for investigating GPR84 biology. My initial objective will be to improve the potency of the compound by exploring structure-activity relationships through iteratively synthesising and testing chemical analogues in GPR84-CHO cAMP assays. When a potent agonist has been developed, I will comprehensively characterise its properties including chemical and metabolic stability, solubility, and selectivity against other GPCR targets. This profiling will highlight any limitations of the new probe and identify the appropriate biological contexts for which it can be used to interrogate GPR84 biology.

3.2 Chemical optimisation

3.2.1 Overview

The screening hit **44** can be broadly separated into a lipophilic aromatic region and a polar heterocycle which are connected by an ether linker (Figure 3.2). In this preliminary optimisation programme, I will synthesise analogues with structural modifications for each region in turn and monitor how this affects key compound properties. Improving the potency of the series is the primary concern, but other considerations such as compound solubility will also be evaluated. I used an LC-MS assay to determine the solubility of **44** in pure water as 9 μM. The rigid, aromatic chloronaphthalene moiety is likely to be negatively contributing to poor aqueous solubility, so particular attention will be given to compound solubility when exploring the SAR of this region.

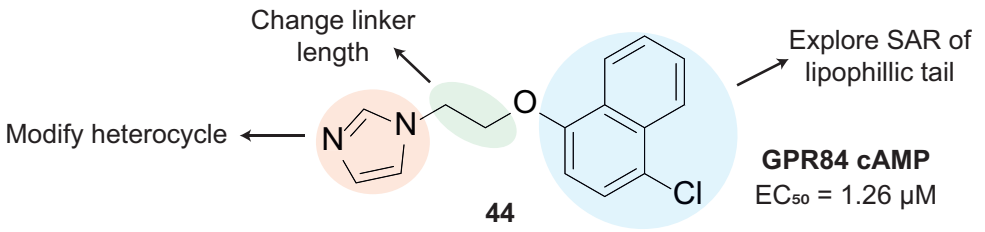

Figure 3.2: SAR overview for compound exploration. GPR84 cAMP potency is given for **44** as synthesised by Mitsunobu chemistry described in 3.2.2, and is the mean ± SEM of 3 independent experiments.

3.2.2 Synthesis

I began by developing two synthetic routes that would enable rapid derivitisation of the compound series. The Mitsunobu reaction with triphenylphosphine and diisopropyl azodicarboxylate (DIAD) enabled coupling of the commercially available ethyl alcohol imidazole and 4-chloronaphthal-2-ol to obtain **44** directly (Table 3.1). Acidification followed by repeated organic washes allowed facile removal of the triphenylphosphine oxide and DIAD oxidation byproducts that are often challenging to remove in Mitsunobu chemistry,[228] with only moderate loss of product in the washing steps. This one-step reaction readily facilitated incorporation of a wide variety of phenolic alcohols to replace the chloronaphthol moiety. The majority of phenols used were commercially available, but 4-chloro-2,3-dimethylphenol **47** was synthesised by chlorination of 2,3-dimethylphenol (Scheme 3.1).

In a similar fashion, Mitsunobu coupling of 4-chloronaphthal-2-ol with various alkyl alcohol heterocycles allowed one-step modification of alkyl linker length and installation of alternative heterocycles (Table 3.2 route A). For cases in which an appropriate heterocyclic alkyl alcohol was not commercially available, I instead used a double alkylation strategy (Table 3.2 route B). Initial reaction of 4-chloronaphthol with the appropriate bromochloroalkane by heating in the presence of potassium hydroxide proceeded in good yields to form compounds **48**-**50**. These chlorinated intermediates were then used as substrates for direct base-mediated alkylation of a variety of nitrogen containing heterocycles. This route enabled rapid installation of multiple different heterocycles in place of imidazole, although the chemistry is limited to N-substitution of NH heterocycles.

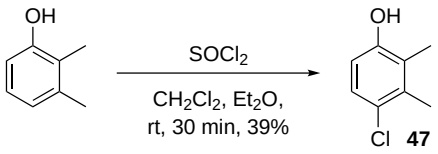

Scheme 3.1: Synthesis of 4-chloro-2,3-dimethylphenol **47**.

Table 3.1: Synthesis of **44** analogues with different hydrophobic groups.

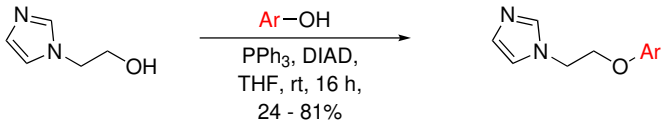

Compound	Ar	Yield (%)
44	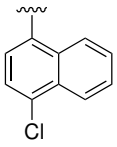	48
51	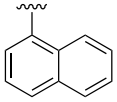	53
52	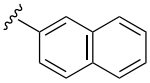	69
53	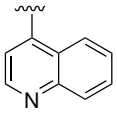	52
54	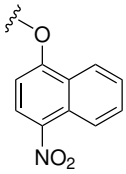	81
55	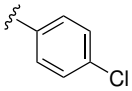	43
56	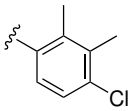	49
57	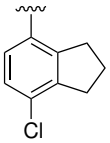	24
58	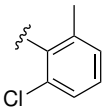	27

Table 3.2: Synthesis of **44** analogues with various heterocycles and alkyl linkers by two different synthetic routes. For route B, the yield refers only to the final step. [a] Reaction heated at 140 °C by microwave.

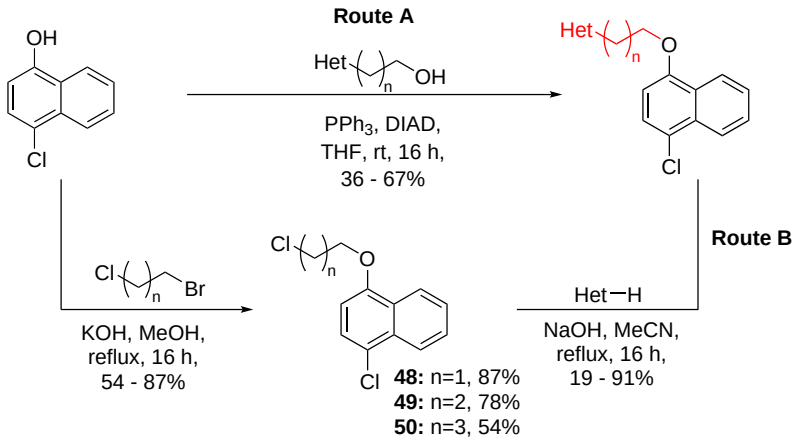

Compound	R	Route	Yield (%)
44	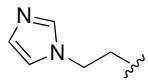	A	48
59	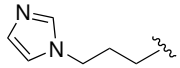	A	52
60	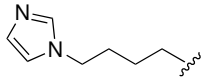	B	91
61	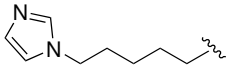	B	73
62	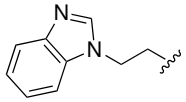	B	63
63	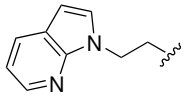	B	38
64	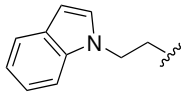	B	75
65	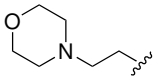	B	57
66	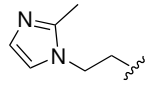	B	66
67	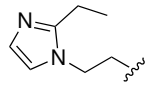	B	81
68	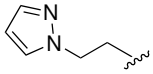	B	73
69	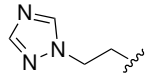	B[a]	19
70	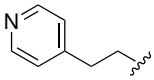	A	58
71	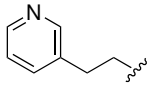	A	36
72	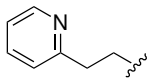	A	67

3.2.3 Biological testing

Alkyl linker SAR

Initially, I investigated how modifying the length of the ether linker between the naphthalene and heterocycle moieties in **44** would affect GPR84 activity. Other series of GPR84 agonists have shown significant dependence on the length of alkyl substituents; Liu et al. observed potency changes of over an order of magnitude in GPR84 potency following a change of just one carbon unit in the tail of **19**, while very long chain lengths resulted in the loss of activity.[136] This suggests that important hydrophobic interactions occur between the ligand and GPR84 within a binding pocket of limited size. In my compound series (Table 3.3), increasing the linker length correlated with gradually decreasing activity for propyloxy linked **59** and butyloxy linked **60**, while pentyloxy linked compound **61** was completely inactive. Overall, while there is some tolerance for increased chain length, this does not confer improved potency.

Table 3.3: cAMP inhibition data for analogues of **44** with longer alkyl linkers. Data are means ± SEM ($n = 3$)

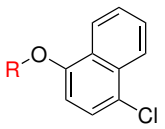

Compound	R	EC_{50} (μM)	pEC_{50}	Efficacy (% capric acid)
44	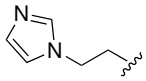	1.23	5.91 ± 0.09	94.6 ± 1.4
59	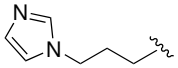	2.26	5.65 ± 0.15	90.6 ± 2.6
60	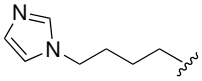	5.49	5.26 ± 0.16	81.7 ± 4.8
61	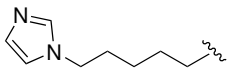	> 10	< 5	23.7 ± 3.0

Chloronaphthol SAR

The hydrophobic chloronaphthol region of **44** could be expected to occupy the same region of the GPR84 binding site as the long alkyl tails of agonists such as 6-OAU, ZQ-16, and **19**. In that compound class significant flexibility for different lipophilic substituents has previously been observed, including aromatic rings and saturated cycloalkanes, although the addition

of polarity to this region is generally not tolerated.[138] To investigate if similar trends would be observed in my compound series, I initially removed the 4-chloro substituent for **51** and regioisomer **52** which resulted in complete loss of activity (Table 3.4). Similarly 4-quinolinol **53** showed no activity. Surprisingly, however, replacing the chloro substituent with a nitro group in **54** resulted in no loss of activity. A substituent in the 4-position is therefore required to maintain activity, but both lipophilic halogens and polar nitro groups are tolerated. The introduction of the charged nitro group in **54** also improved the aqueous solubility to 26 µM, 3 times that of the equivalent chloro derivative **44**.

I next sought to see if compounds containing monocyclic lipophilic rings would maintain their activity at GPR84. 4-chlorophenol **55** was inactive at GPR84, but showed a vastly improved aqueous solubility of 4.2 mM compared to naphthol compound **44**. This validates breaking up the aromatic naphthalene system as a strategy for improving the solubility of the compound series. Speculating that hydrophobic substituents at the 2- and 3- positions of the 4-chlorophenol might rescue activity, I tested dimethyl analogue **56** but this too was inactive. Linking the alkyl substituents as a fused cyclopentyl ring in **57** or shifting the positions of the substituents in **58** also failed to restore any GPR84 activity. Overall then, no improvements in compound potency were achieved through modification of the naphthalene system, although solubility was greatly enhanced in compounds with monocyclic hydrophobic regions at the cost of GPR84 activity. However, inclusion of a polar nitro group at the 4-position was tolerated and suggests the introduction of further polarity into the compound at this position as a future optimisation strategy.

Table 3.4: cAMP inhibition data for analogues of **44** with different lipophilic groups. Data are means ± SEM ($n = 3$)

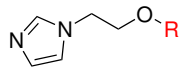

Compound	R	EC_{50} (μM)	pEC_{50}	Efficacy (% capric acid)
44	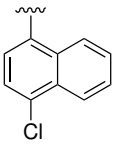	1.23	5.91 ± 0.09	94.6 ± 1.4
51	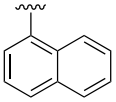	> 10	< 5	53.4 ± 11
52	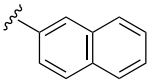	> 10	< 5	24.5 ± 5.5
53	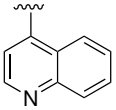	> 10	< 5	-46.8 ± 19
54	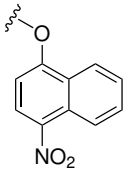	0.589	6.23 ± 0.22	94.6 ± 5.7
55	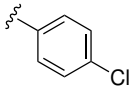	> 10	< 5	28.8 ± 3.2
56	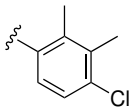	> 10	< 5	30.0 ± 7.8
57	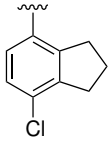	> 10	< 5	25.2 ± 7.7
58	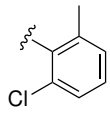	> 10	< 5	15.2 ± 10

Heterocycle SAR

Having demonstrated high sensitivity to variation in the lipophilic region of **44**, I next explored how modifying the polar heterocycle would impact on GPR84 activity. Initially, I screened a variety of nitrogen containing heterocycles to gauge tolerance to modification in this area (Table 3.5). Fused heterocycles benzoimidazole **62**, pyrrolopyridine **63**, and indole **64** all displayed no activity. Similarly, the saturated heterocycle morpholine derivative **65** was inactive. Inclusion of alkyl substituents on the imidazole ring (**66**-**67**) also led to a drop in potency, suggesting the SAR in this region of the compound is similarly inflexible. Furthermore, pyrazole **68** and triazole **69** are both inactive, demonstrating that small changes to the spatial or electronic properties of the aromatic nitrogen of **44** have a significant impact on GPR84 activity.

To further investigate how the nitrogen lone pair might be important for the compound activity, I tested pyridyl derivatives **70**-**72**. Compound overlays of imidazole **44** and 3-pyridyl derivative **71** suggest that the nitrogen lone pairs overlap well, whereas the 2- and 4-pyridine regioisomers are poorer matches (Figure 3.3). Accordingly, 3-pyridyl **71** showed a doubling in potency over imidazole **44**, while the 2- and 4-pyridyl regioisomers were inactive (Table 3.6). The strong activity dependence of the position of the nitrogen lone pair indicates that a highly directional polar interaction, such as a hydrogen bond, is important for the binding of the compounds to GPR84.

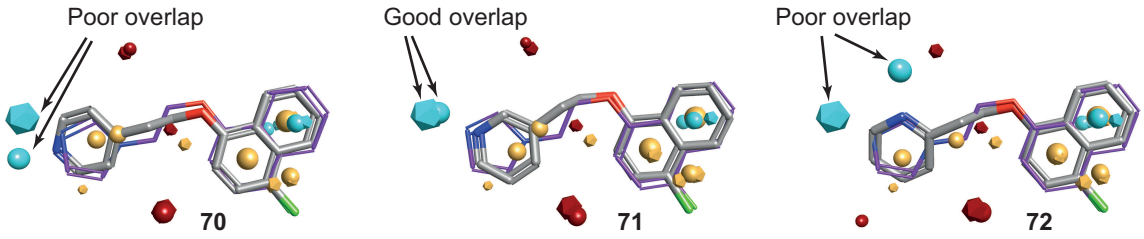

Figure 3.3: The nitrogen lone pair of 44 is most closely overlaid with 3-pyridine 71. Pyridyl derivatives **70**, **71**, and **72** (in grey) were overlaid with imidazole **44** (in purple) in Forge®. Common areas of positive charge (red), negative charge (blue), and hydrophobic regions (gold) are highlighted. The nitrogen lone pair of the imidazole **44** shows best overlap with GPR84 active 3-pyridyl **71**, whereas inactive compounds **70** and **72** show poor overlap. The orientation of the N lone pair is therefore important for the GPR84 activity of the compound series.

Table 3.5: cAMP inhibition data for analogues of **44** with different heterocycles. Data are means ± SEM ($n = 3$)

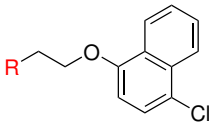

Compound	R	EC_{50} (μM)	pEC_{50}	Efficacy (% capric acid)
44	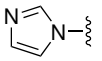	1.23	5.91 ± 0.09	94.6 ± 1.4
62	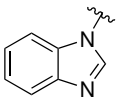	> 10	< 5	9.50 ± 10
63	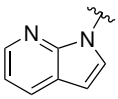	> 10	< 5	-4.49 ± 5.0
64	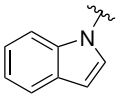	> 10	< 5	-8.25 ± 8.8
65	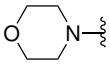	> 10	< 5	16.0 ± 2.6
66	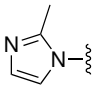	> 10	< 5	44.7 ± 6.6
67	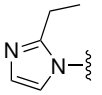	6.13	5.21 ± 0.12	87.9 ± 4.8
68	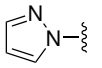	> 10	< 5	12.2 ± 11.9
69	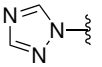	> 10	< 5	43.5 ± 5.2
70	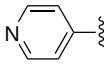	> 10	< 5	52 ± 15.7
71	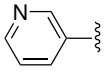	0.558	6.25 ± 0.02	96 ± 1.5
72	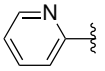	> 10	< 5	6 ± 13.4

3.2.4 Follow-up synthesis and testing

Speculating that a stronger hydrogen bond acceptor would confer superior potency, I oxidised the pyridyl derivatives **70**-**72** to form the equivalent pyridine *N*-oxides **73**-**75**. Pyridine *N*-oxides form strong hydrogen bonds through the electron rich heterocyclic *N*-oxide, and are stronger acceptors than both pyridines and imidazoles.[229] Oxidation was achieved using *m*-CPBA with the respective pyridyl derivative, after which the pure compounds were obtained using a low-yielding recrystallisation purification procedure (Scheme 3.2). Given the comparable potency of chloro- and nitro-naphthalene derivatives, I also synthesised pyridyl nitro-naphthalene derivatives **76** and **77** by Mitsunobu chemistry and then oxidised **76** with H_2O_2 to form the *N*-oxide derivative **78**.

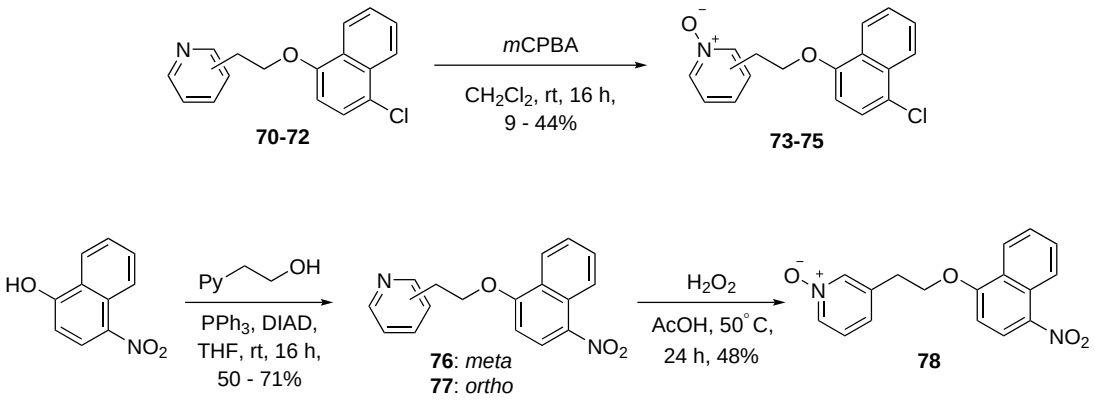

Scheme 3.2: Synthesis of pyridine *N*-oxide derivatives.

4-Pyridine *N*-oxide **73** showed improved potency over the equivalent pyridyl compound **70** (Table 3.6), while oxidation of 3-pyridyl **71** led to the most potent compound in the series, **74** (DL-175), which shows activity akin to the widely used GPR84 tool compound 6-OAU. Moreover, the polar pyridine *N*-oxide moiety led to improved aqueous solubility of 17 µM for **74**. The 2-pyridine *N*-oxide regioisomer **75** was inactive, potentially enabling it to act as a useful structure matched negative control compound for **74**.

Finally, I looked to see if combining the potent pyridine *N*-oxide with the polar nitronaphthalene moiety might further enhance the compound activity (Table 3.7). The 3-pyridine nitro-derivative **76** showed a potency jump over the nitronaphthalene imidazole **54** similar to the equivalent chloro-derivative **71**, while the 2-pyridine regioisomer **77** was again inactive. Oxidation of 3-pyridyl **76** to the equivalent *N*-oxide **78** increased the potency to a com-

Table 3.6: cAMP inhibition data for pyridine *N*-oxide analogues of **44**. Data are means ± SEM ($n = 3$)

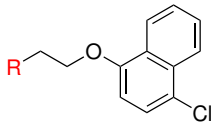

Compound	R	EC_{50} (μM)	pEC_{50}	Efficacy (% capric acid)
44	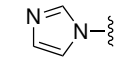	1.23	5.91 ± 0.09	94.6 ± 1.4
73	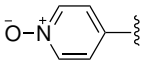	0.285	6.55 ± 0.15	96.3 ± 1.7
74	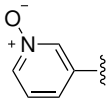	0.0333	7.48 ± 0.053	102 ± 0.31
75	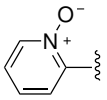	> 10	< 5	21.2 ± 21

parable level to **74**. Nitro and chloro substituents in the 4-position of the naphthalene ring therefore have similar impacts on compound potency, despite the steric and electronic differences of the two groups. The low nanomolar potency of both 3-pyridine *N*-oxide derivatives **74** and **78** is appropriate for a chemical probe, and better or comparable to other GPR84 agonists such as embelin and 6-OAU. However, aromatic nitro groups are associated with significant toxic, mutagenic, and carcinogenic properties through the formation of reactive nitroso or hydroxylamine metabolites and their associated reactive oxygen species.[230] For this reason, I chose to take forward chloro-derivative **74** (DL-175) and its inactive regioisomer **75** as candidates for further characterisation as GPR84 tool compounds.

Table 3.7: cAMP inhibition data for nitro-naphthalene analogues of **44**. Data are means ± SEM ($n = 3$)

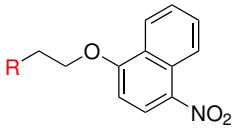

Compound	R	EC_{50} (μM)	pEC_{50}	Efficacy (% capric acid)
54	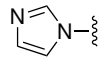	0.589	6.23 ± 0.22	94.6 ± 5.7
76	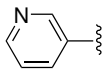	0.294	6.53 ± 0.18	95.8 ± 0.74
77	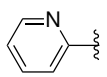	> 10	< 5	45.4 ± 33
78	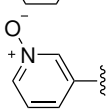	0.0402	7.40 ± 0.018	98.0 ± 4.0

3.3 DL-175 characterisation

3.3.1 Solubility

As I stated in the previous section, the solubility of DL-175 in pure water was determined to be 17 µM. A more relevant test for an *in vitro* tool compound is solubility in the presence of organic co-solvents such as DMSO. To test this, I diluted 10 mM DMSO compound stock solutions in phosphate buffered saline (PBS), and then measured absorbance at 750 nm to detect if compound precipitation had occurred (Figure 3.4). DL-175 and **75** both showed no precipitation up to 200 µM, whereas GPR84 agonist 6-OAU began precipitating out of solution at 100 µM. DL-175 and its inactive analogue **75** therefore both have suitable solubility for use in *in vitro* biological assays.

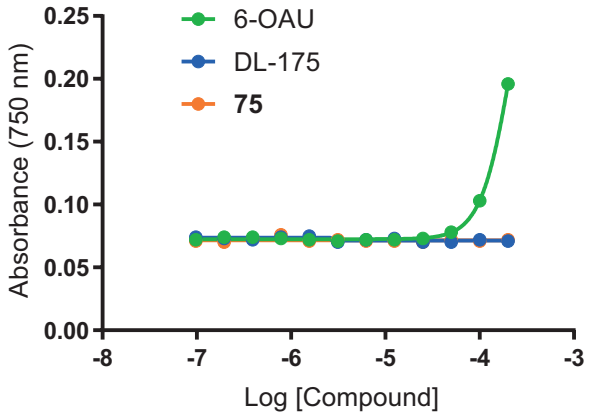

Figure 3.4: DL-175 shows superior solubility to GPR84 agonist 6-OAU. 10 mM DMSO stocks of DL-175, 6-OAU, and **75** were diluted in PBS and absorbance at 750 nm measured. 6-OAU shows increased absorbance at high concentrations showing compound precipitation is occurring, whereas DL-175 and **75** have good solubility beyond 100 µM.

3.3.2 Chemical stability

Compounds that are rapidly degraded in physiological aqueous conditions make poor chemical probes as the compound concentration reduces over time, and also because degradation byproducts can interfere with biological assay systems. *In vivo* chemical probes that are orally dosed must also be stable in the acidic conditions of the stomach. I investigated the chemical stability of DL-175 and **75** by incubating the compounds in buffered solutions of different pH at 37 °C with mechanical shaking and monitored the remaining compound

concentrations up to 48 hours (Figure 3.5). After three hours negligible degradation of both DL-175 and **75** had occurred, including at pH 2.5, and even after 48 h over 80 % of DL-175 remained.

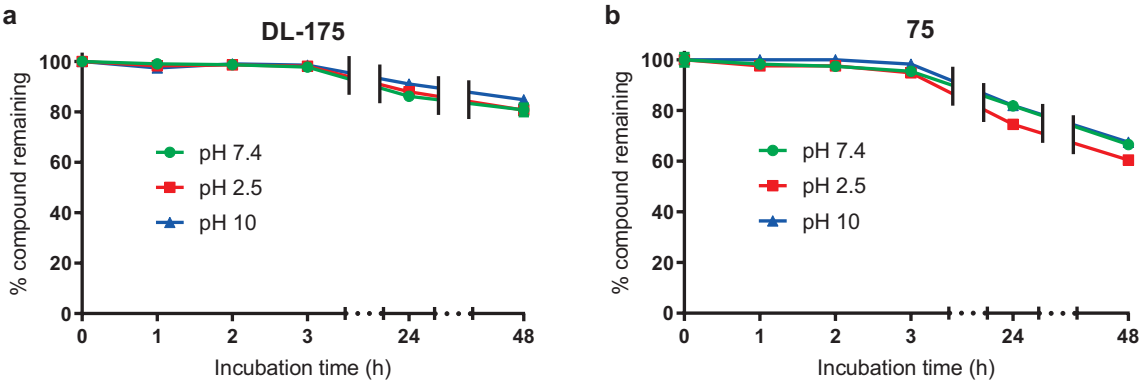

Figure 3.5: DL-175 and **75** both show negligible degradation in various pH buffers at 37 °C after 3 h. Data are given as as a percentage of the compound concentration measured by LC-MS at time zero, and are given as mean ± SD of 3 measurements at each timepoint.

3.3.3 Selectivity

I next turned to investigating the selectivity of DL-175 for GPR84 over other protein targets. First I confirmed that DL-175 inhibition of cAMP accumulation in GPR84-CHO cells is absent in untransfected CHO cells, demonstrating the GPR84 specificity of the observed $G_{\alpha i}$ response (Appendix Figure 2). Compound selectivity issues are more likely against other GPCR family members because the common structural topology and conserved sequences of GPCRs leads to similar ligand binding sites.[231] To establish the GPR84 selectivity of DL-175 against a broad range of receptors, I screened the compound in GPCR profiling panels. In a panel of 14 human GPCRs across multiple receptor families, DL-175 showed no significant activation of any receptors in cAMP or Ca^{2+} flux functional assays (Figure 3.6a). Importantly, no activity was observed at the FFARs 1-4, which might be expected to share ligand binding site features with GPR84 given their similar lipid agonists. However, the adenosine A_3 and cannabinoid CB_2 receptors appear to show some negative activation that could be indicative of inverse agonism.

To further establish the selectivity profile of DL-175, I employed a commercial panel of 168 GPCRs that uses a β-arrestin recruitment assay format to monitor receptor activation

(Figure 3.6b-c). In agonist mode, 3 µM DL-175 failed to induce activation in all 168 GPCRs (full list in Appendix Table 3). Similarly, in antagonist mode, pre-treatment with DL-175 did not significantly inhibit the activation of any of the 168 GPCRs with their reference agonists. Notably, the A_3 and CB_2 receptors showed no agonism or antagonism in this screening panel, suggesting the apparent inverse agonism observed in Figure 3.6a was a spurious result. Overall, DL-175 shows a clean selectivity profile across a wide range of GPCR targets and in both second messenger functional assays and β-arrestin recruitment assays.

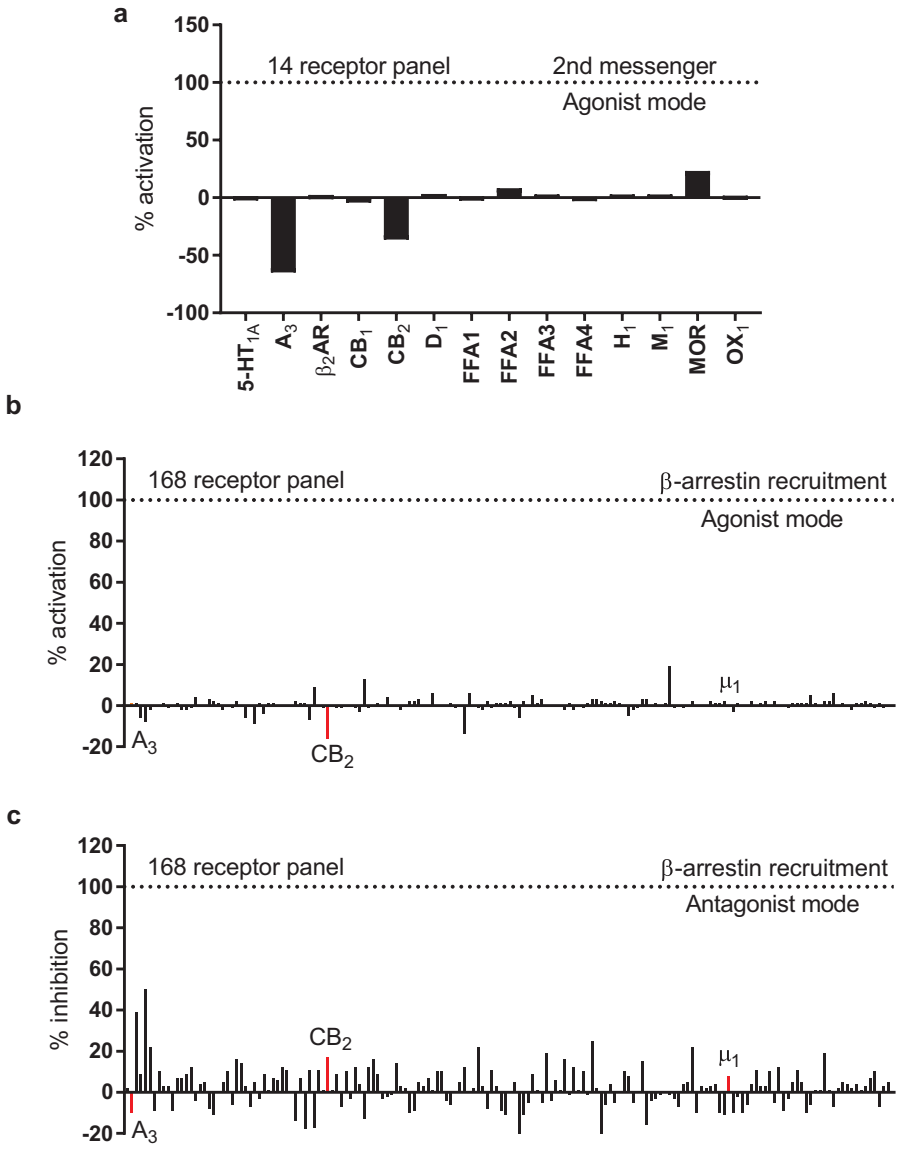

Figure 3.6: DL-175 does not activate or inhibit a wide range of other GPCRs. (a) DL-175 (3 µM) shows no significant activation of 14 common GPCRs in second messenger cellular assays. **(b)** DL-175 (3 µM) does not induce β-arrestin recruitment in 168 different GPCRs. **(c)** Pre-treatment with DL-175 (3 µM) shows no antagonism of 168 GPCRs each stimulated with a reference ligands. Note that the A_3 receptor and CB_2 receptor which appear to show some negative activation in **(a)** show no activation or inhibition in **(b)** and **(c)** respectively and are therefore likely spurious results. All screening panels were performed by Eurofins DiscoverX. For a full list of GPCRs tested, see Appendix Table 3.

3.3.4 Metabolic stability

I next investigated the capacity of DL-175 to resist metabolism. Compounds that are rapidly cleared by first-pass metabolism are likely to have limited utility as *in vivo* chemical probes. To test this in an *in vitro* setting, I incubated compounds with S9 fractions of murine liver homegenates that contain enzymes responsible for phase I metabolism, and monitored the concentration of unmetabolised compound at different timepoints using LC-MS (Figure 3.7). The control compound imipramine showed moderately quick metabolism as previously demonstrated in liver microsomes,[232] while an in-house compound, LJC-275, known to be labile to metabolism displayed the expected rapid degradation. DL-175 showed good stability towards S9 metabolism, with a half life of 73 min. To gain insights into the primary regions of metabolism for DL-175, I tested **44** and **71** with imidazole and pyridine rings respectively in place of the pyridine *N*-oxide ring (Figure 3.7). Imidazole **44** was significantly more stable to S9 incubation, suggesting the heterocyclic ring as an important site of metabolism for this compound series.

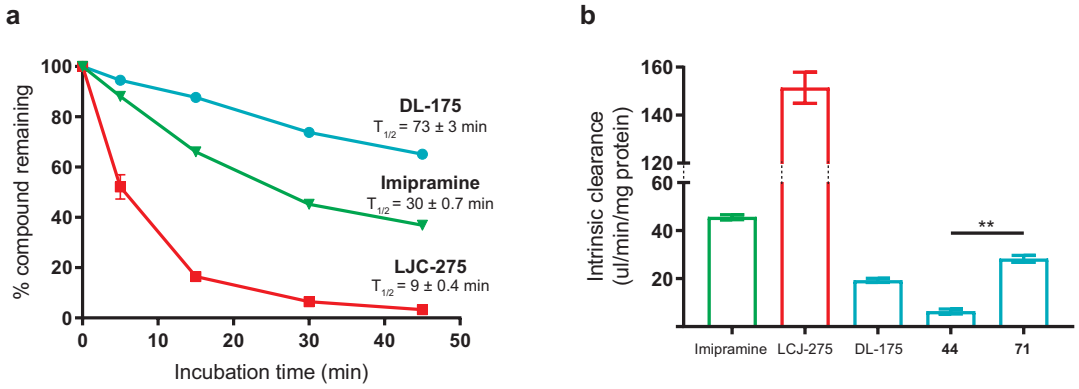

Figure 3.7: The DL-175 compound series is resistant to metabolism by S9 fraction. **(a)** Timecourse for degradation of compounds incubated with S9 fractions. Imipramine is a published compound with a well established metabolic profile. LJC-275 is an in-house positive control that is known to be rapidly metabolised. **(b)** S9 data represented as intrinsic clearance. The reduced metabolism of imidazole **44** suggests the heterocyclic ring as a major site of metabolism. Data are pooled means ± SEM from 3 independent experiments. Statistical analysis was performed using a one-way ANOVA with Tukey's multiple comparisons test. ** $P < 0.01$ for indicated comparison.

To understand how DL-175 is metabolised in a more physiologically relevant setting, I employed two commercial metabolic profiling services that use whole cell murine liver hepatocytes. In this format DL-175 was very rapidly degraded with both companies reporting a half-life of less than 10 min (Figure 3.8a). Given the poor stability of DL-175 under these

conditions, I opted to commission a metabolite identification study of the compound to determine the major routes of metabolism. DL-175 was incubated with whole cell murine hepatocytes for 60 min and the resulting metabolites characterised using LC-MS/MS (Figure 3.8b). 76 % of the metabolites detected showed oxidation of the pyridine *N*-oxide ring, of which 8 % had formed the glucouronide conjugate. Dihydroxylation of the naphthalene ring was identified as a minor route of metabolism, with 12 % of fragments showing modification in that region. Future optimisation work to reduce the metabolic liability of the compound series should therefore focus on blocking oxidation of the pyridine *N*-oxide ring system.

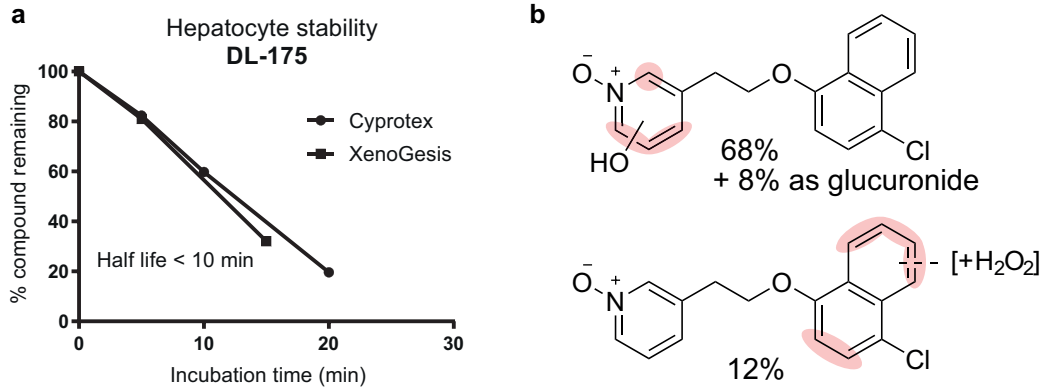

Figure 3.8: DL-175 is rapidly metabolised by whole-cell hepatocytes. **(a)** DL-175 was incubated with murine liver hepatocytes for up to 60 minutes and the concentration of compound remaining determined by LC-MS/MS. Two separate companies, Cyprotex and XenoGesis, returned similar results. **(b)** Tentative structural assignments given to fragments identified by LC-MS/MS after 60 min incubation of DL-175 with murine hepatocytes (performed by XenoGesis). The remaining 12 % are unidentified metabolites.

3.4 Discussion

In this chapter, I aimed to develop a high quality GPR84 agonist chemical probe suitable for interrogating the biology of the receptor. Using screening hit **44** identified in Chapter 2 as a starting point, I performed a preliminary medicinal chemistry optimisation study that resulted in a 40-fold increase of potency at GPR84. The optimised compound, DL-175, was comprehensively characterised and demonstrated to be appropriately soluble, stable, and selective for use as an *in vitro* tool compound. In addition, I identified an inactive regioisomer of DL-175 that can be used as a structurally matched negative control in future experiments into GPR84 pharmacology and function.

The structure-activity relationship of the new compound series was generally sensitive

to minor chemical modifications. An interesting exception is the tolerated replacement of the lipophilic chlorine substituent for a highly polar nitro group. The inclusion of a polar, electron withdrawing group on the naphthalene moiety is attractive as it simultaneously improves the solubility of the compound while reducing the lipophilicity. Given the well studied toxic liabilities of aromatic nitro groups, a number of drug discovery programmes have reported bioisosteric replacements. For example, Merck identified a ROMK potassium channel inhibitor that contained two aromatic nitro groups critical to the potency of the compound; benzonitrile, phthalide, and furazan all succesfully replaced the nitrophenyl groups without loss of potency or selectivity.[233] As nitrile groups are also commonly used bioisosteres for chlorine atoms,[234] the synthesis of a 4-cyanonaphth-1-ol derivative is particularly appealing as future work for this project.

I chose to initially test the metabolic stability of compounds using an S9 fraction assay instead of a liver microsomal assay, as S9 fractions contain both cytosolic enzymes and microsomal enzymes and thus provide more metabolic information.[235] However, the S9 assay appeared to significantly underestimate the rate of degradation of DL-175 compared to hepatocytes. This is likely because S9 fractions have limited phase II metabolism and are less metabolically active than other *in vitro* assay formats,[236] exemplified by published liver microsome data of imipramine that reports half-lives more than twice as fast as I observed with S9 incubations.[232,237] The data obtained from whole cell hepatocyte assays most closely reflects the *in vivo* situation as all relevant phase I and phase II enzymes are present at the physiological concentration. The poor metabolic stability of DL-175 in this assay therefore precludes it from use as an *in vivo* probe.

The metabolite identification study identified hydroxylation of the pyridine N-oxide ring as a primary route of metabolic modification for DL-175. One possible hydroxylation mechanism involves the enzyme aldehyde oxidase (AOX) (Figure 3.9), which has been implicated in catalysing the oxidation of aza-aromatic compounds through nucleophilic attack at electropositive carbons.[238] While pyridine *N*-oxides have not previously been demonstrated as substrates for AOX, nucleophilic attack could be envisioned at the electrophilic sites *ortho* to the *N*-oxide group of DL-175. Installing methyl groups at vulnerable positions has previ-

ously been effective in blocking AOX metabolism,[239] and therefore synthesising a methylated compound such as **79** may be an effective strategy here given alkylated imidazole **67** retained activity at GPR84. Alternatively, if CYP450 enzymes catalyse hydroxylation of the pyridine ring then inclusion of another nitrogen atom as a pyrimidine *N*-oxide ring will reduce ring lipophilicity and electron density and consequently limit CYP450 mediated oxidation.[240] The enzymes involved in metabolising DL-175 can be identified through S9 incubations in the absence of NADPH cofactors: oxidative metabolism in this case must occur through non-CYP450 enzymes such as AOX, whose involvement can be specifically confirmed using an AOX inhibitor.[238]

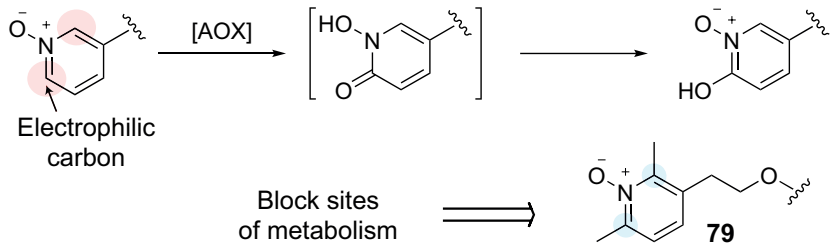

Figure 3.9: Aldehyde oxidase metabolism could be responsible for heterocycle hydroxylation. Compound **79** may exhibit higher metabolic stability than DL-175 as the methyl groups block the electrophilic carbons from attack.

Selectivity issues amongst the available GPR84 chemical tools are a significant issue in the published literature, with both embelin and DIM used to investigate GPR84 biology despite their known off-target effects.[132,141,142] Even reported GPR84 probes that have resulted from medicinal chemical optimisation studies have shown poor selectivity, as was highlighted recently for DIM derivative PSB-16671 which retained the ability to activate G_i proteins in GPR84-KO neutrophils.[137] I used commercial GPCR screening panels to demonstrate the GPR84 selectivity of DL-175 against 168 other GPCRs. Promiscuity against other protein targets remains possible, so in Chapter 5 I go on to use GPR84-KO macrophages and specific GPR84 antagonists to confirm that responses induced by DL-175 are GPR84 mediated. Furthermore, inactive analogue **75** can be used in tandem with DL-175 to increase confidence that observed biological responses are not simply scaffold related non-specific effects. Having confirmed that DL-175 possesses suitable chemical and biological properties for use as a chemical probe, in the next chapter I will further characterise the signalling pathways downstream of DL-175 mediated GPR84 activation.

Chapter 4

GPR84 biased signalling

4.1 Introduction

4.1.1 Aims and overview

In previous chapters, I described the development of a GPR84 agonist that is structurally distinct compared to any published agonists. New chemotypes of GPCR ligands often display novel biology by interacting with different binding sites or by stabilising alternative receptor conformations.[188] In this chapter, I therefore aim to further characterise the pharmacology of DL-175 at GPR84 and identify any differences in downstream signalling between GPR84 agonist scaffolds. In particular, I will use a GPR84-CHO β-arrestin recruitment assay to monitor the activation of β-arrestin signalling by DL-175, and compare to GPR84-CHO cAMP assays to see if bias towards either pathway is present. Initially, I will validate the correct functioning of the β-arrestin recruitment assay by testing a variety of GPR84 agonists with published β-arrestin activity data. I will then perform direct comparisons of DL-175 to other GPR84 agonists in order to detect and quantify any bias for G protein or β-arrestin signalling. Appropriate characterisation of the signalling pathways activated by DL-175 compared to other GPR84 agonists in transfected cell lines will enable future studies into the consequences of biased signalling at GPR84 in various biological systems.

4.2 β-arrestin recruitment

4.2.1 Aggregation interference

To monitor the recruitment of β-arrestin to GPR84, I employed the DiscoverX PathHunter® assay system that uses β-galactosidase enzyme fragmentation technology.[241] CHO cells that overexpress human GPR84 tagged with a β-galactosidase fragment are co-expressed with a fusion protein of β-arrestin 2 and a catalytically inactive mutant of β-galactosidase. Upon GPR84 activation β-arrestin binds to the receptor, bringing together the enzyme fragments and resulting in an increase in catalytic activity that produces a detectable chemiluminescent signal.

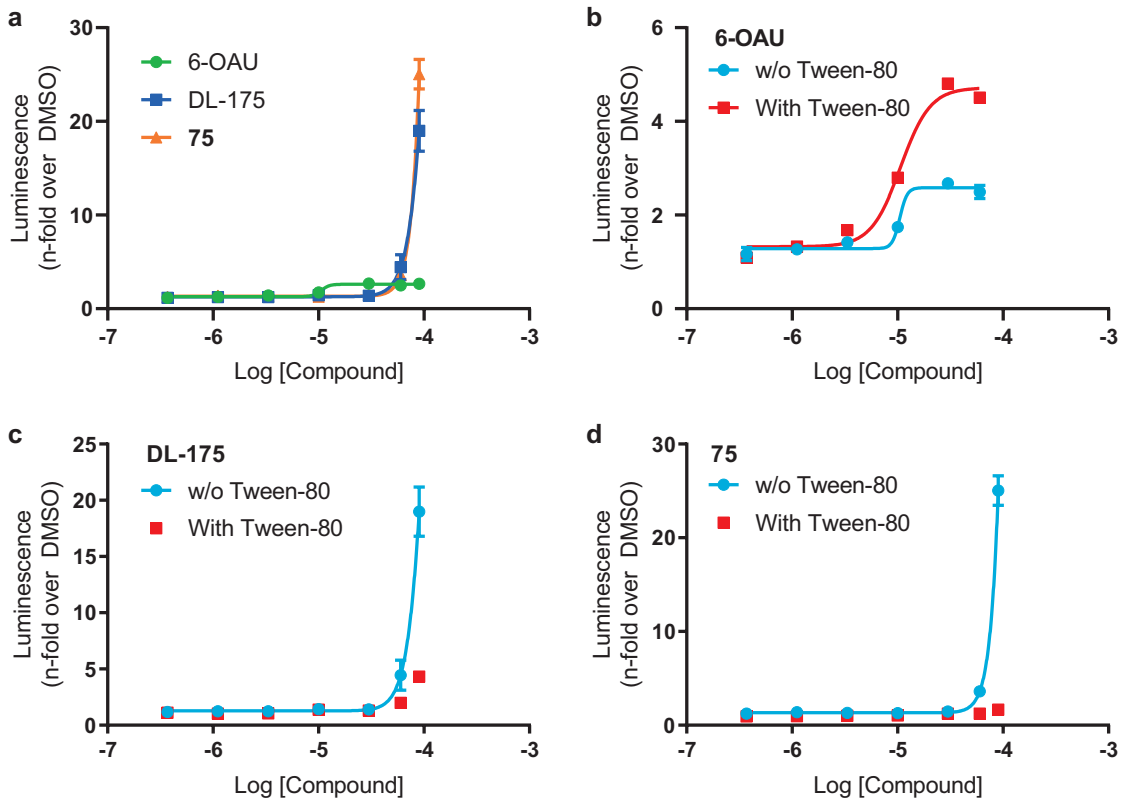

Figure 4.1: DL-175 causes an abnormal, detergent sensitive response in GPR84 β-arrestin recruitment assays. **(a)** 6-OAU induces a dose-dependent increase in luminescence in GPR84-CHO β-arrestin recruitment assays, but the responses to DL-175 and **75** have very high efficacy, steep Hill slopes, and fail to plateau. **(b)** The response to 6-OAU is similar in the presence of 0.025 % Tween-80 detergent, but **(c)** DL-175 and **(d)** **75** responses are ablated by the addition of detergent. Data are given as means ± SD of two technical replicates.

GPR84 agonist 6-OAU induces a dose-dependent increase in luminescence that corresponds to activation of the β-arrestin pathway (Figure 4.1a). DL-175, however, induced a

response with a very steep Hill slope that failed to plateau and with 5 times greater efficacy than 6-OAU. Tellingly, DL-175 analogue **75** induced a similar response despite being completely inactive in cAMP assays, suggesting that the observed responses do not represent genuine GPR84 activation and that some common structural feature of the two compounds may be causing assay interference.

One mechanism by which small molecules can interfere with biological assays is through the formation of soluble colloidal aggregates that non-specifically interact with proteins to modulate their behaviour.[242] Such aggregates form by the self-assembly of organic compounds in aqueous solution at a critical aggregation concentration (CAC), and then rapidly redissolve when diluted below the CAC.[243] This micelle-like behavior of promiscuous aggregating compounds results in dose-dependent responses with a characteristically steep Hill slope,[209] similar to those observed for DL-175 and **75**. To determine if colloidal aggregation was responsible for these atypical responses in the GPR84-CHO β-arrestin assay, I supplemented the assay media with 0.025 % Tween-80, a nonionic detergent previously demonstrated to be non-toxic to cells.[244] The inclusion of detergent in biochemical and cellular assays raises the CAC for small molecules and is widely used to prevent interference and identify false positives by compound aggregation.[245,246] 6-OAU induces similar responses regardless of the presence of detergent (Figure 4.1b), demonstrating that the cells and assay readout remain functional under these conditions. The responses to DL-175 and **75**, however, are greatly reduced in the presence of Tween-80 (Figure 4.1c-d). The detergent sensitivity of the abnormal responses to DL-175 and **75** is strong evidence that they result from compound aggregation at high concentrations.

4.2.2 NMR detection of aggregates

I next sought to obtain physical evidence of colloidal aggregates in aqueous DL-175 solutions. The unique chemical environment of soluble aggregates enables the use of nuclear magnetic resonance (NMR) techniques to detect their presence. One approach exploits the concentration sensitivity of aggregates and uses ^{1}H NMR to report structural changes in aggregates and their environment upon dilution.[247] I diluted a 10 mM DMSO-d_6 stock solution

of DL-175 in a 50 mM Na_3PO_4 D_2O solution to micromolar concentrations at which the formation of aggregates might be expected, and recorded ^{1}H NMR spectra (Figure 4.2). A compound that remains dissolved in a monomeric form would be expected to show increases in signal intensity as the concentration increases, without changes in chemical shift or peak shape. At high concentrations, various peaks in the NMR spectra of DL-175 are seen to experience changes in chemical shift. This is evidence that soluble aggregates are forming at similar concentrations to which the anomalous responses in β-arrestin recruitment assays is observed.

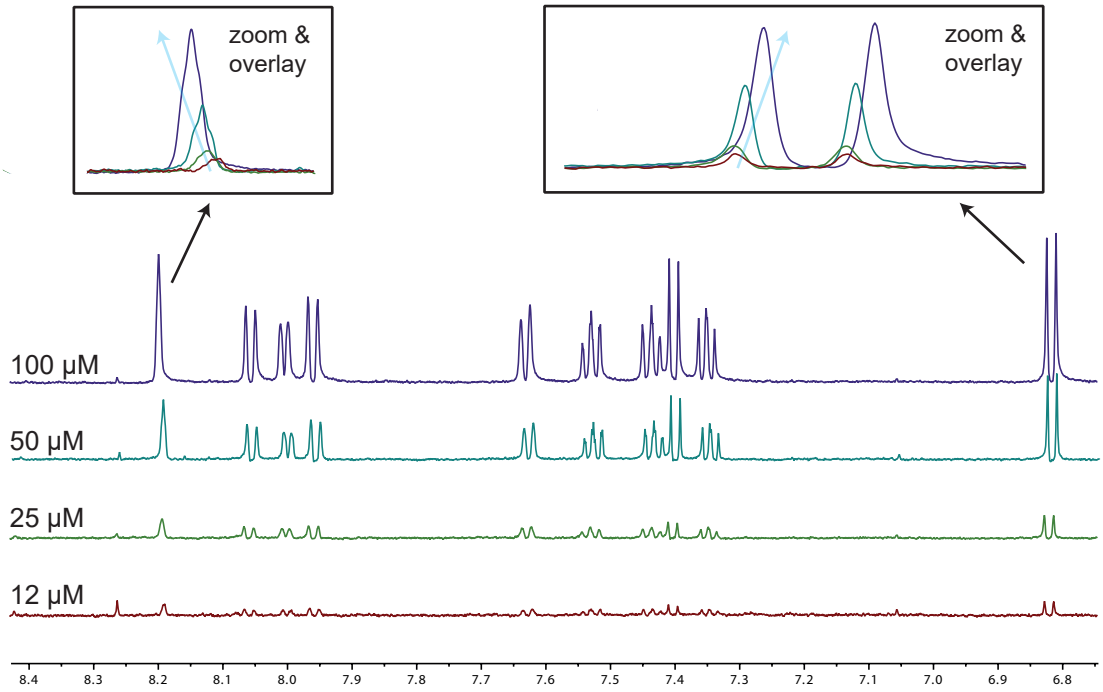

Figure 4.2: DL-175 shows unusual dilution trends in ^{1}H NMR spectra characteristic of aggregation. ^{1}H NMR spectra DL-175 at various concentrations in aqueous buffer are shown. Certain peaks when superimposed show subtle changes in chemical shift upon dilution. These observations suggest changes in DL-175 chemical environment occur at high concentration in aqueous buffer, which is likely due to colloidal aggregate formation. Spectra are referenced to residual DMSO solvent.

A second NMR method for observing aggregate formation is waterLOGSY (water-Ligand Observed via Gradient SpectroscopY).[248] This experiment is based on the transfer of magnetisation from irradiated bulk water to small molecules and macromolecules by the nuclear Overhauser effect (NOE). WaterLOGSY exploits the difference in sign of the NOE signal for small molecules that experience rapid molecular tumbling and large molecules that tumble relatively slowly.[249] Small molecules free in solution have a positive NOE signal, whereas col-

loidal aggregates receive a negative NOE. The waterLOGSY spectrum[a] of DL-175 (500 µM in PBS) shows a negative NOE signal indicative of large colloidal aggregates in solution (Figure 4.3a). The addition of 0.025 % Tween-80 reduces the negative NOE signal, corresponding to a greater proportion of DL-175 existing in monomeric form (Figure 4.3b). This waterLOGSY experiment therefore demonstrates that DL-175 is liable to form aggregates at high concentrations in aqueous solutions, and that DL-175 aggregate formation is reduced by the presence of detergent.

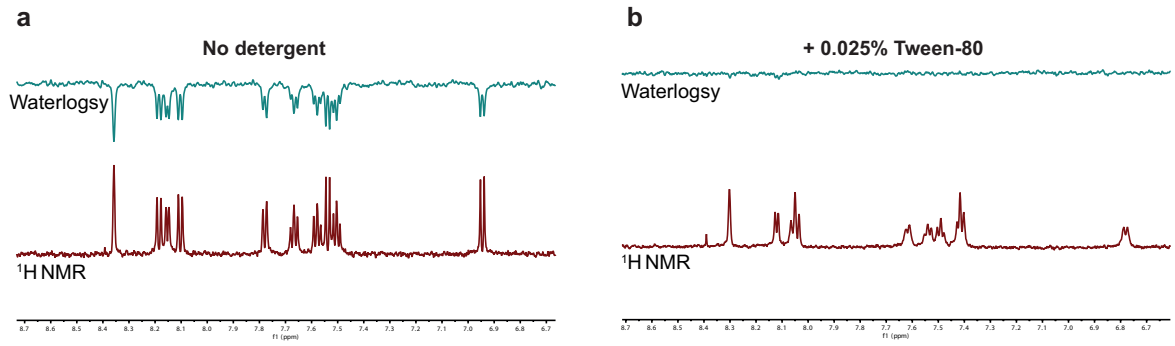

Figure 4.3: DL-175 forms aggregates at high concentrations which are reduced with detergent. **(a)** WaterLOGSY and ^{1}H NMR of DL-175 (500 µM) in pH 7.4 PBS solution. **(b)** WaterLOGSY of DL-175 (500 µM) as previously but with 0.025 % Tween-80 detergent included in the buffer solution.

4.2.3 GPR84 β-arrestin recruitment

I next tested a range of published GPR84 agonists to confirm their ability to recruit β-arrestin in GPR84-CHO cells in the presence of Tween-80. 6-OAU, ZQ-16, embelin, PSB-16434, and **19** all induced a dose-dependent luminescent signal corresponding to GPR84 and β-arrestin association (Figure 4.4). Each agonist is less potent than in GPR84 cAMP assays, suggesting strong system bias that may reflect the reduced signal amplification of β-arrestin recruitment assay formats.[250] Importantly, the rank order of potency of the compounds was the same as previously published.[138,145] However, my observed EC_{50} values are almost two orders of magnitude lower than previously reported by Pillaiyar et al., despite using the same cell-line and detection reagents.

Given the significant disparity between published data for GPR84 β-arrestin recruitment and my observations, I turned to a third-party to confirm the veracity of my results. I liaised

[a]WaterLOGSY experiments were performed by Dr Carole Bataille.

Table 4.1: Comparison of reported β-arrestin activity data for various GPR84 agonists. My data are pooled means ± SEM of n = 3–4 experiments, the data from Pillaiyar et al. is reproduced verbatim, the data from the assay manufacturer, DiscoverX, are EC_{50} values from one experiment.

	EC_{50} (μM)		
Compound	**Pillaiyar et al.**	**Our data**	**DiscoverX**
Capric acid	6.1	Inactive	Inactive
DL-175	n.d.	Inactive	Inactive
Embelin	0.42	19	3.85
6-OAU	0.11	11.47	5.38
ZQ-16	0.078	9.43	n.d.
19	n.d.	0.474	0.047

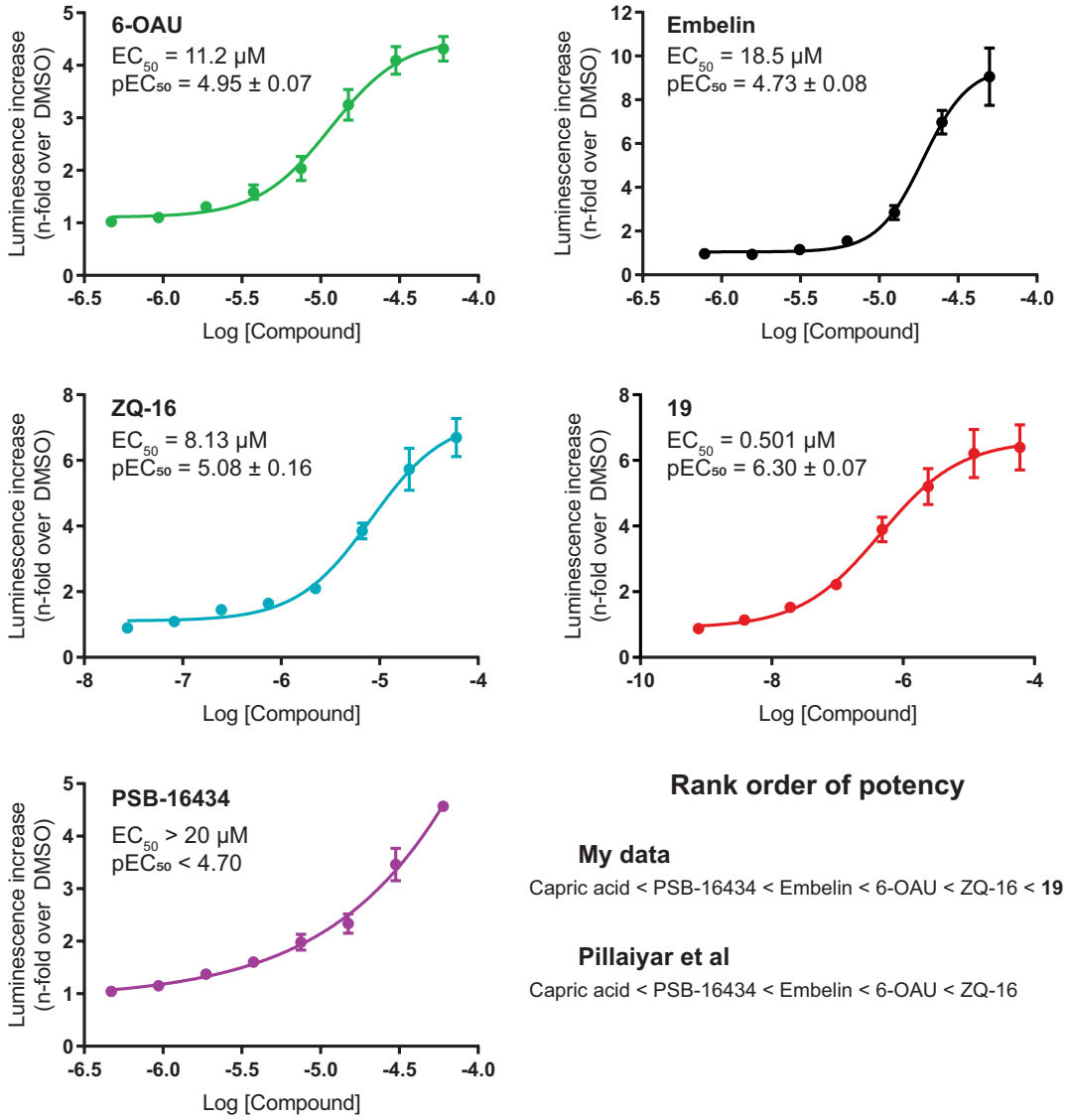

Figure 4.4: GPR84 agonists have the same rank potency in β-arrestin assays as previously reported. β-arrestin recruitment dose-responses for 6-OAU, embelin, ZQ-16, **19**, and PSB-16434. Capric acid produced no response up to 100 μM in my hands. Data are pooled means ± SEM of n = 3–4 independent experiments.

with the assay manufacturer, DiscoverX, and they agreed to blind-test a number of GPR84 agonists to give an independent EC_{50} read-out. DiscoverX reported intermediate EC_{50} values that were more similar to my values than to Pillaiyar et al. (Table 4.1). Notably, both DiscoverX and I measured no activation of β-arrestin signalling by capric acid up to 100 μM. Overall, although significant differences in absolute potency were reported by all three groups, my β-arrestin recruitment data reports the same rank order of potency as both the published literature and the assay manufacturer.

To investigate why I observed lower potency for GPR84 agonists compared to Pillaiyar et al., I first evaluated the levels of GPR84 expressed in the stable transfected cell lines. Reduced cellular receptor expression would be expected to result in lower activity for the agonists. In the absence of specific GPR84 antibodies[125] I used quantitative reverse transcription PCR (RT-qPCR) to determine hGPR84 mRNA levels in the different CHO cell lines, relative to the CHO housekeeping genes actin and GAPDH.[251] I found that the two different GPR84-CHO cell lines for cAMP and β-arrestin assays displayed similar levels of receptor expression (Figure 4.5). The relatively low potency of GPR84 agonists in my arrestin recruitment assay is therefore not a result of lower GPR84 transcriptional expression.

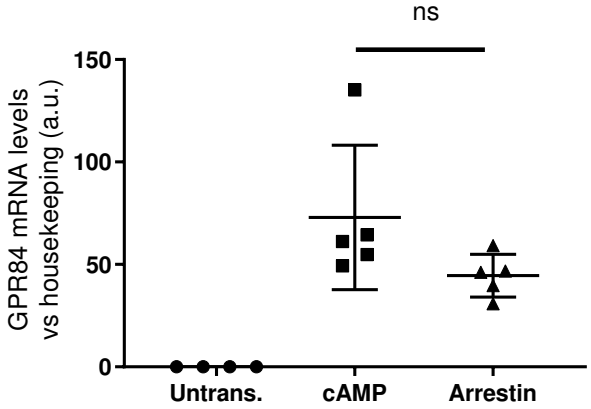

Figure 4.5: GPR84 expression levels are similar in different GPR84-CHO cell lines. RT-qPCR was performed for hGPR84 and expression compared relative to CHO housekeeping genes actin and GAPDH. The tested cell lines were DiscoverX HitHunter® GPR84-CHO cells (cAMP), DiscoverX PathHunter® GPR84-CHO cells (arrestin), and untransfected CHO-K1 cells. Data are displayed as means ± SEM of 4 or 5 independent cell preparations from different passages. Statistical analysis was performed by an unpaired t-test. ns = not significant.

4.2.4 Signalling bias of DL-175

I next set out to characterise the signalling bias of DL-175 in GPR84-CHO cellular assays. Typically, the signalling bias of an compound is quantified relative to the response recorded for the endogenous agonist of the receptor. In this case, however, no response is observed with the GPR84 endogenous agonist capric acid so I instead compared DL-175 to the commonly used GPR84 tool compound 6-OAU. I performed a direct comparison of the two ligands in GPR84-CHO cAMP and β-arrestin recruitment assays to enable the relative signalling bias to be observed. The two GPR84 agonists show similar responses in cAMP assays, demonstrating comparable engagement of G_i signalling pathways (Figure 4.6a). In β-arrestin recruitment assays, 6-OAU induces a saturating response that confirms the effective recruitment of β-arrestin following 6-OAU mediated GPR84 activation (Figure 4.6b). In contrast, DL-175 produces no significant response even at the highest concentration tested. This suggests that DL-175 preferentially activates G protein signalling pathways compared to 6-OAU.

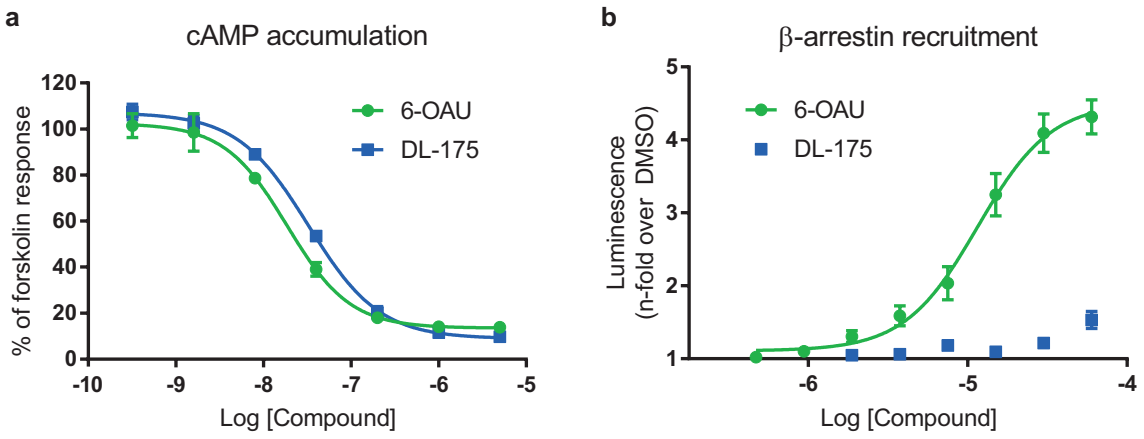

Figure 4.6: DL-175 is G protein biased in GPR84-CHO assays relative to 6-OAU. (a) Dose-response of 6-OAU and DL-175 in an assay measuring the inhibition of forskolin induced cAMP accumulation in GPR84-CHO cells. 6-OAU EC_{50} = 19 nM; DL-175 EC_{50} = 33 nM. Data plotted as percentage of the response to forksolin in the absence of agonists. **(b)** Dose-response of agonists in GPR84-CHO β-arrestin recruitment assays in the presence of Tween-80. 6-OAU EC_{50} = 11 μM; DL-175 EC_{50} > 60 μM. All data are pooled means ± SEM of three independent experiments.

To further validate the apparent biased agonism at GPR84, I compared the activity of DL-175 with the GPR84 agonist reported to show the most G protein signalling bias thus far, PSB-16434.[138] DL-175 showed significantly less activation of β-arrestin signalling than PSB-16434 despite their relatively small difference in cAMP potency (Figure 4.7a-b), consistent with DL-175 exhibiting significant signalling bias at GPR84. I next examined if DL-175 would block

6-OAU mediated β-arrestin recruitment in GPR84-CHO cells. Pre-incubation with DL-175 significantly reduced β-arrestin recruitment to GPR84 in response to the EC_{80} concentration of 6-OAU (Figure 4.7c). DL-175 therefore acts as an effective antagonist of GPR84 β-arrestin signalling by virtue of binding to the receptor without efficacy for β-arrestin recruitment.

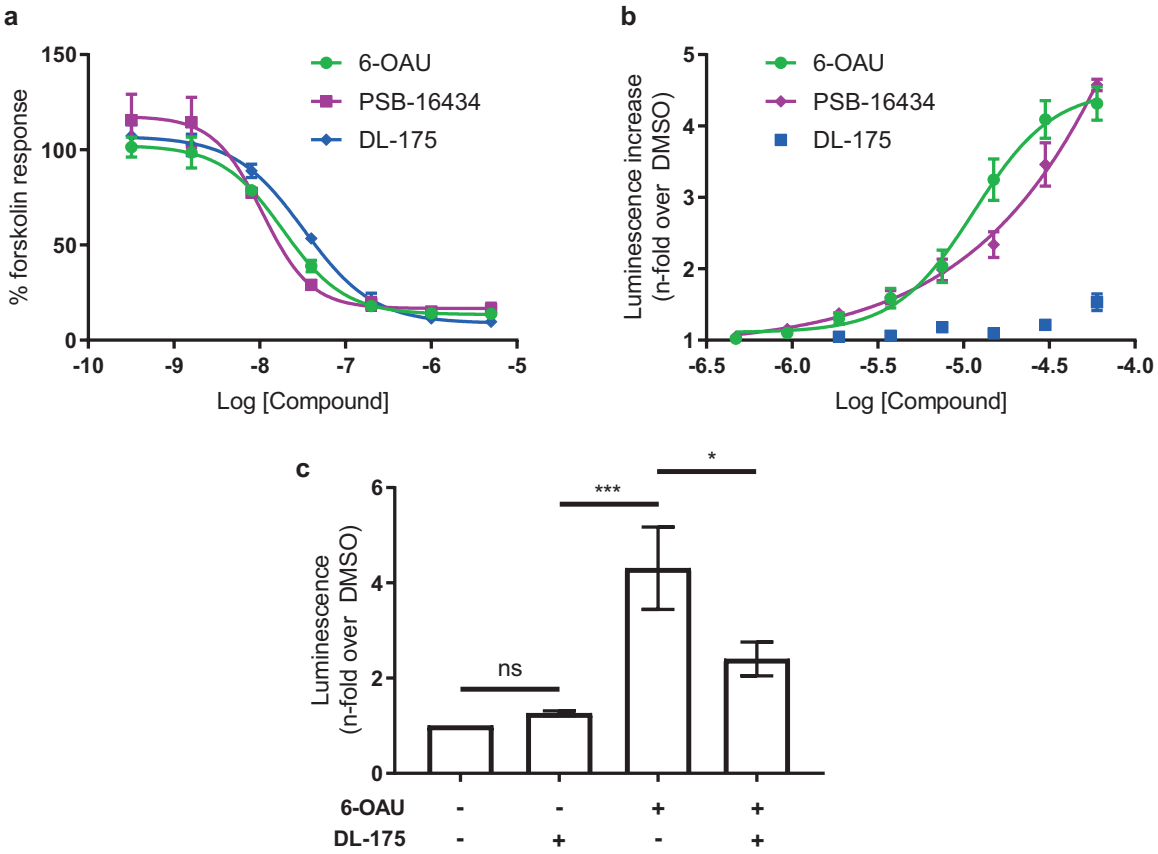

Figure 4.7: DL-175 is a G-protein biased GPR84 agonist. (a-b) Comparison of DL-175 and 6-OAU with a previously reported G protein biased GPR84 agonist, PSB-16434, in GPR84-CHO cAMP and β-arrestin assays. DL-175 shows a clear preference for G_i activation over β-arrestin recruitment. Data are pooled means ± SEM of 3 independent experiments. **(c)** Pre-incubation with DL-175 (40 µM) significantly reduces β-arrestin recruitment following 6-OAU stimulation at the EC_{80} concentration (24 µM). Data is displayed normalised to the DMSO control. Statistical analysis was performed on the raw data using randomised block ANOVA with Tukey's multiple comparisons test. ns = not significant, * $P < 0.05$, ** $P < 0.01$, *** $P < 0.001$ for indicated comparisons.

Efficacious β-arrestin recruitment can require sufficient expression of G protein-coupled receptor kinases (GRKs) that may not be present in the CHO cell background.[252,253] In studies on the µ-opioid receptor, co-expression of GRK2 resulted in enhanced potency and efficacy of various opioid agonists in µ-CHO β-arrestin recruitment assays, and revealed strong β-arrestin activity for previously weak partial agonists.[64,252] I therefore sought to determine if overexpression of GRK2 in GPR84-CHO cells would reveal DL-175 activation of GPR84 β-arrestin signalling. First, I confirmed that transfection efficiencies of greater than 85 % were

achieved in GPR84-CHO cells using a GFP expression plasmid and lipofectamine transfection reagents (Appendix Figure 3). Using the same conditions, I transfected GPR84-CHO cells with either a hGRK2 expression plasmid or an equivalent concentration of an empty vector, before running the β-arrestin recruitment assay with 6-OAU and DL-175. DL-175 remained completely inactive for GPR84 β-arrestin recruitment in cells that overexpress hGRK2 (Figure 4.8a-b). 6-OAU retained activity, but surprisingly showed reduced efficacy in cells with enhanced GRK2 expression (Figure 4.8c), suggesting that the regulation of β-arrestin recruitment to GPR84 may differ compared to other GPCRs such as the μ-opioid receptor.

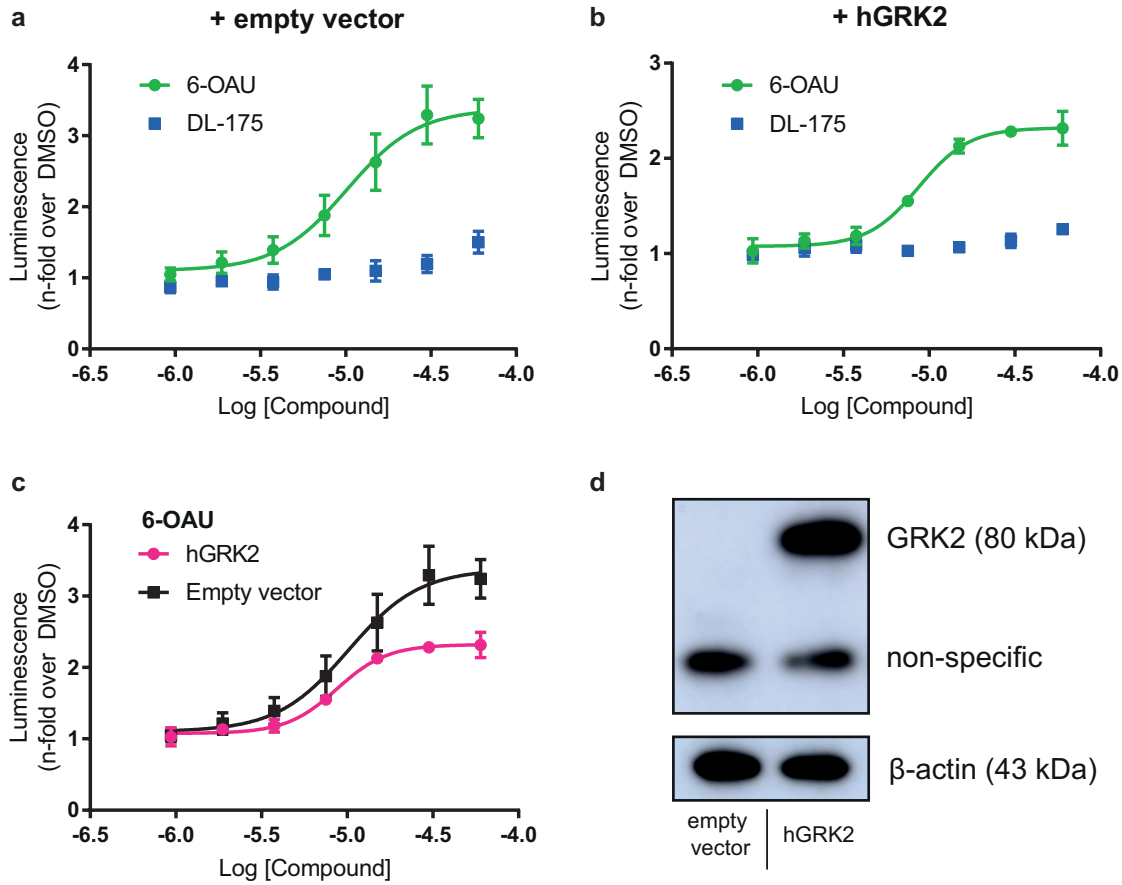

Figure 4.8: DL-175 remains inactive for β-arrestin recruitment in GPR84-CHO cells that overexpress GRK2. (a) GPR84-CHO cells were transfected with either **(a)** an empty vector or **(b)** hGRK2 and then tested for β-arrestin recruitment induced by 6-OAU or DL-175. **(c)** 6-OAU had lower efficacy in cells that overexpress hGRK2. **(d)** Western blot demonstrating successful transfection and overexpression of GRK2 in GPR84-CHO cells. Data in **a–c** are means ± SEM of 3 independent experiments.

4.3 Discussion

This chapter describes a series of experiments that aim to investigate the signalling pathways downstream of GPR84 activation by DL-175 in transfected cell systems. In GPR84-CHO β-arrestin recruitment assays, both DL-175 and inactive analogue **75** induced detergent-sensitive responses with very high efficacy and steep Hill slopes suggestive of non-specific assay interference by compound aggregation. I used NMR techniques to confirm that DL-175 was liable to form soluble aggregates at high concentrations in aqueous media. Using Tween-80 to prevent aggregation, I measured the same GPR84 agonist rank order of potency in β-arrestin assays as previously reported, although my absolute activity values were less potent. DL-175 was inactive in β-arrestin recruitment assays, and was significantly more G protein biased than both 6-OAU, and a previously reported GPR84 biased agonist, PSB-16434. To confirm the G protein bias of DL-175, I demonstrated effective antagonism of β-arrestin signalling in GPR84-CHO cells. Finally, I overexpressed GRK2 in GPR84-CHO to enhance β-arrestin recruitment and demonstrated that DL-175 remains inactive.

Predicting if a compound is likely to be a potential aggregator based on its chemical scaffold is challenging, with one such aggregation prediction tool, Aggregator Advisor,[254] finding that DL-175 is structurally dissimilar to any known aggregators. However, the detergent sensitive nature of the abnormal β-arrestin responses, coupled with the physical NMR data is strong evidence that the compound does aggregate at high concentrations. That these aggregation effects are caused by soluble colloids and not insoluble precipitate can be seen from the compound solubility data I previously presented in section 3.3.1. Additional methods that would provide further evidence of aggregate formation include dynamic light scattering and transmission electron microscopy,[242,255] with both these techniques enabling a better determination of the CAC for DL-175 in aqueous solutions.

Aggregation interference has been most studied in enzymatic assays, where colloidal aggregates are known to sequester and denature soluble proteins resulting in enzyme inhibition.[256] Colloidal inhibition of membrane proteins including GPCRs has also been demonstrated, although the mechanism of this disruption is less clear.[257] In the case of DL-175 in β-arrestin recruitment assays, the luminescent signal is 5 times greater than the maximum

efficacy of other GPR84 agonists, suggesting interference with the enzymatic luminescent readout is responsible rather than aggregate mediated GPR84 activation. Direct sequestering of tagged GPR84 and β-arrestin through colloidal membrane disruption, for example, could facilitate enzyme complementation and lead-to an artificially inflated luminescent output.

The aggregating behaviour of DL-175 at high concentrations is a clear limitation for its use with *in vitro* assays. However, small molecule aggregators are very common, with one study demonstrating that 19 % of a randomly selected library of drug-like compounds showed detergent sensitive enzyme inhibition indicative of aggregation at 30 μM.[255] A compound that aggregates at high concentration may still have valuable biological activity in its monomeric form, as illustrated by the 39 FDA approved drugs that are known aggregators.[254] The EC_{50} of DL-175 in GPR84-CHO cAMP assays is more than three orders of magnitude lower than the concentration at which interference in β-arrestin assays is observed, providing a significant concentration window within which the compound can be used. To confirm that the GPR84 activity of DL-175 occurs through the monomeric form, the absence of detergent sensitivity should be demonstrated for the DL-175 GPR84-CHO cAMP activity. However, this assay format is not tolerant of detergent, with Tween-80 apparently blocking forskolin stimulation of adenylate cyclase. In Chapter 5 I go on to demonstrate GPR84 activation in primary cells at low concentrations that is blocked by specific GPR84 antagonists and in GPR84 knockouts, data that is unlikely to be a consequence of aggregate activity. Finally, **75** is inactive in cAMP assays despite showing the same aggregating properties as DL-175, further validating the GPR84 activity of DL-175 as genuine.

A primary reason why I observed aggregating behaviour in GPR84 β-arrestin recruitment assays was that the low sensitivity of the assay required high concentrations of agonist to reach saturating levels of activation. Compared to two publications from the Muller group[138,145] my measured EC_{50} values are much less potent, although DiscoverX independently reported activities that are also relatively less potent. Other publications also report GPR84 β-arrestin data more similar to my own: Yin et al. found no activation of β-arrestin signalling by capric acid in the same DiscoverX PathHunter GPR84-CHO assay,[141] while a separate group measured an EC_{50} value of 1.75 μM for 6-OAU activation of GPR84 β-arrestin

signalling in GPR84-HEK293 cells.[135] I confirmed that my GPR84-CHO cell lines had similar GPR84 expression, and additionally confirmed that cell passage number did not influence agonist activity up to 10 passages. Comparing the expression of GPR84, G proteins, β-arrestin, and GRKs between the cells I used and those used by Pillaiyar et al. may provide an insight into the disparity between our respective results.

A direct comparison between 6-OAU and DL-175 in GPR84-CHO cell assays revealed that DL-175 preferentially activates G protein signalling pathways. The apparent absence of β-arrestin signalling was confirmed by demonstrating effective antagonism of 6-OAU mediated GPR84-arrestin interactions. Further evidence of biased signalling in this transfected CHO cell-system could be achieved using different assay formats to detect receptor-arrestin interactions. For example, fluorescent tagging of both β-arrestin and the C-terminus of GPR84 would enable β-arrestin recruitment to the receptor to be visualised by fluorescence microscopy.[258] However, preliminary experiments I performed with GPR84-CHO cells indicated poor translocation of GFP-β-arrestin 2 from the cytoplasm following 6-OAU or **19** stimulation. Alternatively, receptor internalisation could be investigated as a proxy for β-arrestin recruitment. This would require labelling GPR84 with an N-terminal epitope tag that could be used to monitor agonist-promoted changes in surface receptor expression using flow cytometry.[259]

As no response to DL-175 was observed in β-arrestin recruitment assays, it was not possible to quantify the bias of DL-175 relative to other GPR84 agonists. I employed GRK2 overexpression to enhance β-arrestin signalling, a strategy previously demonstrated to improve the dynamic range of β-arrestin signalling at the μ-opioid receptor,[64,252] without affecting the relative bias of the opioid ligands.[253] GRK overexpression in GPR84-CHO cells did not reveal DL-175 β-arrestin signalling, and the unchanged potency and reduced efficacy of 6-OAU suggests that GPR84 is not subject to the same regulation by GRK2 as the μ-opioid receptor. It is known that GPCRs show differences in the GRK subtype that regulate them. For example, the recruitment of β-arrestin to the vasopressin receptor 2 and angiotensin II receptor in HEK293 cells was mediated primarily by GRK2 and GRK3,[260,261] whereas only phosphorylation by GRK2 and GRK6 would recruit β-arrestin to the β_2-adrenergic receptor in the

same cell type.[262] In the latter example, however, overexpression of any of the four ubiquitous GRKs enhanced β-arrestin recruitment, at odds with my findings for GPR84. One possible explanation rests upon the observation that different GRKs phosphorylate distinct sets of sites on a GPCR, resulting in cell-type specific GPCR "barcodes" that determine the conformation of β-arrestin binding and the subsequent functional outcomes of β-arrestin signalling.[263,264] A study of CXCR4 signalling in HEK293 cells, for example, demonstrated that GRK3 and GRK6 were primarily involved in positively regulating ERK1/2 activation, whereas GRK2 phosphorylation negatively regulated ERK1/2 signalling.[265] Furthermore, site-specific phosphorylation of CXCR4 by GRK3 or PKC was required for efficacious β-arrestin recruitment.[266] Applied to GPR84 then, it is possible that the specific GRK2 phosphorylation sites on the receptor do not regulate β-arrestin 2 recruitment such that overexpression of GRK2 in CHO cells does not enhance β-arrestin recruitment. Knockdown of each GRK in turn in GPR84-CHO cells would enable identification of the GRK subtype responsible for β-arrestin recruitment to GPR84, and subsequent overexpression of that GRK could enhance β- arrestin signalling and reveal DL-175 activity.

Overall, DL-175 shows clear G protein biased agonism in GPR84-CHO cells compared to the literature tool agonist 6-OAU. Given the significant difference in signalling pathway activation between the two ligands, a direct comparison will enable investigation of the consequences of functional selectivity at the GPR84 and help in understanding the role of β-arrestin recruitment in creating functional responses following receptor stimulation. In the next chapter I will use 6-OAU and DL-175 to activate GPR84 in macrophage signalling and functional assays, and demonstrate that the differential signalling at GPR84 causes distinct functional responses in disease-relevant immune cells.

Chapter 5

GPR84 biased agonists and immune cells

5.1 Introduction

5.1.1 Recombinant versus native cells

GPCR pharmacology is primarily studied in transfected cell systems that may not reflect the signalling that occurs in primary cells and *in vivo* settings. For example, while recombinant signalling assays typically show the coupling of a GPCR to a single G protein, GPCRs in native cells are capable of activating multiple different G protein pathways. This is exemplified by the β_2AR which is usually G_s coupled in recombinant cell assays, but couples to both G_s and G_i in cardiac myocytes to control contraction rate and promote cell survival responses respectively.[267] Importantly, the inflated receptor expression and non-physiological expression of signalling proteins in recombinant cells can lead to misleading depictions of signalling bias. For example, the α_{1A}AR agonist A61603 displays significant bias towards cAMP accumulation over Ca^{2+} flux in CHO cells with high α_{1A} expression, but no detectable bias in CHO cells with lower receptor levels.[268] Furthermore, the relative expression of the receptor signalling machinery can impact upon signalling bias. Modifying the G_α protein stoichiometry, for example, in β_2AR expressing HEK293 cells changes the relative potency of adrenergic ligands for different G protein pathways.[269]

GPR84 is notable for its significant induction in tissue and immune cells upon inflammatory stimulus. The fluctuating levels of GPR84 expression in physiological cells could there-

fore result in changes of signalling bias that are poorly represented by reductionist recombinant cell signalling assays. Furthermore, GPR84-expressing immune cells display changes in expression of signalling molecules according to developmental state and environmental context. For example, exposure to inflammatory stimuli causes significant changes in macrophage expression of signalling proteins, with LPS stimulation enhancing levels of GRK2 while concurrently reducing levels of GRK5/6 and β-arrestin 1.[270] In the adaptive immune system, B- and T-cells that have been activated and are proliferating display increased $G_{\alpha i}$ and decreased $G_{\alpha s}$ isoform expression.[271] These changes in receptor and signalling molecule expression may lead to differential bias across tissue types and disease states. Referred to as dynamic bias,[272] these *in vivo* changes in bias are challenging to account for in recombinant cell signalling assays of the type employed in chapter 4. In this chapter I will therefore investigate the signalling and functional responses induced by GPR84 agonists in physiologically relevant immune cells including primary macrophages and monocytes. First I will briefly introduce two key immune cell functions under GPR84 regulation: phagocytosis and chemotaxis.

5.1.2 Phagocytosis

Phagocytosis is the process by which cells recognise and ingest large (>1 μm) particles.[273] Professional phagocytes such as macrophages, monocytes, and neutrophils use phagocytosis to remove foreign particles and microbial pathogens, and the process therefore contributes to the innate immune system's first line of defence against infection. Apoptotic cells are also targets for phagocytes and are ingested in a similar process known as efferocytosis which clears dying cells from damaged tissue. Receptors on the surface of phagocytes detect target particles either by recognition of pathogen-associated molecular patterns (PAMPs), or by recognition of proteins called opsonins that circulate the body and specifically bind foreign material.[274] Upon binding of a ligand or antigen, a cellular signalling cascade is activated and results in actin remodelling around the ligand-receptor complex that ultimately leads to internalisation as a membrane-bound phagosome. The phagosome then matures within the cell by interaction with endocytic vesicles to become acidified and obtain mi-

crobicidal properties that destroys the ingested particle.[275] The phagocytosis of opsonised particles and *E.coli* by macrophages can be enhanced by activation of GPR84, potentially by increasing expression of the phagocytic Fcγ receptor.[125]

5.1.3 Chemotaxis

Chemotaxis is the directed migration of cells towards a chemical signal. This process is a crucial component of the innate and adaptive immune systems, where chemokine peptides orchestrate the recruitment of immune cells to sites of infection and tissue damage.[276] GPCRs, such as the chemokine receptors, are responsible for sensing chemotactic signals and initiating cell migration. Upon binding a chemoattractant ligand, diverse GPCR signalling through a combination of $G_{\alpha i}$, $G_{\alpha 12/13}$, $G_{\beta\gamma}$, and β-arrestin results in actin polymerisation and actomyosin assembly to cause major cytoskeletal rearrangements.[277–279] These structural redistributions occur in a coordinated fashion to polarise the cell according to the direction of ligand binding event. A cell in a chemoattractant concentration-gradient will therefore experience a net polarisation that promotes leading-edge formation and motility towards the chemical signal. The chemokine receptors are the primary receptors involved in leukocyte migration, but GPR84 activation has been demonstrated to induce chemotaxis in transfected CHO cells, U937 macrophage-like cells, and primary neutrophils.[128,137,280]

5.1.4 Aims and overview

In this chapter I aim to investigate the ramifications of biased agonism at GPR84 in disease-relevant primary murine macrophages and human U937 macrophages. I hypothesise that selective activation of different signalling pathways downstream of GPR84 through ligand bias will result in distinct cellular and functional macrophage responses. To investigate this I will perform a direct comparison of GPR84 agonists 6-OAU and DL-175, which show comparable activation of G protein signalling but different activation of β-arrestin signalling. First, I will use an impedance signalling assay to characterise macrophage responses to different GPR84 agonists and demonstrate the specificity of the induced responses, before determining how biased GPR84 agonists influence macrophage chemotaxis and phagocytosis *in vitro*.

5.2 Macrophage impedance signalling

I first sought to characterise the signalling induced by 6-OAU and DL-175 in primary murine bone marrow-derived macrophages (BMDMs) that have previously been demonstrated to express GPR84 by our lab.[125] In order to gain an integrated view of macrophage GPR84 signalling, I employed an impedance sensing assay that enables label-free monitoring of native cell responses to GPCR stimulation in real-time (described in section 2.4.2). As the expression of GPR84 mRNA in macrophages is heavily regulated by their activation state, I initially tested GPR84 agonists in differentially polarised BMDMs. Both 6-OAU and DL-175 induced a rapid response in the BMDMs at 1 µM, with the cell index measure of cellular impedance peaking within 10 min before decaying to the baseline at different rates (Figure 5.1). For both compounds, the greatest response was observed in LPS stimulated, pro-inflammatory M1 macrophages, with smaller responses observed in alternatively activated IL-4 stimulated M2 cells, and unstimulated M0 cells. These results correlate well with previously reported GPR84 mRNA expression data and subsequent experiments were performed with LPS stimulated macrophages to achieve maximal responses.[125]

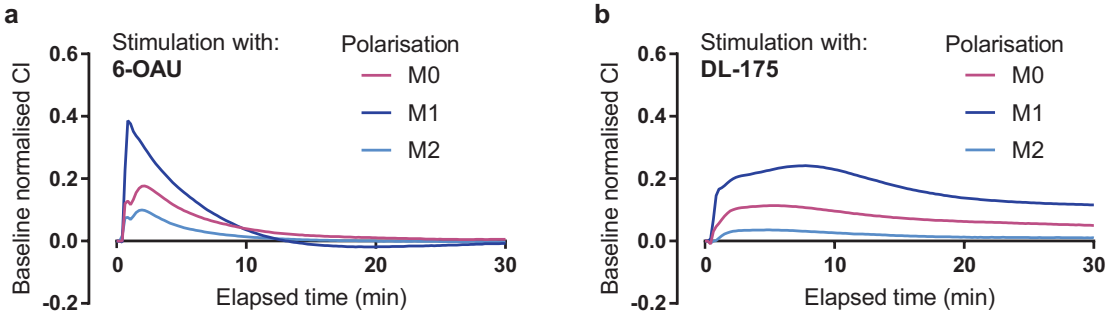

Figure 5.1: LPS stimulated macrophages have the largest response to GPR84 agonists. Impedance traces of differentially polarized BMDMs (M1 = 16 h LPS pretreatment; M2 = 16 h IL-4 pretreatment; M0 = vehicle pretreatment) following stimulation with 1 µM GPR84 agonists **(a)** 6-OAU and **(b)** DL-175. The traces are baseline corrected for stimulation with vehicle (0.3 % DMSO. Data are pooled means of $n = 4$ biological replicates.

I next set out to demonstrate the GPR84 specificity of the observed BMDM impedance responses. I used BMDMs obtained from GPR84 homozygous knock-out ($GPR84^{-/-}$) mice[a] and compared their responses to wild-type (WT) cells. $GPR84^{-/-}$ BMDMs showed no response to both 6-OAU and DL-175, but responded normally to complement component C5a

[a] $GPR84^{-/-}$ mice were kindly provided by Prof. Claudia Monaco.

(Figure 5.2). This experiment confirms that 6-OAU and DL-175 selectively activate GPR84 in primary BMDMs over the many other GPCRs expressed in murine BMDMs and further demonstrates the absence of non-specific effects such as membrane perturbation by ligand aggregation.

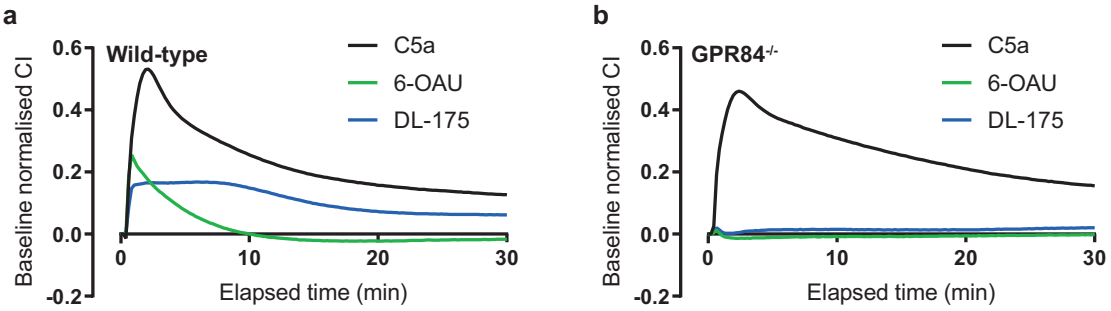

Figure 5.2: BMDM impedance responses to 6-OAU and DL-175 are mediated by GPR84. Impedance traces of M1 polarised **(a)** wild-type and **(b)** GPR84$^{-/-}$ BMDMs following stimulation with C5a (10 nM), 6-OAU (1 μM), or DL-175 (1 μM). The traces are baseline corrected for stimulation with vehicle (0.3 % DMSO for GPR84 agonists and media alone for C5a). Data are pooled means of $n = 3$ biological replicates.

I then stimulated M1 polarised BMDMs with 6-OAU or DL-175 at range of concentrations to estimate the potency of each compound at GPR84 in physiological cells (Figure 5.3). Both agonists displayed concentration-dependent responses, and quantification by magnitude of the initial response demonstrated that 6-OAU and DL-175 have comparable potencies in primary macrophages, as expected from the similar EC_{50} values observed in GPR84-CHO cAMP assays. There is, however, a clear difference in the profile of the impedance traces for the two agonists, with DL-175 inducing a more sustained response than the acute response seen at high concentrations with 6-OAU.

To further investigate the apparently unique impedance signalling profile of DL-175, I compared BMDM responses to a range of published GPR84 ligands (Figure 5.4). The structurally similar agonists 6-OAU, ZQ-16, and **19** each induced a rapid increase in cell index which returns to the baseline within 10 min. In contrast, DL-175 causes a sustained response in which the cell index remains elevated for over 30 min, while inactive DL-175 analogue **75** caused no response as expected. Plotting the area under the curve of the impedance traces illustrates the differences between agonists and suggests that novel signalling is occurring with DL-175 (Figure 5.4b).

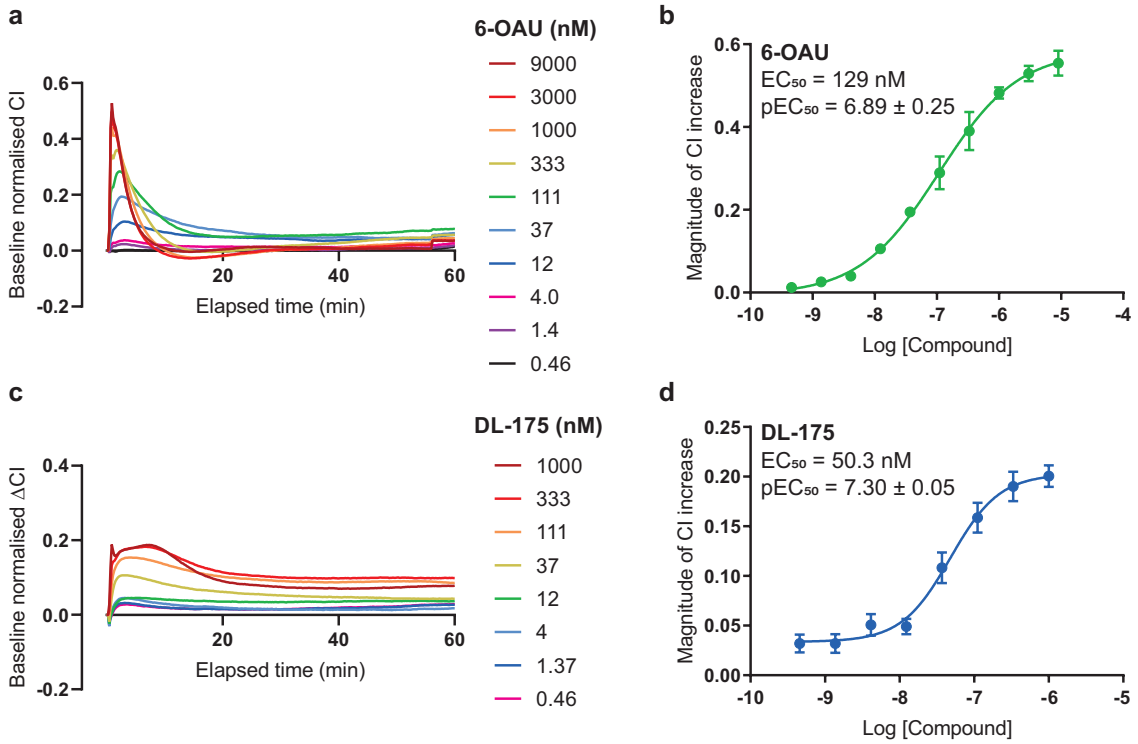

Figure 5.3: 6-OAU and DL-175 BMDM impedance responses are concentration dependent. **(a)** and **(c)** show M1 polarised BMDM impedance traces in response to different concentrations of 6-OAU and DL-175 respectively. **(b)** and **(d)** show quantification by the magnitude of the initial peak, enabling EC_{50} values to be generated. Impedance traces are baseline corrected for stimulation with 0.3 % DMSO vehicle. Data are pooled means ± SEM of $n = 4$ biological replicates.

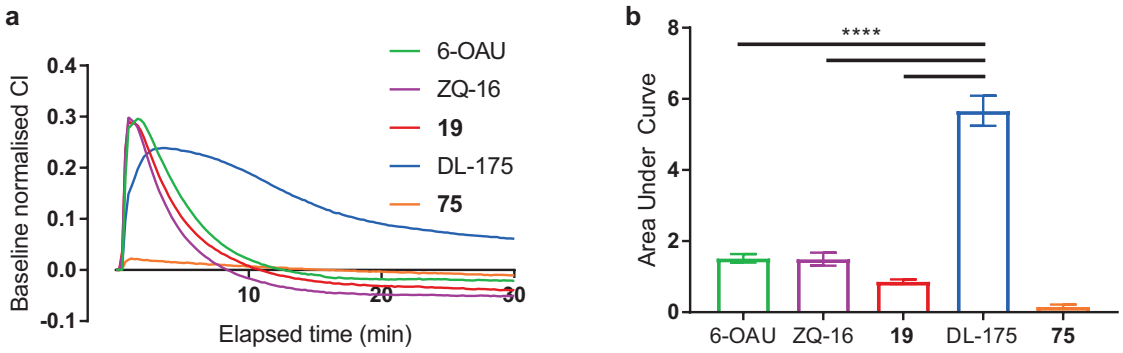

Figure 5.4: DL-175 displays novel signalling in primary BMDMs. **(a)** Impedance traces of M1 polarised BMDMs for various GPR84 agonists (1 µM) and inactive DL-175 analogue **75**. **(b)** Quantification by area under curve of the curve for 60 min following agonist stimulation. Impedance traces are baseline corrected for stimulation with 0.3 % DMSO vehicle. Data are pooled means ± SEM of 3 biological replicates. Statistical analysis was conducted using one-way ANOVA with Sidak's multiple comparisons test. **** $P < 0.0001$ for indicated comparisons.

I then set out to establish if the difference in responses observed for the G protein biased agonist DL-175 were a consequence of the absence of β-arrestin signalling. First, I used the $G_{\alpha i}$ inhibitor PTX to block the expected G protein signalling pathway (Figure 5.5). The responses to both 6-OAU and DL-175 were ablated by PTX pre-treatment, suggesting that $G_{\alpha i}$ protein engagement is essential for creating the cytoskeletal response. To investigate if β-arrestin interactions could modify the shape of the impedance response, I employed an inhibitor of GRK2/3, CMPD101, that would be expected to limit phosphorylation of GPR84 and thus indirectly prevent the recruitment of β-arrestin to the receptor. I pre-treated BMDMs with CMPD101 at various concentrations and then measured the impedance response to 6-OAU or DL-175 stimulation (Figure 5.6). Quantification by measuring the area under curve demonstrates that increased GRK2/3 inhibition is associated with more sustained responses to 6-OAU, such that at high concentrations of CMPD101, the 6-OAU response resembles that of DL-175. GRK2/3 inhibition also results in a more sustained response to DL-175, although the effect is much less pronounced than for 6-OAU. Together, these data suggest that differences in GRK regulation of GPR84 signalling underlie the singular macrophage response to DL-175. Both β-arrestin 2 and GRK2 are expressed in pro-inflammatory macrophages,[270] however β-arrestin knockdown experiments will be required to confirm if GPR84-arrestin interactions induced by GRKs are directly responsible for these cell impedance observations.

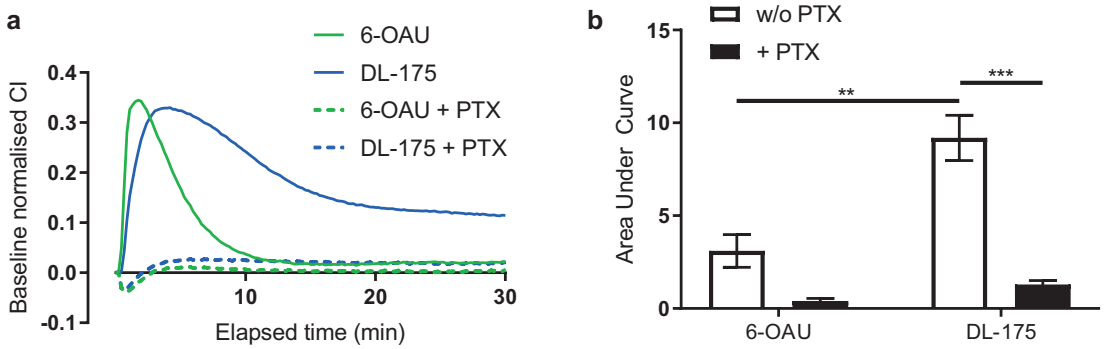

Figure 5.5: $G_{\alpha i}$ activation is required for GPR84 macrophage impedance responses. **(a)** Impedance traces of BMDMs responding to 6-OUA or DL-175 (1 μM) following 16 h pre-treatment with $G_{\alpha i}$ inhibitor PTX (200 ng/ml) or vehicle. **(b)** Quantification of impedance traces by area under curve shows that PTX pre-treatment blocks BMDM responses to both 6-OAU and DL-175 (1 μM). Data are pooled means ± SEM of $n = 3$ biological replicates. Impedance traces are baseline corrected for stimulation with 0.3 % DMSO vehicle. Statistical analysis was performed using one-way ANOVA with Sidak's multiple comparisons test. *P < 0.05, **P < 0.01, ***P < 0.001 for indicated comparisons.

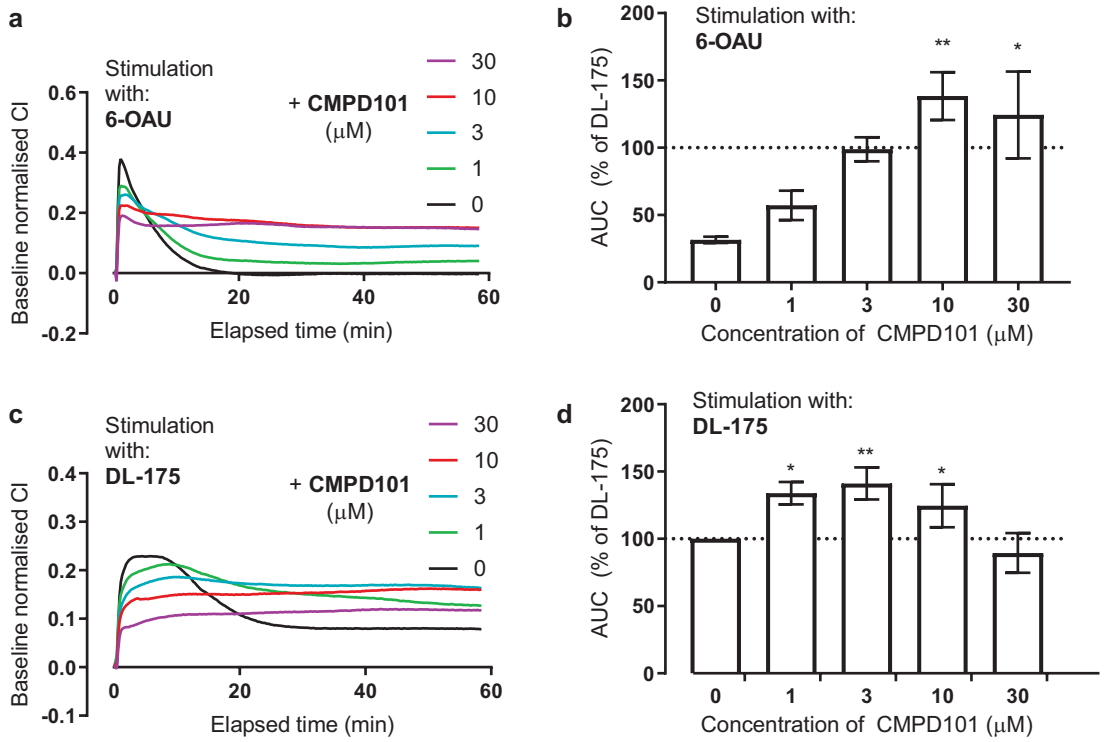

Figure 5.6: Inhibition of GRK 2/3 is associated with more sustained macrophage impedance responses. M1 polarised BMDMs were pre-treated with GRK2/3 inhibitor CMPD101 at the indicated concentration for 2 h and then stimulated with 1 μM **(a)** 6-OAU or **(c)** DL-175. **(b)** and **(d)** show the respective quantifications by area under the curve up to 60 min as a percentage of the response to DL-175 (1 μM) without pre-treatment. Data are pooled means ± SEM from $n = 4$ biological replicates. Impedance traces are baseline corrected for stimulation with 0.3 % DMSO vehicle. Statistical analysis was performed using randomised block ANOVA on the raw data with Dunnet's multiple comparisons test. * $P < 0.05$, ** $P < 0.01$ compared to 0 μM CMPD101.

To determine if human macrophage populations would also exhibit differing responses to the GPR84 agonists, I used phorbol 12-myristate 13-acetate (PMA) differentiated human U937 macrophage-like cells that express GPR84 mRNA to similar levels as primary macrophages.[281] As expected, DL-175 stimulation of M1 polarised U937 cells resulted in a more sustained impedance response than treatment with 6-OAU (Figure 5.7), although this difference was less marked than in primary macrophages. Inactive DL-175 analogue **75** elicited no response, while pre-incubation with GPR84 antagonist **38** blocked all responses except that to C5a, confirming the specificity of the induced signal. The differential impedance signalling observed with DL-175 therefore extends to a human myeloid cell line.

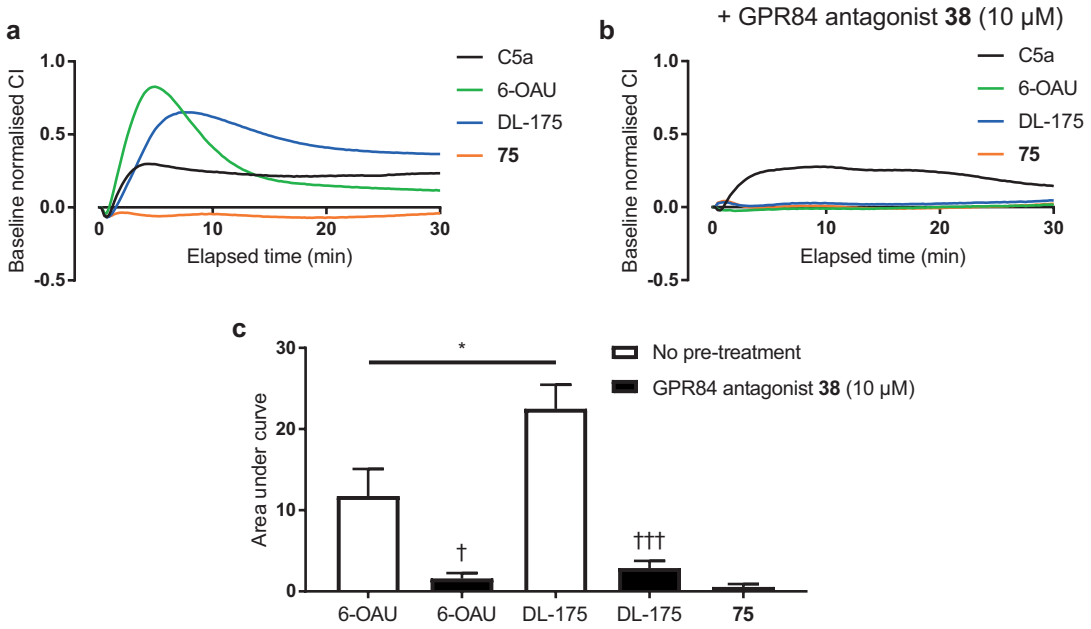

Figure 5.7: 6-OAU and DL-175 induce different impedance responses in U937 macrophages through GPR84. **(a)** Impedance traces for PMA differentiated, LPS treated U937 cells in response to 10 nM C5a or 1 µM 6-OAU, DL-175, or **75**. **(b)** Pre-treatment with GPR84 antagonist **38** (10 µM) for 1 h blocks all U937 responses to GPR84 agonists without affecting the response to C5a. **(c)** Quantification by area under curve for 60 min following agonist addition in **(a)** and **(b)**. Data are pooled means ± SEM of $n = 3$ independent experiments. Impedance traces are baseline corrected for stimulation with 0.3 % DMSO vehicle. Statistical analysis was conducted using one-way ANOVA with Sidak's multiple comparisons test. *P < 0.05 for indicated comparison. † P < 0.05, †† P < 0.01, ††† P < 0.001 compared to the same treatment but without pre-incubation with the GPR84 antagonist.

5.3 GPR84 regulation of macrophage function

Having demonstrated that DL-175 induces distinct responses in macrophage impedance signalling assays, I next sought to determine how GPR84 agonists with different signalling bias may influence macrophage function. As GPCR mediated impedance responses are linked to changes in the actin skeleton, it is likely that the diverse impedance traces induced by GPR84 agonists reflect alternative macrophage cytoskeletal rearrangement.[197] Remodelling of the actin cytoskeleton is essential for macrophage functions such as phagocytosis and chemotaxis, so I initially investigated if GPR84 biased agonists might show differences in their regulation of these processes.

5.3.1 Phagocytosis

We have previously demonstrated in our lab that 6-OAU activation of GPR84 in murine macrophages is associated with enhanced phagocytic capacity.[125] To see if DL-175 would have similar effects on phagocytosis, I used flow cytometry to measure the uptake of opsonised FITC labelled 2 µm beads in M1 polarised U937 macrophages. In this assay, cells are stimulated with the GPR84 agonists before a 4 h incubation with beads, after which the cells are repeatedly washed and flow cytometry used to measure the number of cells containing at least one bead. GPR84 activation with both 6-OAU and DL-175 led to a small but statistically significant augmentation of bead phagocytosis, which GPR84 inactive DL-175 analogue **75** failed to replicate (Figure 5.8a-f). To confirm that I was measuring phagocytosis of the beads and not simply adhesion, I used a confocal microscopy Z-stack to show that the fluorescent beads were fully encapsulated within the cell membrane (Figure 5.8g). Both GPR84 agonists therefore show similar effects on human U937 macrophage phagocytosis, despite their different signalling bias.

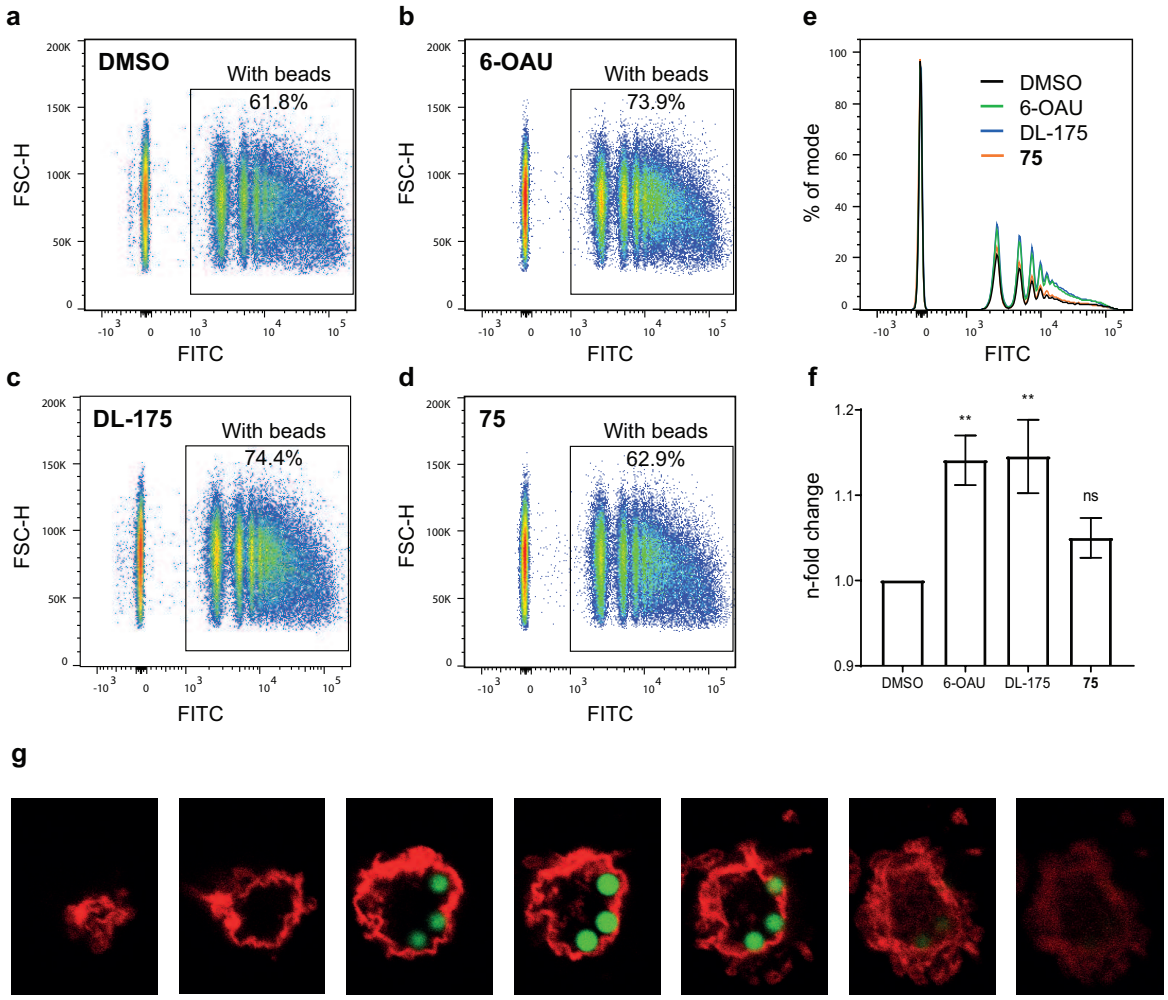

Figure 5.8: 6-OAU and DL-175 both enhance phagocytosis in U937 macrophages. (a-d) Representative flow cytometry plots of U937 cells incubated with fluorescently labelled beads and different compound pre-treatments. Cells with beads are gated according to FITC fluorescence. **(e)** Representative histogram showing the frequency of cells with different levels of fluorescence. Peaks corresponding to different numbers of phagocytosed beads are visible. **(f)** Pooled data showing the percentage of cells with beads as n-fold change over DMSO. **(g)** Representative Z-stack images taken with a fluorescence confocal microscope demonstrate that beads have been taken up within the cell. LPS treated U937 macrophages incubated with opsonised FITC labelled 2 µm beads (green) were fixed, permeabilised and the actin skeleton labelled with phalloidin (red). Data are means ± SEM for $n = 3$ independent experiments. Statistical analysis was conducted by one-way ANOVA with Sidak's multiple comparisons correction. ns = not significant, **P < 0.01 compared to DMSO treatment.

5.3.2 Chemotaxis

As previously outlined, GPR84 has been described as a chemotactic receptor variously in primary neutrophils, CHO cells, and U937 macrophages.[128,137,280] I therefore next determined if biased GPR84 agonists may have different abilities to promote immune cell migration. For this, I used a modified Boyden chamber assay where cells seeded into an upper chamber migrate along a chemoattractant gradient through a porous membrane, before adhering to an electrode in the lower chamber.[282] The migration of cells can therefore be observed in real time by increases in the cell index measure of cellular impedance.

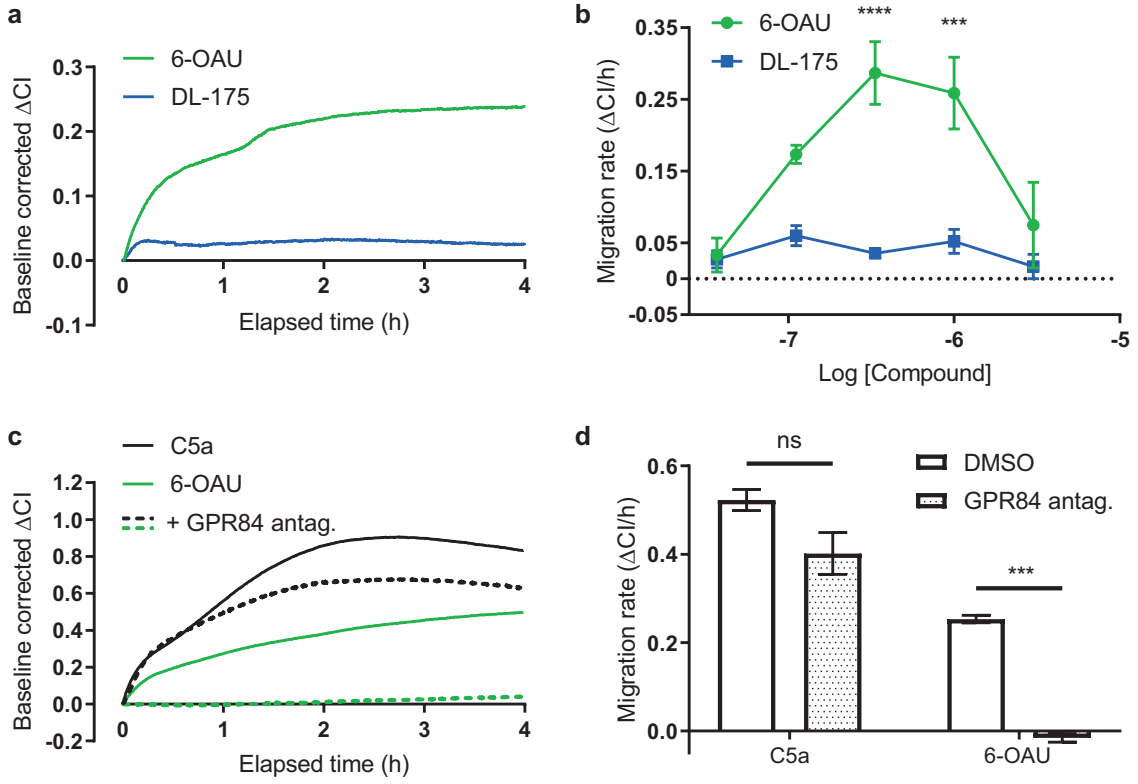

Figure 5.9: DL-175 is a less effective chemoattractant than 6-OAU for human U937 macrophages. **(a)** U937 cells migrate towards GPR84 agonists (1 µM) in a real-time chemotaxis assay, baseline corrected for migration towards vehicle. **(b)** Dose-response curves for U937 chemotaxis to GPR84 agonists quantified by slope analysis. **(c)** Real-time chemotaxis of U937 cells towards C5a (10 nM) or 6-OAU (333 nM), following pre-treatment with either DMSO or GPR84 antagonist **38** (10 µM). Data shown for each pre-treatment group baseline corrected for migration to vehicle. **(d)** Quantification by slope analysis shows that GPR84 antagonism with **38** blocks only 6-OAU and not C5a mediated chemotaxis. Real-time chemotaxis traces are representative figures of $n = 3$ independent experiments with 2–3 technical replicates per condition. Quantifications **(b)** and **(d)** are shown as pooled means ± SEM of $n = 3$ independent experiments. Statistical analysis was performed by one-way ANOVA with Sidak's multiple comparisons test. ns = not significant, *P < 0.05, **P < 0.01, ***P < 0.001, ****P < 0.0001 for 6-OAU vs DL-175 at the indicated concentration in **(b)** and indicated comparisons in **(d)**.

6-OAU provoked chemotaxis of M1 polarised U937 macrophages with a classical bell-shaped concentration dependence that is characteristic of chemotaxis.[283] In contrast, G protein biased agonist DL-175 failed to induce significant migration of U937 cells at the same concentration despite their comparable potency in GPR84-CHO cAMP assays. The GPR84 specificity of the 6-OAU induced migration was demonstrated by pre-treatment with a GPR84 antagonist, which blocked migration of U937 cells to 6-OAU, while not affecting migration to complement component C5a. These data suggest that biased signalling by DL-175 at GPR84 enables the selective activation of functional responses in human U937 macrophages.

I next used pharmacological inhibition of key downstream GPR84 molecules to dissect the signalling required for GPR84 mediated chemotaxis. Pre-treatment with $G_{\alpha i}$ inhibitor PTX blocked U937 cell chemotaxis towards 6-OAU, indicating that G protein signalling is required for GPR84 mediated migration (Figure 5.10). However, the failure of G protein biased agonist DL-175 to induce GRP84 mediated chemotaxis suggests that additional signalling machinery beyond $G_{\alpha i}$ must also be engaged following GPR84 stimulation to enable a migratory response. To see if β-arrestin signalling is required for 6-OAU promoted macrophage chemotaxis, I pre-treated U937 cells with CMPD101 to block GRK2/3 mediated β-arrestin recruitment. GRK2/3 inhibition had no effect on U937 macrophage chemotaxis, suggesting that β-arrestin recruitment must be mediated by GRK4/5/6 or another kinase if β-arrestin signalling is important in GPR84 macrophage chemotaxis.

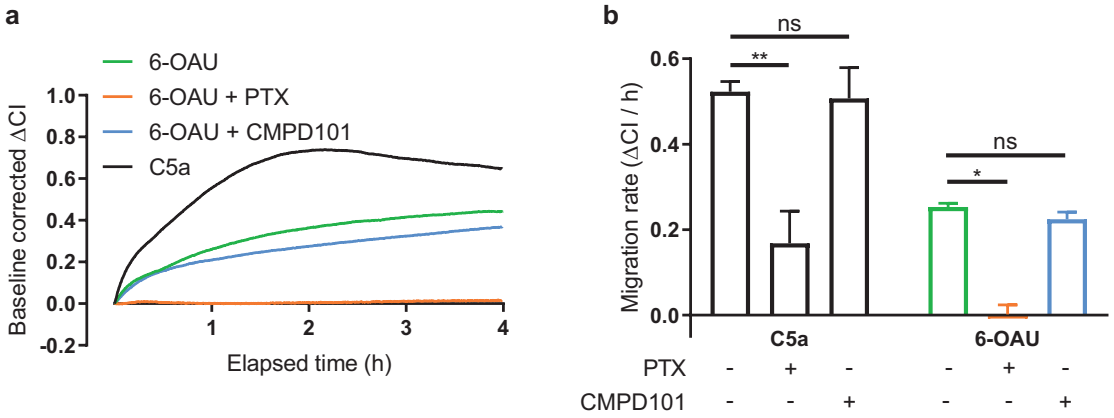

Figure 5.10: GPR84 mediated chemotaxis requires $G_{\alpha i}$ activation. **(a)** Representative real-time chemotaxis traces for M1 polarised U937 cells migrating to C5a or 6-OAU with different pre-treatments. **(b)** Quantification by slope analysis demonstrates that PTX blocks 6-OAU chemotaxis but CMPD101 GRK2/3 inhibition has no effect. Chemotaxis traces are representative of $n = 3$ independent experiments and **(b)** shows are pooled means ± SEM. Statistical analysis was performed using one-way ANOVA with Tukey's multiple comparisons test. ns = not significant, *P < 0.05, **P < 0.01 for indicated comparisons.

Finally, I investigated the chemotactic responses of primary human monocytes to the two GPR84 agonists. Monocytes express GPR84 in their basal state, but the role of the receptor in promoting monocyte chemotaxis has not yet been described despite the importance of the process in chronic disease states such as atherosclerosis.[284] I used magnetic-activated cell sorting to isolate primary human monocytes from peripheral blood mononuclear cells (PBMCs), themselves prepared from blood samples taken from healthy volunteers.[b] I then used flow cytometry to confirm that the resulting cell population comprised more than 80 % $CD14^+$ monocytes (Figure 5.11).

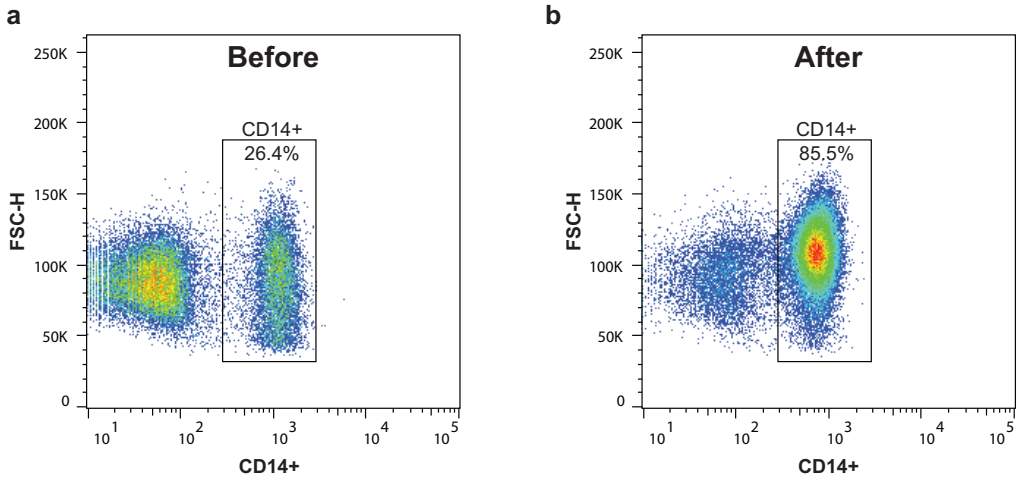

Figure 5.11: Magnetic-activated cell sorting enables isolation of a relatively high purity monocyte population from PBMCs. Flow cytometry shows the percentage of $CD14^+$ cells in the population **(a)** before and **(b)** after magnetic-activated cell sorting (MACS). The purity of monocyte cell population increases from 26 % to 86 % following MACS purification.

In real-time chemotaxis assays, 6-OAU induced migration of human monocytes across a broad range of concentrations, demonstrating for the first time the role of GPR84 in regulating monocyte chemotaxis (Figure 5.12). DL-175 can also induce monocyte chemotaxis, although with a different concentration-response profile to 6-OAU despite their similar potency in GPR84-CHO cAMP assays. At 1 µM and above, for example, DL-175 is a significantly less effective chemoattractant than 6-OAU. The two structurally distinct GPR84 agonists therefore exhibit distinct functional behaviour across multiple immune cell types, including primary human myeloid cells.

[b] PBMCs were isolated from whole blood samples by Dr Gareth Purvis.

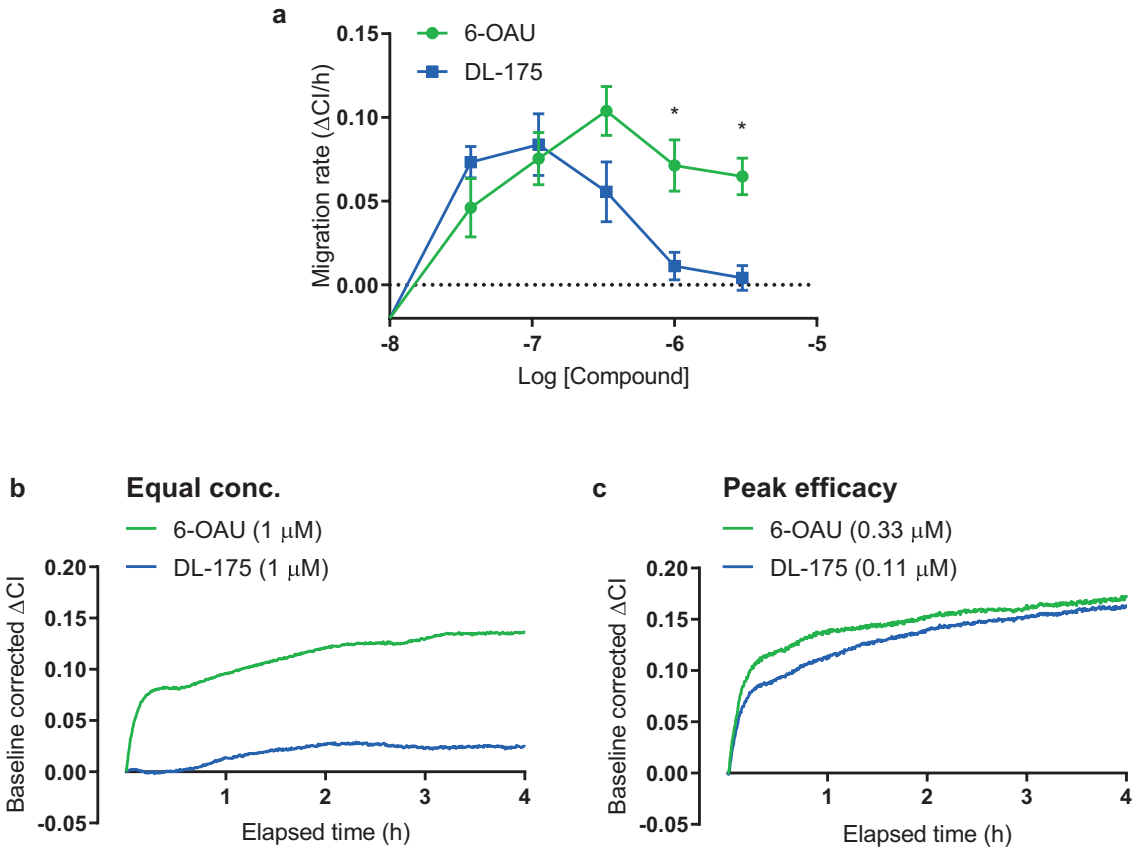

Figure 5.12: 6-OAU and DL-175 induce monocyte chemotaxis with distinct concentration-response profiles. **(a)** Concentration-response curves for human monocyte chemotaxis towards 6-OAU or DL-175, quantified by slope analysis. Representative real-time chemotaxis curves are shown for the two agonists at **(b)** equal concentration (1 μM) and **(c)** the peak efficacy for each compound: 333 nM for 6-OAU; 111 nM for DL-175. Chemotaxis traces **(b-c)** are representative of $n = 4$ human donors and independent experiments. Data in **(a)** are pooled means from $n = 4$ experiments. Statistical analysis was performed using two-way ANOVA with Sidak's multiple comparisons correction. *P < 0.05 for 6-OAU vs DL-175 at the indicated concentrations.

5.4 Discussion

In this chapter I investigated the responses induced by GPR84 agonists 6-OAU and DL-175 in physiologically relevant immune cells with endogenous GPR84 expression. In impedance signalling assays with primary murine macrophages, DL-175 elicited novel responses suggestive of differential signalling pathway activation. This alternative signalling was observed to extend to a human macrophage U937 cell line and, furthermore, in U937 macrophage functional assays DL-175 showed a markedly reduced ability to induce chemotaxis compared to 6-OAU, despite causing similar levels of phagocytosis enhancement in the same cells. Finally, I demonstrated for the first time that GPR84 agonists act as chemoattractants for primary human monocytes and that in this cell type both 6-OAU and DL-175 provoke migration, but with different concentration-response profiles. This work demonstrates that biased agonism at GPR84 enables the selective activation of functional responses in immune cells.

A key finding in this chapter was the markedly different impedance responses induced in primary macrophages by 6-OAU and DL-175. The label-free impedance sensing methodology enables a direct comparison of responses from different cell types that express GPR84. As previously noted, human U937 macrophages show similar but reduced differences in response to 6-OAU and DL-175. Notably, however, GPR84-CHO cells show identical responses to both 6-OAU and DL-175 (Figure 5.13), suggesting that this difference in response to biased GPR84 agonists may only manifest in cells with physiological levels of receptor expression and coupling. Previous studies on GPR84 have found divergent signalling in different cell types, exemplified by the observation that GPR84 agonists do not inhibit cAMP production in primary macrophages as seen in recombinant cells, but instead potentiates cAMP production through a $G_{i\beta\gamma}$ dependent mechanism.[129] My work further serves to highlight the limitations of comparing agonists with subtle downstream signalling differences in artifical recombinant cell systems.

A primary limitation of the impedance signalling approach is that the different observed responses cannot easily be attributed to a specific pathway. In the broadest sense, impedance sensing measures changes in actin cytoskeletal dynamics that result in morphological or ad-

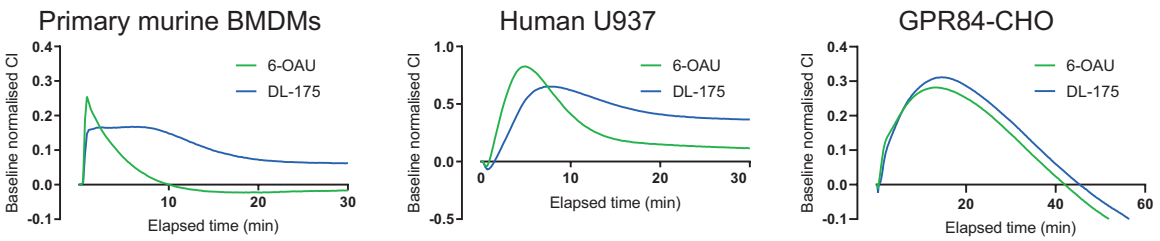

Figure 5.13: The differential responses to 6-OAU and DL-175 observed in macrophages are not present in recombinant cells. Impedance traces in response to GPR84 agonists (1 μM) for primary murine BMDMs, human U937 macrophages, and GPR84-CHO cells. 6-OAU and DL-175 show different responses in both BMDMs and U937 macrophages, but elicit similar responses in GPR84-CHO cells. Data for GPR84-CHO cells is representative of $n = 2$ experiments; data for BMDMs and U937 cells is pooled means for $n = 3$ independent experiments.

hesion changes, such that cytochalasin D inhibition of actin polymerisation blocks GPCR impedance responses.[197] Pharmacological inhibition of different components of GPCR signalling can reveal their contribution to aspects of the impedance signal, as demonstrated for β_2AR activation in HEK293 cells where $G_{\alpha s}$, G_i, and $G_{\beta\gamma}$ signalling can be attributed to different components of the impedance profile.[285] I used genetic ablation of GPR84 and pharmacological inhibition of G protein and arrestin signalling to understand the signalling events constituting the primary macrophage impedance response to GPR84 agonists. The complete absence of response to 6-OAU and DL-175 in GPR84$^{-/-}$ macrophages confirmed the GPR84 specificity of the impedance response, and further confirmed the selectivity of DL-175 as a high-quality chemical tool. Blocking $G_{\alpha i}$ signalling with PTX ablated all responses to GPR84 agonists, suggesting that G protein engagement is essential for the creation of the macrophage cytoskeletal response. This result is consistent with a recent study in HEK293 cells which demonstrated that a dynamic mass redistribution (DMR) biosensing assay could detect G protein but not β-arrestin signalling.[51] Grundmann et al. found that PTX ablated DMR responses to activation of G_i coupled D prostanoid receptor 2 without blocking β-arrestin signalling, whereas depleting β-arrestin in the HEK293 cells only reduced the amplitude of the DMR signal without entirely blocking it.

I used GRK2/3 inhibitor CMPD101 to investigate the role of β-arrestin in creating and shaping primary macrophage impedance responses to GPR84 agonists. I found that GRK2/3 inhibition resulted in more sustained macrophage responses to 6-OAU that resemble those induced by DL-175. These observations are consistent with DL-175 acting as a G protein

biased ligand that fails to engage β-arrestin signalling, so that removing the β-arrestin contribution to the impedance signal results in 6-OAU and DL-175 inducing similar responses. However, there are a number of limitations to this experiment, and more work must be done to confirm these tentative observations. Importantly, GRK2/3 inhibition is an indirect method of preventing β-arrestin signalling and I can therefore only ascribe the changes in signal to GRK2/3 regulation rather than directly implicate β-arrestin. Indeed, in chapter 4, my experiments with GKR2 overexpression (Figure 4.8) suggested that other GRK isoforms were responsible for GPR84 phosphorylation in recombinant cells. Furthermore, GRK2/3 inhibition failed to block 6-OAU promoted U937 chemotaxis despite the literature that suggests that β-arrestin signalling is required for chemotaxis (discussed below). This suggests that, at least in U937 macrophages, GRK2/3 is not involved in β-arrestin recruitment to GPR84. Future experiments should look to use β-arrestin deficient primary macrophages to confirm if the significant differences in 6-OAU and DL-175 macrophage impedance responses is due to arrestin biased agonism.

Consistent with their different profiles in macrophage impedance signalling assays, 6-OAU and DL-175 have strikingly different abilities to provoke chemotaxis of human U937 macrophages. Given the marked G protein bias of DL-175 in recombinant cells, one explanation for this observation is that DL-175 similarly fails to recruit β-arrestin in U937 macrophages and the initiation of migration requires β-arrestin dependent signalling. This hypothesis is in line with a body of evidence implicating β-arrestin recruitment as a pre-requisite for chemotaxis. The β-arrestin dependence of chemotaxis was first shown by the impaired chemotaxis of β-arrestin 2 deficient lymphocytes towards CXCL12,[286] and has subsequently also been demonstrated in non-chemokine GPCRs such as protease-activated receptor 2[287] and the angiotensin-II type 1A receptor.[288] The role of β-arrestin in macrophage chemotaxis is relatively unexplored, although it has been shown that CCL5 induced chemotaxis of primary human macrophages requires cooperative signalling between G protein and β-arrestin pathways.[289] Together, these studies give credence to the theory that differences in β-arrestin signalling underlie the differing migratory responses to 6-OAU and DL-175. Moreover, there is precedent for G protein biased ligands eliciting reduced chemotaxis in immune cells; Smith

et al. demonstrated that a G protein biased CXCR3 ligand elicited less chemotaxis in primary human T-cells than a β-arrestin biased CXCR3 ligand.[6] Importantly, β-arrestin signalling was directly implicated for the difference in T-cell chemotaxis to biased CXCR3 ligands by β-arrestin 2 knockout. Future study into GPR84 should aim to use siRNA knockdown of β-arrestin 1/2 to confirm that the lack of U937 macrophage chemotaxis to DL-175 is a consequence of the absence of β-arrestin signalling.

In primary human monocytes DL-175 does induce chemotaxis and with a greater apparent potency than 6-OAU. The differing migration of macrophages and monocytes to DL-175 may result from different regulation of chemotaxis in the two cell types. For example, if β-arrestin signalling is required for macrophage chemotaxis but not for monocytes, then G protein biased DL-175 would be expected to elicit chemotaxis in only the latter cell type. Alternatively, β-arrestin recruitment may be equally required for monocyte chemotaxis but the differing stoichiometry of G protein, β-arrestin and GRK signalling molecules may mean that the signalling bias of DL-175 is different in monocytes so that it does recruit β-arrestin. Relatively few studies of monocyte chemotaxis have directly explored the role of β-arrestin signalling. For example, Liu et al. investigated how TLR activation can enhance monocyte migration to CCL2 through negative regulation of GRK2, but the role of β-arrestin signalling was not considered.[290] Nevertheless, the potential for biased ligands to differentially promote monocyte migration has been investigated in the chemokine system. Rajagopal et al. observed that G protein biased ligands for CCR10 showed greater ability to elicit primary human monocyte migration than ligands with β-arrestin bias, similar to my findings.[54] However, they found the opposite to be true for CXCR3 where ligands with greater efficacy for β-arrestin signalling would induce greater chemotaxis. These contrary findings suggest that the role of β-arrestin signalling in chemotaxis differs between GPCRs. Testing the migration of monocytes from β-arrestin knockout mice to GPR84 agonists would clarify the role of β-arrestin signalling in monocyte chemotaxis and provide further insight into the differing responses to 6-OAU and DL-175 across immune cell types.

One limitation of this study arises from my use of the U937 cell line to investigate macrophage function. U937 and the similar THP-1 are human monocytic leukaemia cell lines that can

be differentiated *in vitro* to provide a readily available supply of human macrophage-like cells. While widely used, it remains unclear how well such surrogate systems can emulate the biology of the primary macrophage. For example, PMA differentiation of THP-1 cells was shown to induce morphological changes and confer apoptosis resistance similar to primary monocyte derived macrophages, but the surrogate macrophages displayed significantly higher constitutive levels of TNF-α and IL-1β secretion and showed differing cytokine release profiles in response to TLR2 stimulation.[291] Furthermore, in functional assays, U937 cells have shown significantly lower levels of mycobacterial phagocytosis than both primary monocyte-derived macrophages and THP-1 macrophages.[292] Overall, while macrophage surrogate cell lines are a valuable tool for investigating macrophage function, my results showing differential regulation of macrophage chemotaxis by biased GPR84 agonists should be repeated with primary human monocyte-derived macrophages to confirm the translational relevance of these observations.

Chapter 6

Conclusion

6.1 Key findings

Development of a high-quality GPR84 chemical probe

The first aim of this thesis was to develop a structurally novel, high-quality GPR84 chemical probe that could be used to interrogate the biology of the receptor. I achieved this using a ligand-based virtual screening approach to identify new GPR84 agonist scaffolds, followed by medicinal chemistry optimisation to develop a potent GPR84 agonist, DL-175. I identified some limitations of this compound, including aggregation at very high concentrations and metabolic instability in hepatocytes that precludes *in vivo* use, but also demonstrated high GPR84 selectivity using GPCR screening panels, primary GPR84 knockout macrophages, and a GPR84 antagonist. DL-175, in tandem with its inactive analogue **75**, is therefore a high-quality *in vitro* chemical probe which will be of significant use to researchers investigating GPR84.

DL-175 is a biased GPR84 agonist in recombinant and primary cells

Structurally distinct GPCR agonists are more likely to display novel pharmacology,[188] so my second aim was to determine if DL-175 might interact differently with GPR84 compared to other reported ligands. I used recombinant cell signalling assays to demonstrate that DL-175 shows significantly G protein biased signalling at GPR84. Furthermore, I then demonstrated

that biased GPR84 agonists induce novel responses in primary macrophage impedance signalling assays and provided preliminary evidence implicating differences in β-arrestin signalling for these differential responses.

Biased GPR84 agonists cause distinct functional responses in macrophages

My final aim was to investigate if novel GPR84 agonists might reveal new biology of GPR84 in disease-relevant cells. Through a direct comparison of 6-OAU and DL-175, I demonstrated that biased GPR84 agonists can induce distinct patterns of functional behaviour in human U937 macrophage-like cells. The two agonists showed markedly different abilities to activate immune cell chemotaxis, while causing similar levels of phagocytosis enhancement in the same cells. This work therefore highlights that biased agonism at GPR84 enables the selective activation of immune cell functional responses, with significant implications for our understanding and therapeutic targeting of the receptor.

6.2 Future work and outlook

Throughout this thesis I have discussed various possible avenues for further research, including validating my virtual screening approach (section 2.5.1), developing a metabolically stable *in vivo* GPR84 probe (section 3.4), investigating the role of GRKs in regulating GPR84 biology (section 4.3), and proving that β-arrestin recruitment is required for GPR84 chemotaxis (section 5.4). In this section I will discuss the possible binding modes of DL-175 at GPR84, consider the therapeutic potential of GPR84 biased agonism, and consider how we might identify new endogenous agonists of GPR84.

6.2.1 Binding mode of DL-175 at GPR84

The ligand-based virtual screening methodology employed in the development of DL-175 should only identify ligands that bind in the orthosteric site as no information about other regions of the protein is known. However, it remains possible that allosteric ligands could be identified by chance, and my deliberate choice of the most structurally novel validated

screening hit (section 2.5.2) increases the possibility that DL-175 may target an alternative binding site. Allosteric ligands may have very different impact on biological systems *in vivo* through cooperativity with endogenous ligands, and so identifying the binding mode of DL-175 is an important additional component of its characterisation as a GPR84 chemical probe.

The only conclusive means of proving the binding mode of DL-175 would be to obtain GPR84-DL-175 and GPR84-capric acid crystal structures for a direct comparison. Beyond this experimentally challenging approach, other studies could provide an insight into the likely binding site of DL-175. Ligands that bind allosterically often show cooperativity with orthosteric ligands by changing their affinity or efficacy at the receptor. Co-stimulating GPR84 with a concentration range of capric acid and varying concentrations of DL-175 would reveal if the latter can modify the activity of the former. If cooperativity is present, this is strong evidence that DL-175 is binding at an alternative site. If no cooperativity is observed, however, this could still mean they bind at different sites but without affecting each others binding, so further experiments would need to be performed.

Mutaganesis studies have demonstrated that capric acid, embelin, and ZQ-16 all lose activity in a Arg^{172}Ala GPR84 mutant, with the protonated arginine residue suggested to act as a charge partner for the carboxylate moiety of orthosteric fatty acid ligands.[127] Importantly, ago-allosteric ligand DIM retains activity in the mutant receptor, showing that it retains functional activity. Generating a CHO cell line that overexpresses the Arg^{172}Ala GPR84 mutant and testing the activity of DL-175 in this assay would therefore provide useful information regarding the ligand binding site.

6.2.2 Therapeutically exploiting biased GPR84 agonists

GPR84 is viewed as a potential therapeutic target for many diseases, and biased agonism may provide an alternative means of modulating the receptor activity. GPR84 mediated phagocytosis enhancement could be therapeutically beneficial in various disease states, such as increasing bacterial clearance in sepsis or promoting efferocytosis in atherosclerotic plaques.[293,294] In particular, activation of GPR84 in microglia appears to have protective effects on cognition in mice models of Alzheimer's disease, potentially by increasing clearance of degener-

ating dendrites.[154] In contrast, dysregulated activation of immune cell chemotaxis is associated with numerous pathological inflammatory processes.[295] Functionally selective agonists such as DL-175 may therefore enable more effective targeting of beneficial GPR84 functions such as phagocytosis, without adverse side-effects resulting from immune cell chemotaxis. Future studies may additionally focus on how biased agonism influences pro-inflammatory signalling mediated by GPR84 activation, such as 6-OAU induced NF-κB activation or inflammatory cytokine secretion from macrophages.[125] NF-κB activation, for example, is regulated by β-arrestin in many GPCRs,[48,296] and G protein biased GPR84 agonists may show reduced activation of these pathways and reduced side effects *in vivo*.

GPR84 antagonism to reduce pro-inflammatory signalling is the only clinically tested approach for targeting the receptor in chronic inflammatory disease to date, but biased agonism may provide an alternative strategy. As demonstrated in Figure 4.7c, DL-175 is capable of antagonising β-arrestin signalling while continuing to activate G protein pathways. In this sense, DL-175 can be considered a β-arrestin biased antagonist, which may provide greater therapeutic selectivity *in vivo*. The use of biased agonists to selectively antagonise specific pathways has precedence at the dopamine D_2R, where G protein biased partial agonists can selectively block D_2R β-arrestin signalling for antipsychotic efficacy in mice with reduced motoric side effects.[297] Given the failure of GPR84 antagonists in clinical trials for colitis, and the lack of data describing the impact of GPR84 agonists *in vivo*, it is clear that greater understanding of the pathophysiological roles of different signalling pathways is required before biased signalling can be therapeutically exploited at GPR84.

6.2.3 Identifying endogenous GPR84 ligands

Over a decade since MCFAs were first established as low-potency agonists for GPR84, it remains unproven as to whether circulating levels of MCFAs can be routinely high enough to activate the receptor *in vivo*. Dietary MCFAs are believed to be rapidly metabolised in the liver, such that the human plasma concentration of capric acid is generally less than 0.5 μM, a level significantly below that required to activate the receptor.[298] It is therefore likely that additional, as yet undiscovered, endogenously produced ligands can also activate GPR84.

Alternative natural ligands may show distinct signalling bias to MCFAs, or may bind allosterically and enhance the GPR84 activity of MCFAs themselves in physiological settings. As the work in this thesis demonstrates, endogenous agonists with diverse signalling bias at GPR84 may cause different functional outcomes. Until the signalling bias of genuine endogenous GPR84 agonists is well characterised, it will remain unclear how relevant the distinct *in vitro* functional responses to surrogate agonists such as 6-OAU and DL-175 are *in vivo*.

An obvious starting point for discovering higher potency natural GPR84 agonists is MCFAs themselves. Hydroxylated fatty acids show improved potency at GPR84,[128] and other fatty acid metabolites generated *in vivo* could display higher activity still. Interestingly, in the course of my research, I identified that MCFAs were also capable of activating the cannabinoid CB_1 and CB_2 receptors with only slightly reduced potency to GPR84. This result implies some commonality of binding site between the two receptors, and suggests that testing members of the endocannabinoid family at GPR84 may be worthwhile. Ngo et al. systematically compared binding site similarity between all class A GPCRs by analysing sequence, solved crystal structures, and known ligands, and then used this approach to identify surrogate agonists for orphan receptor GPR37L1.[299] In their organisation of GPCRs by pharmacological similarity, GPR84 was associated most closely with orphan receptors GPR18, GPR35, and GPR161. GPR35 is activated by a range of ligands with low potency such as kyneuric acid,[300] while GPR161 is yet to be liganded.[126] GPR18 is activated by cannabinoid analogues such as *N*-arachidonylglycine,[126,301] further strengthening the association of GPR84 with the endocannabinoid system. Beyond focusing on these potential ligands, a future deorphanisation campaign for GPR84 might use a classical reverse pharmacology approach with tissue lipid extracts tested against the receptor, and lipidomics protocols applied to identify any active compounds. GPR84 is induced in inflammatory diseases and shows particularly high expression in brain microglia,[125,153] so testing lipid extracts from patients or models of diseases such as multiple sclerosis may be productive in the continuing search for novel GPR84 endogenous agonists.

Chapter 7

Experimental methods

7.1 Biological and chemical methods and assays

7.1.1 Reagents

All cell culture media, buffers and other laboratory chemicals were obtained from Sigma Aldrich unless otherwise stated. G418 was purchased from Alfa Aesar. 6-OAU was purchased from AstaTech. PSB-16434 (**21**) was synthesised by Dr Carole Bataille at the University of Oxford. GRK 2/3 inhibitor CMPD101 was purchased from Tocris. The G_i-coupled signalling inhibitor pertussis toxin (PTX) was obtained from Cayman Chemical. Phorbol 12-myristate 13-acetate (PMA) was purchased from Cambridge Biosciences. Pooled mouse (CD-1) S9 fractions, TrypLE™ Express reagent, and Alexa Fluor® 546 phalloidin were purchased from ThermoFisher Scientific. Fluoresbrite™ Yellow Green Microspheres 2 µm for bead phagocytosis were purchased from Polysciences. Recombinant murine IL-4 was purchased from PeproTech. NADPH tetrasodium salt was purchased from Santa Cruz Biotechnology. Recombinant mouse complement component C5a was purchased from R&D Systems. CIM-plate 16 and E-plate 96 PET were purchased from ACEA Biosciences. AssayComplete™ Cell Culture Kit-107, AssayComplete™ Cell detachment reagent, AssayComplete™ Cell Plating Reagent 2, PathHunter® detection kit, and HitHunter® cAMP Assay for small molecules were obtained from Eurofins DiscoverX. Human GRK2 expression plasmid was purchased from Stratech. GRK2 antibody and β-actin antibody were obtained from Cell Signalling Technologies.

7.1.2 Virtual screening

The quantitative Structure-Activity Relationship (QSAR) model was developed using Forge™ (Version 10.5.0, 2017, Cresset).[302] A previously reported dataset of 32 structurally related GPR84 agonists comprised the training set used to construct the model.[136] Initially, 3 of the most potent compounds were overlaid using FieldTemplater™ in Forge™ to develop a predicted active conformation pharmacophore, which was used as a reference to which the training set was aligned. Compounds were aligned by substructure using very slow and accurate settings, and conformations were visually checked and manually realigned. The QSAR model was generated using Leave-Many-Out cross validation (Q^2 = 0.729, R^2 = 0.902, RMSE = 0.395, 3 PLS components). Compound structures from an in-house library were then aligned to the model and activity at GPR84 was predicted. Compounds that Forge™ considered a bad, poor, or OK fit to the model were excluded and the remaining compounds ranked by predicted activity.

As the biological data for the training set was generated from a calcium flux assay, the difference in signal amplification between the two assay formats must be accounted for when comparing predicted activities to the activity measured in cAMP assays. A correction factor determined by comparing the activity of 6-OAU in the two assays was therefore applied to the results:

$$cAMP\ predicted\ pEC_{50} = predicted\ pEC_{50} + 1.5$$

7.1.3 Cell culture

CHO cells

GPR84-CHO cells were maintained in AssayComplete™ Cell Culture Kit-107 supplemented with G418 (800 µg/ml). GPR84-CHO PathHunter® cells were maintained in AssayComplete™ Cell Culture Kit-107 supplemented with G418 (800 µg/ml) and Hygromycin B (300 µg/ml). Untransfected CHO-K1, β_2-adrenergic-CHO and CB_1-CHO cells were maintained in Ham's-F12 media supplemented with 10 % heat inactivated foetal bovine serum (FBS) and 1 % peni-

cillin/streptomycin. AssayComplete™ cell detachment reagent was used to passage CHO cells for culturing and prior to experiments.

Murine Bone Marrow-Derived Macrophages (BMDMs)

Bone marrow-derived macrophages were generated as previously described.[303] Briefly, fresh bone marrow cells from tibiae and femurs of male C57BL/6 and GPR84-KO mice were isolated and cultured in Dulbecco's Modified Eagle's medium (DMEM) supplemented with 10 % FBS, 10 % L929 cell-conditioned media as a source of macrophage colony-stimulating factor,[304] and 1 % penicillin/ streptomycin for 7 days. Bone marrow cells were seeded into 8 ml of medium in 100 mm non-tissue culture treated Petri dishes. On day 5, an additional 5 ml of medium was added. Gentle scraping was used to lift cells off dish surface. BMDMs were then counted and resuspended in FBS-free media at the desired cell concentration for use in experiments. Macrophage differentiation was confirmed using flow cytometry with staining for $CD11b^+$ and $F4/80^+$. Macrophage preparation was performed by various postdocs in the lab of Prof. David Greaves.

U937 cells

U937 cells were cultured in suspension in RPMI 1640 with L-glutamine and supplemented with 10 % FBS and 1 % penicillin/streptomycin. For use in experiments, U937 cells were differentiated by additionally supplementing culture medium with phorbol 12-myristate 13-acetate (PMA) (10 ng/ml) for 24 h on non-tissue culture treated plastic. After 24 h, the media was aspirated and replaced with fresh media without PMA, after which the cells were further treated or detached using gentle scraping as required for experiments.

Human monocytes

Peripheral blood mononuclear cells (PBMCs) were purified from leukocyte cones from healthy volunteers (NHSBTS, Oxford, UK) by density centrifugation over Ficoll-Paque PLUS (GE Healthcare Life Sciences). The PBMC layer was carefully harvested and then washed twice with PBS. Monocytes were then isolated from PBMCs by negative selection using a cocktail of anti-

biotin microbeads and biotin conjugated antibodies targeted against non-monocytes and MACS® separation (Miltenyi Biotec). Isolated cells were counted and immediately resuspended in media at the appropriate concentration for use in experiments. The purity of the cell population was determined using flow cytometry. In brief, cells (5×10^5) were pelleted by centrifugation at 300 x g for 5 min at 4°C and resuspended in FACS buffer (PBS containing 1 % FBS) supplemented with an Fc receptor blocking antibody (anti-mouse CD16/32, clone 93, Biolegend, UK) and left on ice for 30 min. Cells were then stained for surface marker $CD14^+$ (anti-human CD14-APC, clone 61D3, eBioscience) and left for 30 min on ice. Cells were pelleted by centrifugation at 300 x g for 5 min at 4 °C, resuspended in 4 % paraformaldehyde and analysed using a BD Fortessa X-20 flow cytometer (BD Biosciences) and FlowJo software (V10, Tree Star).

7.1.4 Biological Assays

Intracellular cAMP

Intracellular cAMP levels were measured using the DiscoverX HitHunter® Assay following the manufacturer's protocol. Briefly, CHO-K1 cells stably expressing the human GPR84, β_2 adrenergic, or CB_1 receptors were plated into a half-area 96-well plate (15000 cells/well) and incubated at 37 °C, 5 % CO_2 for 24 h before the medium was removed and replaced with PBS. For G_i coupled GPR84 and CB_1 receptors, the cells were then simultaneously treated with 25 µM forskolin and agonist for 30 min at 37 °C, 5 % CO_2. In the case of the G_s coupled β_2 adrenergic receptor no forskolin was used. Cell lysis and cAMP detection were performed as per the manufacturer's protocol. Luminescence measurements were taken using a PHERAstar FS microplate reader (BMG Labtech).

β-Arrestin recruitment

The recruitment of β-arrestin 2 to GPR84 was measured using the DiscoverX PathHunter® assay following the manufacturers protocol. In brief, CHO-K1 cells stably expressing human GPR84 receptor tagged on the C-terminus with an enzyme fragment and β-arrestin fused to an N-terminal deletion mutant of beta-galactosidase were seeded in half-area 96-well plates

at a density of 5000 cells/well in 50 µl AssayComplete™ Cell Plating 2 Reagent and incubated at 37 °C, 5 % CO_2 for 24 h. To prevent compound aggregation at high concentrations, agonist solutions were prepared in PBS with Tween-80 (final conc. of 0.025 %). The cells were stimulated with agonist for 90 min at 37 °C, 5 % CO_2. In antagonist mode, cells were stimulated with compound in Tween-80 solution (final conc. 0.025 %) for 15 min, before stimulation with agonist in PBS for 90 min. Cell lysis and luminescence detection were performed as per the manufacturer's protocol. Luminescence measurements were taken using a PHERAstar FS microplate reader (BMG Labtech).

To measure β-arrestin recruitment in the presence or absence of GKR2, GPR84-CHO PathHunter® cells were transfected with a vector containing hGRK2 or an equivalent concentration of pcDNA3.1 using Lipofectamine 2000 (ThermoFisher) according to the manufacturer's protocol. 24 hours post-transfection, the transfected cells were washed and detached in preparation for testing arrestin recruitment as described above. Agonist stimulation of transfected cells therefore occurred 48 hours post-transfection. Tween-80 (0.025 %) was again used to prevent compound aggregation at high concentrations. To confirm overexpression of hGRK2 by Western blotting, transfected cells were lysed 48 hours post-transfection using RIPA buffer supplemented with protease inhibitors followed by manual disruption. Lysates were centrifuged at 16,000 xg for 15 min at 4 °C and protein concentration of the supernatants was confirmed using a BCA protein assay kit (ThermoFisher). Western blotting was performed as previously described.[125]

Bead phagocytosis

PMA differentiated U937 cells were seeded in tissue-culture treated 12-well plates in RPMI 1640 containing 10 % FBS, 1 % penicillin/streptomycin, and LPS (100 ng/ml) at 4×10^5 cells/well. The cells were incubated at 37 °C, 5 % CO_2 for 16 h, after which the media was aspirated and replaced with fresh media without LPS and containing test compounds (1 µM) or vehicle (0.3 % DMSO) and the cells incubated for a further 1 h. Fluorescently labelled 2 µm beads that had been opsonised in human serum for 1 h at 37 °C were then added to the cells (1.6×10^6 beads/well) and the plate briefly centrifuged (15 s at 300 x g) before further incubation at

37 °C, 5 % CO_2. After 4 h the media was aspirated and the cells washed three times with PBS. The cells were detached from the plate by incubation with TrypLE™ Express at 37 °C, 5 % CO_2 for 10 min followed by vigorous pipetting. The cells were then pelleted by centrifugation at 300 x g for 5 min, resuspended in FACS buffer (PBS containing 1 % FBS) and analysed using a BD Fortessa X-20 flow cytometer (BD Biosciences) and FlowJo software (V10, Tree Star).

For confocal imaging of phagocytosed beads, U937 cells were seeded in tissue culture treated 8-well µ-slide dishes (ibidi) at 4×10^4 cells/well. The assay was run as above with beads added in 4:1 ratio of beads to cell (1.6×10^5 beads/well). After incubation with beads, the cells were washed with PBS three times and fixed by the addition of 4 % paraformaldehyde in PBS for 10 min. The cells were washed with PBS and then 0.5 % triton X-100 was added to permeabilise the membrane. The cells were washed with PBS and 5 U/ml Alexa Fluor® 546 phalloidin was added for 30 min to visualise F-actin. The samples were imaged using an Olympus Fluoview FV1200 inverted confocal microscope (Olympus).

ACEA xCELLigence cellular impedance

The wells of a 96-well E-plate were filled with 50 µl of media, after which the plate was loaded into an RTCA-SP system (ACEA Biosciences) and a background reading taken. Cells were seeded into the wells in 50 µl of media for a final volume of 100 µl. For experiments with BMDMs, serum-free DMEM with 1 % penicillin/streptomycin was used and the cell density was 5.0×10^4 cells/well. For experiments with PMA differentiated U937 cells, RPMI 1640 containing 10 % FBS and 1 % penicillin/streptomycin was used and the cell density was 2.0×10^5 cells/well. For experiments on BMDM polarisation, the media also contained either LPS (100 ng/ml), IL-4 (20 ng/ml) or no additional supplement. For all other experiments with BMDMs or U937 cells the media contained LPS (100 ng/ml). The cells were incubated for 16 h at 37 °C, 5 % CO_2 after which the lid of the E-plate was removed and replaced with a metal frame that allows addition of compounds while impedance recording is taking place. When pre-treatments were required, the compound, or DMSO control, was added to the well for the indicated time prior to agonist stimulation. The system was set to start recording Cell

Index (CI) measurements every 10 s, after which the agonists were added as DMSO solutions in 10 µl of media (final DMSO concentration of 0.3 %). Recordings were taken for 60 min at 37 °C, 5 % CO_2. Impedance data is displayed as follows: DMSO stimulated cells were used to establish a baseline; results were baseline-subtracted and expressed as the normalised cell index, defined as the cell index at a given time divided by the cell index at the point of compound addition. To determine the potency of the agonists through concentration-responses, the magnitude of the impedance response was calculated as the maximum cell index minus the initial cell index and is displayed normalised to the maximum response. Area under the curve for the first 60 min following agonist stimulation was calculated using GraphPad prism 7 (GraphPad software).

ACEA xCELLigence real-time chemotaxis

PMA differentiated U937 cells in 100 mm non-tissue culture treated Petri dishes were treated with LPS (100 ng/ml) in RPMI 1640 with 10 % FBS and 1 % penicillin/streptomycin and incubated at 37 °C, 5 % CO_2 for 16 h. The cells were detached by gentle scraping and resuspended in chemotaxis buffer (Ham's-F12 media with 0.1 % BSA). For experiments requiring pre-treatment with DMSO (0.3 %), GPR84 antagonist (10 µM), or pertussis toxin (200 ng/ml), the cells were incubated in suspension with supplemented chemotaxis buffer for 1 h, 1 h, or 2 h respectively at 37 °C, 5 % CO_2. Primary human monocytes were used immediately after isolation and were not LPS treated.

Real-time chemotaxis was conducted using an RTCA-DP system (ACEA Biosciences).[282] The lower chamber of an CIM-16 plate was filled with 160 µl chemotaxis buffer supplemented with the test compound or DMSO (0.3 %). The plate was assembled, and the upper chamber filled with 50 µl of chemotaxis buffer. If cells were being pre-treated with GPR84 antagonist (10 µM) or pertussis toxin (200 ng/ml), the upper chamber of those wells in the chemotaxis plate were also supplemented with the same concentration. Following equilibration at 37 °C for 30 min, the plate was transferred to the RTCA-DP system and a background reading recorded. Cells were added to the top chamber in 50 µl chemotaxis buffer (1.5×10^5 cells/well for U937 cells; 2.0×10^5 cells/well for human monocytes). The plate was incubated at room

temperature for 5 min before being returned to the RTCA-DP machine and Cell Index (CI) measurements were taken every 15 s for 4 h at 37 °C, 5 % CO_2. Real-time chemotaxis data is displayed as the change in Cell Index from the addition of cells (Δ Cell Index) and is baseline subtracted from cells migrating to vehicle. The data was quantified as the migration rate by plotting the linear regression of the first 90 min of migration and determining the gradient using GraphPad Prism 7.

Compound aggregation by waterLOGSY

WaterLOGSY experiments were conducted at a ^{1}H frequency of 600 MHz using a Bruker Avance spectrometer equipped with a BBI probe. All experiments were conducted at 298 K. 3 mm diameter NMR tubes with a sample volume of 200 µl were used in all experiments. Solutions were buffered using an H_2O PBS buffer corrected to pH 7.4 or with "tween buffer" that additionally contained 0.025 % Tween-80. The sample preparation is exemplified as follows, the compound (10 µl of a 10 mM solution in DMSO-d6) was added to an eppendorf before sequential addition of D_2O (20 µl) and the appropriate buffer (170 µl). The resulting solution was spun to ensure full mixing and transferred to a 3 mm NMR tube before the run.

DiscoverX GPCR β-arrestin recruitment screening

Screening of DL-175 against 168 GPCRs in a β-arrestin recruitment assay (gpcrMAX) was performed by Eurofins DiscoverX. Briefly, PathHunter® cell lines were seeded in white walled 384-well microplates and incubated at 37 °C for the appropriate time until testing. For agonist determination, cells were incubated with DL-175 (3 µM) at room temperature or 37 °C for 90 or 180 min depending on the GPCR being tested. For antagonist determination, cells were incubated with DL-175 (3 µM) at 37 °C for 30 min, before cells were stimulated with a reference agonist at the EC_{80} concentration. Cell lysis and detection reagents were then added and incubated at room temperature for 1 h, after which luminescence measurements were taken using a PerkinElmer Envision microplate reader. A full list of GPCRs tested can be found in Appendix Table 3.

Eurofins GPCR screening

Screening of DL-175 against a panel of 14 GPCRs in 2nd messenger functional assays was performed by Eurofins. CHO or HEK293 cells expressing the relevant GPCR were seeded in 96-well or 384-well microplates at an appropriate cell density in HBSS buffer with HEPES (20 mM) or DMEM buffer with 1 % FBS. For both G_i and G_s coupled GPCRs, the buffer also included a reference agonist or the test compound (3 µM). G_s coupled GPCRs also included a phosphodiesterase inhibitor, while G_i coupled GPCRs were further stimulated with an adenylyl cyclase activator. Cells were incubated with the compounds for a length of time specific to the GPCR being tested, before the cells were lysed and the fluorescence acceptor (d2-labelled cAMP) and fluorescence donor (anti-cAMP antibody labelled with europium cryptate) were added. After 60 min at room temperature, the fluorescence transfer was measured at λ_{ex} = 337 nm and λ_{em} = 620 nm and 665 nm using a microplate reader (Envison, Perkin Elmer). For G_q coupled GPCRs, the cell buffer also contained Fluo-4 Direct (Invitrogen) and probenecid and the cells were incubated for 60 min at 37 °C and then 15 min at room temperature. The plate was placed in a microplate reader (CellLux, PerkinElmer) which is used for the addition of the reference agonist or test compound and the changes in fluorescence intensity were then read.

7.1.5 Compound stability and solubility assays

Chemical stability

Buffer solutions were prepared using distilled water and adjusted to the appropriate pH: 0.1 M solution of KCl was adjusted to pH 2 with 1 M HCl; 0.1 M solution of glycine was adjusted to pH 10 with 1 M NaOH; 0.1 M commercially available PBS was used at pH 7.4. DL-175 and inactive analogue **75** were each dissolved in the buffers (final concentration 100 µM, 5 % DMSO) and incubated at 37 °C for up to 48 h. Samples were analysed at the indicated time points on an Agilent 1260 Infinity II LC-MS using peak integration of UV absorption at 280 nm to monitor compound concentration.

S9 metabolic stability

Wells of a 96-well plate were filled with 0.1 M PBS (87.5 µl), DL-175 acetonitrile stock (5 µl, 20 µM), and murine liver S9 fractions from a pool of male CD-1 mice (2.5 µl, 20 mg/ml) and the solution was incubated for 10 min at 37 °C. A solution of NADPH in 0.1 M PBS (5 µl, 20 mM) was added to each well to initiate the reaction (final volume 100 µl; final DL-175 concentration 1 µM). The plate was incubated at 37 °C and the reaction was quenched by the addition of 100 µl of methanol at 0, 5, 15, 30, and 45 min time points. After the final time point, the plate was centrifuged at 1450 x g for 5 min. The supernatant was removed and diluted 1 in 4 in distilled water before testing on an Agilent 1260 Infinity II LC-MS using Single Ion Monitoring to monitor compound concentration by the integration of mass peaks.

Hepatocyte metabolic stability

The hepatocyte stability assay was performed by Cyprotex plc. Williams E media supplemented with 2 mM L-glutamine and 25 mM HEPES and DL-175 (3 µM; final DMSO concentration 0.25 %) was pre-incubated at 37 °C. A suspension of cryopreserved pooled murine hepatocytes (final cell density $0.5 \cdot 10^6$ cells/ml) in Williams E media supplemented with 2 mM L-glutamine and 25 mM HEPES was added to initiate the reaction with a final volume of 500 µl. The reaction was quenched by addition of 50 µl of incubate to 100 µl acetonitrile containing internal standard at 0, 10, 20, 40, and 60 min time points. The samples were analysed using LC-MS/MS to determine the compound remaining as a percentage of the initial time point.

Compound solubility

Approximately 1 mg of the compound of interest was weighed into a glass vial, and an appropriate volume of PBS to give a concentration of 1 mg/ml was then added. The solution was sonicated for 30 s and then agitated at high speed in a vortex shaker for 1 h. The solution was filtered through a 0.45 µm syringe filter tip and then analysed on an Agilent 1260 Infinity II LC-MS using peak integration of UV absorption at 280 or 254 nm depending on the compound tested. To determine solubility, a calibration curve was generated by LC-MS analysis of DMSO solutions of the target compound at 500, 100, 50, and 10 µg/ml.

Compound precipitation

A 10 mM DMSO stock of the compound of interest was diluted to the appropriate top concentration in PBS. This compound PBS stock was further serially diluted in PBS across a 96 well plate, so that each well contained 100 µl compound PBS solution. The absorption of each well at 750 nm was recorded using a PHERAstar FS microplate reader (BMG Labtech).

7.1.6 Statistics

Unless otherwise stated, all biological data is shown as pooled means ± SEM of at least $n = 3$ biological replicates or independent experiments except for real-time chemotaxis data in which representative examples of $n = 3$ experiments are shown. Statistical significance was determined using one-way or two-way analysis of variance (ANOVA) or randomised block ANOVA for data normalised to a control,[305] using Sidak's or Tukey's multiple comparisons test using GraphPad Prism 7 software. A P value of < 0.05 was taken to be statistically significant.

7.2 Chemical methods and synthesis

7.2.1 Reagents

All commercially available reagents and solvents were used without further purification unless specified. H_2O was de-ionised and microfiltered using a Milli-Q® Millipore machine. Brine refers to a sat. aq. solution of NaCl. *In vacuo* refers to the use of a rotary evaporator attached to a diaphragm pump. All reactions using water-sensitive reagents were carried out under an N_2 atmosphere and using oven dried glassware. Thin layer chromatography was performed on aluminium plates coated with 60 F254 silica and visualised under UV light (254 nm). Column chromatography was carried out either using Kiesel gel 60 silica in a glass column, or using a Biotage SP4 automated flash column chromatography platform.

7.2.2 Compound characterisation

Melting points were recorded on an EZ-Melt Automated Melting Point Apparatus (EZ Melt). NMR spectra were recorded on Bruker Avance spectrometers (AVIII 400, AVII 500) in the deuterated solvent stated, with chemical shifts (δ) reported in ppm. The multiplicity of each signal is indicated by: s (singlet); br. s (broad singlet); d (doublet); t (triplet); q (quartet); quint (quintuplet); dd (doublet of doublets); td (triplet of doublets); qt (quartet of triplets); or m (multiplet). Coupling constants(*J*) are reported in Hz and rounded to the nearest 0.1. Accurate mass measurements were obtained to four decimal places using a Bruker MicroTOF spectrometer or a Micromass GCT instrument by the mass spectrometry service of the Chemistry Research Laboratory, University of Oxford, UK. LC/MS spectra were obtained using an Agilent 1260 Infinity II with Diode Array and Single Quadrupole Detectors. The LC/MS method was as follows: Agilent Poroshell 120 EC-C18 2.7 µm, 50 x 4.6 mm; A = water + 0.1 % formic acid; B = MeCN + 0.1 % formic acid; 40 °C; %B: 0.00 min 20 %, 2.45 min 98 %, 4.90 min 98 %, 5.00 min 20 %, 6.00 min 20 %; 1.35 ml/ min

7.2.3 Synthetic protocols

General Procedure A: Mitsunobu reaction

Triphenylphosphine (1.5 equiv) was added to a stirred solution of requisite alkyl alcohol (1 equiv), requisite phenolic alcohol (1.5 equiv) and diisopropyl azodicarboxylate (1.5 equiv) in dry THF, and the mixture was stirred at rt. After 16 h the solvent was evaporated and the residue taken up in aq. 1 M HCl. The aqueous phase was washed repeatedly with Et_2O (x4) before being basified by the addition of aq. 1 M NaOH. The aqueous layer was extracted with EtOAc (x2), and the resulting organic layer was washed with brine, dried over $MgSO_4$, filtered, and evaporated *in vacuo*.

General Procedure B: Nucleophilic substitution of alkyl chloride

In a sealed tube, a solution of the appropriate heterocycle (1.00 equiv) and NaOH (10 equiv) in MeCN was heated at 50 °C for 30 min. The requisite alkyl chloride (1 equiv) in MeCN

(0.5 ml) was then added dropwise and the reaction heated at 70 °C for 16 h. After cooling to rt, the mixture was filtered and the solvent evaporated *in vacuo*.

2-(Hexylthio)-6-hydroxypyrimidin-4(3*H*)-one (ZQ-16, 18)

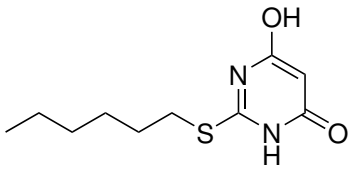

A mixture of 2-mercaptopyrimidine-4,6-diol (1.00 g, 6.94 mmol), 1-bromohexane (3.44 g, 20.8 mmol), KOH (1.17 g, 20.8 mmol), and KI (115 mg, 694 µmol) in EtOH/H_2O (70:35, 105 ml) was heated at reflux for 6 h. The mixture was cooled to rt and diluted with EtOAc (150 ml) and H_2O (100 ml). The organic layer was separated and washed with brine, dried over $MgSO_4$, and concentrated *in vacuo*. The crude product was purified by silica gel column chromatography (20:1 CH_2Cl_2/MeOH) to yield **18** as a pale orange solid (86 mg, 6 %); **mp** 163–165 °C; **^{1}H NMR** (500 MHz, $CDCl_3$) δ 5.46 (1H, s), 3.16 (2H, t, J = 7.3 Hz), 1.75 – 1.63 (2H, m), 1.47 – 1.37 (2H, m), 1.36 – 1.25 (4H, m), 0.89 (3H, t, J = 6.5 Hz); **LRMS (ESI +ve)** 251 $[M+Na]^+$, 229 $[M+H]^+$. These data are in agreement with those previously reported.[136]

4-Hydroxy-6-nonylpyridin-2(1H)-one (19)

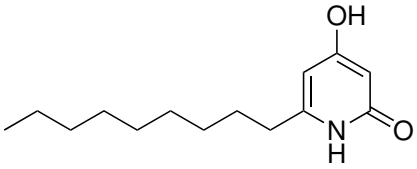

Aqueous ammonia (28 % w/w, 3.0 ml) and H_2O (1.2 ml) were added to **30** (144 mg, 602 µmol) and the mixture heated at 130 °C with a reflux condenser for 6 h. After cooling, the mixture was diluted with H_2O (6 ml) and then acidified to pH 1 by the addition of 0.5 M HCl. The precipitated solid was filtered and dried *in vacuo* to afford **19** as a white solid (133 mg, 93 %); **mp** 272–273 °C; **^{1}H NMR** (400 MHz, DMSO – d_6) δ 10.90 (1H, s), 10.32 (1H, s), 5.58 (1H, d, J = 2.2 Hz), 5.33 (1H, d, J = 2.2 Hz), 2.33 (2H, t, J = 7.6 Hz), 1.51 (2H, quint, J = 2.3 Hz), 1.31–1.19 (12H, m), 0.85 (3H, t, J = 6.7 Hz); **LRMS (ESI +ve)** 238 $[M+H]^+$. These data are in agreement with those previously reported.[136]

Ethyl 3-oxododecanoate (27)

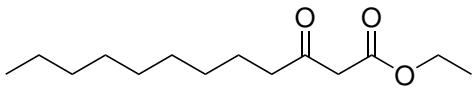

A suspension of NaH (406 mg, 16.9 mmol) in dry THF (20 ml) was cooled to 0 °C, and ethyl acetoacetate (2.00 g, 15.4 mmol) slowly added. The mixture was stirred at 0 °C for 10 min after which *n*-BuLi (1.08 g, 16.9 mmol) was added and the reaction stirred for a further 10 min at 0 °C. 1-Bromooctane (2.97 g, 15.4 mmol) was added and the mixture stirred for 30 min at 0 °C before being allowed to warm to rt and stirred for 16 h. The reaction was quenched with H_2O (10 ml) and taken to pH 7 with conc. aq. HCl. The mixture was extracted with EtOAc (3×25 ml) and the organic phases washed with H_2O (30 ml), brine (40 ml), dried over $MgSO_4$, filtered, and concentrated *in vacuo*. The crude oil was purified using silica gel column chromatography (98:2 PE:EtOAc) to give **27** as a colourless oil (1.09 g, 29 %); **^{1}H NMR** (400 MHz, DMSO – d_6) δ 4.08 (2H, q, J = 7.1 Hz), 3.56 (2H, s), 2.50 (2H, t, J = 7.1 Hz), 1.45 (2H, quint, J = 7.1 Hz), 1.21 (12H, s), 1.18 (3H, t, J = 7.1 Hz), 0.85 (3H, t, J = 7.0 Hz); **LRMS (ESI +ve)** 265 $[M+Na]^+$. These data are in agreement with those previously reported.[136]

3-Oxododecanoic acid (28)

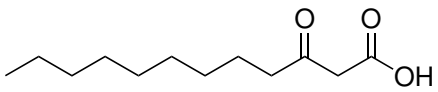

Compound **27** (1.12 g, 4.63 mmol) and NaOH (555 mg, 13.9 mmol) were dissolved in MeOH/H_2O (1:1, 46 ml) and the mixture stirred at rt for 18 h. Solvent was removed *in vacuo*, the crude residue redissolved in H_2O (20 ml), and then acidified using 10 % (w/w) aq. HCl. The precipitate was isolated by vacuum filtration and dried to afford **28** as a white residue (657 mg, 66 %); **^{1}H NMR** (400 MHz, DMSO – d_6) δ 3.43 (2H, s), 2.40 (1H, t, J = 7.3 Hz), 2.06 (1H, s), 1.44 (2H, m), 1.31–1.19 (12H, m), 0.85 (3H, t, J = 6.7 Hz); **LRMS (ESI +ve)** 215 $[M+H]^+$. These data are in agreement with those previously reported.[136]

3-Decanoyl-4-hydroxy-6-nonyl-2H-pyran-2-one (29)

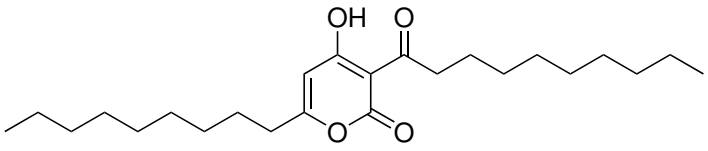

1,1'-Carbonyldiimidazole (689 mg, 4.25 mmol) in dry THF (10 ml) was added to a stirred solution of **28** (650 mg, 3.03 mmol) in dry THF (20 ml) and the mixture was stirred for 24 h at rt. The reaction was acidified to pH 1 with 0.5 M aq. HCl and then extracted with EtOAc (3 × 25 ml). The combined organic phases were washed with brine (30 ml), dried over $MgSO_4$ and solvent evaporated *in vacuo*. The crude residue was recrystallised from MeOH to give **29** as a white solid (273 mg, 46 %); **mp** 72–75 °C; **^{1}H NMR** (400 MHz, $CDCl_3$) δ 5.91 (1H, s), 3.07 (2H, t, *J* = 7.6 Hz), 2.47 (2H, t, *J* = 7.6 Hz), 1.71–1.60 (4H, m), 1.42–1.20 (24H, m), 0.91–0.85 (6H, m); **LRMS (ESI +ve)** 393 $[M+H]^+$. These data are in agreement with those previously reported.[136]

4-Hydroxy-6-nonyl-2H-pyran-2-one (30)

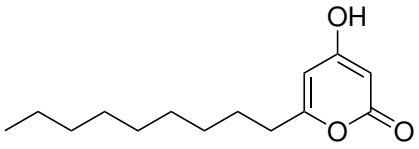

H_2SO_4 (aq. 90 % v/v, 2 ml) was added to **29** (243 mg, 0.62 mmol) and the mixture heated at 130 °C for 1 h. After cooling, the reaction mixture was poured onto ice water (20 ml) and extracted with EtOAc (3 × 20 ml). The organic phases were washed with H_2O (30 ml), dried over $MgSO_4$ and the solvent removed *in vacuo*. The crude residue was purified by silica gel column chromatography (95:5 CH_2Cl_2/MeOH) to afford **30** as a white solid (144 mg, 97 %); **mp** 70–74 °C; **^{1}H NMR** (400 MHz, $CDCl_3$) δ 5.96 (1H, d, *J* = 2.1 Hz), 5.56 (1H, d, *J* = 2.1 Hz), 2.47 (2H, t, *J* = 7.6 Hz) 1.64 (2H, quint, *J* = 7.6 Hz), 1.39–1.18 (12H, m), 0.88 (3H, t, *J* = 0.88 Hz); **LRMS (ESI +ve)** 239 $[M+H]^+$. These data are in agreement with those previously reported.[136]

1-(3-Methoxyphenethyl)urea (31)

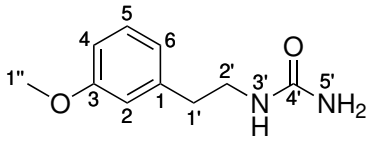

3-Methoxyphenethylamine (8.63 g, 57.1 mmol) and urea (13.7 g, 228 mmol) were dissolved in H_2O (70 ml) before sequential addition of aq. conc. HCl (1.04 ml) and AcOH (3.1 ml), and the reaction stirred at reflux for 5 d. After cooling to rt, the formed solid was filtered, washed with H_2O, and dried to afford **31** as an off-white solid (9.37 g, 84 %); **mp** 99–101 °C; $\nu_{\mathbf{max}}$ (thin film) 3452 (N–H), 3332 (N–H), 2956 (C–H) 1644 (C=O), 1586, 1553; **^{1}H NMR** (500 MHz, $CDCl_3$) δ 7.20 (1H, app t, J = 7.7 Hz, H_5), 6.79 – 6.71 (3H, m, H_2, H_4, and H_6), 4.97 (1H, br t, J = 6.0 Hz, $H_{3'}$), 4.55 (2H, br s, $H_{5'}$), 3.78 (3H, s, $H_{1''}$), 3.39 (2H, app q, J = 6.6 Hz, $H_{2'}$), 2.76 (2H, t, J = 6.9 Hz, $H_{1'}$); **^{13}C NMR** (125 MHz, $CDCl_3$) δ 159.9 (C_3), 159.0 ($C_{4'}$), 140.8 (C_1), 129.7 (C_5), 121.3 (C_2), 114.7 (C_6), 111.9 (C_4), 55.3 ($C_{1''}$), 41.7 ($C_{2'}$), 36.4 ($C_{1'}$); **LRMS (ESI +ve)** 217 $[M+Na]^+$, 195 $[M+H]^+$; **HRMS (ESI +ve)** $C_{10}H_{14}N_2O_2$ $[M+H^+]$ *calc.* 195.1134, *found* 195.1128

1-(3-Hydroxyphenethyl)urea (32)

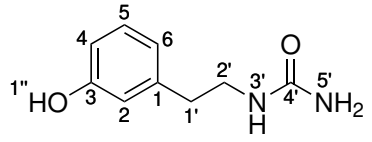

A solution of **31** (9.00 g, 46.3 mmol) in conc. HBr (63 ml, 48 % w/w aq.) was stirred at reflux for 20 h. The mixture was cooled, basified with NaOH (5 M, aq.), and then extracted with EtOAc (4 × 50 ml). The organic phases were dried over $MgSO_4$, filtered, and evaporated *in vacuo* to give **32** as a grey solid (7.12 g, 85 %); **mp** 115–118 °C; $\nu_{\mathbf{max}}$ (thin film) 3439 (N–H), 3333 (N–H), br 3013 (O–H), 1637 (C=O), 1581, 1537; **^{1}H NMR** (400 MHz, DMSO–d_6) δ 9.27 (1H, br s, $H_{1''}$), 7.06 (1H, app td, J = 7.2, 1.8 Hz, H_5), 6.63 – 6.56 (3H, m, H_2, H_4, and H_6), 5.91 (1H, br t, J = 5.9 Hz, $H_{3'}$), 5.45 (2H, br s, $H_{5'}$), 3.16 (2H, td, J = 7.5, 5.9 Hz, $H_{2'}$), 2.57 (2H, t, J = 7.5 Hz, $H_{1'}$); **^{13}C NMR** (101 MHz, DMSO–d_6) δ 158.1 ($C_{4'}$), 157.8 (C_3), 141.6 (C_1), 129.7 (C_5), 119.7 (C_2), 116.0 (C_6), 113.4 (C_4), 41.2 ($C_{2'}$), 36.7 ($C_{1'}$); **LRMS (ESI +ve)** 203 $[M+Na]^+$, 181 $[M+H]^+$; **HRMS (ESI +ve)** $C_9H_{12}N_2O_2$ $[M+H^+]$ *calc.* 181.0977, *found* 181.0970

1-(3-(Allyloxy)phenethyl)urea (33)

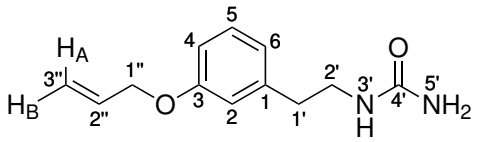

Allyl bromide (4.03 g, 33.3 mmol) was added to a solution of **32** (3.00 g, 16.7 mmol) and K_2CO_3 (6.90 g, 49.9 mmol) in dry DMF (20.7 ml) and stirred at rt for 3 d. The mixture was evaporated to dryness and the crude residue taken up in EtOAc (100 ml). The organic phase was washed with H_2O (60 ml), sat. Na_2CO_3 (60 ml), and brine (60 ml), dried over $MgSO_4$, filtered, and concentrated *in vacuo*. The crude product was purified using silica gel column chromatography (95:5 CH_2Cl_2/MeOH) to afford **33** as a white solid (3.01 g, 82 %); **mp** 75–77 °C; ν_{max} (thin film) 3359 (N–H), 3158 (N–H), 2947 (C–H), 1678 (C=C), 1637 (C=O), 1593; **^{1}H NMR** (400 MHz, CD_3OD) δ7.14 (1H, app t, J = 8.1 Hz, H_5), 6.79 – 6.71 (3H, m, H_2, H_4, and H_6), 6.02 (1H, ddt, J = 17.3, 10.5, 5.2 Hz, $H_{2''}$), 5.36 (1H, app dq, J = 17.3, 1.6 Hz, $H_{3''A}$), 5.20 (1H, app dq, J = 10.5, 1.6 Hz, $H_{3''B}$), 4.48 (2H, app dt, J = 5.2, 1.6 Hz, $H_{1''}$), 3.33 – 3.26 (2H, m, $H_{2'}$, 2.70 (2H, t, J = 7.2 Hz, $H_{1'}$); **^{13}C NMR** (101 MHz, CD_3OD) δ 160.8 (C_3), 158.8 ($C_{4'}$), 140.9 (C_1), 133.6 ($C_{2''}$), 129.1 (C_5), 121.0 (C_2), 116.0 ($C_{3''}$), 114.9 (C_6), 112.2 (C_4), 68.3 ($C_{1''}$), 41.1 ($C_{2'}$), 36.0 ($C_{1'}$); **LRMS (ESI +ve)** 243 $[M+Na]^+$, 221 $[M+H]^+$; **HRMS (ESI +ve)** $C_{12}H_{16}N_2O_2$ $[M+H^+]$ *calc.* 221.1290, *found* 221.1285

1-(3-(Allyloxy)phenethyl)pyrimidine-2,4,6(1*H*,3*H*,5*H*)-trione (34)

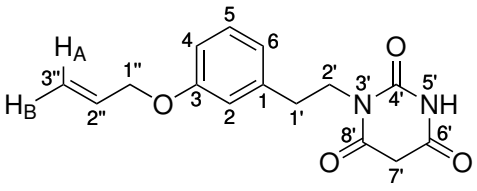

Sodium metal (209 mg, 9.08 mmol) was dissolved in EtOH (14.6 ml), before addition of diethyl malonate (1.45 g, 9.08 mmol) and the mixture heated at reflux for 1 h. **33** (1.00 g, 4.54 mmol) was then added and the mixture further heated at reflux for 12 h. The reaction was cooled to rt and acidified with HCl (1 M, aq.). The resulting precipitate was filtered, washed with H_2O and dried *in vacuo* to afford **34** as a white solid (1.30 g, 50 %); **mp** 149–151 °C; ν_{max} (thin film)

3193, 3091, 2964 (C–H), 1708 (C=O), 1681 (C=O), 1662 (C=O); **^{1}H NMR** (500 MHz, $CDCl_3$) δ 8.18 (1H, br s, $H_{5'}$), 7.21 (1H, app t, J = 7.8 Hz, H_5), 6.87 – 6.74 (3H, m, H_2, H_4, and H_6), 6.05 (1H, ddt, J = 17.3, 10.6, 5.3 Hz, $H_{2''}$), 5.42 (1H, app dq, J = 17.3, 1.6 Hz, $H_{3''A}$), 5.29 (1H, app dq, J = 10.6, 1.6 Hz, $H_{3''B}$), 4.53 (2H, app dt, J = 5.3, 1.6 Hz, $H_{1''}$), 4.12 – 4.05 (2H, m, $H_{2'}$), 3.61 (2H, s, $H_{7'}$), 2.95 – 2.76 (2H, m, $H_{1'}$); **^{13}C NMR** (125 MHz, $CDCl_3$) δ 165.0 ($C_{8'}$), 164.2 ($C_{6'}$), 158.9 (C_3), 150.1 ($C_{4'}$), 139.2 (C_1), 133.4 ($C_{2''}$), 129.7 (C_5), 121.6 (C_2), 117.8 ($C_{3''}$), 115.6 (C_6), 113.1 (C_4), 68.9 ($C_{1''}$), 42.5 ($C_{2'}$), 39.4 ($C_{7'}$), 34.1 ($C_{1'}$); **HRMS (ESI +ve)** $C_{15}H_{16}N_2O_4$ [M+H$^+$] *calc.* 289.1183, *found* 289.1183.

9-(Allyloxy)-2-chloro-6,7-dihydro-4*H*-pyrimido[6,1-*a*]isoquinolin-4-one (35)

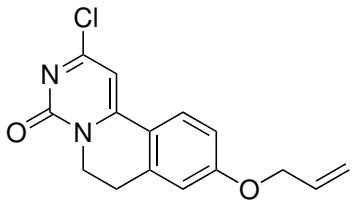

A solution of **34** (1.10 g, 3.82 mmol) in $POCl_3$ (8.25 ml) was heated at 50 °C for 3 d. After cooling, $POCl_3$ was evaporated, the crude residue taken up in CH_2Cl_2 (60 ml) and quenched with aq. sat. $NaHCO_3$ (30 ml). The organic phase was further washed with aq. sat. $NaHCO_3$ (30 ml), H_2O (2 × 30 ml), and brine (30 ml). The organic phase was dried over $MgSO_4$, filtered, and concentrated *in vacuo*. Alkene **35** was obtained as an orange solid (782 mg, crude yield 71 %) and was used in the next step without further purification.

2-((1,4-Dioxan-2-yl)methoxy)-9-(allyloxy)-6,7-dihydro-4*H*-pyrimido[6,1-*a*]-isoquinolin-4-one (36)

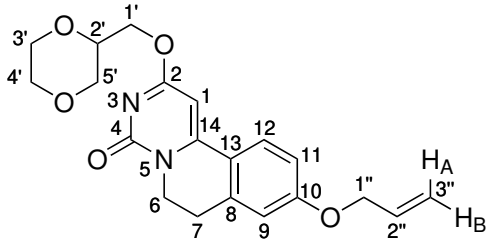

(1,4-Dioxan-2-yl)methanol (363 mg, 3.08 mmol) was added to a suspension of NaH (123 mg,

3.08 mmol) in dry $CHCl_2$ (1.9 ml) at 0 °C and stirred at rt for 15 min before addition of a solution of compound **35** (444 mg, 1.54 mmol) in dry CH_2Cl_2 (4.5 ml). The mixture was warmed to rt and stirred for 16 h. The reaction was quenched with aq. sat. NH_4Cl (5 ml) and the organic phase washed with H_2O (5 ml), dried over $MgSO_4$, filtered, and concentrated *in vacuo* to give **36** as a pale yellow solid (242 mg, 43 %); **mp** 141–142 °C; ν_{max} (thin film) 2955, 2852, 1651 (C=O), 1606; **^{1}H NMR** (500 MHz, $CDCl_3$) δ 7.62 (1H, d, J = 8.8 Hz, H_{12}), 6.90 (1H, dd, J = 8.8, 2.6 Hz, H_{11}), 6.79 (1H, d, J = 2.6 Hz, H_9), 6.27 (1H, s, H_1), 6.04 (1H, ddt, J = 17.3, 10.5, 5.2 Hz, $H_{2''}$), 5.42 (1H, app dq, J = 17.3, 1.5 Hz, $H_{3''A}$), 5.33 (1H, app dq, J = 10.5, 1.5 Hz, $H_{3''B}$), 4.60 (2H, app dt, J = 5.2, 1.5 Hz, $H_{1''}$), 4.43 (1H, dd, J = 11.9, 3.8 Hz, $H_{1'A}$), 4.38 (1H, dd, J = 11.9, 6.3 Hz, $H_{1'B}$), 4.21 – 4.17 (2H, m, H_6), 3.97 (1H, dddd, J = 10.1, 6.3, 3.8, 2.6 Hz, $H_{2'}$), 3.87 – 3.75 (3H, m, $H_{4'A}$, $H_{4'B}$, and $H_{5'A}$), 3.74 – 3.70 (1H, m, $H_{3'A}$), 3.65 (1H, app td, J = 11.3, 2.9 Hz, $H_{3'B}$), 3.47 (1H, dd, J = 11.5, 10.1 Hz, $H_{5'B}$), 2.96 (2H, t, J = 6.5 Hz, H_7); **^{13}C NMR** (125 MHz, $CDCl_3$) δ 170.9 (C_2), 161.7 (C_{10}), 157.2 (C_4), 152.6 (C_{14}), 138.4 (C_8), 132.5 ($C_{2''}$), 127.9 (C_{12}), 120.0 (C_{13}), 118.5 ($C_{3''}$), 114.7 (C_{11}), 113.9 (C_9), 89.2 (C_1), 73.4 ($C_{2'}$), 69.1 ($C_{1''}$), 68.0 ($C_{5'}$), 66.8 ($C_{4'}$), 66.5 ($C_{3'}$), 66.1 ($C_{1'}$), 40.5 (C_6), 28.3 (C_7); **LRMS (ESI +ve)** 393 $[M+Na]^+$, 371 $[M+H]^+$; **HRMS (ESI +ve)** $C_{20}H_{22}N_2O_5$ $[M+H^+]$ *calc.* 371.1607, *found* 371.1599

2-((1,4-Dioxan-2-yl)methoxy)-9-hydroxy-6,7-dihydro-4*H*-pyrimido[6,1-*a*]-isoquinolin-4-one (37)

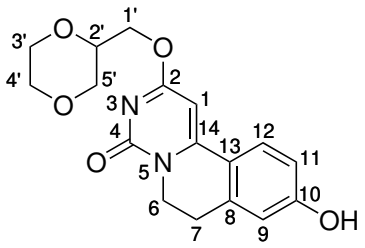

K_2CO_3 (44.7 mg, 324 mmol), $Pd(PPh_3)_4$ (9.36 mg, 8.10 µmol), and **36** (60.0 mg, 162 µmol) were dissolved in degassed CH_2Cl_2/MeOH (1:1, 1.6 ml). The mixture was further degassed with N_2 and stirred at rt for 2 h before addition of H_2O (2 ml) and the aqueous layer separated. The pH was adjusted to pH 1 with HCl (2 M, aq.) and the resulting precipitate was filtered, washed with H_2O and dried to afford **37** as a pale yellow solid (40 mg, 75 %); **mp** 254–256 °C; ν_{max} (thin film) 3013 (O–H), 2957, 1637 (C=O); **^{1}H NMR** (500 MHz, DMSO–d_6) δ 10.31 (1H, s, –

O*H*), 7.84 (1H, d, J = 8.7 Hz, H_{12}), 6.77 (1H, dd, J = 8.7, 2.5 Hz, H_{11}), 6.74 (1H, d, J = 2.5 Hz, H_9), 6.45 (1H, s, H_1), 4.27 – 4.20 (2H, m, $H_{1'A}$ and $H_{1'B}$), 4.01 – 3.96 (2H, m, H_6), 4.01 – 3.96 (2H, m, H_6), 3.84 (1H, dddd, J = 10.0, 6.0, 4.0, 2.5 Hz, $H_{2'}$), 3.81 – 3.73 (2H, m, $H_{4'A}$ and $H_{5'A}$), 3.68 – 3.63 (1H, m, $H_{3'A}$), 3.60 (1H, app td, J = 11.1, 2.6 Hz, $H_{4'B}$), 3.49 (1H, app td, J = 11.1, 2.7 Hz, $H_{3'B}$), 3.37 (1H, dd, J = 11.4, 10.0 Hz, $H_{5'B}$), 2.90 (2H, t, J = 6.5 Hz, H_7); **^{13}C NMR** (125 MHz, DMSO–d_6) δ 170.2 (C_2), 160.9 (C_{10}), 155.7 (C_4), 152.8 (C_{14}), 138.7 (C_8), 128.7 (C_{12}), 117.8 (C_{13}), 114.9 (C_{11}), 114.3 (C_9), 87.4 (C_1), 72.8 ($C_{2'}$), 67.2 ($C_{5'}$), 65.7 ($C_{4'}$), 65.7 ($C_{3'}$), 65.2 ($C_{1'}$), 40.1 (C_6), 27.1 (C_7); **LRMS (ESI +ve)** 353 $[M+Na]^+$, 331 $[M+H]^+$; **HRMS (ESI +ve)** $C_{17}H_{18}N_2O_5$ $[M+H^+]$ *calc.* 331.1289, *found* 331.1287

2-((1,4-dioxan-2-yl)methoxy)-9-(pyridin-2-ylmethoxy)-6,7-dihydro-4*H*-pyrimido[6,1-*a*]isoquinolin-4-one (GPR84 antagonist 38)

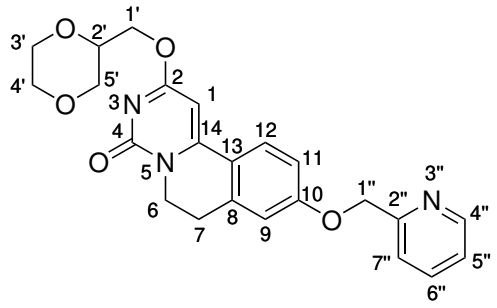

A solution of **37** (30 mg, 90.8 µmol), 2-(chloromethyl)pyridine (22.3 mg, 136 µmol), K_2CO_3 (43.9 mg, 318 µmol), and KI (15.1 mg, 90.8 µmol) in MEK (1.5 ml) was heated at 80 °C for 16 h in a sealed tube. After cooling, the mixture was evaporated to dryness and the crude residue purified by silica gel column chromatography (97:3 CH_2Cl_2/MeOH) to give **38** as a white solid (33 mg, 87 %); **mp** 196–198 °C; ν_{max} (thin film) 2955, 1662 (C=O), 1602, 1593; **^{1}H NMR** (500 MHz, $CDCl_3$) δ 8.62 (1H, d, J = 4.9 Hz, $H_{4''}$), 7.74 (1H, td, J = 7.8, 1.8 Hz, $H_{6''}$), 7.63 (1H, d, J = 8.8 Hz, H_{12}), 7.49 (1H, d, J = 7.8 Hz, $H_{7''}$), 7.29–7.24 (1H, m, $H_{5''}$), 6.98 (1H, dd, J = 8.8, 2.6 Hz, H_{11}), 6.88 (1H, d, J = 2.6 Hz, H_9), 6.27 (1H, s, H_1), 5.26 (2H, s, $H_{1''}$), 4.43 (1H, dd, J = 12.0, 3.8 Hz, $H_{1'A}$), 4.38 (1H, dd, J = 12.0, 6.3 Hz, $H_{1'B}$), 4.24 – 4.13 (2H, m, H_6), 3.97 (1H, dddd, J = 10.1, 6.3, 3.8, 2.6 Hz, $H_{2'}$), 3.89 – 3.70 (4H, m, $H_{3'A}$, $H_{4'A}$, $H_{4'B}$, and $H_{5'A}$), 3.65 (1H, ddd, J = 11.7, 10.7, 3.1 Hz, $H_{3'B}$), 3.48 (1H, dd, J = 11.5, 10.1 Hz, $H_{5'B}$), 2.96 (2H, t, J = 6.5 Hz, H_7); **^{13}C NMR** (125 MHz, $CDCl_3$) δ 170.9 (C_2), 161.5 (C_{10}), 157.2 (C_4), 156.4 ($C_{2''}$), 152.5 (C_{14}),

149.6 ($C_{4''}$), 138.6 (C_8), 137.2 ($C_{6''}$), 128.0 (C_{12}), 123.2 ($C_{5''}$), 121.5 ($C_{7''}$), 120.4 (C_{13}), 114.8 (C_{11}), 114.1 (C_9), 89.3 (C_1), 73.4 ($C_{2'}$), 71.0 ($C_{1''}$), 68.0 ($C_{5'}$), 66.8 ($C_{4'}$), 66.6 ($C_{3'}$), 66.1($C_{1'}$), 40.5 (C_6), 28.3 (C_7); Purity by **LC-MS** UV (280 nm): > 97%; **LRMS (ESI +ve)** 444 $[M+Na]^+$, 422 $[M+H]^+$; **HRMS (ESI +ve)** $C_{23}H_{23}N_3O_5$ $[M+H^+]$ *calc.* 422.1711, *found* 422.1700

1-(2-((4-Chloronaphthalen-1-yl)oxy)ethyl)-1*H*-imidazole (44)

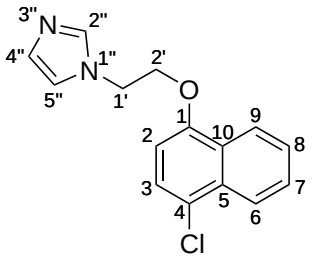

Following general procedure A, 1-(2-hydroxyethyl)imidazole (200 mg, 1.78 mmol) was reacted with 4-chloro-1-naphthol (478 mg, 2.68 mmol), diisopropyl azodicarboxylate (541 mg, 2.68 mmol), and triphenylphosphine (702 mg, 2.68 mmol) in dry THF (8.8 ml). The crude compound was purified using silica gel flash column chromatography (3:97 $MeOH/CH_2Cl_2$) to afford **44** as a white solid (117 mg, 48 %); **mp** 119–120 °C; ν_{max} (thin film) 1265 (C–O); **^{1}H NMR** (500 MHz, $CDCl_3$) δ 8.23 – 8.15 (2H, m, H_6 and H_9), 7.68 (1H, s, $H_{2''}$), 7.63 (1H, ddd, J = 8.3, 6.9, 1.5 Hz, H_7), 7.56 (1H, ddd, J = 8.2, 6.9, 1.5 Hz, H_8), 7.43 (1H, d, J = 8.2 Hz, H_3), 7.11 – 7.10 (2H, m, $H_{4''}$ and $H_{5''}$), 6.66 (1H, d, J = 8.2 Hz, H_2), 4.49 (2H, t, J = 5.2 Hz, $H_{1'}$), 4.38 (2H, t, J = 5.2 Hz, $H_{2'}$); **^{13}C NMR** (125 MHz, $CDCl_3$) δ 152.9 (C_1), 137.7 ($C_{2''}$), 131.5 (C_5), 130.0 ($C_{4''}$), 127.9 (C_7), 126.53 (C_8), 126.48 (C_{10}), 125.6 (C_3), 124.5 (C_6), 124.4 (C_4), 122.2 (C_9), 119.4 ($C_{5''}$), 104.9 (C_2), 67.7 ($C_{2'}$), 46.6 ($C_{1'}$); **LRMS (ESI +ve)** 275 $[M(^{37}Cl)+H]^+$, 273 $[M(^{35}Cl)+H]^+$; **HRMS (ESI +ve)** $C_{15}H_{13}N_2O^{35}Cl$ $[M+H^+]$ *calc.* 273.0789, *found* 273.0788

4-Chloro-2,3-dimethylphenol (47)

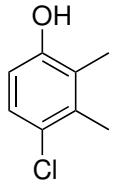

A solution of SO_2Cl_2 (1 M, 1.0 ml, 2.46 mmol) in dry CH_2Cl_2 was added to 2,3-dimethylphenol (300 mg, 2.46 mmol). The mixture was stirred and dry Et_2O (182 mmol, 2.46 mmol) was slowly added. The reaction was stirred for 30 min, after which the solvent was evaporated and the resulting residue taken up in $CHCl_3$ (10 ml). The organic phase was washed with H_2O (10 ml), brine (10 ml), dried over $MgSO_4$, filtered, and evaporated *in vacuo*. The crude product was purified by recrystallisation from pentane to afford **47** as white needles (150 mg, 39 %); **mp** 82–83 °C (pentane), lit. mp 81–82 °C (hexane); **^{1}H NMR** (400 MHz, $CDCl_3$) δ 7.07 (1H, d, J = 8.5 Hz), 6.58 (1H, d, J = 8.5 Hz), 4.64 (1H, s), 2.33 (3H, s), 2.20 (3H, s); **^{13}C NMR** (101 MHz, $CDCl_3$) δ 152.2, 135.9, 126.8, 126.4, 124.5, 113.6, 16.9, 12.7. These data are in agreement with those previously reported by Sato et.al.[306]

1-Chloro-4-(2-chloroethoxy)naphthalene (48)

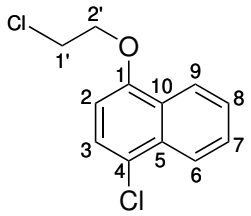

KOH (330 mg, 5.88 mmol), and 1-bromo-2-chloroethane (1.81 g, 12.6 mmol) were added sequentially to a suspension of 4-chloro-1-naphthol (750 mg, 4.20 mmol) in MeOH (5.6 ml) and the mixture stirred at reflux for 16 h. After cooling to rt, the solvent was evaporated and the crude residue taken up in EtOAc (15 ml) before washing with H_2O (15 ml) and brine (2 × 15 ml). The organic phase was dried over $MgSO_4$, filtered, and evaporated *in vacuo*. The crude compound was purified by silica gel column chromatography (95:5 pentane/EtOAc) to afford **48** as a yellow oil (875 mg, 87 %); ν_{max} (thin film) 2980 (C–H), 1263 (C–O); **^{1}H NMR** (400 MHz, $CDCl_3$) δ 8.33 (1H, ddd, J = 8.3, 1.4, 0.7 Hz, H_9), 8.21 (1H, ddd, J = 8.5, 1.3, 0.7 Hz,

H_6), 7.63 (1H, ddd, J = 8.3, 6.8, 1.3 Hz, H_7), 7.56 (1H, ddd, J = 8.5, 6.8, 1.4 Hz, H_8), 7.45 (1H, d, J = 8.2 Hz, H_3), 6.71 (1H, d, J = 8.2 Hz, H_2), 4.39 (2H, t, J = 5.7 Hz, $H_{2'}$), 3.96 (2H, t, J = 5.7 Hz, $H_{1'}$); **^{13}C NMR** (101 MHz, $CDCl_3$) δ 153.2 (C_1), 131.5 (C_5), 127.8 (C_7), 126.7 (C_{10}), 126.3 (C_8), 125.7 (C_3), 124.4 (C_6), 124.1 (C_4), 122.6 (C_9), 105.2 (C_2), 68.6 ($C_{2'}$), 42.1 ($C_{1'}$); **HRMS** (EI^+) $C_{12}H_{10}O^{35}Cl_2$ $[M]^+$ *calc.* 240.0109, *found* 240.0101

1-Chloro-4-(4-chlorobutoxy)naphthalene (49)

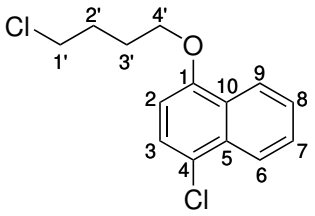

KOH (110 mg, 1.96 mmol) was added to a suspension of 4-chloronaphthol (250 mg, 1.40 mmol) in MeOH (1.9 ml). 1-Bromo-2-chlorobutane (720 mg, 4.20 mmol) was added and the mixture heated at reflux for 16 h. After cooling to rt the solvent was evaporated and the residue taken up in EtOAc (10 ml) and washed with H_2O (5 ml) and brine (2 × 5 ml). The organic phase was dried over $MgSO_4$, filtered, and evaporated before purification by silica gel column chromatography (1:99 EtOAc/pentane) to afford **49** as a purple oil (295 mg, 78 %); 1263 (C – O); **^{1}H NMR** (500 MHz, $CDCl_3$) δ 8.28 (1H, dt, J = 8.4, 1.0 Hz, H_9), 8.20 (1H, dt, J = 8.5, 1.0 Hz, H_6), 7.62 (1H, ddd, J = 8.5, 6.8, 1.0 Hz, H_7), 7.54 (1H, ddd, J = 8.4, 6.8, 1.0 Hz, H_8), 7.44 (1H, d, J = 8.2 Hz, H_3), 6.71 (1H, d, J = 8.2 Hz, H_2), 4.18 – 4.14 (2H, m, $H_{4'}$), 3.71 – 3.64 (2H, m, $H_{1'}$), 2.14 – 2.05 (4H, m, $H_{2'}$ and $H_{3'}$); **^{13}C NMR** (125 MHz, $CDCl_3$) δ 153.8 (C_1), 131.4 (C_5), 127.6 (C_7), 126.8 (C_{10}), 126.1 (C_8), 125.9 (C_3), 124.4 (C_6), 123.3 (C_4), 122.5 (C_9), 104.7 (C_2), 67.6 ($C_{4'}$), 44.9 ($C_{1'}$), 29.6 ($C_{2'}$), 26.8 ($C_{3'}$); Mass spectrometry (ESI and EI) failed to detect this compound.

1-Chloro-4-((5-chloropentyl)oxy)naphthalene (50)

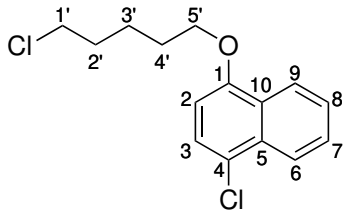

KOH (88.0 mg, 1.57 mmol) was added to a suspension of 4-chloronaphthol (200 mg, 1.12 mmol) in MeOH (1.5 ml). 1-Bromo-2-chloropentane (623 mg, 3.36 mmol) was added and the mixture heated at reflux for 16 h. After cooling to rt the solvent was evaporated and the residue taken up in EtOAc (5 ml) and washed with H_2O (5 ml) and brine (2 × 5 ml). The organic phase was dried over $MgSO_4$, filtered, and evaporated before purification by silica gel column chromatography (10:90 EtOAc/pentane) to afford **50** as a colourless oil (171 mg, 54 %); ν_{max} (thin film) 1263 (C–O); **^{1}H NMR** (500 MHz, $CDCl_3$) δ 8.32 (1H, d, J = 8.3 Hz, H_9), 8.22 (1H, d, J = 8.3 Hz, H_6), 7.63 (1H, ddd, J = 8.3, 6.8, 1.3 Hz, H_7), 7.55 (1H, ddd, J = 8.3, 6.8, 1.3 Hz, H_8), 7.45 (1H, d, J = 8.2 Hz, H_3), 6.68 (1H, d, J = 8.2 Hz, H_2), 4.10 (2H, t, J = 6.3 Hz, $H_{5'}$), 3.60 (2H, t, J = 6.6 Hz, $H_{1'}$), 1.99 – 1.87 (4H, m, $H_{2'}$ and $H_{4'}$), 1.77 – 1.68 (2H, m, $H_{3'}$); **^{13}C NMR** (125 MHz, $CDCl_3$) δ 153.9 (C_1), 131.4 (C_5), 127.6 (C_7), 126.8 (C_{10}), 126.0 (C_8), 125.9 (C_3), 124.3 (C_6), 123.1 (C_4), 122.5 (C_9), 104.6 (C_2), 68.1 ($C_{5'}$), 45.0 ($C_{1'}$), 32.4 ($C_{2'}$), 28.6 ($C_{4'}$), 23.8 ($C_{3'}$); Mass spectrometry (ESI and EI) failed to detect this compound.

1-(2-(Naphthalen-1-yloxy)ethyl)-1*H*-imidazole (51)

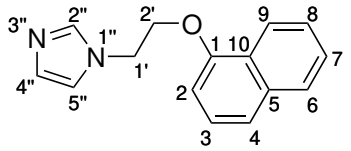

Following general procedure A, 1-(2-hydroxyethyl)imidazole (75.0 mg, 669 µmol) was reacted with 1-naphthol (145 mg, 1.00 mmol), diisopropyl azodicarboxylate (203 mg, 1.00 mmol), and triphenylphosphine (263 mg, 1.00 mmol) in dry THF (3.3 ml). The crude compound was purified using silica gel flash column chromatography (3:97 MeOH/CH_2Cl_2) to afford **51** as a white solid (84 mg, 53 %); **mp** 96–97 °C; ν_{max} (thin film) 1269 (C–O); **^{1}H NMR** (500 MHz, $CDCl_3$) δ 8.21 – 8.14 (1H, m, H_9), 7.83 – 7.77 (1H, m, H_6), 7.68 (1H, app t, J = 1.1 Hz, $H_{2''}$),

7.53 – 7.47 (2H, m, H_7 and H_8), 7.46 (1H, d, J = 8.0 Hz, H_4), 7.35 (1H, app t, J = 8.0 Hz, H_3), 7.12 (1H, app t, J = 1.1 Hz, $H_{5''}$), 7.09 (1H, app t, J = 1.1 Hz, $H_{4''}$), 6.75 (1H, d, J = 8.0 Hz, H_2), 4.47 (2H, t, J = 5.1 Hz, $H_{1'}$), 4.39 (2H, t, J = 5.1 Hz, $H_{2'}$); **^{13}C NMR** (125 MHz, $CDCl_3$) δ 153.8 (C_1), 137.7 ($C_{2''}$), 134.7 (C_5), 129.9 ($C_{4''}$), 127.7 (C_6), 126.8 (C_8), 125.8 (C_7), 125.7 (C_3), 125.5 (C_{10}), 121.8 (C_9), 121.4 (C_4), 119.5 ($C_{5''}$), 104.9 (C_2), 67.5 ($C_{2'}$), 46.7 ($C_{1'}$); **LRMS (ESI +ve)** 239 $[M+H]^+$; **HRMS (ESI +ve)** $C_{15}H_{14}N_2O$ $[M+H^+]$ *calc.* 239.1184, *found* 239.1179

1-(2-(Naphthalen-2-yloxy)ethyl)-1*H*-imidazole (52)

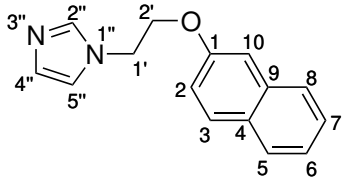

Following general procedure A, 1-(2-hydroxyethyl)imidazole (75.0 mg, 669 µmol) was reacted with 2-naphthol (144.7 mg, 1.00 mmol), diisopropyl azodicarboxylate (203 mg, 1.00 mmol), and triphenylphosphine (263 mg, 1.00 mmol) in dry THF (3.3 ml). The crude compound was purified using silica gel flash column chromatography (3:97 $MeOH/CH_2Cl_2$) to afford **52** as a white solid (110 mg, 69 %); **mp** 143–144 °C; ν_{max} (thin film) 1258 (C – O); **^{1}H NMR** (500 MHz, $CDCl_3$) δ 7.78 – 7.73 (2H, m, H_3 and H_5), 7.71 (1H, dd, J = 8.3, 1.1 Hz, H_8), 7.63 (1H, s, $H_{2''}$), 7.44 (1H, ddd, J = 8.3, 6.9, 1.3 Hz, H_7), 7.35 (1H, ddd, J = 8.0, 6.9, 1.1 Hz, H_6), 7.13 (1H, dd, J = 8.9, 2.5 Hz, H_2), 7.10 – 7.06 (3H, m, $H_{4''}$, $H_{5''}$ and H_{10}), 4.41 – 4.37 (2H, m, $H_{1'}$), 4.36 – 4.31 (2H, m, $H_{2'}$); **^{13}C NMR** (125 MHz, $CDCl_3$) δ 156.0 (C_1), 137.7 ($C_{2''}$), 134.4 (C_9), 129.9 (C_3), 129.8 ($C_{4''}$), 129.4 (C_4), 127.8 (C_5), 126.9 (C_8), 126.7 (C_7), 124.2 (C_6), 119.5 ($C_{5''}$), 118.7 (C_2), 107.0 (C_{10}), 67.3 ($C_{2'}$), 46.6 ($C_{1'}$); **LRMS (ESI +ve)** 239 $[M+H]^+$; **HRMS (ESI +ve)** $C_{15}H_{14}ON_2$ $[M+H^+]$ *calc.* 239.1184, *found* 239.1179

4-(2-(1*H*-Imidazol-1-yl)ethoxy)quinoline (53)

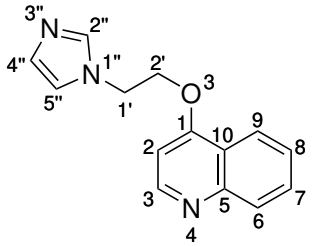

Following general procedure A, 1-(2-hydroxyethyl)imidazole (50.0 mg, 446 µmol) was reacted with quinolin-4-ol (97.1 mg, 669 µmol), diisopropyl azodicarboxylate (135 mg, 669 µmol), and triphenylphosphine (175 mg, 669 µmol) in dry THF (2.2 ml). The crude compound was purified using silica gel flash column chromatography (initial eluent 10:90 MeOH/EtOAc, then flushed with 10:90 MeOH/CH_2Cl_2) to afford **53** as a white solid (55 mg, 52 %); **mp** 56–58 °C; ν_{max} (thin film) 1508, 1314 (C–O); **^{1}H NMR** (500 MHz, $CDCl_3$) δ 8.72 (1H, d, J = 5.2 Hz, H_3), 8.13 (1H, dd, J = 8.5, 1.3 Hz, H_9), 8.03 (1H, d, J = 8.4 Hz, H_6), 7.71 (1H, ddd, J = 8.5, 6.9, 1.5 Hz, H_7), 7.67 (1H, s, $H_{2''}$), 7.53 (1H, ddd, J = 8.4, 6.9, 1.3 Hz, H_8), 7.09 (2H, app s, $H_{4''}$ and $H_{5''}$), 6.66 (1H, d, J = 5.2 Hz, H_2), 4.51 (2H, t, J = 5.0 Hz, $H_{1'}$), 4.44 (2H, t, J = 5.0 Hz, $H_{2'}$); **^{13}C NMR** (125 MHz, $CDCl_3$) δ 160.6 (C_1), 151.2 (C_3), 149.4 (C_5), 137.6 ($C_{2''}$), 130.2 (C_7), 130.1 ($C_{4''}$), 129.2 (C_6), 126.3 (C_8), 121.5 (C_9), 121.1 (C_{10}), 119.4 ($C_{5''}$), 100.6 (C_2), 67.5 ($C_{2'}$), 46.2 ($C_{1'}$); **LRMS (ESI +ve)** 240 $[M+H]^+$; **HRMS (ESI +ve)** $C_{14}H_{13}N_3O$ $[M+H^+]$ *calc.* 240.1137, *found* 240.1132

1-(2-((4-Nitronaphthalen-1-yl)oxy)ethyl)-1*H*-imidazole (54)

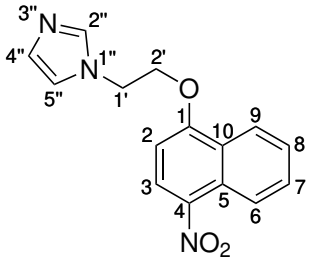

Following general procedure A, 1-(2-hydroxyethyl)imidazole (300 mg, 2.68 mmol) was reacted with 4-nitro-1-naphthol (759 mg, 4.01 mmol), diisopropyl azodicarboxylate (811 mg, 4.01 mmol), and triphenylphosphine (1.05 g, 4.01 mmol) in dry THF (13.2 ml). The crude product was purified using silica gel flash column chromatography (gradient elution 1% → 5% MeOH in CH_2Cl_2) to afford **54** as a yellow solid (615 mg, 81 %); **mp** 132–134 °C; ν_{max}

(thin film) 1509 (N–O), 1320 (N–O), 1270 (C–O); **^{1}H NMR** (500 MHz, $CDCl_3$) δ 8.73, (1H, dt, *J* = 8.8, 0.9 Hz, H_6), 8.32 (1H, d, *J* = 8.6 Hz, H_3), 8.27 (1H, dt, *J* = 8.5, 1.0 Hz, H_9), 7.74 (1H, ddd, *J* = 8.6, 6.9, 1.4 Hz, H_7), 7.69 (1H, s, $H_{2''}$), 7.61 (1H, ddd, *J* = 8.2, 6.9, 1.1 Hz, H_8), 7.12 – 7.10 (2H, m, $H_{4''}$ and $H_{5''}$), 6.70 (1H, d, *J* = 8.6 Hz, H_2), 4.55 (2H, t, *J* = 5.0 Hz, $H_{1'}$), 4.05 (2H, t, *J* = 5.0 Hz, $H_{2'}$); **^{13}C NMR** (125 MHz, $CDCl_3$) δ 158.6 (C_1), 140.2 (C_4), 137.7 ($C_{2''}$), 130.4 (C_7), 130.3 ($C_{4''}$), 127.2 (C_8), 126.9 (C_5), 126.7 (C_3), 125.5 (C_{10}), 123.7 (C_6), 122.4 (C_9), 119.3 ($C_{5''}$), 102.7 (C_2), 68.2 ($C_{2'}$), 46.3 ($C_{1'}$); **LRMS (ESI +ve)** 284 $[M+H]^+$; **HRMS (ESI +ve)** $C_{15}H_{13}N_3O_3$ $[M+H^+]$ *calc.* 284.1035, *found* 284.1030

1-(2-(4-Chlorophenoxy)ethyl)-1*H*-imidazole (55)

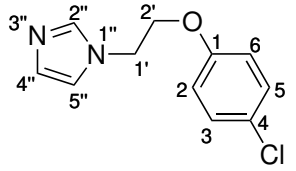

Following general procedure A, 1-(2-hydroxyethyl)imidazole (75.0 mg, 669 μmol) was reacted with 4-chlorophenol (129 mg, 1.00 mmol), diisopropyl azodicarboxylate (203 mg, 1.00 mmol), and triphenylphosphine (263 mg, 1.00 mmol) in dry THF (3.3 ml). The crude compound was purified using silica gel flash column chromatography (3:97 $MeOH/CH_2Cl_2$) to afford **55** as a yellow oil (64 mg, 43 %); ν_{max} (thin film) 1491, 1239 (C–O); **^{1}H NMR** (500 MHz, $CDCl_3$) δ 7.53 (1H, s, $H_{2''}$), 7.24 – 7.19 (2H, m , H_3 and H_5), 7.06 (1H, s, $H_{4''}$), 7.02 (1H, s, $H_{5''}$), 6.80 – 6.74 (2H, m, H_2 and H_6), 4.32 (2H, t, *J* = 5.1 Hz, $H_{1'}$), 4.17 (2H, t, *J* = 5.1 Hz, $H_{2'}$); **^{13}C NMR** (125 MHz, $CDCl_3$) δ 156.7 (C_1), 137.6 ($C_{2''}$), 129.8 ($C_{4''}$), 129.6 (C_3 and C_5), 126.7 (C_4), 119.4 ($C_{5''}$), 115.9 (C_2 and C_6), 67.7 ($C_{2'}$), 46.5 ($C_{1'}$); **LRMS (ESI +ve)** 225 $[M(^{37}Cl)+H]^+$, 223 $[M(^{35}Cl)+H]^+$; **HRMS (ESI +ve)** $C_{11}H_{11}N_2O^{35}Cl$ $[M+H^+]$ *calc.* 223.0638, *found* 223.0633

1-(2-(4-Chloro-2,3-dimethylphenoxy)ethyl)-1*H*-imidazole (56)

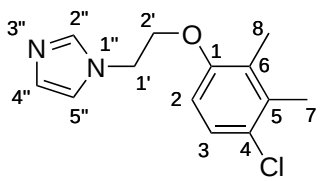

Following general procedure A, 1-(2-hydroxyethyl)imidazole (40.0 mg, 357 μmol) was reacted

with **47** (70.0 mg, 446 µmol), diisopropyl azodicarboxylate (108 mg, 535 µmol), and triphenylphosphine (140 mg, 535 µmol) in dry THF (1.8 ml). The crude product was purified using silica gel flash chromatography (gradient elution 1% → 5% MeOH in CH_2Cl_2) to afford **56** as a white solid (44 mg, 49 %); **mp** 72–74 °C; ν_{max} (thin film) 2980 (C – H), 1260 (C – O); **^{1}H NMR** (500 MHz, $CDCl_3$) δ 7.59 (1H, s, $H_{2''}$), 7.12 (1H, d, J = 8.7 Hz, H_3), 7.07 (1H, s, $H_{5''}$), 7.03 (1H, s, $H_{4''}$), 6.55 (1H, d, J = 8.7 Hz, H_2), 4.35 (2H, t, J = 5.1 Hz, $H_{1'}$), 4.16 (2H, t, J = 5.1 Hz, $H_{2'}$), 2.31 (3H, s, H_7), 2.14 (3H, s, H_8); **^{13}C NMR** (125 MHz, $CDCl_3$) δ 154.6 (C_1), 137.7 ($C_{2''}$), 136.0 (C_5), 129.8 ($C_{4''}$), 127.4 (C_4), 127.3 (C_6), 126.5 (C_3), 119.4 ($C_{5''}$), 109.9 (C_2), 67.9 ($C_{2'}$), 46.7 ($C_{1'}$), 16.9 (C_7), 12.9 (C_8); **LRMS (ESI +ve)** 253 [M(^{37}Cl)+H]$^+$, 251 [M(^{35}Cl)+H]$^+$; **HRMS (ESI +ve)** $C_{13}H_{15}N_2O^{35}Cl$ [M+H$^+$] *calc.* 251.0951, *found* 251.0948

1-(2-((7-Chloro-2,3-dihydro-1*H*-inden-4-yl)oxy)ethyl)-1*H*-imidazole (57)

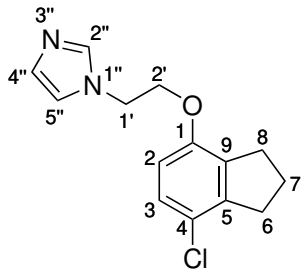

Following general procedure A, 1-(2-hydroxyethyl)imidazole (50.0 mg, 446 µmol) was reacted with 7-chloro-2,3-dihydro-1*H*-inden-4-ol (113 mg, 669 µmol), diisopropyl azodicarboxylate (135 mg, 669 µmol), and triphenylphosphine (175 mg, 669 µmol) in dry THF (2.2 ml). The crude compound was purified using silica gel flash column chromatography (gradient elution 1% → 5% MeOH in CH_2Cl_2) to afford **57** as a white solid (28 mg, 24 %); **mp** 86–88 °C; ν_{max} (thin film) 1268 (C – O); **^{1}H NMR** (500 MHz, $CDCl_3$) δ 7.59 (1H, s, $H_{2''}$), 7.09 – 7.05 (3H, m, H_3, $H_{4''}$ and $H_{5''}$), 6.52 (1H, d, J = 8.5 Hz, H_2), 4.34 (2H, t, J = 5.0 Hz, $H_{1'}$), 4.18 (2H, t, J = 5.0 Hz, $H_{2'}$), 2.94 (2H, t, J = 7.6 Hz, H_6), 2.09 (2H, t, J = 7.6 Hz, H_8), 2.09 (2H, quint, J = 7.6 Hz, H_7); **^{13}C NMR** (125 MHz, $CDCl_3$) δ 153.2 (C_1), 144.5 (C_5), 137.8 ($C_{2''}$), 134.1 (C_9), 129.7 ($C_{4''}$), 127.2 (C_3), 123.3 (C_4), 119.6 ($C_{5''}$), 110.5 (C_2), 67.5 ($C_{2'}$), 46.7 ($C_{1'}$), 32.9 (C_6), 30.6 (C_8), 24.2 (C_7); **LRMS (ESI +ve)** 265 [M(^{37}Cl)+H]$^+$, 263 [M(^{35}Cl)+H]$^+$; **HRMS (ESI +ve)** $C_{14}H_{15}N_2O^{35}Cl$ [M+H$^+$] *calc.* 263.0951, *found* 263.0947

1-(2-(2-Chloro-6-methylphenoxy)ethyl)-1*H*-imidazole (58)

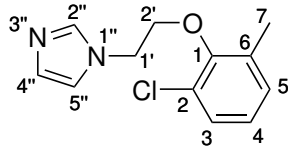

Following general procedure A, 1-(2-hydroxyethyl)imidazole (50.0 mg, 446 µmol) was reacted with 2-chloro-6-methylphenol (95.0 mg, 669 µmol), diisopropyl azodicarboxylate (135 mg, 669 µmol), and triphenylphosphine (175 mg, 669 µmol) in dry THF (2.2 ml). The crude compound was purified using silica gel flash chromatography (gradient elution 1% → 5% MeOH in CH_2Cl_2) to afford **58** as a yellow oil (29 mg, 27 %); ν_{max} (thin film) 1261 (C–O), 1225; **^{1}H NMR** (500 MHz, $CDCl_3$) δ 7.64 (1H, s, $H_{2''}$), 7.19 (1H, dd, J = 7.8, 1.7 Hz, H_3), 7.09 (2H, m, $H_{4''}$ and $H_{5''}$), 7.03 (1H, dd, J = 7.8, 1.7 Hz, H_5), 6.95 (1H, app t, J = 7.8 Hz, H_4), 4.36, (2H, t, J = 5.1 Hz, $H_{1'}$), 4.14 (2H, t, J = 5.1 Hz, $H_{2'}$), 2.05 (3H, s, H_7); **^{13}C NMR** (125 MHz, $CDCl_3$) δ 152.5 (C_1), 137.9 ($C_{2''}$), 133.3 (C_6), 129.9 (C_5), 129.7 ($C_{4''}$), 128.2 (C_3), 127.8 (C_2), 125.3 (C_4), 119.7 ($C_{5''}$), 71.4 ($C_{2'}$), 47.4 ($C_{1'}$), 16.0 (C_7); **LRMS (ESI +ve)** 239 $[M(^{37}Cl)+H]^+$, 237 $[M(^{35}Cl)+H]^+$; **HRMS (ESI +ve)** $C_{12}H_{13}N_2O^{35}Cl$ $[M+H^+]$ *calc.* 237.0795, *found* 237.0790

1-(3-((4-Chloronaphthalen-1-yl)oxy)propyl)-1*H*-imidazole (59)

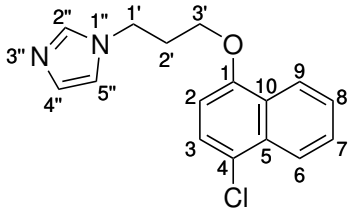

Following general procedure A, 1-(3-hydroxypropyl)-1*H*-imidazole (50.0 mg, 396 µmol) was reacted with 4-chloro-1-naphthol (106 mg, 594 µmol), diisopropyl azodicarboxylate (120 mg, 594 µmol), and triphenylphosphine (156 mg, 594 µmol) in dry THF (2.2 ml). The crude compound was purified using silica gel flash column chromatography (2:98 MeOH/CH_2Cl_2) to afford **59** as a yellow oil (25 mg, 52 %); ν_{max} (thin film) 1263 (C–O); **^{1}H NMR** (500 MHz, $CDCl_3$) δ 8.27 (1H, d, J = 8.3 Hz, H_9), 8.23 (1H, d, J = 8.4 Hz, H_6), 7.64 (1H, ddd J = 8.4, 6.8, 1.3 Hz, H_7), 7.57 (1H, ddd, J = 8.3, 6.8, 1.3 Hz, H_8), 7.49 (1H, s, $H_{2''}$), 7.44 (1H, d, J = 8.2 Hz, H_3), 7.07 (1H, s, $H_{4''}$), 6.93 (1H, s, $H_{5''}$), 6.67 (1H, d, J = 8.2 Hz, H_2), 4.30 (2H, t, J = 6.7 Hz, $H_{1'}$), 4.08 (2H,

t, J = 5.7 Hz, $H_{3'}$), 2.38 (2H, app quint, J = 6.3 Hz, $H_{2'}$); **^{13}C NMR** (125 MHz, $CDCl_3$) δ 153.2 (C_1), 137.5 ($C_{2''}$), 131.5 (C_5), 130.0 ($C_{4''}$), 127.8 (C_7), 126.6 (C_{10}), 126.3 (C_3), 125.9 (C_8), 124.6 (C_6), 123.9 (C_4), 122.1 (C_9), 119.1 ($C_{5''}$), 104.9 (C_2), 64.3 ($C_{3'}$), 43.7 ($C_{1'}$), 30.9 ($C_{2'}$); **LRMS (ESI +ve)** 287 $[M+H]^+$; **HRMS (ESI +ve)** $C_{16}H_{15}N_2O^{35}Cl$ $[M+H^+]$ *calc.* 287.0951, *found* 287.0945

1-(4-((4-Chloronaphthalen-1-yl)oxy)butyl)-1*H*-imidazole (60)

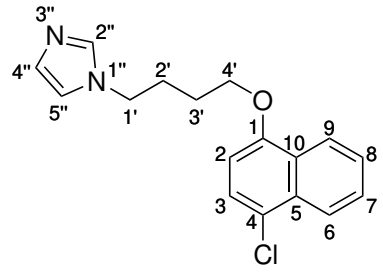

Following general procedure B, imidazole (19.0 mg, 279 μmol) was reacted with NaOH (111 mg, 2.79 mmol) and **49** (75.0 mg, 279 μmol) in MeCN (1.5 ml). The crude compound was purified using silica gel flash column chromatography (2:98 $MeOH/CH_2Cl_2$) to afford **60** as a white solid (76 mg, 91 %); **mp** 96–98 °C; ν_{max} (thin film) 1376, 1263 (C–O); **^{1}H NMR** (500 MHz, $CDCl_3$) δ 8.24 (1H, d, J = 8.3 Hz, H_9), 8.20 (1H, d, J = 8.3 Hz, H_6), 7.62 (1H, ddd, J = 8.4, 6.8, 1.3 Hz, H_7), 7.56 – 7.51 (2H, m, H_8 and $H_{2''}$), 7.44 (1H, d, J = 8.2 Hz, H_3), 7.09 (1H, s, $H_{4''}$), 6.95 (1H, s, $H_{5''}$), 6.88 (1H, d, J = 8.2 Hz, H_2), 4.12 (2H, t, J = 6.0 Hz, $H_{4'}$), 4.07 (2H, t, J = 7.0 Hz, $H_{1'}$), 2.13 – 2.05 (2H, m, $H_{2'}$), 1.97 – 1.88 (2H, m, $H_{3'}$); **^{13}C NMR** (125 MHz, $CDCl_3$) δ 153.7 (C_1), 137.2 ($C_{2''}$), 131.5 (C_5), 129.8 ($C_{4''}$), 127.7 (C_7), 126.7 (C_{10}), 126.2 (C_8), 125.9 (C_3), 124.5 (C_6), 123.5 (C_4), 122.3 (C_9), 118.9 ($C_{5''}$), 104.8 (C_2), 67.6 ($C_{4'}$), 46.9 ($C_{1'}$), 28.3 ($C_{2'}$), 26.5 ($C_{3'}$); **LRMS (ESI +ve)** 303 $[M(^{37}Cl)+H]^+$, 301 $[M(^{35}Cl)+H]^+$; **HRMS (ESI +ve)** $C_{17}H_{17}N_2O^{35}Cl$ $[M+H^+]$ *calc.* 301.1108, *found* 301.1103

1-(5-((4-Chloronaphthalen-1-yl)oxy)pentyl)-1*H*-imidazole (61)

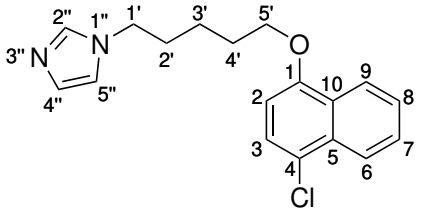

Following general procedure B, imidazole (18.0 mg, 265 μmol) was reacted with NaOH (106 mg,

2.65 mmol) and **50** (75.0 mg, 265 µmol) in MeCN (1.5 ml). The crude compound was purified using silica gel flash chromatography (2:98 MeOH/CH_2Cl_2) to afford **61** as a white solid (61 mg, 73 %); **mp** 111–113 °C; ν_{max} (thin film) 1263 (C–O); **^{1}H NMR** (500 MHz, $CDCl_3$) δ 8.24 (1H, d, J = 8.4 Hz, H_9), 8.19 (1H, d, J = 8.4 Hz, H_6), 7.61 (1H, ddd, J = 8.3, 6.8, 1.2 Hz, H_7), 7.53 (1H, ddd, J = 8.3, 6.8, 1.2 Hz, H_8), 7.48 (1H, s, $H_{2''}$), 7.43 (1H, d, J = 8.2 Hz, H_3), 7.07 (1H, s, $H_{4''}$), 6.91 (1H, s, $H_{5''}$), 6.68 (1H, d, J = 8.2 Hz, H_2), 4.10 (2H, t, J = 6.2 Hz, $H_{5'}$), 3.98 (2H, t, J = 7.1 Hz, $H_{1'}$), 1.98 – 1.86 (4H, m, $H_{2'}$ and $H_{4'}$), 1.62 – 1.53 (2H, m, $H_{3'}$); **^{13}C NMR** (125 MHz, $CDCl_3$) δ 153.8 (C_1), 137.2 ($C_{2''}$), 131.4 (C_5), 129.7 ($C_{4''}$), 127.6 (C_7), 126.7 (C_{10}), 126.1 (C_8), 125.9 (C_3), 124.4 (C_6), 123.3 (C_4), 122.4 (C_9), 118.9 ($C_{5''}$), 104.7 (C_2), 67.9 ($C_{5'}$), 47.0 ($C_{1'}$), 31.0 ($C_{2'}$), 28.8 ($C_{4'}$), 23.6 ($C_{3'}$); **LRMS (ESI +ve)** 315 $[M+H]^+$; **HRMS (ESI +ve)** $C_{18}H_{19}N_2O^{35}Cl$ $[M+H^+]$ *calc.* 315.1264, *found* 315.1261

1-(2-((4-Chloronaphthalen-1-yl)oxy)ethyl)-1*H*-benzo[*d*]imidazole (62)

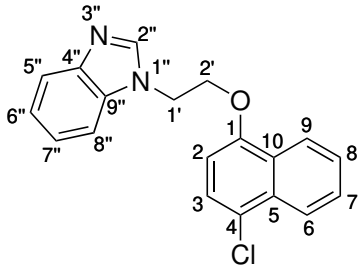

Following general procedure B, benzimidazole (36.8 mg, 311 µmol) was reacted with NaOH (124 mg, 3.11 mmol) and **48** (75.0 mg, 311 µmol) in MeCN (1.5 ml). The crude compound was purified using silica gel flash chromatography (99:1 CH_2Cl_2/MeOH) to afford **62** as a pale yellow solid (63 mg, 63 %); **mp** 119–120 °C; ν_{max} (thin film) 1262 (C–O); **^{1}H NMR** (400 MHz, $CDCl_3$) δ 8.17 (1H, d, J = 8.4 Hz, H_6), 8.12 (1H, s, $H_{2''}$), 8.12 – 8.09 (1H, m, H_9), 7.84 (1H, d, J = 7.6 Hz, $H_{5''}$), 7.60 (1H, ddd, J = 8.4, 6.8, 1.3 Hz, H_7), 7.53 – 7.48 (2H, m, H_8 and $H_{8''}$), 7.38 (1H, d, J = 8.2 Hz, H_3), 7.35 (1H, app td, J = 7.6, 1.3 Hz, $H_{7''}$), 7.31 (1H, app td, J = 7.6, 1.3 Hz, $H_{6''}$), 6.63 (1H, d, J = 8.2 Hz, H_2), 4.70 (2H, t, J = 5.2 Hz, $H_{1'}$), 4.45 (2H, t, J = 5.2 Hz, $H_{2'}$); **^{13}C NMR** (101 MHz, $CDCl_3$) δ 152.8 (C_1), 144.0 ($C_{4''}$), 143.5 ($C_{2''}$), 133.9 ($C_{9''}$), 131.5 (C_5), 127.9 (C_7), 126.5 (C_8), 126.4 (C_{10}), 125.5 (C_3), 124.5 (C_6), 124.4 (C_4), 123.3 ($C_{7''}$), 122.5 ($C_{6''}$), 122.2 (C_9), 120.8 ($C_{5''}$), 109.4 ($C_{8''}$), 104.9 (C_2), 66.5 ($C_{2'}$), 44.5 ($C_{1'}$); **LRMS (ESI +ve)** 325 $[M(^{37}Cl)+H]^+$,

323 [M(^{35}Cl)+H]$^+$; **HRMS (ESI +ve)** $C_{19}H_{15}N_2O^{35}Cl$ [M+H$^+$] *calc.* 323.0946, *found* 323.0946.

1-(2-((4-Chloronaphthalen-1-yl)oxy)ethyl)-1*H*-pyrrolo[2,3-*b*]pyridine (63)

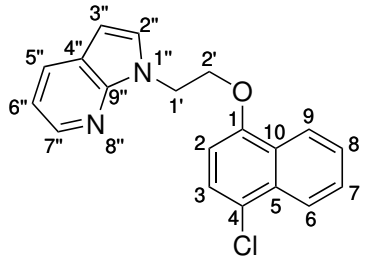

Following general procedure B, 7-azaindole (36.8 mg, 311 µmol) was reacted with NaOH (124 mg, 3.11 mmol) and **48** (75.0 mg, 311 µmol) in MeCN (1.5 ml). The crude compound was purified using silica gel flash chromatography (CH_2Cl_2) to afford **63** as a pale yellow solid (38 mg, 38 %) ; **mp** 108–109 °C; ν_{max} (thin film) 2980 (C–H), 1261 (C–O); **^{1}H NMR** (400 MHz, $CDCl_3$) δ 8.35 (1H, dd, J = 4.7, 1.6 Hz, $H_{7''}$), 8.21 – 8.19 (1H, m, H_9), 8.19 – 8.16 (1H, m, H_6), 7.92 (1H, dd, J = 7.8, 1.6 Hz, $H_{5''}$), 7.60 (1H, ddd, J = 8.4, 6.8, 1.3 Hz, H_7), 7.52 (1H, ddd, J = 8.2, 6.8, 1.3 Hz, H_8), 7.46 (1H, d, J = 3.5 Hz, $H_{2''}$), 7.39 (1H, d, J = 8.3 Hz, H_3), 7.09 (1H, dd, J = 7.8, 4.7 Hz, $H_{6''}$), 6.67 (1H, d, J = 8.3 Hz, H_2), 6.49 (1H, d, J = 3.5 Hz, $H_{3''}$), 4.85 (2H, t, J = 5.2 Hz, $H_{1'}$), 4.50 (2H, t, J = 5.2 Hz, $H_{2'}$); **^{13}C NMR** (101 MHz, $CDCl_3$) δ 153.3 (C_1), 147.6 ($C_{9''}$), 143.0 ($C_{7''}$), 131.4 (C_5), 129.1 ($C_{5''}$), 129.0 ($C_{2''}$), 127.7 (C_7), 126.6 (C_{10}), 126.2 (C_8), 125.8 (C_3), 124.4 (C_6), 123.8 (C_4), 122.4 (C_9), 121.0 ($C_{4''}$), 116.1 ($C_{6''}$), 104.9 (C_2), 100.0 ($C_{3''}$), 67.5 ($C_{2'}$), 44.2 ($C_{1'}$); **LRMS (ESI +ve)** 325 [M(^{37}Cl)+H]$^+$, 323 [M(^{35}Cl)+H]$^+$; **HRMS (ESI +ve)** $C_{19}H_{15}N_2O^{35}Cl$ [M+H$^+$] *calc.* 323.0946, *found* 323.0945

1-(2-((4-Chloronaphthalen-1-yl)oxy)ethyl)-1*H*-indole (64)

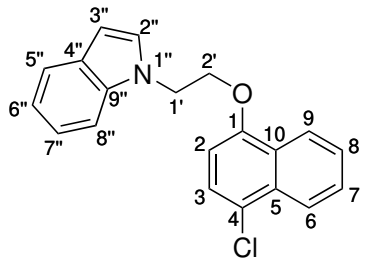

Following general procedure B, indole (36.4 mg, 311 µmol) was reacted with NaOH (124 mg, 3.11 mmol) and **48** (75.0 mg, 311 µmol) in MeCN (1.5 ml). The crude compound was purified

using silica gel column chromatography (95:5 EtOAc/pentane) to afford **64** as a white solid (75 mg, 75 %); **mp** 134–136 °C; ν_{max} (thin film) 1263 (C–O); **^{1}H NMR** (400 MHz, $CDCl_3$) δ 8.20 – 8.18 (1H, m, H_6), 8.18 – 8.16 (1H, m, H_9), 7.67 (1H, dd, J = 8.0, 1.0 Hz, $H_{5''}$), 7.61 (1H, ddd, J = 8.3, 6.8, 1.3 Hz, H_7), 7.52 (1H, ddd, J = 8.2, 6.8, 1.2 Hz, H_8), 7.47 (1H, dd, J = 8.4, 0.9 Hz, $H_{8''}$), 7.39 (1H, d, J = 8.2 Hz, H_3), 7.30 (1H, d, J = 3.1 Hz, $H_{2''}$), 7.29 – 7.25 (1H, m, $H_{7''}$), 7.16 (1H, ddd, J = 8.0, 7.0, 0.9 Hz, $H_{6''}$), 6.61 (1H, d, J = 8.2 Hz, H_2), 6.57 (1H, dd, J = 3.1, 1.0 Hz, $H_{3''}$), 4.66 (2H, t, J = 5.5 Hz, $H_{1'}$), 4.41 (2H, t, J = 5.5 Hz, $H_{2'}$); **^{13}C NMR** (101 MHz, $CDCl_3$) δ 153.3 (C_1), 136.2 ($C_{9''}$), 131.4 (C_5), 128.9 ($C_{4''}$), 128.4 ($C_{2''}$), 127.7 (C_7), 126.6 (C_{10}), 126.2 (C_8), 125.7 (C_3), 124.4 (C_6), 124.0 (C_4), 122.5 (C_9), 121.9 ($C_{7''}$), 121.3 ($C_{5''}$), 119.8 ($C_{6''}$), 109.3 ($C_{8''}$), 104.8 (C_2), 102.1 ($C_{3''}$), 67.3 ($C_{2'}$), 45.7 ($C_{1'}$); **HRMS (ESI +ve)** $C_{20}H_{16}NO^{35}Cl$ [M+H$^+$] *calc.* 322.0999, *found* 322.0955

4-(2-((4-Chloronaphthalen-1-yl)oxy)ethyl)morpholine (65)

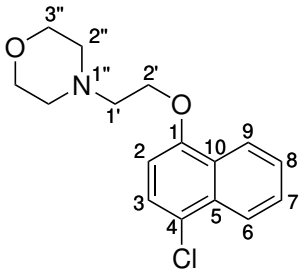

A mixture of morpholine (27.1 mg, 311 µmol), **48** (75.0 mg, 311 µmol), and K_2CO_3 (86.0 mg, 620 µmol) in MeCN (1.5 ml) was stirred at 85 °C in a sealed tube for 36 h. After cooling, the mixture was filtered, the solvent evaporated, and the crude residue purified by silica gel column chromatography (97:3 CH_2Cl_2/MeOH) to afford **65** as a white solid (52 mg, 57 %) ; **mp** 35–39 °C; ν_{max} (thin film) 2980 (C–H), 1265 (C–O); **^{1}H NMR** (500 MHz, $CDCl_3$) δ 8.27 (1H, dt, J = 8.4, 1.1 Hz, H_9), 8.23 – 8.16 (1H, m, H_6), 7.62 (1H, ddd, J = 8.4, 6.8, 1.1 Hz, H_7), 7.54 (1H, ddd, J = 8.4, 6.8, 1.3 Hz, H_8), 7.45 (1H, d, J = 8.2 Hz, H_3), 6.72 (1H, d, J = 8.2 Hz, H_2), 4.28 (2H, t, J = 5.6 Hz, $H_{2'}$), 3.75 (4H, m, $H_{3''}$), 2.96 (2H, t, J = 5.6 Hz, $H_{1'}$), 2.68 – 2.62 (4H, m, $H_{2''}$); **^{13}C NMR** (125 MHz, $CDCl_3$) δ 153.7 (C_1), 131.5 (C_5), 127.6 (C_7), 126.8 (C_{10}), 126.1 (C_8), 125.9 (C_3), 124.4 (C_6), 123.5 (C_4), 122.5 (C_9), 104.9 (C_2), 67.2 ($C_{3''}$), 66.9 ($C_{2'}$), 57.7 ($C_{1'}$), 54.3 ($C_{2''}$); **LRMS (ESI +ve)** 294 [M(^{37}Cl)+H]$^+$, 292 [M(^{35}Cl)+H]$^+$; **HRMS (ESI +ve)** $C_{16}H_{18}O_2N^{35}Cl$ [M+H$^+$] *calc.*

292.1099, *found* 292.1100

1-(2-((4-Chloronaphthalen-1-yl)oxy)ethyl)-2-methyl-1*H*-imidazole (66)

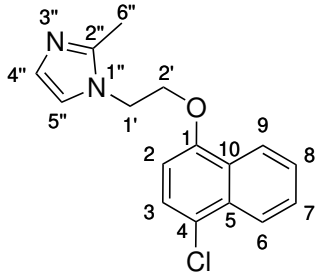

Following general procedure B, 2-methyl imidazole (25.5 mg, 311 µmol) was reacted with NaOH (124 mg, 3.11 mmol) and **48** (75.0 mg, 311 µmol) in MeCN (1.5 ml). The crude compound was purified using silica gel flash chromatography (3:97 $MeOH/CH_2Cl_2$) to afford **66** as a white solid (59 mg, 66 %); **mp** 116–118 °C; ν_{max} (thin film) 1262 (C–O); **^{1}H NMR** (500 MHz, $CDCl_3$) δ 8.20 (1H, dt, J = 8.5, 1.0 Hz, H_6), 8.15 (1H, dt, J = 8.3, 1.0 Hz, H_9), 7.62 (1H, ddd, J = 8.4, 6.8, 1.3 Hz, H_7), 7.55 (1H, ddd, J = 8.2, 6.8, 1.2 Hz, H_8), 7.43 (1H, d, J = 8.2 Hz, H_3), 7.03 (1H, d, J = 1.4 Hz, $H_{5''}$), 6.95 (1H, d, J = 1.4 Hz, $H_{4''}$), 6.66 (1H, d, J = 8.2 Hz, H_2), 4.42 – 4.37 (2H, m, $H_{1'}$), 4.37 – 4.33 (2H, m, $H_{2'}$), 2.51 (3H, s, $H_{6''}$); **^{13}C NMR** (125 MHz, $CDCl_3$) δ 152.9 (C_1), 144.9 ($C_{2''}$), 131.5 (C_5), 127.8 (C_7), 127.7 ($C_{4''}$), 126.5 (C_{10}), 126.4 (C_8), 125.6 (C_3), 124.5 (C_6), 124.3 (C_4), 122.2 (C_9), 119.6 ($C_{5''}$), 104.9 (C_2), 67.4 ($C_{2'}$), 45.5 ($C_{1'}$), 13.4 ($C_{6''}$); **LRMS (ESI +ve)** 289 [M(^{37}Cl)+H]$^+$, 287 [M(^{35}Cl)+H]$^+$; **HRMS (ESI +ve)** $C_{16}H_{15}N_2O^{35}Cl$ [M+H$^+$] *calc.* 287.0951, *found* 287.0945

1-(2-((4-Chloronaphthalen-1-yl)oxy)ethyl)-2-ethyl-1*H*-imidazole (67)

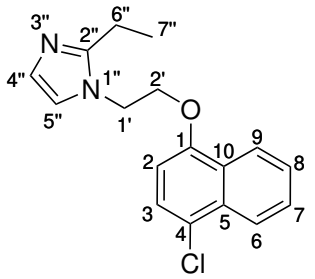

Following general procedure B, 2-ethyl imidazole (29.9 mg, 311 µmol) was reacted with NaOH (124 mg, 3.11 mmol) and **48** (75.0 mg, 311 µmol) in MeCN (1 ml). The crude compound was purified using silica gel flash chromatography (2:98 $MeOH/CH_2Cl_2$) to afford **67** as a white

solid (76 mg, 81 %); **mp** 97–98 °C; ν_{max} (thin film) 1377, 1262 (C–O); **^{1}H NMR** (500 MHz, $CDCl_3$) δ 8.20 (1H, d, J = 8.3 Hz, H_6), 8.15 (1H, d, J = 8.3 Hz, H_9), 7.62 (1H, ddd, J = 8.3, 6.9, 1.4 Hz, H_7), 7.54 (1H, ddd, J = 8.3, 6.8, 1.2 Hz, H_8), 7.42 (1H, d, J = 8.2 Hz, H_3), 7.03 (1H, d, J = 1.4 Hz, $H_{5''}$), 6.99 (1H, d, J = 1.4 Hz, $H_{4''}$), 6.66 (1H, d, J = 8.2 Hz, H_2), 4.42 – 4.38 (2H, m, $H_{1'}$), 4.37 – 4.34 (2H, m, $H_{2'}$), 2.81 (2H, q, J = 7.5 Hz, $H_{6''}$), 1.40 (3H, t, J = 7.5 Hz, $H_{7''}$); **^{13}C NMR** (125 MHz, $CDCl_3$) δ 153.0 (C_1), 149.5 ($C_{2''}$), 131.5 (C_5), 127.8 (C_7), 127.8 ($C_{4''}$), 126.5 (C_{10}), 126.4 (C_8), 125.6 (C_3), 124.5 (C_6), 124.4 (C_4), 122.2 (C_9), 119.5 ($C_{5''}$), 105.0 (C_2), 67.6 ($C_{2'}$), 45.1 ($C_{1'}$), 20.4 ($C_{6''}$), 12.3 ($C_{7''}$); **LRMS (ESI +ve)** 303 [M(^{37}Cl)+H]$^+$, 301 [M(^{35}Cl)+H]$^+$; **HRMS (ESI +ve)** $C_{17}H_{17}N_2O^{35}Cl$ [M+H$^+$] *calc.* 301.1108, *found* 301.1103

1-(2-((4-Chloronaphthalen-1-yl)oxy)ethyl)-1*H*-pyrazole (68)

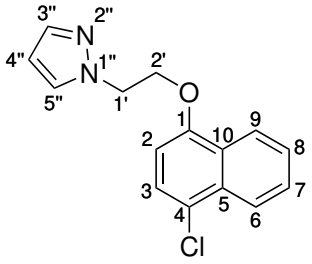

Following general procedure B, pyrazole (21.2 mg, 311 µmol) was reacted with NaOH (124 mg, 3.11 mmol) and **48** (75.0 mg, 311 µmol) in MeCN (1.5 ml). The crude compound was purified using silica gel flash chromatography (98:2 CH_2Cl_2/MeOH) to afford **68** as an off-white solid (62 mg, 73 %); **mp** 102–103 °C; ν_{max} (thin film) 1263 (C–O); **^{1}H NMR** (400 MHz, $CDCl_3$) δ 8.22 – 8.15 (2H, m, H_6 and H_9), 7.64 – 7.58 (2H, m, H_7 and $H_{5''}$), 7.54 – 7.49 (2H, m, H_8 and $H_{3''}$), 7.42 (1H, d, J = 8.2 Hz, H_3), 6.68 (1H, d, J = 8.2 Hz, H_2), 6.28 (1H, app t, J = 2.1 Hz, $H_{4''}$), 4.67 (2H, t, J = 5.2 Hz, $H_{1'}$), 4.50 (2H, t, J = 5.2 Hz, $H_{2'}$); **^{13}C NMR** (101 MHz, $CDCl_3$) δ 153.0 (C_1), 139.9 ($C_{3''}$), 131.4 (C_5), 130.2 ($C_{5''}$), 127.6 (C_7), 126.5 (C_{10}), 126.1 (C_8), 125.6 (C_3), 124.3 (C_6), 123.9 (C_4), 122.2 (C_9), 105.8 ($C_{4''}$), 105.0 (C_2), 67.1 ($C_{2'}$), 51.5 ($C_{1'}$); **LRMS (ESI +ve)** 275 [M(^{37}Cl)+H]$^+$, 273 [M(^{35}Cl)+H]$^+$; **HRMS (ESI +ve)** $C_{15}H_{13}N_2O^{35}Cl$ [M+H$^+$] *calc.* 273.0789, *found* 273.0789

1-(2-((4-Chloronaphthalen-1-yl)oxy)ethyl)-1*H*-1,2,4-triazole (69)

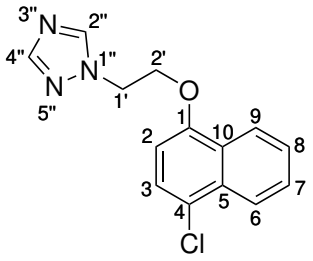

A mixture of 1,2,4-triazole (75.0 mg, 311 µmol) and NaOH (124 mg, 3.11 mmol) in MeCN (1.0 ml) was heated at reflux for 30 min. After cooling to rt, compound **48** (75.0 mg, 311 µmol) in MeCN (1.0 ml) was added and the mixture transferred to a sealed microwave vial. The mixture was then heated at 140 °C for 30 min under microwave radiation, cooled to rt, filtered, and concentrated *in vacuo*. The crude product was purified by silica gel column chromatography (3:97 MeOH/CH_2Cl_2) to afford **69** as a yellow-red solid (16 mg, 19 %); **mp** 134–136 °C; ν_{max} (thin film) 1263 (C–O); **^{1}H NMR** (500 MHz, $CDCl_3$) δ 8.30 (1H, s, $H_{2''}$), 8.20 (1H, dt, J = 8.5, 1.0 Hz, H_6), 8.09 (1H, dt, J = 8.4, 1.1 Hz, H_9), 7.98 (1H, s, $H_{4''}$), 7.62 (1H, ddd, J = 8.5, 6.8, 1.1 Hz, H_7), 7.53 (1H, ddd, J = 8.4, 6.8, 1.0 Hz, H_8), 7.43 (1H, d, J = 8.2 Hz, H_3), 6.70 (1H, d, J = 8.2 Hz, H_2), 4.72 (2H, t, J = 5.0 Hz, $H_{1'}$), 4.52 (2H, t, J = 5.0 Hz, $H_{2'}$); **^{13}C NMR** (125 MHz, $CDCl_3$) δ 152.8 (C_1), 152.5 ($C_{4''}$), 144.1 ($C_{2''}$), 131.5 (C_5), 127.9 (C_7), 126.6 (C_8), 126.5 (C_{10}), 125.6 (C_3), 124.6 (C_6), 124.5 (C_4), 122.0 (C_9), 105.1 (C_2), 66.2 ($C_{2'}$), 49.3 ($C_{1'}$); **LRMS (ESI +ve)** 276 [M(^{37}Cl)+H]$^+$, 274 [M(^{35}Cl)+H]$^+$; **HRMS (ESI +ve)** $C_{14}H_{12}N_3O^{35}Cl$ [M+H$^+$] *calc.* 274.0742, *found* 274.0742

4-(2-((4-Chloronaphthalen-1-yl)oxy)ethyl)pyridine (70)

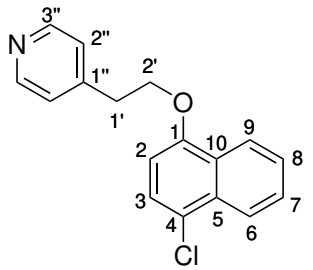

Following general procedure A, 4-(2-hydroxyethyl)pyridine (50 mg, 406 µmol) was reacted with 4-chloro-1-naphthol (109 mg, 609 µmol), diisopropyl azodicarboxylate (123 mg, 609 µmol),

and triphenylphosphine (160 µg, 609 µmol) in dry THF (2.2 ml). The crude product was purified using silica gel flash column chromatography (97:3 CH_2Cl_2/MeOH) to afford **70** as a pale yellow solid (67 mg, 58 %); **mp** 81–82 °C; ν_{max} (thin film) 1260 (C-O); **^{1}H NMR** (400 MHz, $CDCl_3$) δ 8.60 – 8.53 (2H, m, $H_{3''}$), 8.24 – 8.14 (2H, m, H_9 and H_6), 7.61 (1H, ddd, *J* = 8.3, 6.9, 1.3 Hz, H_7), 7.52 (1H, ddd, *J* = 8.3, 6.9, 1.2 Hz, H_8), 7.43 (1H, d, *J* = 8.2 Hz, H_3), 7.32 – 7.27 (2H, m, $H_{2''}$), 6.71 (1H, d, *J* = 8.2 Hz, H_2), 4.38 (2H, t, *J* = 6.4 Hz, $H_{2'}$), 3.24 (2H, t, *J* = 6.4 Hz, $H_{1'}$); **^{13}C NMR** (101 MHz, $CDCl_3$) δ 153.5 (C_1), 150.1 ($C_{3''}$), 147.5 ($C_{1''}$), 131.5 (C_5), 127.7 (C_7), 126.7 (C_{10}), 126.2 (C_8), 125.8 (C_3), 124.5 ($C_{2''}$), 124.4 (C_6), 123.7 (C_4), 122.4 (C_9), 104.8 (C_2), 67.8 ($C_{2'}$), 35.2 ($C_{1'}$); **LRMS (ESI +ve)** 286 [M(^{37}Cl)+H]$^+$, 284 [M(^{35}Cl)+H]$^+$; **HRMS (ESI +ve)** $C_{17}H_{14}NO^{35}Cl$ [M+H$^+$] *calc.* 284.0837, *found* 284.0837

3-(2-((4-Chloronaphthalen-1-yl)oxy)ethyl)pyridine (71)

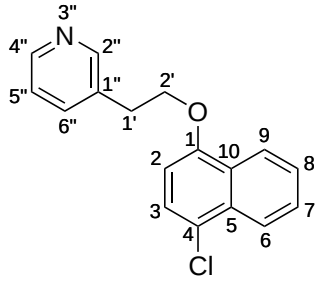

Following general procedure A, 3-(2-hydroxyethyl)pyridine (300 mg, 2.44 mmol) was reacted with 4-chloro-1-naphthol (653 mg, 3.65 mmol), diisopropyl azodicarboxylate (739 mg, 3.65 mmol), and triphenylphosphine (958 mg, 3.65 mmol) in dry THF (13 ml). The crude product was purified using silica gel flash column chromatography (98:2 CH_2Cl_2/MeOH) to afford **71** as a yellow solid (249 mg, 36 %); **mp** 63–65 °C; ν_{max} (thin film) 2360, 1374, 1263 (C – O); **^{1}H NMR** (500 MHz, $CDCl_3$) δ 8.65 (1H, d, *J* = 2.3 Hz, $H_{2''}$), 8.51 (1H, dd, *J* = 4.9, 1.7 Hz, $H_{4''}$), 8.22 (1H, d, *J* = 8.4 Hz, H_9), 8.19 (1H, d, *J* = 8.3 Hz, H_6), 7.69 (1H, app dt, *J* = 7.9, 2.0 Hz, $H_{6''}$), 7.61 (1H, ddd, *J* = 8.4, 6.8, 1.3 Hz, H_7), 7.53 (1H, ddd, *J* = 8.3, 6.8, 1.2 Hz, H_8), 7.43 (1H, d, *J* = 8.2 Hz, H_3), 7.28 – 7.25 (1H, m, $H_{5''}$), 6.71 (1H, d, *J* = 8.2 Hz, H_2), 4.35 (2H, t, *J* = 6.4 Hz, $H_{2'}$), 3.25 (2H, t, *J* = 6.4 Hz, $H_{1'}$); **^{13}C NMR** (125 MHz, $CDCl_3$) δ 153.6 (C_1), 150.1 ($C_{2''}$), 148.3 ($C_{4''}$), 136.6 ($C_{6''}$), 134.1 ($C_{1''}$), 131.5 (C_5), 127.7 (C_7), 126.7 (C_{10}), 126.2 (C_8), 125.8 (C_3), 124.4 (C_6), 123.7 (C_4), 123.6 ($C_{5''}$), 122.4 (C_9), 104.8 (C_2), 68.5 ($C_{2'}$), 33.3 ($C_{1'}$); **LRMS (ESI +ve)** 286 [M(^{37}Cl)+H]$^+$, 284 [M(^{35}Cl)+H]$^+$; **HRMS (ESI +ve)** $C_{17}H_{14}NO^{35}Cl$ [M+H$^+$] *calc.* 284.0837, *found* 284.0837

2-(2-((4-Chloronaphthalen-1-yl)oxy)ethyl)pyridine (72)

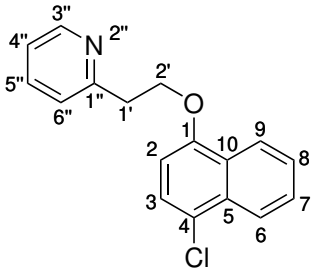

Following general procedure A, 2-(2-hydroxyethyl)pyridine (50.0 mg, 406 µmol) was reacted with 4-chloro-1-naphthol (109 mg, 609 µmol), diisopropyl azodicarboxylate (123 mg, 609 µmol), and triphenylphosphine (160 mg, 609 µmol) in dry THF (2.2 ml). The crude compound was purified using silica gel flash column chromatography (97:3 CH_2Cl_2/MeOH) to afford **72** as a yellow oil (77 mg, 67 %); ν_{max} (thin film) 1590, 1375, 1262 (C–O); **^{1}H NMR** (400 MHz, $CDCl_3$) δ 8.57 (1H, ddd, J = 4.9, 1.8, 1.0 Hz, $H_{3''}$), 8.27 – 8.10 (2H, m, H_6 and H_9), 7.65 (1H, app td, J = 7.8, 1.8 Hz, $H_{5''}$), 7.59 (1H, ddd, J = 8.2, 6.8, 1.4 Hz, H_7), 7.49 (1H, ddd, J = 8.3, 6.8, 1.3 Hz, H_8), 7.43 (1H, d, J = 8.2 Hz, H_3), 7.35 (1H, app dt, J = 7.8, 1.0 Hz, $H_{6''}$), 7.16 (1H, ddd, J = 7.8, 4.9, 1.0 Hz, $H_{4''}$), 6.77 (1H, d, J = 8.2 Hz, H_2), 4.53 (2H, t, J = 6.5 Hz, $H_{2'}$), 3.41 (2H, t, J = 6.5 Hz, $H_{1'}$); **^{13}C NMR** (101 MHz, $CDCl_3$) δ 158.6 ($C_{1''}$), 153.8 (C_1), 149.6 ($C_{3''}$), 136.6 ($C_{5''}$), 131.4 (C_5), 127.5 (C_7), 126.8 (C_{10}), 126.0 (C_8), 125.9 (C_3), 124.3 (C_6), 123.9 ($C_{6''}$), 123.3 (C_4), 122.5 (C_9), 121.8 ($C_{4''}$), 105.0 (C_2), 67.8 ($C_{2'}$), 38.2 ($C_{1'}$); **LRMS (ESI +ve)** 286 [M(^{37}Cl)+H]$^+$, 284 [M(^{35}Cl)+H]$^+$; **HRMS (ESI +ve)**$C_{17}H_{14}NO^{35}Cl$ [M+H$^+$] *calc.* 284.0837, *found* 284.0838

4-(2-((4-Chloronaphthalen-1-yl)oxy)ethyl)pyridine 1-oxide (73)

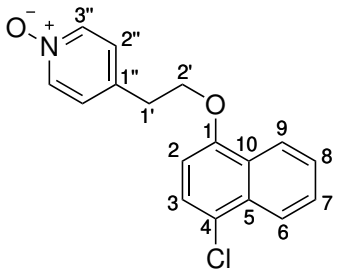

3-Chloroperbenzoic acid (274 mg, ≥ 50 % by weight, 793 µmol) was added to a solution of **70** (150.0 mg, 529 µmol) in $CHCl_3$ (3.0 ml) at 0 °C. The reaction was stirred at rt for 20 h. The mixture was diluted with CH_2Cl_2 (20 ml) and poured onto aq. sat. $NaHCO_3$ (50 ml). The organic

phase was separated and the aqueous phase extracted with CH_2Cl_2 (3 × 20 ml). The combined organic phases were washed with brine (30 ml), dried over $MgSO_4$, filtered, and evaporated *in vacuo*. The crude product was purified by silica gel column chromatography (90:10 EtOAc/MeOH) and then recrystalised from Et_2O to afford **73** as a white solid (14.0 mg, 9 %); **mp** 97–98 °C (Et_2O); ν_{max} (thin film) 1375 (N–O), 1263 (C–O); **^{1}H NMR** (500 MHz, $CDCl_3$) δ 8.20 (1H, d, J = 8.4 Hz, H_6), 8.19 – 8.16 (2H, m, $H_{3''}$), 8.12 (1H, d, J = 8.3 Hz, H_9), 7.62 (1H, ddd, J = 8.4, 6.9, 1.1 Hz, H_7), 7.52 (1H, ddd, J = 8.2, 6.9, 1.1 Hz, H_8), 7.44 (1H, d, J = 8.2 Hz, H_3), 7.29 – 7.26 (2H, m, $H_{2''}$), 6.72 (1H, d, J = 8.2 Hz, H_2), 4.37 (2H, t, J = 6.0 Hz, $H_{2'}$), 3.23 (2H, t, J = 6.0 Hz, $H_{1'}$).**^{13}C NMR** (125 MHz, $CDCl_3$) δ 153.2 (C_1), 139.2 ($C_{3''}$), 138.0 ($C_{1''}$), 131.5 (C_5), 127.8 (C_7), 126.7 ($C_{2''}$), 126.6 (C_{10}), 126.4 (C_8), 125.7 (C_3), 124.6 (C_6), 124.1 (C_4), 122.1 (C_9), 104.9 (C_2), 67.3 ($C_{2'}$), 34.3 ($C_{1'}$); **LRMS (ESI +ve)** 324 [M(^{37}Cl)+Na]$^+$, 322 [M(^{35}Cl)+Na]$^+$, 302 [M(^{37}Cl)+H]$^+$, 300 [M(^{35}Cl)+H]$^+$; **HRMS (ESI +ve)** $C_{17}H_{14}O_2N^{35}Cl$ [M+H$^+$] *calc.* 300.0786, *found* 300.0787

3-(2-((4-Chloronaphthalen-1-yl)oxy)ethyl)pyridine 1-oxide (74)

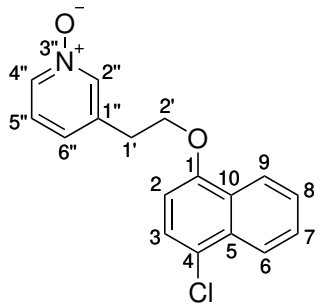

3-Chloroperbenzoic acid (365 mg, ≥ 50 % by weight, 1.06 mmol) was added to a solution of **71** (200.0 mg, 705 µmol) in $CHCl_3$ (4.0 ml) at 0 °C. The reaction was stirred at rt for 20 h. The mixture was diluted with CH_2Cl_2 (20 ml) and poured onto sat. $NaHCO_3$ (50 ml). The organic phase was separated and the aqueous phase extracted with CH_2Cl_2 (3×20 ml). The combined organic phases were washed with aq. NaOH (1 M, 3 × 30 ml), H_2O (30 ml, and brine (30 ml), dried over $MgSO_4$, filtered, and evaporated *in vacuo*. The crude product was purified by silica gel column chromatography (97:3 CH_2Cl_2/MeOH) and then further purified by hot filtration and recrystallisation from Et_2O to afford **74** as a white solid (26 mg, 12 %); **mp** 93–94 °C; ν_{max} (thin film)1375 (N–O), 1263 (C–O); **^{1}H NMR** (500 MHz, $CDCl_3$) δ 8.29 (1H, s, $H_{2''}$), 8.19 (1H,

dd, $J = 8.4, 1.0$ Hz, H_6), 8.18 – 8.15 (1H, m, H_9), 8.13 (1H, app dt, $J = 6.3, 1.5$ Hz, $H_{4''}$), 7.62 (1H, ddd, $J = 8.4, 6.8, 1.3$ Hz, H_7), 7.54 (1H, ddd $J = 8.2, 6.8, 1.2$ Hz, H_8), 7.43 (1H, d, $J = 8.2$ Hz, H_3), 7.31 – 7.28 (1H, m, $H_{6''}$), 7.24 (1H, dd, $J = 7.8, 6.3$ Hz, $H_{5''}$), 6.70 (1H, d, $J = 8.2$ Hz, H_2), 4.36 (2H, t, $J = 6.1$ Hz, $H_{2'}$), 3.21 (2H, t, $J = 6.1$ Hz, $H_{1'}$); **^{13}C NMR** (125 MHz, $CDCl_3$) δ 153.2 (C_1), 139.7 ($C_{2''}$), 138.1 ($C_{1''}$), 137.7 ($C_{4''}$), 131.5 (C_5), 127.8 (C_7), 126.9 ($C_{6''}$), 126.6 (C_{10}), 126.4 (C_8), 125.9 ($C_{5''}$), 125.7 (C_3), 124.5 (C_6), 124.1 (C_4), 122.2 (C_9), 104.8 (C_2), 67.5 ($C_{2'}$), 32.9 ($C_{1'}$); **LRMS (ESI +ve)** 324 [M(^{37}Cl)+Na]$^+$, 322 [M(^{35}Cl)+Na]$^+$, 302 [M(^{37}Cl)+H]$^+$, 300 [M(^{35}Cl)+H]$^+$; **HRMS (ESI +ve)** $C_{17}H_{14}O_2N^{35}Cl$ [M+H$^+$] *calc.* 300.0786, *found* 300.0786; Purity by **LC-MS** UV (280 nm): > 97%

2-(2-((4-Chloronaphthalen-1-yl)oxy)ethyl)pyridine 1-oxide (75)

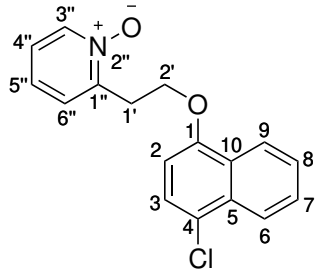

3-Chloroperbenzoic acid (274 mg, ≥ 50 % by weight, 793 µmol) was added to a solution of **72** (150.0 mg, 529 µmol) in $CHCl_3$ (3.0 ml) at 0 °C. The reaction was stirred at rt for 20 h. The mixture was diluted with CH_2Cl_2 (30 ml) and poured onto aq. sat. $NaHCO_3$ (30 ml). The organic phase was separated and the aqueous phase extracted with CH_2Cl_2 (2 × 30 ml). The combined organic phases were washed with aq. NaOH, (1 M, 3 × 40 ml), H_2O (40 ml), and brine (30 ml), dried over $MgSO_4$, filtered, and evaporated *in vacuo*. The crude product was purified by silica gel column chromatography (95:5 CH_2Cl_2/MeOH) and then further purified by silica gel column chromatography (96:4 EtOAc/MeOH) to afford **75** as an off-white solid (70.0 mg, 44 %); **mp** 59–61 °C; **ν_{max}** (thin film) 1375 (N – O), 1263 (C – O); **^{1}H NMR** (500 MHz, $CDCl_3$) δ 8.28 (1H, dd, $J = 6.3, 1.5$ Hz, $H_{3''}$), 8.18 (1H, app dt, $J = 8.4, 1.1$ Hz, H_6), 8.14 (1H, app dt, $J = 8.3, 1.1$ Hz, H_9), 7.59 (1H, ddd, $J = 8.4, 6.9, 1.1$ Hz, H_7), 7.49 (1H, ddd, $J = 8.3, 6.9, 1.1$ Hz, H_8), 7.45 – 7.41 (2H, m, H_3 and $H_{6''}$), 7.23 (1H, app td, $J = 7.7, 1.5$ Hz, $H_{5''}$), 7.19 (1H, ddd, $J = 7.7, 6.3, 2.3$ Hz, $H_{4''}$), 6.79 (1H, d, $J = 8.3$ Hz, H_2), 4.57 (2H, t, $J = 5.9$ Hz, $H_{2'}$), 3.55 (2H, t, $J = 5.9$ Hz, $H_{1'}$); **^{13}C NMR** (125 MHz, $CDCl_3$) δ 153.4 (C_1), 149.1 ($C_{1''}$), 139.8 ($C_{3''}$), 131.4 (C_5),

127.5 (C_7), 127.2 ($C_{6''}$), 126.6 (C_{10}), 126.0 (C_3), 125.9 (C_8), 125.8 ($C_{5''}$), 124.44 ($C_{4''}$), 124.42 (C_6), 123.5 (C_4), 122.3 (C_9), 105.0 (C_2), 64.2 ($C_{2'}$), 31.5 ($C_{1'}$); Purity by **LC-MS** UV (280 nm): > 97%; **LRMS (ESI +ve)** 324 [M(^{37}Cl)+Na]$^+$, 322 [M(^{35}Cl)+Na]$^+$, 302 [M(^{37}Cl)+H]$^+$, 300 [M(^{35}Cl)+H]$^+$; **HRMS (ESI +ve)** $C_{17}H_{14}O_2N^{35}Cl$ [M+H$^+$] *calc.* 300.0786, *found* 300.0787

3-(2-((4-Nitronaphthalen-1-yl)oxy)ethyl)pyridine (76)

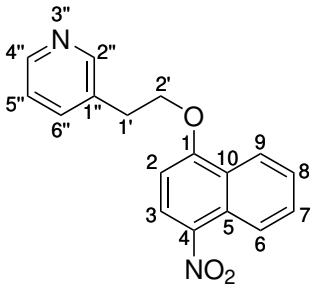

Following general procedure A, 3-(2-hydroxyethyl)pyridine (150 mg, 1.22 mmol) was reacted with 4-nitro-1-naphthol (346 mg, 1.83 mmol), diisopropyl azodicarboxylate (369 mg, 1.83 mmol), and triphenylphosphine (479 mg, 1.83 mmol) in dry THF (6.6 ml). The crude product was purified using silica gel flash column chromatography (gradient elution 1% → 3% MeOH in CH_2Cl_2) followed by trituration in Et_2O to afford **76** as a brown solid (179 mg, 50 %); **mp** 93–94 °C; ν_{max} (thin film) 1505 (N–O), 1317 (N–O), 1267 (C–O); **^{1}H NMR** (500 MHz, $CDCl_3$) δ 8.75 (1H, dt, J = 8.6, 0.9 Hz, H_6), 8.67 (1H, d, J = 2.0 Hz, $H_{2''}$), 8.53 (1H, dd, J = 4.9, 1.7 Hz, $H_{4''}$), 8.36 (1H, d, J = 8.7 Hz, H_2), 8.32 – 8.28 (1H, m, H_9), 7.73 (1H, ddd, J = 8.6, 6.9, 1.4 Hz, H_7), 7.69 (1H, app td, J = 7.8, 2.0 Hz, $H_{6''}$), 7.59 (1H, ddd, J = 8.2, 6.9, 1.1 Hz, H_8), 7.29 (1H, ddd, J = 7.8, 4.9, 0.9 Hz, $H_{5''}$), 6.79 (1H, d, J = 8.7 Hz, H_2), 4.47 (2H, t, J = 6.4 Hz, $H_{2'}$), 3.30 (2H, t, J = 6.4 Hz, $H_{1'}$); **^{13}C NMR** (125 MHz, $CDCl_3$) δ 159.5 (C_1), 150.5 ($C_{2''}$), 148.5 ($C_{4''}$), 139.6 (C_4), 136.5 ($C_{6''}$), 133.4 ($C_{1''}$), 130.3 (C_7), 127.1 (C_3), 127.0 (C_5), 126.9 (C_8), 125.7 (C_{10}), 123.7 ($C_{5''}$), 123.6 (C_6), 122.7 (C_9), 102.7 (C_2), 69.1 ($C_{2'}$), 33.0 ($C_{1'}$); **LRMS (ESI +ve)** 295 [M+H]$^+$; **HRMS (ESI +ve)** $C_{17}H_{14}N_2O_3$ [M+H$^+$] *calc.* 295.1083, *found* 295.1077

2-(2-((4-Nitronaphthalen-1-yl)oxy)ethyl)pyridine (77)

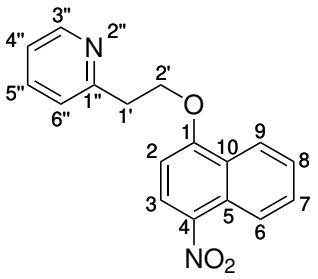

Following general procedure A, 2-(2-hydroxyethyl)pyridine (150 mg, 1.22 mmol) was reacted with 4-nitro-1-naphthol (346 mg, 1.83 mmol), diisopropyl azodicarboxylate (369 mg, 1.83 mmol), and triphenylphosphine (479 mg, 1.83 mmol) in dry THF (6.6 ml). The crude product was purified using silica gel flash column chromatography (gradient elution 1% → 3% MeOH in CH_2Cl_2) to afford **77** as a green solid (253 mg, 71 %); **mp** 103–104 °C; $\nu_{\mathbf{max}}$ (thin film) 1505 (N–O), 1317 (N–O), 1268 (C–O); **^{1}H NMR** (500 MHz, $CDCl_3$) δ 8.75 (1H, d, J = 7.8 Hz, H_6), 8.58 (1H, d, J = 4.6 Hz, $H_{3''}$), 8.37 (1H, d, J = 8.7 Hz, H_3), 8.27 (1H, d, J = 8.3 Hz, H_9), 7.71 (1H, ddd, J = 8.7, 6.9, 1.4 Hz, H_7), 7.67 (1H, app td J = 7.7, 1.9 Hz, $H_{5''}$), 7.54 (1H, ddd, J = 8.3, 6.9, 1.2 Hz, H_8), 7.34 (1H, d, J = 7.7 Hz, $H_{6''}$), 7.18 (1H, dd, J = 7.7, 4.6 Hz, $H_{4''}$), 6.85 (1H, d, J = 8.7 Hz, H_2), 4.67 (2H, t, J = 6.5 Hz, $H_{2'}$), 3.45 (2H, J = 6.5 Hz, $H_{1'}$); **^{13}C NMR** (125 MHz, $CDCl_3$) δ 159.9 (C_1), 157.9 ($C_{1''}$), 149.8 ($C_{3''}$), 139.3 (C_4), 136.7 ($C_{5''}$), 130.1 (C_7), 127.4 (C_3), 127.0 (C_5), 126.6 (C_8), 125.7 (C_{10}), 123.9($C_{6''}$), 123.6 (C_6), 122.8 (C_9), 122.0 ($C_{4''}$), 102.9 (C_2), 68.4 ($C_{2'}$), 37.8 ($C_{1'}$); **LRMS (ESI +ve)** 295 $[M+H]^+$; **HRMS (ESI +ve)** $C_{17}H_{14}N_2O_3$ $[M+H^+]$ *calc.* 295.1083, *found* 295.1077

3-(2-((4-Nitronaphthalen-1-yl)oxy)ethyl)pyridine 1-oxide (78)

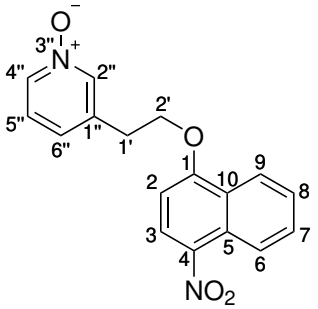

A mixture of **76** (75 mg, 254 µmol), aq. H_2O_2 (30 % (w/w), 208 µl, 204 mmol), and AcOH (44 µl, 765 µmol) was heated at 50 °C for 24 h. After cooling to rt, aq. NaOH (1 M, 5 ml) was added

and the mixture extracted with EtOAc (4 × 10 ml). The combined organic phases were washed with brine, dried over $MgSO_4$, filtered, and concentrated *in vacuo*. The crude product was purified by silica gel column chromatography (gradient elution 1% → 5% MeOH in CH_2Cl_2) to afford **78** as a yellow solid (38 mg, 48 %); **mp** 139–140 °C; ν_{max} (thin film) 1511 (N–O), 1320 (N–O), 1269 (C–O); **^{1}H NMR** (500 MHz, $CDCl_3$) δ 8.74 (1H, d, J = 8.6 Hz, H_6), 8.35 (1H, d, J = 8.7 Hz, H_3), 8.30 (1H, s, $H_{2''}$), 8.24 (1H, d, J = 8.3 Hz, H_9), 8.14 (1H, app dt, J = 6.1, 1.6 Hz, $H_{4''}$), 7.73 (1H, ddd, J = 8.6, 6.9, 1.4 Hz, H_7), 7.60 (1H, ddd, J = 8.3, 6.9, 1.2 Hz, H_8), 7.32 – 7.23 (2H, m, $H_{5''}$ and $H_{6''}$), 6.79 (1H, d, J = 8.7 Hz, H_2), 4.48 (2H, t, J = 6.1 Hz, $H_{2'}$), 3.26 (2H, t, J = 6.1 Hz, $H_{1'}$); **^{13}C NMR** (125 MHz, $CDCl_3$) δ 159.1 (C_1), 139.9 (C_4), 139.6 ($C_{2''}$), 137.9 ($C_{4''}$), 137.5 ($C_{1''}$), 130.3 (C_7), 127.1 (C_8), 127.0 (C_5), 126.9 (C_3), 126.7 ($C_{6''}$), 126.0 ($C_{5''}$), 125.6 (C_{10}), 123.7 (C_6), 122.5 (C_9), 102.7 (C_2), 68.1 ($C_{2'}$), 32.6 ($C_{1'}$); **LRMS (ESI +ve)** 333 $[M+Na]^+$, 311 $[M+H]^+$; **HRMS (ESI +ve)** $C_{17}H_{14}N_2O_4$ $[M+H^+]$ *calc.* 311.1032, *found* 311.1026

Bibliography

(1) Lagerström, M. C.; Schiöth, H. B. Structural diversity of G protein-coupled receptors and significance for drug discovery. *Nature Reviews Drug Discovery* **2008**, *7*, 339–357.

(2) Huang, Y.; Thathiah, A. Regulation of neuronal communication by G protein-coupled receptors. *FEBS Letters* **2015**, *589*, 1607–1619.

(3) Wang, J.; Gareri, C.; Rockman, H. A. G-Protein–Coupled Receptors in Heart Disease. *Circulation Research* **2018**, *123*, 716–735.

(4) Hauser, A. S. et al. Trends in GPCR drug discovery: new agents, targets and indications. *Nature Reviews Drug Discovery* **2017**, *16*, 829–842.

(5) Sriram, K.; Insel, P. A. G Protein-Coupled Receptors as Targets for Approved Drugs: How Many Targets and How Many Drugs? *Molecular pharmacology* **2018**, *93*, 251–258.

(6) Smith, J. S.; Lefkowitz, R. J.; Rajagopal, S. Biased signalling: from simple switches to allosteric microprocessors. *Nature Reviews Drug Discovery* **2018**, *17*, 243–260.

(7) Santos, R. et al. A comprehensive map of molecular drug targets. *Nature Reviews Drug Discovery* **2017**, *16*, 19–34.

(8) Walker, M. J. The major impacts of James Black's drug discoveries on medicine and pharmacology. *Trends in Pharmacological Sciences* **2011**, *32*, 183–188.

(9) Oprea, T. I. et al. Unexplored therapeutic opportunities in the human genome. *Nature Reviews Drug Discovery* **2018**, *17*, 317–332.

(10) Hilger, D.; Masureel, M.; Kobilka, B. K. Structure and dynamics of GPCR signaling complexes. *Nature Structural & Molecular Biology* **2018**, *25*, 4–12.

(11) Fredriksson, R. et al. The G-protein-coupled receptors in the human genome form five main families. Phylogenetic analysis, paralogon groups, and fingerprints. *Molecular Pharmacology* **2003**, *63*, 1256–1272.

(12) Hollenstein, K. et al. Insights into the structure of class B GPCRs. *Trends in pharmacological sciences* **2014**, *35*, 12–22.

(13) Chun, L.; Zhang, W.-h.; Liu, J.-f. Structure and ligand recognition of class C GPCRs. *Acta Pharmacologica Sinica* **2012**, *33*, 312–323.

(14) Cherezov, V. et al. High-resolution crystal structure of an engineered human beta2-adrenergic G protein-coupled receptor. *Science (New York, N.Y.)* **2007**, *318*, 1258–65.

(15) Rasmussen, S. G. F. et al. Crystal structure of the human β2 adrenergic G-protein-coupled receptor. *Nature* **2007**, *450*, 383–387.

(16) Pándy-Szekeres, G. et al. GPCRdb in 2018: adding GPCR structure models and ligands. *Nucleic Acids Research* **2018**, *46*, D440–D446.

(17) Venkatakrishnan, A. J. et al. Molecular signatures of G-protein-coupled receptors. *Nature* **2013**, *494*, 185–194.

(18) White, J. F. et al. Structure of the agonist-bound neurotensin receptor. *Nature* **2012**, *490*, 508–513.

(19) Erlandson, S. C.; McMahon, C.; Kruse, A. C. Structural Basis for G Protein–Coupled Receptor Signaling. *Annual Review of Biophysics* **2018**, *47*, 1–18.

(20) Audet, M.; Stevens, R. C. Emerging structural biology of lipid G protein-coupled receptors. *Protein Science* **2019**, *28*, 292–304.

(21) Hanson, M. A. et al. Crystal structure of a lipid G protein-coupled receptor. *Science (New York, N.Y.)* **2012**, *335*, 851–5.

(22) Zheng, Y. et al. Structure of CC chemokine receptor 2 with orthosteric and allosteric antagonists. *Nature* **2016**, *540*, 458–461.

(23) Ericksen, S. S. et al. Ligand selectivity of D2 dopamine receptors is modulated by changes in local dynamics produced by sodium binding. *The Journal of pharmacology and experimental therapeutics* **2009**, *328*, 40–54.

(24) Moo, E. V. et al. Utility of an "Allosteric Site-Impaired" M2 Muscarinic Acetylcholine Receptor as a Novel Construct for Validating Mechanisms of Action of Synthetic and Putative Endogenous Allosteric Modulators. *Molecular pharmacology* **2018**, *94*, 1298–1309.

(25) Kruse, A. C. et al. Activation and allosteric modulation of a muscarinic acetylcholine receptor. *Nature* **2013**, *504*, 101–106.

(26) Van der Westhuizen, E. T. et al. Endogenous allosteric modulators of G protein-coupled receptors. *The Journal of pharmacology and experimental therapeutics* **2015**, *353*, 246–60.

(27) Burger, W. A. C. et al. Toward an understanding of the structural basis of allostery in muscarinic acetylcholine receptors. *The Journal of general physiology* **2018**, *150*, 1360–1372.

(28) Rasmussen, S. G. F. et al. Crystal structure of the β2 adrenergic receptor–Gs protein complex. *Nature* **2011**, *477*, 549–555.

(29) Latorraca, N. R.; Venkatakrishnan, A. J.; Dror, R. O. GPCR Dynamics: Structures in Motion. *Chemical Reviews* **2017**, *117*, 139–155.

(30) Wettschureck, N.; Offermanns, S. Mammalian G Proteins and Their Cell Type Specific Functions. *Physiological Reviews* **2005**, *85*, 1159–1204.

(31) Cabrera-Vera, T. M. et al. Insights into G Protein Structure, Function, and Regulation. *Endocrine Reviews* **2003**, *24*, 765–781.

(32) Simonds, W. F. G protein regulation of adenylate cyclase. *Trends in Pharmacological Sciences* **1999**, *20*, 66–73.

(33) Hubbard, K. B.; Hepler, J. R. Cell signalling diversity of the Gqα family of heterotrimeric G proteins. *Cellular Signalling* **2006**, *18*, 135–150.

(34) Suzuki, N.; Hajicek, N.; Kozasa, T. Regulation and physiological functions of G12/13-mediated signaling pathways. *Neuro-Signals* **2009**, *17*, 55–70.

(35) Brandt, D. R.; Ross, E. M. GTPase activity of the stimulatory GTP-binding regulatory protein of adenylate cyclase, Gs. Accumulation and turnover of enzyme-nucleotide intermediates. *The Journal of biological chemistry* **1985**, *260*, 266–72.

(36) Logothetis, D. E. et al. The βγ subunits of GTP-binding proteins activate the muscarinic K+ channel in heart. *Nature* **1987**, *325*, 321–326.

(37) Waard, M. D. et al. Direct binding of G-protein βλ complex to voltage-dependent calcium channels. *Nature* **1997**, *385*, 446–450.

(38) Tang, W. et al. Type-specific regulation of adenylyl cyclase by G protein beta gamma subunits. *Science* **1991**, *254*, 1500–1503.

(39) Crespo, P. et al. Ras-dependent activation of MAP kinase pathway mediated by G-protein βγ subunits. *Nature* **1994**, *369*, 418–420.

(40) Stephens, L. et al. A novel phosphoinositide 3 kinase activity in myeloid-derived cells is activated by G protein beta gamma subunits. *Cell* **1994**, *77*, 83–93.

(41) Khan, S. M. et al. The Expanding Roles of G βγ Subunits in G Protein–Coupled Receptor Signaling and Drug Action. *Pharmacological Reviews* **2013**, *65*, 545–577.

(42) Gulati, S. et al. Targeting G protein-coupled receptor signaling at the G protein level with a selective nanobody inhibitor. *Nature Communications* **2018**, *9*, 1996.

(43) Gainetdinov, R. R. et al. Desensitization of G protein-coupled receptors and neuronal functions. *Annual Review of Neuroscience* **2004**, *27*, 107–144.

(44) Hanyaloglu, A. C.; von Zastrow, M. Regulation of GPCRs by Endocytic Membrane Trafficking and Its Potential Implications. *Annual Review of Pharmacology and Toxicology* **2008**, *48*, 537–568.

(45) Lee, K. B. et al. Arrestin-independent internalization of the m1, m3, and m4 subtypes of muscarinic cholinergic receptors. *The Journal of biological chemistry* **1998**, *273*, 12967–72.

(46) Goodman, O. B. et al. β-Arrestin acts as a clathrin adaptor in endocytosis of the β2-adrenergic receptor. *Nature* **1996**, *383*, 447–450.

(47) Luttrell, L. M. et al. Beta-arrestin-dependent formation of beta2 adrenergic receptor-Src protein kinase complexes. *Science (New York, N.Y.)* **1999**, *283*, 655–61.

(48) Gao, H. et al. Identification of β-Arrestin2 as a G Protein-Coupled Receptor-Stimulated Regulator of NF-κB Pathways. *Molecular Cell* **2004**, *14*, 303–317.

(49) Shenoy, S. K. et al. beta-arrestin-dependent, G protein-independent ERK1/2 activation by the beta2 adrenergic receptor. *The Journal of biological chemistry* **2006**, *281*, 1261–73.

(50) Beaulieu, J.-M. et al. An Akt/beta-arrestin 2/PP2A signaling complex mediates dopaminergic neurotransmission and behavior. *Cell* **2005**, *122*, 261–73.

(51) Grundmann, M. et al. Lack of beta-arrestin signaling in the absence of active G proteins. *Nature Communications* **2018**, *9*, 341.

(52) Rajagopal, S.; Rajagopal, K.; Lefkowitz, R. J. Teaching old receptors new tricks: biasing seven-transmembrane receptors. *Nature Reviews Drug Discovery* **2010**, *9*, 373–386.

(53) Leach, K.; Charlton, S.; Strange, P. Analysis of second messenger pathways stimulated by different chemokines acting at the chemokine receptor CCR5. *Biochemical Pharmacology* **2007**, *74*, 881–890.

(54) Rajagopal, S. et al. Biased agonism as a mechanism for differential signaling by chemokine receptors. *The Journal of biological chemistry* **2013**, *288*, 35039–48.

(55) Kenakin, T.; Christopoulos, A. Signalling bias in new drug discovery: detection, quantification and therapeutic impact. *Nature Reviews Drug Discovery* **2013**, *12*, 205–216.

(56) Rajagopal, S. et al. Quantifying Ligand Bias at Seven-Transmembrane Receptors. *Molecular Pharmacology* **2011**, *80*, 367.

(57) Urs, N. M. et al. Distinct cortical and striatal actions of a β-arrestin–biased dopamine D2 receptor ligand reveal unique antipsychotic-like properties. *Proceedings of the National Academy of Sciences* **2016**, *113*, E8178–E8186.

(58) Siuda, E. R. et al. Biased mu-opioid receptor ligands: a promising new generation of pain therapeutics. *Current Opinion in Pharmacology* **2017**, *32*, 77–84.

(59) Seth, P. et al. Overdose deaths involving opioids, cocaine, and psychostimulants - United States, 2015-2016. *American Journal of Transplantation* **2018**, *18*, 1556–1568.

(60) Matthes, H. W. D. et al. Loss of morphine-induced analgesia, reward effect and withdrawal symptoms in mice lacking the μ-opioid-receptor gene. *Nature* **1996**, *383*, 819–823.

(61) Bohn, L. M. et al. Enhanced morphine analgesia in mice lacking beta-arrestin 2. *Science (New York, N.Y.)* **1999**, *286*, 2495–8.

(62) Bohn, L. M. et al. μ-Opioid receptor desensitization by β-arrestin-2 determines morphine tolerance but not dependence. *Nature* **2000**, *408*, 720–723.

(63) Chen, X.-T. et al. Structure–Activity Relationships and Discovery of a G Protein Biased μ Opioid Receptor Ligand, [(3-Methoxythiophen-2-yl)methyl](2-[(9R)-9-(pyridin-2-yl)-6-oxaspiro-[4.5]decan-9-yl]ethyl)amine (TRV130), for the Treatment of Acute Severe Pain. *Journal of Medicinal Chemistry* **2013**, *56*, 8019–8031.

(64) Manglik, A. et al. Structure-based discovery of opioid analgesics with reduced side effects. *Nature* **2016**, *537*, 185–190.

(65) Schmid, C. L. et al. Bias Factor and Therapeutic Window Correlate to Predict Safer Opioid Analgesics. *Cell* **2017**, *171*, 1165–1175.e13.

(66) Soergel, D. G. et al. Biased agonism of the μ-opioid receptor by TRV130 increases analgesia and reduces on-target adverse effects versus morphine: A randomized, double-blind, placebo-controlled, crossover study in healthy volunteers. *PAIN* **2014**, *155*, 1829–1835.

(67) Viscusi, E. R. et al. A randomized, phase 2 study investigating TRV130, a biased ligand of the μ-opioid receptor, for the intravenous treatment of acute pain. *PAIN* **2016**, *157*, 264–272.

(68) Singla, N. et al. A randomized, Phase IIb study investigating oliceridine (TRV130), a novel μ-receptor G-protein pathway selective (μ-GPS) modulator, for the management of moderate to severe acute pain following abdominoplasty. *Journal of Pain Research* **2017**, *Volume 10*, 2413–2424.

(69) Hill, R. et al. The novel μ-opioid receptor agonist PZM21 depresses respiration and induces tolerance to antinociception. *British Journal of Pharmacology* **2018**, *175*, 2653–2661.

(70) Altarifi, A. A. et al. Effects of acute and repeated treatment with the biased mu opioid receptor agonist TRV130 (oliceridine) on measures of antinociception, gastrointestinal function, and abuse liability in rodents. *Journal of Psychopharmacology* **2017**, *31*, 730–739.

(71) Negus, S. S.; Freeman, K. B. Abuse Potential of Biased Mu Opioid Receptor Agonists. *Trends in pharmacological sciences* **2018**, *39*, 916–919.

(72) Milligan, G. et al. Complex Pharmacology of Free Fatty Acid Receptors. *Chemical Reviews* **2017**, *117*, 67–110.

(73) Civelli, O. et al. G Protein–Coupled Receptor Deorphanizations. *Annual Review of Pharmacology and Toxicology* **2013**, *53*, 127–146.

(74) He, W. et al. Citric acid cycle intermediates as ligands for orphan G-protein-coupled receptors. *Nature* **2004**, *429*, 188–193.

(75) Rubic, T. et al. Triggering the succinate receptor GPR91 on dendritic cells enhances immunity. *Nature Immunology* **2008**, *9*, 1261–1269.

(76) Littlewood-Evans, A. et al. GPR91 senses extracellular succinate released from inflammatory macrophages and exacerbates rheumatoid arthritis. *The Journal of experimental medicine* **2016**, *213*, 1655–62.

(77) Kotarsky, K. et al. A human cell surface receptor activated by free fatty acids and thiazolidinedione drugs. *Biochemical and Biophysical Research Communications* **2003**, *301*, 406–410.

(78) Itoh, Y. et al. Free fatty acids regulate insulin secretion from pancreatic β cells through GPR40. *Nature* **2003**, *422*, 173–176.

(79) Briscoe, C. P. et al. The orphan G protein-coupled receptor GPR40 is activated by medium and long chain fatty acids. *The Journal of biological chemistry* **2003**, *278*, 11303–11.

(80) Brown, A. J. et al. The Orphan G protein-coupled receptors GPR41 and GPR43 are activated by propionate and other short chain carboxylic acids. *The Journal of biological chemistry* **2003**, *278*, 11312–9.

(81) Hirasawa, A. et al. Free fatty acids regulate gut incretin glucagon-like peptide-1 secretion through GPR120. *Nature Medicine* **2005**, *11*, 90–94.

(82) Wang, J. et al. Medium-chain fatty acids as ligands for orphan G protein-coupled receptor GPR84. *The Journal of biological chemistry* **2006**, *281*, 34457–64.

(83) Alvarez-Curto, E.; Milligan, G. Metabolism meets immunity: The role of free fatty acid receptors in the immune system. *Biochemical Pharmacology* **2016**, *114*, 3–13.

(84) Recio, C. et al. The Role of Metabolite-Sensing G Protein-Coupled Receptors in Inflammation and Metabolic Disease. *Antioxidants & Redox Signaling* **2018**, *29*, 237–256.

(85) Ulven, T.; Christiansen, E. Dietary Fatty Acids and Their Potential for Controlling Metabolic Diseases Through Activation of FFA4/GPR120. *Annual Review of Nutrition* **2015**, *35*, 239–263.

(86) Sills, M. A.; Forsythe, W. I.; Haidukewych, D. Role of octanoic and decanoic acids in the control of seizures. *Archives of Disease in Childhood* **1986**, *61*, 1173–1177.

(87) Papamandjaris, A. A.; Macdougall, D. E.; Jones, P. J. Medium chain fatty acid metabolism and energy expenditure: Obesity treatment implications. *Life Sciences* **1998**, *62*, 1203–1215.

(88) Kuehl, F. A.; Egan, R. W. Prostaglandins, arachidonic acid, and inflammation. *Science (New York, N.Y.)* **1980**, *210*, 978–84.

(89) Serhan, C. N.; Levy, B. D. Resolvins in inflammation: emergence of the pro-resolving superfamily of mediators. *Journal of Clinical Investigation* **2018**, *128*, 2657–2669.

(90) Ferré, P. The biology of peroxisome proliferator-activated receptors: relationship with lipid metabolism and insulin sensitivity. *Diabetes* **2004**, *53 Suppl 1*, S43–50.

(91) Christiansen, E. et al. Activity of dietary fatty acids on FFA1 and FFA4 and characterisation of pinolenic acid as a dual FFA1/FFA4 agonist with potential effect against metabolic diseases. *British Journal of Nutrition* **2015**, *113*, 1677–1688.

(92) Bergman, E. N. Energy contributions of volatile fatty acids from the gastrointestinal tract in various species. *Physiological reviews* **1990**, *70*, 567–90.

(93) Waldecker, M. et al. Inhibition of histone-deacetylase activity by short-chain fatty acids and some polyphenol metabolites formed in the colon. *The Journal of Nutritional Biochemistry* **2008**, *19*, 587–593.

(94) Tsujihata, Y. et al. TAK-875, an Orally Available G Protein-Coupled Receptor 40/Free Fatty Acid Receptor 1 Agonist, Enhances Glucose-Dependent Insulin Secretion and Improves Both Postprandial and Fasting Hyperglycemia in Type 2 Diabetic Rats. *Journal of Pharmacology and Experimental Therapeutics* **2011**, *339*, 228–237.

(95) Burant, C. F. et al. TAK-875 versus placebo or glimepiride in type 2 diabetes mellitus: a phase 2, randomised, double-blind, placebo-controlled trial. *Lancet (London, England)* **2012**, *379*, 1403–11.

(96) Li, X. et al. Fasiglifam (TAK-875) Inhibits Hepatobiliary Transporters: A Possible Factor Contributing to Fasiglifam-Induced Liver Injury. *Drug Metabolism and Disposition* **2015**, *43*, 1751–1759.

(97) Otieno, M. A. et al. Fasiglifam (TAK-875): Mechanistic Investigation and Retrospective Identification of Hazards for Drug Induced Liver Injury. *Toxicological Sciences* **2018**, *163*, 374–384.

(98) Lin, D. C.-H. et al. Identification and Pharmacological Characterization of Multiple Allosteric Binding Sites on the Free Fatty Acid 1 Receptor. *Molecular Pharmacology* **2012**, *82*, 843–859.

(99) Yabuki, C. et al. A Novel Antidiabetic Drug, Fasiglifam/TAK-875, Acts as an Ago-Allosteric Modulator of FFAR1. *PLoS ONE* **2013**, *8*, e76280.

(100) Luo, J. et al. A Potent Class of GPR40 Full Agonists Engages the EnteroInsular Axis to Promote Glucose Control in Rodents. *PLoS ONE* **2012**, *7*, e46300.

(101) Hauge, M. et al. GPR40 (FFAR1) - Combined Gs and Gq signaling in vitro is associated with robust incretin secretagogue action ex vivo and in vivo. *Molecular metabolism* **2015**, *4*, 3–14.

(102) Srivastava, A. et al. High-resolution structure of the human GPR40 receptor bound to allosteric agonist TAK-875. *Nature* **2014**, *513*, 124–127.

(103) Lu, J. et al. Structural basis for the cooperative allosteric activation of the free fatty acid receptor GPR40. *Nature Structural & Molecular Biology* **2017**, *24*, 570–577.

(104) Ho, J. D. et al. Structural basis for GPR40 allosteric agonism and incretin stimulation. *Nature Communications* **2018**, *9*, 1645.

(105) Hudson, B. D. et al. Defining the molecular basis for the first potent and selective orthosteric agonists of the FFA2 free fatty acid receptor. *The Journal of biological chemistry* **2013**, *288*, 17296–312.

(106) Lee, T. et al. Identification and functional characterization of allosteric agonists for the G protein-coupled receptor FFA2. *Molecular pharmacology* **2008**, *74*, 1599–609.

(107) Hudson, B. D. et al. Complex Pharmacology of Novel Allosteric Free Fatty Acid 3 Receptor Ligands. *Molecular Pharmacology* **2014**, *86*, 200–210.

(108) Gentile, C. L.; Weir, T. L. The gut microbiota at the intersection of diet and human health. *Science (New York, N.Y.)* **2018**, *362*, 776–780.

(109) Maslowski, K. M. et al. Regulation of inflammatory responses by gut microbiota and chemoattractant receptor GPR43. *Nature* **2009**, *461*, 1282–1286.

(110) Macia, L. et al. Metabolite-sensing receptors GPR43 and GPR109A facilitate dietary fibre-induced gut homeostasis through regulation of the inflammasome. *Nature Communications* **2015**, *6*, 6734.

(111) Smith, P. M. et al. The microbial metabolites, short-chain fatty acids, regulate colonic Treg cell homeostasis. *Science (New York, N.Y.)* **2013**, *341*, 569–73.

(112) Ang, Z. et al. FFAR2-FFAR3 receptor heteromerization modulates short-chain fatty acid sensing. *The FASEB Journal* **2018**, *32*, 289–303.

(113) Shimpukade, B. et al. Discovery of a Potent and Selective GPR120 Agonist. *Journal of Medicinal Chemistry* **2012**, *55*, 4511–4515.

(114) Hudson, B. D. et al. The pharmacology of TUG-891, a potent and selective agonist of the free fatty acid receptor 4 (FFA4/GPR120), demonstrates both potential opportunity and possible challenges to therapeutic agonism. *Molecular pharmacology* **2013**, *84*, 710–25.

(115) Oh, D. Y. et al. A Gpr120-selective agonist improves insulin resistance and chronic inflammation in obese mice. *Nature Medicine* **2014**, *20*, 942–947.

(116) Ichimura, A. et al. Dysfunction of lipid sensor GPR120 leads to obesity in both mouse and human. *Nature* **2012**, *483*, 350–354.

(117) Oh, D. Y. et al. GPR120 Is an Omega-3 Fatty Acid Receptor Mediating Potent Anti-inflammatory and Insulin-Sensitizing Effects. *Cell* **2010**, *142*, 687–698.

(118) Bonnefond, A. et al. Contribution of the low-frequency, loss-of-function p.R270H mutation in FFAR4 (GPR120) to increased fasting plasma glucose levels. *Journal of medical genetics* **2015**, *52*, 595–8.

(119) Vestmar, M. A. et al. Functional and genetic epidemiological characterisation of the FFAR4 (GPR120) p.R270H variant in the Danish population. *Journal of medical genetics* **2016**, *53*, 616–23.

(120) Engelstoft, M. S. et al. Seven transmembrane G protein-coupled receptor repertoire of gastric ghrelin cells. *Molecular Metabolism* **2013**, *2*, 376–392.

(121) Wittenberger, T.; Schaller, H.; Hellebrand, S. An expressed sequence tag (EST) data mining strategy succeeding in the discovery of new G-protein coupled receptors. *Journal of Molecular Biology* **2001**, *307*, 799–813.

(122) Yousefi, S. et al. Cloning and expression analysis of a novel G-protein-coupled receptor selectively expressed on granulocytes. *Journal of Leukocyte Biology* **2001**, *69*, 1045–1052.

(123) Nagasaki, H. et al. Inflammatory changes in adipose tissue enhance expression of GPR84, a medium-chain fatty acid receptor: TNFα enhances GPR84 expression in adipocytes. *FEBS Letters* **2012**, *586*, 368–372.

(124) Abdel-Aziz, H. et al. GPR84 and TREM-1 Signaling Contribute to the Pathogenesis of Reflux Esophagitis. *Molecular Medicine* **2015**, *21*, 1011–1024.

(125) Recio, C. et al. Activation of the Immune-Metabolic Receptor GPR84 Enhances Inflammation and Phagocytosis in Macrophages. *Frontiers in Immunology* **2018**, *9*, 1419.

(126) Alexander, S. P. et al. The concise guide to pharmacology 2017/18: G protein-coupled receptors. *British Journal of Pharmacology* **2017**, *174*, S17–S129.

(127) Mahmud, Z. A. et al. Three classes of ligands each bind to distinct sites on the orphan G protein-coupled receptor GPR84. *Scientific reports* **2017**, *7*, 17953.

(128) Suzuki, M. et al. Medium-chain Fatty Acid-sensing Receptor, GPR84, Is a Proinflammatory Receptor. *Journal of Biological Chemistry* **2013**, *288*, 10684–10691.

(129) Gaidarov, I. et al. Embelin and its derivatives unravel the signaling, proinflammatory and antiatherogenic properties of GPR84 receptor. *Pharmacological Research* **2018**, *131*, 185–198.

(130) Chitra, M. et al. Antitumor, Anti-Inflammatory and Analgesic Property of Embelin, a Plant Product. *Chemotherapy* **1994**, *40*, 109–113.

(131) Chitra, M.; Devi, C. S. S.; Sukumar, E. Antibacterial activity of embelin. *Fitoterapia* **2003**, *74*, 401–3.

(132) Nikolovska-Coleska, Z. et al. Discovery of embelin as a cell-permeable, small-molecular weight inhibitor of XIAP through structure-based computational screening of a traditional herbal medicine three-dimensional structure database. *Journal of medicinal chemistry* **2004**, *47*, 2430–40.

(133) Joshi, R.; Kamat, J.; Mukherjee, T. Free radical scavenging reactions and antioxidant activity of embelin: Biochemical and pulse radiolytic studies. *Chemico-Biological Interactions* **2007**, *167*, 125–134.

(134) Gupta, R. et al. Antioxidant activity and protection of pancreatic β-cells by embelin in streptozotocin-induced diabetes. *Journal of Diabetes* **2012**, *4*, 248–256.

(135) Zhang, Q. et al. Discovery and Characterization of a Novel Small-Molecule Agonist for Medium-Chain Free Fatty Acid Receptor G Protein-Coupled Receptor 84. *The Journal of pharmacology and experimental therapeutics* **2016**, *357*, 337–44.

(136) Liu, Y. et al. Design and Synthesis of 2-Alkylpyrimidine-4,6-diol and 6-Alkylpyridine-2,4-diol as Potent GPR84 Agonists. *ACS Medicinal Chemistry Letters* **2016**, *7*, 579–583.

(137) Mancini, S. J. et al. On-target and off-target effects of novel orthosteric and allosteric activators of GPR84. *Scientific Reports* **2019**, *9*, 1861.

(138) Pillaiyar, T. et al. 6-(Ar)Alkylamino-Substituted Uracil Derivatives: Lipid Mimetics with Potent Activity at the Orphan G Protein-Coupled Receptor 84 (GPR84). *ACS Omega* **2018**, *3*, 3365–3383.

(139) Wang, T. T. et al. Broccoli-derived phytochemicals indole-3-carbinol and 3,3-diindolylmethane exerts concentration-dependent pleiotropic effects on prostate cancer cells: Comparison with other cancer preventive phytochemicals. *Molecular Carcinogenesis* **2012**, *51*, 244–256.

(140) Takeda, S. et al. Identification of surrogate ligands for orphan G protein-coupled receptors. *Life Sciences* **2003**, *74*, 367–377.

(141) Yin, H. et al. Lipid G protein-coupled receptor ligand identification using beta-arrestin PathHunter assay. *The Journal of biological chemistry* **2009**, *284*, 12328–38.

(142) Chen, I.; Safe, S.; Bjeldanes, L. Indole-3-carbinol and diindolylmethane as aryl hydrocarbon (Ah) receptor agonists and antagonists in T47D human breast cancer cells. *Biochemical Pharmacology* **1996**, *51*, 1069–1076.

(143) Rothhammer, V.; Quintana, F. J. The aryl hydrocarbon receptor: an environmental sensor integrating immune responses in health and disease. *Nature Reviews Immunology* **2019**, *19*, 184–197.

(144) Turcotte, C. et al. The CB2 receptor and its role as a regulator of inflammation. *Cellular and Molecular Life Sciences* **2016**, *73*, 4449–4470.

(145) Pillaiyar, T. et al. Diindolylmethane Derivatives: Potent Agonists of the Immunostimulatory Orphan G Protein-Coupled Receptor GPR84. *Journal of Medicinal Chemistry* **2017**, *60*, 3636–3655.

(146) Labéguère, F. et al. Novel dihydropyrimidinoisoquinolinones and pharmaceutical compositions thereof for the treatment of inflammatory disorders (gpr84 antagonists). *World patent WO2014095798A1.*, 2013.

(147) Gagnon, L. et al. A Newly Discovered Antifibrotic Pathway Regulated by Two Fatty Acid Receptors: GPR40 and GPR84. *The American Journal of Pathology* **2018**, *188*, 1132–1148.

(148) Khalil, N. et al. Phase 2 clinical trial of PBI-4050 in patients with idiopathic pulmonary fibrosis. *The European respiratory journal* **2019**, *53*, 1800663.

(149) Nikaido, Y. et al. Mutation analysis and molecular modeling for the investigation of ligand-binding modes of GPR84. *The Journal of Biochemistry* **2015**, *157*, 311–320.

(150) Crotti, A.; Ransohoff, R. M. Microglial Physiology and Pathophysiology: Insights from Genome-wide Transcriptional Profiling. *Immunity* **2016**, *44*, 505–515.

(151) Lattin, J. E. et al. Expression analysis of G Protein-Coupled Receptors in mouse macrophages. *Immunome research* **2008**, *4*, 5.

(152) Babcock, A. et al. Chemokine Expression by Glial Cells Directs Leukocytes to Sites of Axonal Injury in the CNS. *Journal of Neuroscience* **2008**, *23*, 7922–7930.

(153) Bouchard, C. et al. G protein-coupled receptor 84, a microglia-associated protein expressed in neuroinflammatory conditions. *Glia* **2007**, *55*, 790–800.

(154) Audoy-Rémus, J. et al. GPR84 deficiency reduces microgliosis, but accelerates dendritic degeneration and cognitive decline in a mouse model of Alzheimer's disease. *Brain, Behavior, and Immunity* **2015**, *46*, 112–120.

(155) Wei, L. et al. Agonists for G-protein-coupled receptor 84 (GPR84) alter cellular morphology and motility but do not induce pro-inflammatory responses in microglia. *Journal of Neuroinflammation* **2017**, *14*, 198.

(156) Grouix, B. et al. PBI-4050 Reduces Stellate Cell Activation and Liver Fibrosis through Modulation of Intracellular ATP Levels and the Liver Kinase B1/AMP-Activated Protein Kinase/Mammalian Target of Rapamycin Pathway. *The Journal of pharmacology and experimental therapeutics* **2018**, *367*, 71–81.

(157) Lavecchia, A.; Giovanni, C. Virtual Screening Strategies in Drug Discovery: A Critical Review. *Current Medicinal Chemistry* **2013**, *20*, 2839–2860.

(158) Ripphausen, P. et al. Quo Vadis, Virtual Screening? A Comprehensive Survey of Prospective Applications. *Journal of Medicinal Chemistry* **2010**, *53*, 8461–8467.

(159) Shoichet, B. K.; Kobilka, B. K. Structure-based drug screening for G-protein-coupled receptors. *Trends in Pharmacological Sciences* **2012**, *33*, 268–272.

(160) Carlsson, J. et al. Structure-Based Discovery of A2A Adenosine Receptor Ligands. *Journal of Medicinal Chemistry* **2010**, *53*, 3748–3755.

(161) Rosenbaum, D. M. et al. GPCR engineering yields high-resolution structural insights into beta2-adrenergic receptor function. *Science (New York, N.Y.)* **2007**, *318*, 1266–73.

(162) Zhang, D. et al. Structural Studies of G Protein-Coupled Receptors. *Molecules and Cells* **2015**, *38*, 836–842.

(163) Li, X. et al. Crystal Structure of the Human Cannabinoid Receptor CB2. *Cell* **2019**, *176*, 459–467.e13.

(164) Wang, L. et al. Structures of the Human PGD2 Receptor CRTH2 Reveal Novel Mechanisms for Ligand Recognition. *Molecular Cell* **2018**, *72*, 48–59.e4.

(165) Wardman, J. H. et al. Identification of a small-molecule ligand that activates the neuropeptide receptor GPR171 and increases food intake. *Science Signaling* **2016**, *9*, ra55–ra55.

(166) Michino, M. et al. Community-wide assessment of GPCR structure modelling and ligand docking: GPCR Dock 2008. *Nature Reviews Drug Discovery* **2009**, *8*, 455–463.

(167) Kufareva, I. et al. Status of GPCR Modeling and Docking as Reflected by Community-wide GPCR Dock 2010 Assessment. *Structure* **2011**, *19*, 1108–1126.

(168) Kufareva, I. et al. Advances in GPCR Modeling Evaluated by the GPCR Dock 2013 Assessment: Meeting New Challenges. *Structure* **2014**, *22*, 1120–1139.

(169) Carlsson, J. et al. Ligand discovery from a dopamine D3 receptor homology model and crystal structure. *Nature Chemical Biology* **2011**, *7*, 769–778.

(170) Beuming, T.; Sherman, W. Current Assessment of Docking into GPCR Crystal Structures and Homology Models: Successes, Challenges, and Guidelines. *Journal of Chemical Information and Modeling* **2012**, *52*, 3263–3277.

(171) Hua, T. et al. Crystal structures of agonist-bound human cannabinoid receptor CB1. *Nature* **2017**, *547*, 468–471.

(172) Costanzi, S.; Vilar, S. In Silico screening for agonists and blockers of the β2 adrenergic receptor: Implications of inactive and activated state structures. *Journal of Computational Chemistry* **2012**, *33*, 561–572.

(173) Kolb, P. et al. Structure-based discovery of beta2-adrenergic receptor ligands. *Proceedings of the National Academy of Sciences of the United States of America* **2009**, *106*, 6843–8.

(174) Katritch, V. et al. Structure-Based Discovery of Novel Chemotypes for Adenosine A2A Receptor Antagonists. *Journal of Medicinal Chemistry* **2010**, *53*, 1799–1809.

(175) Coudrat, T. et al. Structural features embedded in G protein-coupled receptor co-crystal structures are key to their success in virtual screening. *PLOS ONE* **2017**, *12*, e0174719.

(176) Gimeno, A. et al. The Light and Dark Sides of Virtual Screening: What Is There to Know? *International Journal of Molecular Sciences* **2019**, *20*, 1375.

(177) Irwin, J. J.; Shoichet, B. K. ZINC–a free database of commercially available compounds for virtual screening. *Journal of chemical information and modeling* **2005**, *45*, 177–82.

(178) Tikhonova, I. G. et al. Discovery of Novel Agonists and Antagonists of the Free Fatty Acid Receptor 1 (FFAR1) Using Virtual Screening. *Journal of Medicinal Chemistry* **2008**, *51*, 625–633.

(179) Bajusz, D.; Rácz, A.; Héberger, K. Why is Tanimoto index an appropriate choice for fingerprint-based similarity calculations? *Journal of Cheminformatics* **2015**, *7*, 20.

(180) Gianella-Borradori, M. et al. Ligand-based virtual screening identifies a family of selective cannabinoid receptor 2 agonists. *Bioorganic & Medicinal Chemistry* **2015**, *23*, 241–263.

(181) Hansch, C. et al. Correlation of Biological Activity of Phenoxyacetic Acids with Hammett Substituent Constants and Partition Coefficients. *Nature* **1962**, *194*, 178–180.

(182) Mueller, R. et al. Identification of Metabotropic Glutamate Receptor Subtype 5 Potentiators Using Virtual High-Throughput Screening. *ACS Chemical Neuroscience* **2010**, *1*, 288–305.

(183) Zhang, L. et al. Discovery of Novel Antimalarial Compounds Enabled by QSAR-Based Virtual Screening. *Journal of Chemical Information and Modeling* **2013**, *53*, 475–492.

(184) Floresta, G. et al. Discovery of High-Affinity Cannabinoid Receptors Ligands through a 3D-QSAR Ushered by Scaffold-Hopping Analysis. *Molecules* **2018**, *23*, 2183.

(185) Oloff, S.; Mailman, R. B.; Tropsha, A. Application of validated QSAR models of D1 dopaminergic antagonists for database mining. *Journal of Medicinal Chemistry* **2005**, *48*, 7322–7332.

(186) Neves, B. J. et al. QSAR-Based Virtual Screening: Advances and Applications in Drug Discovery. *Frontiers in Pharmacology* **2018**, *9*, 1275.

(187) Lo, Y.-C. et al. Machine learning in chemoinformatics and drug discovery. *Drug Discovery Today* **2018**, *23*, 1538–1546.

(188) Roth, B. L.; Irwin, J. J.; Shoichet, B. K. Discovery of new GPCR ligands to illuminate new biology. *Nature Chemical Biology* **2017**, *13*, 1143–1151.

(189) Zhang, R.; Xie, X. Tools for GPCR drug discovery. *Acta Pharmacologica Sinica* **2012**, *33*, 372–384.

(190) Masand, V. H. et al. Does tautomerism influence the outcome of QSAR modeling? *Medicinal Chemistry Research* **2014**, *23*, 1742–1757.

(191) Wilson, C. C.; Keen, D. A.; Stewart, N. S. On hydrogen atom positions in 3-deazauracil. *Journal of the Chemical Society, Chemical Communications* **1992**, 1160.

(192) Jalbout, A. F. et al. Structures, stabilities and tautomerizations of uracil and diphosphouracil tautomers. *Chemical Physics* **2007**, *332*, 152–161.

(193) Veerasamy, R. et al. Validation of QSAR Models - Strategies and Importance. *International Journal of Drug Design* **2011**, *2*, 511–519.

(194) Dahlin, J. L.; Inglese, J.; Walters, M. A. Mitigating risk in academic preclinical drug discovery. *Nature reviews. Drug discovery* **2015**, *14*, 279–94.

(195) Yu, N. et al. Real-Time Monitoring of Morphological Changes in Living Cells by Electronic Cell Sensor Arrays: An Approach To Study G Protein-Coupled Receptors. *Analytical Chemistry* **2006**, *78*, 35–43.

(196) Grundmann, M. et al. A Molecular Mechanism for Sequential Activation of a G Protein-Coupled Receptor. *Cell Chemical Biology* **2016**, *23*, 392–403.

(197) Peters, M. F.; Scott, C. W. Evaluating Cellular Impedance Assays for Detection of GPCR Pleiotropic Signaling and Functional Selectivity. *Journal of Biomolecular Screening* **2009**, *14*, 246–255.

(198) Baker, D.; Sali, A. Protein structure prediction and structural genomics. *Science (New York, N.Y.)* **2001**, *294*, 93–6.

(199) Wang, S. et al. Structure of the D2 dopamine receptor bound to the atypical antipsychotic drug risperidone. *Nature* **2018**, *555*, 269–273.

(200) Chen, Y.-C. Beware of docking! *Trends in Pharmacological Sciences* **2015**, *36*, 78–95.

(201) Drwal, M. N.; Griffith, R. Combination of ligand- and structure-based methods in virtual screening. *Drug Discovery Today: Technologies* **2013**, *10*, e395–e401.

(202) Hajjo, R. et al. Chemocentric Informatics Approach to Drug Discovery: Identification and Experimental Validation of Selective Estrogen Receptor Modulators as Ligands of 5-Hydroxytryptamine-6 Receptors and as Potential Cognition Enhancers. *Journal of Medicinal Chemistry* **2012**, *55*, 5704–5719.

(203) Golbraikh, A.; Tropsha, A. Beware of q2! *Journal of Molecular Graphics and Modelling* **2002**, *20*, 269–276.

(204) Keserű, G. M.; Makara, G. M. Hit discovery and hit-to-lead approaches. *Drug Discovery Today* **2006**, *11*, 741–748.

(205) Hughes, J. et al. Principles of early drug discovery. *British Journal of Pharmacology* **2011**, *162*, 1239–1249.

(206) Sander, T. et al. DataWarrior: An Open-Source Program For Chemistry Aware Data Visualization And Analysis. *Journal of Chemical Information and Modeling* **2015**, *55*, 460–473.

(207) Cao, Y.; Jiang, T.; Girke, T. A maximum common substructure-based algorithm for searching and predicting drug-like compounds. *Bioinformatics* **2008**, *24*, i366–i374.

(208) Backman, T. W. H.; Cao, Y.; Girke, T. ChemMine tools: an online service for analyzing and clustering small molecules. *Nucleic Acids Research* **2011**, *39*, W486–W491.

(209) Thorne, N.; Auld, D. S.; Inglese, J. Apparent activity in high-throughput screening: origins of compound-dependent assay interference. *Current Opinion in Chemical Biology* **2010**, *14*, 315–324.

(210) Centore, R. et al. Tautomerism in the Fused N-Rich Triazolotriazole Heterocyclic System. *European Journal of Organic Chemistry* **2013**, *2013*, 3721–3728.

(211) Biot, C. et al. 5-Substituted tetrazoles as bioisosteres of carboxylic acids. Bioisosterism and mechanistic studies on glutathione reductase inhibitors as antimalarials. *Journal of Medicinal Chemistry* **2004**, *47*, 5972–5983.

(212) Liao, J.-Z. et al. Coordination polymers of tetrazole-yl acylamide with octahedrally coordinated divalent transition metals: the effects of metal centers and side-groups on the structural topologies and symmetries. *CrystEngComm* **2013**, *15*, 4830.

(213) Filippakopoulos, P. et al. Selective inhibition of BET bromodomains. *Nature* **2010**, *468*, 1067–1073.

(214) O'Dwyer, P. J. et al. In *Clinical Trials*, American Association for Cancer Research: 2016; Vol. 76, CT014–CT014.

(215) Dickinson, M. et al. A Phase I Study of Molibresib (GSK525762), a Selective Bromodomain (BRD) and Extra Terminal Protein (BET) Inhibitor: Results from Part 1 of a Phase I/II Open Label Single Agent Study in Subjects with Non-Hodgkin's Lymphoma (NHL). *Blood* **2018**, *132*, 1682–1682.

(216) Roth, B. L. et al. Salvinorin A: a potent naturally occurring nonnitrogenous kappa opioid selective agonist. *Proceedings of the National Academy of Sciences of the United States of America* **2002**, *99*, 11934–9.

(217) Mahmoudi, T. et al. The kinase TNIK is an essential activator of Wnt target genes. *The EMBO Journal* **2009**, *28*, 3329–3340.

(218) Ho, K.-K. et al. Discovery of 4-phenyl-2-phenylaminopyridine based TNIK inhibitors. *Bioorganic & Medicinal Chemistry Letters* **2013**, *23*, 569–573.

(219) Arrowsmith, C. H. et al. The promise and peril of chemical probes. *Nature Chemical Biology* **2015**, *11*, 536–541.

(220) Roth, B. L.; Sheffler, D. J.; Kroeze, W. K. Magic shotguns versus magic bullets: selectively non-selective drugs for mood disorders and schizophrenia. *Nature Reviews Drug Discovery* **2004**, *3*, 353–359.

(221) Tan, Y. W.; Hong, W. J.; Chu, J. J. H. Inhibition of enterovirus VP4 myristoylation is a potential antiviral strategy for hand, foot and mouth disease. *Antiviral Research* **2016**, *133*, 191–195.

(222) Bhandarkar, S. S. et al. Tris (Dibenzylideneacetone) Dipalladium, a N-Myristoyltransferase-1 Inhibitor, Is Effective against Melanoma Growth In vitro and In vivo. *Clinical Cancer Research* **2008**, *14*, 5743–5748.

(223) Kallemeijn, W. W. et al. Validation and Invalidation of Chemical Probes for the Human N-myristoyltransferases. *Cell chemical biology* **2019**, *26*, 892–900.e4.

(224) Stefaniak, J. et al. Chemical Instability and Promiscuity of Arylmethylidenepyrazolinone-Based MDMX Inhibitors. *ACS Chemical Biology* **2018**, *13*, 2849–2854.

(225) Liu, X. et al. Iniparib Nonselectively Modifies Cysteine-Containing Proteins in Tumor Cells and Is Not a Bona Fide PARP Inhibitor. *Clinical Cancer Research* **2012**, *18*, 510–523.

(226) Taylor, L. et al. Primary Macrophage Chemotaxis Induced by Cannabinoid Receptor 2 Agonists Occurs Independently of the CB2 Receptor. *Scientific Reports* **2015**, *5*, 10682.

(227) Blagg, J.; Workman, P. Choose and Use Your Chemical Probe Wisely to Explore Cancer Biology. *Cancer cell* **2017**, *32*, 9–25.

(228) Swamy, K. C. K. et al. Mitsunobu and Related Reactions: Advances and Applications. *Chemical Reviews* **2009**, *109*, 2551–2651.

(229) Laurence, C. et al. The pKBHX Database: Toward a Better Understanding of Hydrogen-Bond Basicity for Medicinal Chemists. *Journal of Medicinal Chemistry* **2009**, *52*, 4073–4086.

(230) Nepali, K.; Lee, H.-Y.; Liou, J.-P. Nitro-Group-Containing Drugs. *Journal of Medicinal Chemistry* **2019**, *62*, 2851–2893.

(231) Sexton, P. M.; Christopoulos, A. To Bind or Not to Bind: Unravelling GPCR Polypharmacology. *Cell* **2018**, *172*, 636–638.

(232) Riley, R. J.; McGinnity, D. F.; Austin, R. P. A unified model for predicting human hepatic, metabolic clearance from in vitro intrinsic clearance data in hepatocytes and microsomes. *Drug metabolism and disposition: the biological fate of chemicals* **2005**, *33*, 1304–11.

(233) Tang, H. et al. Discovery of Selective Small Molecule ROMK Inhibitors as Potential New Mechanism Diuretics. *ACS Medicinal Chemistry Letters* **2012**, *3*, 367–372.

(234) Fleming, F. F. et al. Nitrile-Containing Pharmaceuticals: Efficacious Roles of the Nitrile Pharmacophore. *Journal of Medicinal Chemistry* **2010**, *53*, 7902–7917.

(235) Richardson, S. J. et al. Efficiency in Drug Discovery: Liver S9 Fraction Assay As a Screen for Metabolic Stability. *Drug metabolism letters* **2016**, *10*, 83–90.

(236) Brandon, E. F. et al. An update on in vitro test methods in human hepatic drug biotransformation research: pros and cons. *Toxicology and Applied Pharmacology* **2003**, *189*, 233–246.

(237) Singh, J. K.; Solanki, A.; Shirsath, V. S. Comparative in-vitro Intrinsic Clearance of Imipramine in Multiple Species Liver Microsomes: Human, Rat, Mouse and Dog. *J Drug Metab Toxicol* **2012**, *3*, 126.

(238) Pryde, D. C. et al. Aldehyde Oxidase: An Enzyme of Emerging Importance in Drug Discovery. *Journal of Medicinal Chemistry* **2010**, *53*, 8441–8460.

(239) Lepri, S. et al. Structure-metabolism relationships in human-AOX: Chemical insights from a large database of aza-aromatic and amide compounds. *Proceedings of the National Academy of Sciences of the United States of America* **2017**, *114*, E3178–E3187.

(240) St. Jean, D. J.; Fotsch, C. Mitigating Heterocycle Metabolism in Drug Discovery. *Journal of Medicinal Chemistry* **2012**, *55*, 6002–6020.

(241) Yan, Y.-X. et al. Cell-Based High-Throughput Screening Assay System for Monitoring G Protein-Coupled Receptor Activation Using β-Galactosidase Enzyme Complementation Technology. *Journal of Biomolecular Screening* **2002**, *7*, 451–459.

(242) McGovern, S. L. et al. A Common Mechanism Underlying Promiscuous Inhibitors from Virtual and High-Throughput Screening. *Journal of Medicinal Chemistry* **2002**, *45*, 1712–1722.

(243) Coan, K. E. D.; Shoichet, B. K. Stoichiometry and Physical Chemistry of Promiscuous Aggregate-Based Inhibitors. *Journal of the American Chemical Society* **2008**, *130*, 9606–9612.

(244) Owen, S. C. et al. Colloidal Aggregation Affects the Efficacy of Anticancer Drugs in Cell Culture. *ACS Chemical Biology* **2012**, *7*, 1429–1435.

(245) McGovern, S. L. et al. A Specific Mechanism of Nonspecific Inhibition. *Journal of Medicinal Chemistry* **2003**, *46*, 4265–4272.

(246) Feng, B. Y.; Shoichet, B. K. A detergent-based assay for the detection of promiscuous inhibitors. *Nature Protocols* **2006**, *1*, 550–553.

(247) LaPlante, S. R. et al. Compound Aggregation in Drug Discovery: Implementing a Practical NMR Assay for Medicinal Chemists. *Journal of Medicinal Chemistry* **2013**, *56*, 5142–5150.

(248) Zega, A. NMR Methods for Identification of False Positives in Biochemical Screens. *Journal of Medicinal Chemistry* **2017**, *60*, 9437–9447.

(249) Huang, R.; Leung, I. K. Protein–Small Molecule Interactions by WaterLOGSY. *Methods in Enzymology* **2019**, *615*, 477–500.

(250) Luttrell, L. M.; Maudsley, S.; Bohn, L. M. Fulfilling the Promise of "Biased" G Protein-Coupled Receptor Agonism. *Molecular Pharmacology* **2015**, *88*, 579–588.

(251) Brown, A. J. et al. Transcriptome-Based Identification of the Optimal Reference CHO Genes for Normalisation of qPCR Data. *Biotechnology Journal* **2018**, *13*, 1700259.

(252) Nickolls, S. A. et al. Co-Expression of GRK2 Reveals a Novel Conformational State of the μ-Opioid Receptor. *PLoS ONE* **2013**, *8*, e83691.

(253) Winpenny, D.; Clark, M.; Cawkill, D. Biased ligand quantification in drug discovery: from theory to high throughput screening to identify new biased μ opioid receptor agonists. *British Journal of Pharmacology* **2016**, *173*, 1393–1403.

(254) Irwin, J. J. et al. An Aggregation Advisor for Ligand Discovery. *Journal of Medicinal Chemistry* **2015**, *58*, 7076–7087.

(255) Feng, B. Y. et al. High-throughput assays for promiscuous inhibitors. *Nature Chemical Biology* **2005**, *1*, 146–148.

(256) Coan, K. E. D. et al. Promiscuous Aggregate-Based Inhibitors Promote Enzyme Unfolding. *Journal of Medicinal Chemistry* **2009**, *52*, 2067–2075.

(257) Sassano, M. F. et al. Colloidal Aggregation Causes Inhibition of G Protein-Coupled Receptors. *Journal of Medicinal Chemistry* **2013**, *56*, 2406–2414.

(258) Oakley, R. H. et al. The Cellular Distribution of Fluorescently Labeled Arrestins Provides a Robust, Sensitive, and Universal Assay for Screening G Protein-Coupled Receptors. *Assay and Drug Development Technologies* **2002**, *1*, 21–30.

(259) Hislop, J. N.; von Zastrow, M. In *Methods in molecular biology (Clifton, N.J.)* 2011; Vol. 746, pp 425–440.

(260) Kim, J. et al. Functional antagonism of different G protein-coupled receptor kinases for beta-arrestin-mediated angiotensin II receptor signaling. *Proceedings of the National Academy of Sciences of the United States of America* **2005**, *102*, 1442–7.

(261) Ren, X.-R. et al. Different G protein-coupled receptor kinases govern G protein and beta-arrestin-mediated signaling of V2 vasopressin receptor. *Proceedings of the National Academy of Sciences of the United States of America* **2005**, *102*, 1448–53.

(262) Violin, J. D.; Ren, X.-R.; Lefkowitz, R. J. G-protein-coupled receptor kinase specificity for beta-arrestin recruitment to the beta2-adrenergic receptor revealed by fluorescence resonance energy transfer. *The Journal of biological chemistry* **2006**, *281*, 20577–88.

(263) Butcher, A. J. et al. Differential G-protein-coupled receptor phosphorylation provides evidence for a signaling bar code. *The Journal of biological chemistry* **2011**, *286*, 11506–18.

(264) Nobles, K. N. et al. Distinct phosphorylation sites on the β(2)-adrenergic receptor establish a barcode that encodes differential functions of β-arrestin. *Science signaling* **2011**, *4*, ra51.

(265) Busillo, J. M. et al. Site-specific phosphorylation of CXCR4 is dynamically regulated by multiple kinases and results in differential modulation of CXCR4 signaling. *The Journal of biological chemistry* **2010**, *285*, 7805–17.

(266) Luo, J. et al. G Protein-Coupled Receptor Kinase 3 and Protein Kinase C Phosphorylate the Distal C-Terminal Tail of the Chemokine Receptor CXCR4 and Mediate Recruitment of β-Arrestin. *Molecular pharmacology* **2017**, *91*, 554–566.

(267) Xiao, R. P. Beta-adrenergic signaling in the heart: dual coupling of the beta2-adrenergic receptor to G(s) and G(i) proteins. *Science's STKE : signal transduction knowledge environment* **2001**, *2001*, re15.

(268) da Silva Junior, E. D. et al. Factors influencing biased agonism in recombinant cells expressing the human α1A -adrenoceptor. *British journal of pharmacology* **2017**, *174*, 2318–2333.

(269) Onfroy, L. et al. G protein stoichiometry dictates biased agonism through distinct receptor-G protein partitioning. *Scientific Reports* **2017**, *7*, 7885.

(270) Loniewski, K. et al. Toll-like receptors differentially regulate GPCR kinases and arrestins in primary macrophages. *Molecular Immunology* **2008**, *45*, 2312–2322.

(271) Grant, K. R. et al. Differential G-protein expression daring B- and T-cell development. *Immunology* **1997**, *90*, 564–571.

(272) Michel, M. C.; Seifert, R.; Bond, R. A. Dynamic bias and its implications for GPCR drug discovery. *Nature Reviews Drug Discovery* **2014**, *13*, 869–869.

(273) Greenberg, S.; Grinstein, S. Phagocytosis and innate immunity. *Current Opinion in Immunology* **2002**, *14*, 136–145.

(274) Flannagan, R. S.; Jaumouillé, V.; Grinstein, S. The Cell Biology of Phagocytosis. *Annual Review of Pathology: Mechanisms of Disease* **2012**, *7*, 61–98.

(275) Fairn, G. D.; Grinstein, S. How nascent phagosomes mature to become phagolysosomes. *Trends in immunology* **2012**, *33*, 397–405.

(276) Sokol, C. L.; Luster, A. D. The chemokine system in innate immunity. *Cold Spring Harbor Perspectives in Biology* **2015**, *7*, 1–20.

(277) Kamp, M. E.; Liu, Y.; Kortholt, A. Function and regulation of heterotrimeric g proteins during chemotaxis. *International Journal of Molecular Sciences* **2016**, *17*, 90.

(278) Kölsch, V.; Charest, P. G.; Firtel, R. A. The regulation of cell motility and chemotaxis by phospholipid signaling. *Journal of cell science* **2008**, *121*, 551–9.

(279) DeFea, K. A. Stop That Cell! β-Arrestin-Dependent Chemotaxis: A Tale of Localized Actin Assembly and Receptor Desensitization. *Annual Review of Physiology* **2007**, *69*, 535–560.

(280) Brys, R. C. X.; Dupont, S. Screening methods to identify compounds useful in the prevention and/or treatment of inflammatory conditions. *World patent WO2013092793A1.*, 2012.

(281) Groot-Kormelink, P. J. et al. Quantitative GPCR and ion channel transcriptomics in primary alveolar macrophages and macrophage surrogates. *BMC Immunology* **2012**, *13*, 57.

(282) Iqbal, A. J. et al. A Real Time Chemotaxis Assay Unveils Unique Migratory Profiles amongst Different Primary Murine Macrophages. *PLoS ONE* **2013**, *8*, e58744.

(283) Foxman, E. F.; Campbell, J. J.; Butcher, E. C. Multistep navigation and the combinatorial control of leukocyte chemotaxis. *The Journal of cell biology* **1997**, *139*, 1349–60.

(284) Ross, R. Atherosclerosis — An Inflammatory Disease. *New England Journal of Medicine* **1999**, *340*, 115–126.

(285) Stallaert, W. et al. Impedance Responses Reveal β2-Adrenergic Receptor Signaling Pluridimensionality and Allow Classification of Ligands with Distinct Signaling Profiles. *PLoS ONE* **2012**, *7*, e29420.

(286) Fong, A. M. et al. Defective lymphocyte chemotaxis in beta-arrestin2- and GRK6-deficient mice. *Proceedings of the National Academy of Sciences of the United States of America* **2002**, *99*, 7478–83.

(287) Zoudilova, M. et al. beta-Arrestins scaffold cofilin with chronophin to direct localized actin filament severing and membrane protrusions downstream of protease-activated receptor-2. *The Journal of biological chemistry* **2010**, *285*, 14318–29.

(288) Hunton, D. L. et al. Beta-arrestin 2-dependent angiotensin II type 1A receptor-mediated pathway of chemotaxis. *Molecular pharmacology* **2005**, *67*, 1229–36.

(289) Cheung, R. et al. An arrestin-dependent multi-kinase signaling complex mediates MIP-1β/CCL4 signaling and chemotaxis of primary human macrophages. *Journal of Leukocyte Biology* **2009**, *86*, 833–845.

(290) Liu, Z. et al. TLR4 Signaling augments monocyte chemotaxis by regulating G protein-coupled receptor kinase 2 translocation. *Journal of immunology (Baltimore, Md. : 1950)* **2013**, *191*, 857–64.

(291) Daigneault, M. et al. The identification of markers of macrophage differentiation in PMA-stimulated THP-1 cells and monocyte-derived macrophages. *PLoS ONE* **2010**, *5*, e8668.

(292) Mendoza-Coronel, E.; Castañón-Arreola, M. Comparative evaluation of in vitro human macrophage models for mycobacterial infection study. *Pathogens and Disease* **2016**, *74*, ftw052.

(293) Danikas, D. D. et al. Prognostic value of phagocytic activity of neutrophils and monocytes in sepsis. Correlation to CD64 and CD14 antigen expression. *Clinical and experimental immunology* **2008**, *154*, 87–97.

(294) Brophy, M. L. et al. Eating the Dead to Keep Atherosclerosis at Bay. *Frontiers in Cardiovascular Medicine* **2017**, *4*, 2.

(295) White, G. E.; Iqbal, A. J.; Greaves, D. R. CC Chemokine Receptors and Chronic Inflammation—Therapeutic Opportunities and Pharmacological Challenges. *Pharmacological Reviews* **2013**, *65*, 47–89.

(296) Sun, J.; Lin, X. β-Arrestin 2 is required for lysophosphatidic acid-induced NF-kB activation. *Proceedings of the National Academy of Sciences* **2008**, *105*, 17085–17090.

(297) Weïwer, M. et al. Functionally Biased D2R Antagonists: Targeting the β-Arrestin Pathway to Improve Antipsychotic Treatment. *ACS Chemical Biology* **2018**, *13*, 1038–1047.

(298) Shrestha, R. et al. Plasma capric acid concentrations in healthy subjects determined by high-performance liquid chromatography. *Annals of Clinical Biochemistry* **2015**, *52*, 588–596.

(299) Ngo, T. et al. Orphan receptor ligand discovery by pickpocketing pharmacological neighbors. *Nature Chemical Biology* **2017**, *13*, 235–242.

(300) Milligan, G. G protein-coupled receptors not currently in the spotlight: free fatty acid receptor 2 and GPR35. *British journal of pharmacology* **2018**, *175*, 2543–2553.

(301) McHugh, D. et al. N-arachidonoyl glycine, an abundant endogenous lipid, potently drives directed cellular migration through GPR18, the putative abnormal cannabidiol receptor. *BMC Neuroscience* **2010**, *11*, 44.

(302) Cheeseright, T. et al. Molecular Field Extrema as Descriptors of Biological Activity: Definition and Validation. *Journal of Chemical Information and Modeling* **2006**, *46*, 665–676.

(303) Marim, F. M. et al. A Method for Generation of Bone Marrow-Derived Macrophages from Cryopreserved Mouse Bone Marrow Cells. *PLoS ONE* **2010**, *5*, ed. by Bozza, P. T., e15263.

(304) Englen, M. D. et al. Granulocyte/macrophage colony-stimulating factor is expressed and secreted in cultures of murine L929 cells. *Journal of immunological methods* **1995**, *184*, 281–3.

(305) Lew, M. Good statistical practice in pharmacology Problem 2. *British Journal of Pharmacology* **2009**, *152*, 299–303.

(306) Sato, Y. et al. Benzoxazole derivatives as novel 5-HT 3 receptor partial agonists in the gut. *Journal of Medicinal Chemistry* **1998**, *41*, 3015–3021.

Appendix

Appendix Table 1: The compound dataset used for external validation of QSAR models. Each compound was screened against the two QSAR models based on the lactim and 2-keto tautomers respectively, prior to biological testing in GPR84-CHO cAMP assays. The observed pEC_{50} are the pooled means of 2–3 independent experiments. The compounds in this dataset were synthesised by Bridget Reeve.

ID	Structure	GPR84 cAMP activity (pEC_{50})		
		Predicted (Lactim)	**Predicted (2-Keto)**	**Observed**
BR-01.4	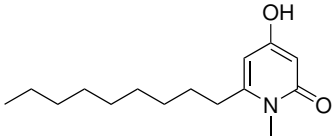	8.2	10	8.2
BR-08	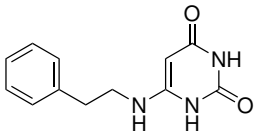	7.4	6.2	6.6
BR-10	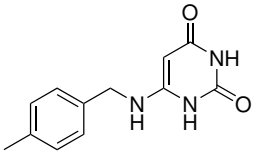	7.9	7.0	6.0
BR-11	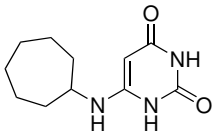	8.1	5.5	5.2
BR-12	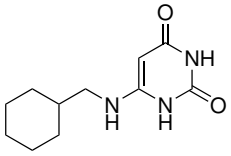	7.2	6.5	5.2
BR-13	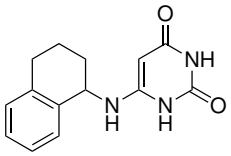	6.2	5.9	5.6
BR-14	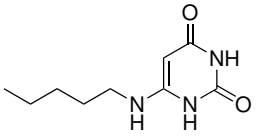	7.1	7.1	6.2
BR-15	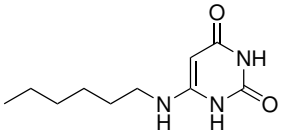	7.8	7.8	6.9
BR-17	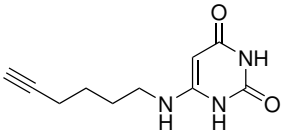	6.9	7.9	6.1
BR-22	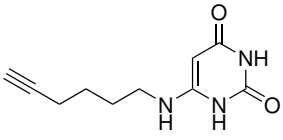	8.8	7.0	6.5

Appendix Table 2: Virtual screening data and biological testing of top-ranked compounds from an in-house 10 000 compound library. Similarity score calculated by Forge is relative to the 6-OAU-like molecules used as an alignment reference for the QSAR model. Activity data are given as the percentage of the response to 6-OAU and are mean ± SD of 3 technical replicates in 1 experiment. Data highlighted in red indicate those compounds considered a screening hit.

ID	Structure	Molecular weight	Similarity	Predicted potency (pEC_{50})	GPR84 activity (% at 30 µM)
S1	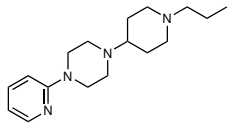	292	0.655	9.5	23.22 ± 4.25
S2	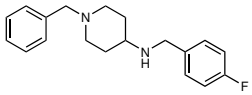	300	0.649	8.3	-30.60 ± 80.25
S3	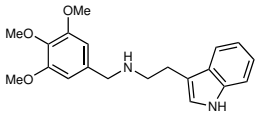	341	0.677	8.0	-4.82 ± 29.77
S4	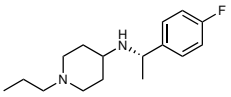	266	0.656	7.9	6.51 ± 22.41
S5	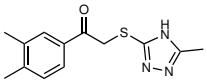	261	0.627	7.1	25.03 ± 10.93
S6	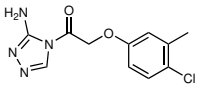	267	0.673	7.1	29.56 ± 30.11
S7	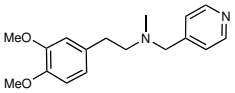	287	0.667	7.1	-63.55 ± 63.57
S8	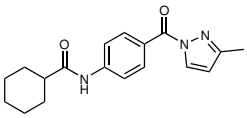	311	0.600	7.0	1.53 ± 39.45
S9	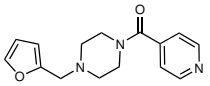	272	0.642	7.0	-63.55 ± 63.57
S10	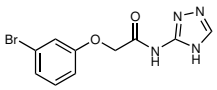	297	0.649	6.9	44.86 ± 1.17
41	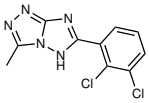	268	0.654	6.7	85.06 ± 12.38
S12	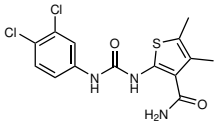	358	0.619	6.6	23.68 ± 13.13
40	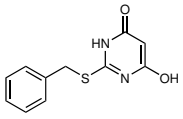	234	0.764	6.6	100.3 ± 2.54
S14	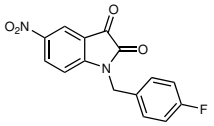	300	0.591	6.6	22.42 ± 53.97

ID	Structure	Molecular weight	Similarity	Predicted potency (pEC_{50})	GPR84 activity (% at 30 μM)
S15	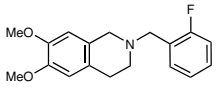	302	0.622	6.5	-25.98 ± 58.96
S16	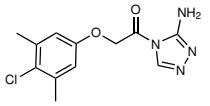	281	0.667	6.5	18.01 ± 37.87
S17	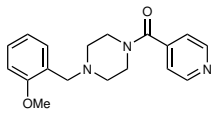	312	0.623	6.4	19.16 ± 14.21
S18	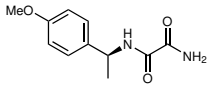	222	0.608	6.3	14.36 ± 24.95
44	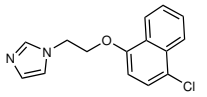	273	0.659	6.3	93.08 ± 0.95
S20	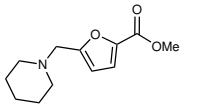	224	0.589	6.3	20.22 ± 41.17
S21	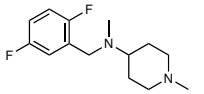	256	0.613	6.2	-96.45 ± 87.40
S22	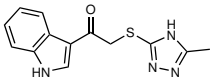	272	0.624	6.2	-110.40 ± 86.23
S23	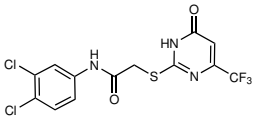	398	0.646	6.1	-10.82 ± 34.27
S24	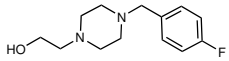	239	0.641	6.1	-60.96 ± 69.33
S25	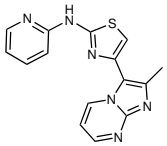	308	0.630	6.1	-11.05 ± 47.17
S26	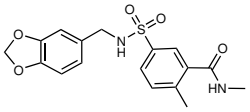	362	0.627	6.1	-43.84 ± 48.96
S27	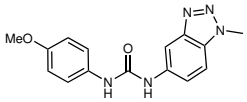	297	0.642	6.0	-64.79 ± 81.78
39	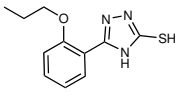	235	0.587	5.9	96.31 ± 13.04
S29	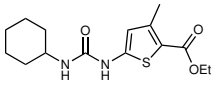	310	0.615	5.9	-15.02 ± 1.67
S30	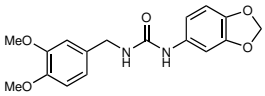	330	0.636	5.8	10.51 ± 11.36
S31	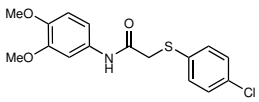	338	0.638	5.8	-70.17 ± 29.79

ID	Structure	Molecular weight	Similarity	Predicted potency (pEC_{50})	GPR84 activity (% at 30 μM)
S32	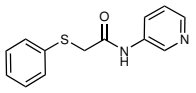	244	0.640	5.8	39.24 ± 30.95
S33	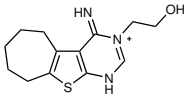	264	0.576	5.7	-35.45 ± 19.63
42	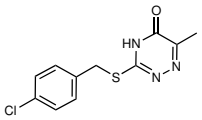	268	0.707	5.6	74.59 ± 13.17
S35	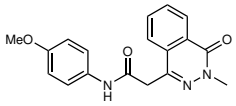	323	0.613	5.6	25.53 ± 15.91
S36	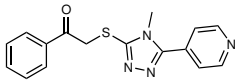	310	0.588	5.6	21.92 ± 25.43
S37	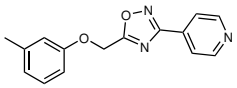	267	0.620	5.6	96.88 ± 5.31
S38	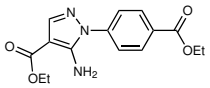	303	0.614	5.6	-100.6 ± 40.78
43	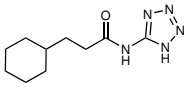	222	0.660	5.5	88.63 ± 5.27
S40	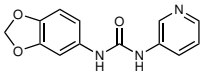	257	0.642	5.4	4.90 ± 11.97
S41	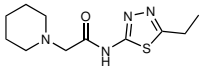	255	0.640	4.9	-16.68 ± 11.65
S42	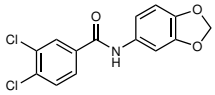	310	0.632	4.7	16.82 ± 20.71
S43	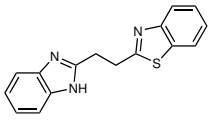	279	0.660	4.7	-0.42 ± 25.43
S44	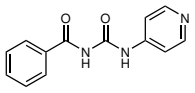	241	0.615	4.7	-11.03 ± 31.91
S45	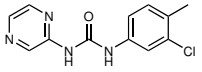	263	0.636	4.7	15.2 ± 12.19

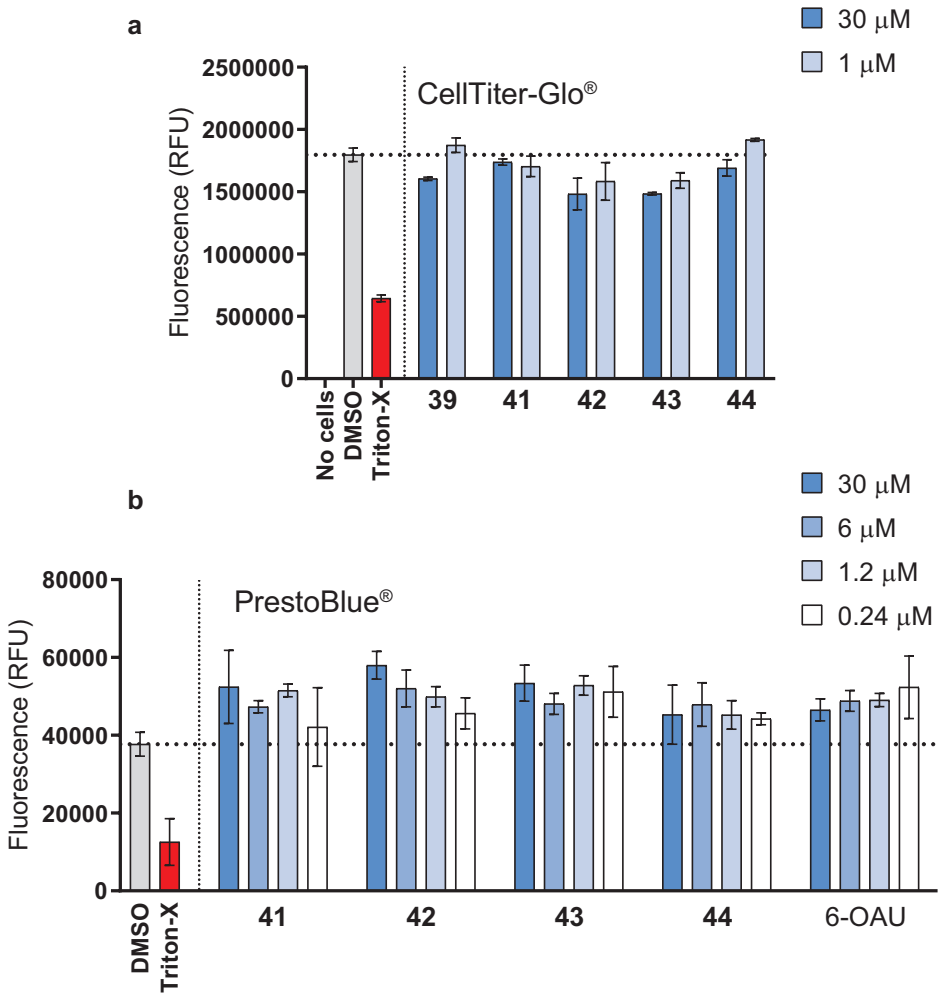

Appendix Figure 1: None of the GPR84 active screening hits show significant cell toxicity. Compounds were tested in two commercial cellular viability assays **(a)** CellTiter-Glo® and **(b)** PrestoBlue®. GPR84-CHO cells were incubated with compounds for 30 min prior to cell lysis. Pre-incubation with Triton X-100 (10 %) was used as a positive control for cell death. Data are shown as means ± SD for 3 technical replicates.

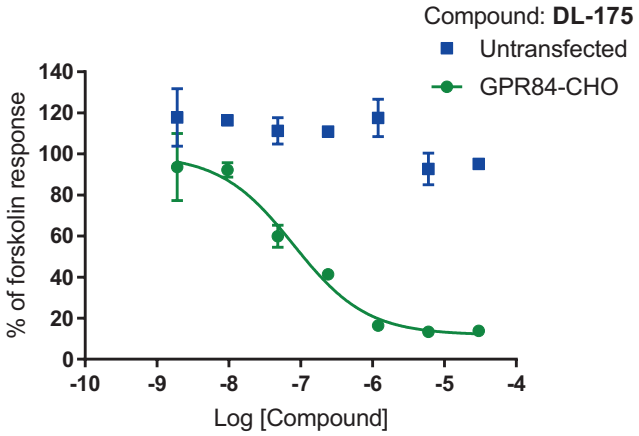

Appendix Figure 2: DL-175 specifically activates GPR84. cAMP accumulation data for DL-175 stimulation of either GPR84-CHO cells or untransfected CHO cells. Data are displayed as mean ± SD for two technical replicates, and are representative of two independent experiments.

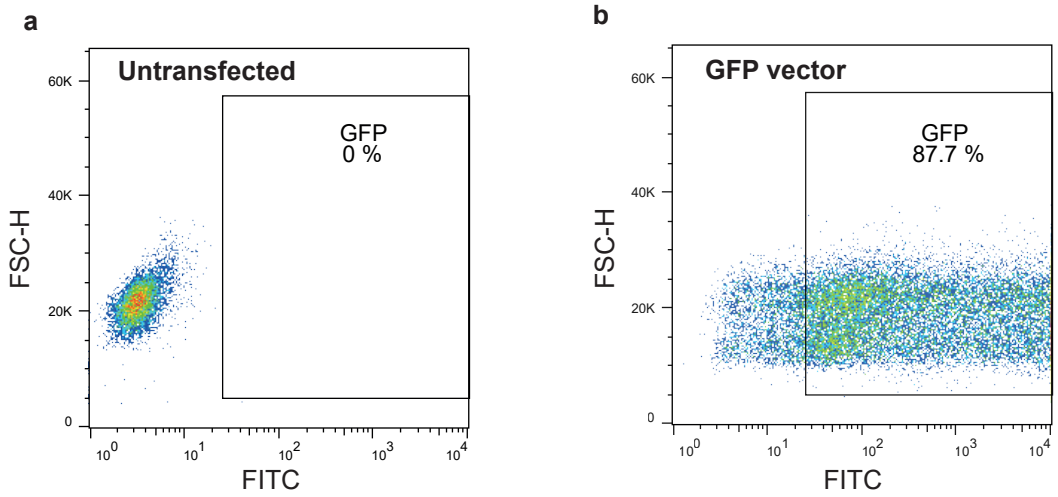

Appendix Figure 3: Confirmation of high transfection efficiencies using lipofectamine with GPR84-CHO cells. GPR84-CHO cells were either **(a)** not transfected, or **(b)** transfected with a GFP expression plasmid and the transfection efficiency determined using flow cytometry to identify the percentage of GFP positive cells.

Appendix Table 3: GPCR screening data with DL-175 tested at 3 µM (gpcrMAX DiscoverX panel). Activity given as % of activity of reference compound in agonist mode, and as the % inhibition of a reference compound in antagonist mode. Data are means of 2 technical replicates.

GPCR gene symbol	Agonist mode (% activity)	Antagonist mode (% inhibition)
ADCYAP1R1	0	2
ADORA3	1	-10
ADRA1B	1	39
ADRA2A	-6	9
ADRA2B	-8	50
ADRA2C	-2	22
ADRB1	0	-9
ADRB2	0	10
AGTR1	1	3
AGTRL1	-1	3
AVPR1A	0	-9
AVPR1B	1	7
AVPR2	-2	7
BDKRB1	-2	9

GPCR gene symbol	Agonist mode (% activity)	Antagonist mode (% inhibition)
BDKRB2	-1	12
BRS3	4	-4
C3AR1	0	4
C5AR1	0	5
C5L2	3	-8
CALCR	2	-11
CALCRL-RAMP1	1	0
CALCRL-RAMP2	-2	5
CALCRL-RAMP3	0	10
CALCR-RAMP2	-1	-6
CALCR-RAMP3	2	16
CCKAR	0	14
CCKBR	-6	3
CCR10	0	-7
CCR1	-9	5
CCR2	1	-3
CCR3	-4	9
CCR4	1	1
CCR5	1	7
CCR6	0	6
CCR7	0	12
CCR8	0	11
CCR9	0	0
CHRM1	2	-14
CHRM2	1	7
CHRM3	1	-18
CHRM4	-7	11
CHRM5	9	-17

GPCR gene symbol	Agonist mode (% activity)	Antagonist mode (% inhibition)
CMKLR1	0	11
CNR1	-1	1
CNR2	-16	17
CRHR1	0	1
CRHR2	-1	9
CRTH2	-1	-7
CX3CR1	0	10
CXCR1	0	-3
CXCR2	-1	12
CXCR3	-3	4
CXCR4	13	-13
CXCR5	-1	12
CXCR6	0	16
CXCR7	1	9
DRD1	0	-3
DRD2L	4	-2
DRD2S	0	-1
DRD3	0	14
DRD4	-2	3
DRD5	0	2
EBI2	2	-10
EDG1	2	-9
EDG3	3	5
EDG4	0	3
EDG5	0	7
EDG6	6	1
EDG7	0	10
EDNRA	0	10

GPCR gene symbol	Agonist mode (% activity)	Antagonist mode (% inhibition)
EDNRB	0	-4
F2R	1	-6
F2RL1	-1	0
F2RL3	0	5
FFAR1	-14	12
FPR1	6	0
FPRL1	0	2
FSHR	-1	22
GALR1	-2	3
GALR2	2	-8
GCGR	-1	11
GHSR	1	3
GIPR	1	-9
GLP1R	1	-11
GLP2R	2	0
GPR1	-1	5
GPR103	-6	-24
GPR109A	2	-11
GPR109B	0	-5
GPR119	5	9
GPR120	1	1
GPR35	3	-5
GPR92	0	19
GRPR	0	-4
HCRTR1	0	6
HCRTR2	0	1
HRH1	-2	16
HRH2	1	-1

GPCR gene symbol	Agonist mode (% activity)	Antagonist mode (% inhibition)
HRH3	-2	12
HRH4	0	1
HTR1A	-1	10
HTR1B	1	-1
HTR1E	3	25
HTR1F	3	2
HTR2A	2	-29
HTR2C	1	-6
HTR5A	1	4
KISS1R	2	-5
LHCGR	1	0
LTB4R	0	10
MC1R	-5	8
MC3R	-2	-5
MC4R	-1	0
MC5R	3	15
MCHR1	3	-16
MCHR2	0	-4
MLNR	1	-3
MRGPRX1	0	-1
MRGPRX2	1	0
MTNR1A	19	-1
NMBR	-1	-3
NMU1R	0	-7
NPBWR1	-1	4
NPBWR2	0	5
NPFFR1	2	22
NPSR1B	0	-10

GPCR gene symbol	Agonist mode (% activity)	Antagonist mode (% inhibition)
NPY1R	0	3
NPY2R	0	2
NTSR1	2	3
OPRD1	1	4
OPRK1	1	-10
OPRL1	2	-11
OPRM1	0	8
OXER1	-3	-10
OXTR	1	-2
P2RY1	0	-10
P2RY11	0	-6
P2RY12	2	4
P2RY2	0	11
P2RY4	1	3
P2RY6	2	3
PPYR1	0	10
PRLHR	2	-5
PROKR1	0	12
PROKR2	0	-9
PTAFR	-1	-3
PTGER2	1	5
PTGER3	1	11
PTGER4	1	5
PTGFR	1	-10
PTGIR	5	-6
PTHR1	1	1
PTHR2	0	1
RXFP3	2	19

GPCR gene symbol	Agonist mode (% activity)	Antagonist mode (% inhibition)
SCTR	2	1
SSTR1	6	-7
SSTR2	0	2
SSTR3	1	5
SSTR5	0	4
TACR1	-2	2
TACR2	1	4
TACR3	1	1
TBXA2R	2	3
TRHR	1	7
TSHR(L)	-1	10
UTR2	1	-7
VIPR1	-1	3
VIPR2	0	5